UNIVERSITE DE NEUCHATEL

Ph.D. prepared in the Microelectronics group of
European Organisation for Nuclear Research (CERN)

presented by

François POWOLNY

The 7^{th} of may 2009

Title :

Characterization of

time resolved photodetector systems

for Positron Emission Tomography

JURY

M. Christophe BALLIF

M. Matthieu DESPEISSE

M. Gunther DISSERTORI

M. Pierre-Andre FARINE

M. Delfo SANFILIPPO

M. Lukas TLUSTOS

Université de Neuchâtel

FACULTE DES SCIENCES
Secrétariat-Décanat de la faculté
- Rue Emile-Argand 11
- CP 158
- CH-2009 Neuchâtel

IMPRIMATUR POUR LA THESE

Characterization of time resolved photodetector systems for Positron Emission Tomography

François POWOLNY

UNIVERSITE DE NEUCHATEL

FACULTE DES SCIENCES

La Faculté des sciences de l'Université de Neuchâtel,
sur le rapport des membres du jury

MM. C. Ballif (directeur de thèse),
P.-A. Farine, M. Despeisse,
G. Dissertori (ETH-Zürich), L. Tlustos (CERN, Genève)
et D. Sanfilippo (ST Microelectronics, Catania)

autorise l'impression de la présente thèse.

Neuchâtel, le 6 août 2009

Le doyen :
F. Kessler

UNIVERSITE DE NEUCHATEL
FACULTE DES SCIENCES
Secrétariat - décanat de la faculté
Rue Emile-Argand 11 - CP 158
CH-2009 Neuchâtel

■ Téléphone : +41 32 718 21 00 ■ E-mail : secretariat.sciences@unine.ch ■ www.unine.ch/sciences

à ma Soizic

Acknowledgement

First of all, I would like to thank Pierre Jarron, who invited me to join his team and who has given me the opportunity to work at CERN, in a very motivating and international environment. Thank you for your trust and for your support.

I am grateful to Mike Letheren, Alessandro Marchioro and Jorgen Christiansen for accepting me in the MIC group. I would like also to thank Christophe Ballif, my thesis director, who took the time to regularly follow my work and whose remarks guided me through important steps during my PhD. Thanks also to Jon Lapington who offered me the possibility to finish my PhD work in excellent conditions.

My very special thanks to Matthieu Despeisse, my colleague, friend and partial supervisor who accepted the huge task to correct my thesis so carefully and to be part of the jury. Thank you for all your encouragements and for the work ethic you taught me.

Muito obrigado to Danielle Moraes who was my first supervisor at CERN and who taught me the very basis of the work. Vielen Danken to Tom Meyer, the project leader of BioCare, who took a lot of time to help me in my work, from the hours in the lab to the deep correction of this thesis. Thanks to Gunther Dissertori, Pierre-Andre Farine, Delfo Sanfilippo and Lukas Tlustos who have accepted the invitation to participate in my jury and who have read this thesis with care.

Thanks to Paul Lecoq, Etiennette Auffray-Hillemanns and Hartmut Hillemanns for all your advice during all our meetings. Thanks to Nicolas Wyrsch from IMT, who has built the a-Si:H MCP structures, for his kindness and all the explanations concerning the technology of the prototypes. Thanks to John Morse and Irina Snigireva from ESRF who gave me the possibility to use the electron gun.

Thank you to the people of the MIC group. Although they were not part of my projects, they were always available to answer my questions and to help me. Thanks to Giovanni Anelli for explaining to me what is an APD (solution page 65), Jan Kaplon and Francis Anghinolfi (respectively the designers of the FEDC05 and NINO chips) for their help, David Porret and Sandra Velitchko for the design of the different boards that I have used.

I would like also to thank Rui de Olivera, Ian Mc Gill, Francoise

Cossey, Antoine Guippet, Nicole Wauquier, Stephanne Excoffier and all the people working with them in the SMD workshop, Bonding Lab and PCB workshop, for the good quality of their work always with the minimal delays.

Moltes gracies to Rafael Ballabriga my colleague and friend for all the discussions, coffee breaks and also for his help in electronics. Thank you to Winnie Wong for her friendship, her refreshing energy and also for all the corrections she did in this thesis.

Huge thanks to all my colleagues and friends: Filip, Giulia, Raquel, Florent, Stefanos, Stefano, Victor, Didier, Barnabe, Alessandro, Sandro, Eduardo, Hugo, Christian(s), Cristian, Filipe, Julie, Caroline, Franz, Nathanael, Johan, Massimo. You make make it very pleasant to work here.

Thanks to my water polo team with whom I escaped from work and from the stress of writing a thesis. Allez Carouge! ($http://www.carouge-natation.com/wp/$).

I would like to thank all my family for their love and support despite the long distance that is now between us.

Finally I would like to express all my love and gratitude to Soizic for all her support and for all the sacrifices she has made for me. This work is dedicated to you.

Key words: Photodetector, Scintillator, time over threshold method, time resolved detection system, Positron Emission Tomography (PET), Hydrogenated amorphous silicon (a-Si:H).

Mots clés: Photodétecteur, scintillateur, système de détection résolu en temps, "time over threshold" méthode, Tomographie par Emission de Positron (TEP), Silicium amorphe hydrogéné.

Abstract

The main topic of this work is the study of detector systems composed of a scintillator, a photodetector and readout electronics, for Positron Emission Tomography (PET). In particular, the timing properties of such detector systems are studied. The first idea is to take advantage of the good timing properties of the NINO chip, which is a fast preamplifier-discriminator developed for the ALICE Time of flight detector at CERN. This chip uses a time over threshold technique that is to be applied for the first time in medical imaging applications. A unique feature of this technique is that it delivers both timing and energy information with a single digital pulse, the time stamp with the rising edge and the energy from the pulse width. This entails substantial simplification of the entire readout architecture of a tomograph.

The scintillator chosen in the detector system is LSO. Crystals of $2 \times 2 \times 10\ mm^3$ were used. For the photodetector, APDs were first used, and were then replaced by SiPMs to make use of their higher gain.

These different elements that constitute the whole detector system are presented, and their functioning is explained.

Within the European FP6 BioCare project, a test setup comprising 2 identical detector systems in coincidence was developed. Each one is composed of a LSO scintillator, an APD, a preamplifier and the NINO readout electronics. The energy resolution was measured to 16% for 511 keV γ-rays. This is comparable to the resolution obtainable with PMT based systems.

The same APD based system was also studied with 122 keV X-rays, to assess its potential for combined PET-CT imaging. The energy resolution in this case was measured to 70% as compared to 50% with PMTs. This is explained by a lack of sensitivity of the readout electronics to low charges.

The time resolution for 2 such detectors in coincidence was demonstrated to be of 1.6 ns FWHM. This is 3 times worse than what one could obtain with PMT based systems under the same conditions. The contributions of the different elements of the detector system to the time precision were identified. The relative contributions of the electronics, the APD and the LSO were found to be 20%, 30% and 50%, respectively.

However, the fact that the LSO crystal dominates the time resolution is partly attributed to the readout mechanism of the APD. The relatively low gain of the APD prevents the readout electronics from detecting fewer than 20 photoelectrons coming from the LSO whereas the PMT is sensitive to a single photon.

Therefore, a new photodetector was chosen and characterized: the Silicon PhotoMultiplier (SiPM). This photodetector finds increasing interest in the scientific community, offering better characteristics than APD in terms of gain and of single photon sensitivity. They could also be used for TOF applications in PET. The SiPM used were supplied by ST microelectronics and tested at CERN in the context of a scientific collaboration. SiPM from Hamamatsu were also tested for comparison.

The study of a $1 \times 1\ mm^2$ SiPM has demonstrated that the time resolution of the SiPM coupled to the NINO chip is of 180 ps rms from the detection of single 405 nm laser photon. This means that this combination of SiPM+NINO can also be used as a detector system for the detection of single photons such as in Cerenkov light detection or in fluorescence spectroscopy, where good time precision is required.

In the case of PET, the response of the SiPM to LSO photons following the interaction of a 511 keV γ-ray was modeled. Since in this case the output current from the SiPM is too high to be directly read out by the NINO circuit, an interface consisting of a differentiating circuit was developed.

Furthermore, the typical size of LSO crystals ($2 \times 2\ mm^2$) together with the high number of SPAD cells required to detect the photons emitted by the LSO implies that larger size SiPM ($3 \times 3\ mm^2$) have to be used. The work done during the thesis has shown a crucial influence of the SiPM terminal capacitance, which may be as high as 320 pF for the Hamamatsu SiPM of $3 \times 3\ mm^2$. In contrast with SiPMs of smaller size,

this capacitance in parallel with a load resistance (e.g. scope or NINO) is large enough to significantly increase the rise time of the SPAD signals to the extent that the timing performance of the ensemble is severely degraded. An improved electronics interface is currently being studied to overcome this limitation.

Another novel photodetector has also been studied in the context of this thesis: the microchannel plate (MCP) that is made of hydrogenated amorphous silicon (a-Si:H). The first samples were developed at the Institute of MicroTechnology (IMT) of Neuchatel and tested at CERN in a scientific collaboration. The advantage of this detector is the possibility to deposit on top of ASIC in a direct and vertical integration. Our preliminary investigation indicate that a current increase takes place along the borders of the MCP pores, possibly indicating the generation of a cascade of secondary electrons.

List of abbreviations

APD	Avalanche PhotoDiode
a-Si:H	Hydrogenated amorphous Silicon
ASIC	Application Specific Integrated Circuit
CERN	European Organisation for Nuclear Research
CFD	Constant Fraction Discriminator
CT	Computed Tomography
DRIE	Deep Reactive Ion Etching
EBIC	Electron-Beam Induced Current
ESRF	European Synchrotron Radiation Facility
FDG	FluoroDeoxyGlucose
FWHM	Full Width at Half Maximum
HPD	Hybrid PhotoDetector
IMT	Institute of MicroTechnology (of Neuchatel)
LHC	Large Hardron Collider
LOR	Line Of Response
LSO	Lutetium OxyorthoSilicate
LUT	Look Up Table
MCA	Multi Channel Analyser
MCP	MicroChannel Plate
MPPC	Multi Pixel Photo Counter
MRI	Magnetic Resonance Imaging
PCB	Printed Circuit Board
PDE	PhotoDetection Efficiency
PET	Positron Emission Tomography
PMT	PhotoMultiplier Tube
QE	Quantum Efficiency
rms	root mean square
SEM	Scanning Electron Microscope

SiPM	Silicon PhotoMultiplier
SPAD	Single Photon Avalanche Diode
STM	ST Microelectronics
TOF	Time Of Flight
TOT	Time Over Threshold
TTS	Transit Time Spread

Contents

Chapter 1

From particle physics to biomedical imaging

1.1 CERN - LHC

CERN is the European Organization for Nuclear Research, the world's largest particle physics laboratory [CERN]. CERN aims to provide physicists the necessary instruments such as accelerators, which accelerate particles to almost the speed of light, and detectors that measure the particles characteristics. By accelerating and colliding particles, physicists can study their interactions, creation and annihilation.

The current project in development at CERN is the Large Hadron Collider (LHC) which is foreseen to start to be operational in 2009. As shown on Figure 1.1, the LHC is a ring of 27 km perimeter installed at a depth of about 100 m underground. It accelerates 2 beams of either protons or lead ions in opposite directions and makes them collide in 4 collision points, each of which is equipped with an experiment:

- ATLAS (A Toroidal LHC Apparatus)
- CMS (Compact Muon Solenoid)
- ALICE (A Large Ion Collider Experiment)
- LHCb (the Large Hadron Collider beauty experiment)

The ALICE experiment was built to understand the origin of quark confinement [ALICE]. It is 26 m long for 16 m high and 16 m wide, has a weight of 10 000 tones and a total of 1 200 000 readout channels. As each of LHC's experiments, it is composed of many sub-detectors, each of which with specific detection goals.

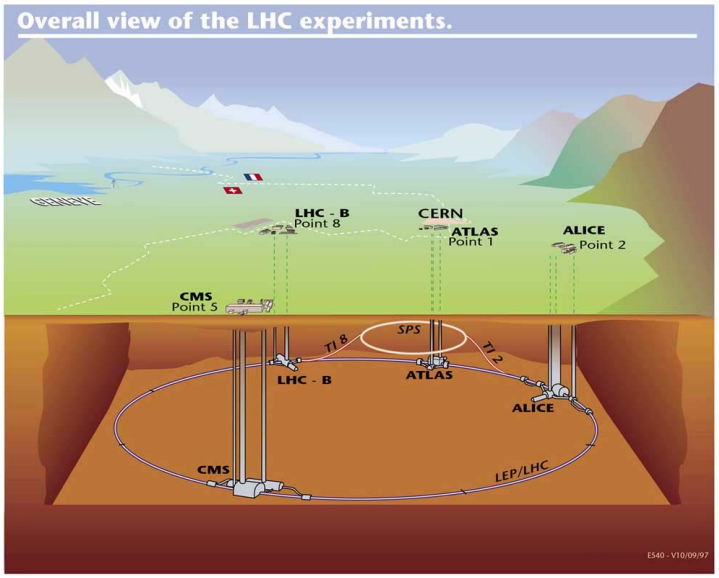

Figure 1.1: CERN experiments along the LHC.

Charged particles in the intermediate momentum range are identified in this experiment by the Time Of Flight (TOF) detector. The time measurement with the TOF, in conjunction with the momentum and track length measured by the tracking detectors, is used to calculate the particle mass [TOF].

The detector chosen for the ALICE TOF is the Multigap Resistive Plate Chamber (MRPC). The signal from the MRPC must be amplified, discriminated so that the particle arrival time on the detector can be measured with a maximum accuracy matching the intrinsic time resolution of the detector. For the front end, the NINO ASIC has been designed by the CERN microelectronics group. It is described in chapter 2.2.1. For the back end, the High Performance Time to Digital Converter (HPTDC) has been designed. This chip developed in the same group, with bin size of 25 ps will be described in chapter 2.2.3. The time resolution of the TOF MRPC is in the range of 50 ps rms.

1.2 Technology transfer

Through the European community, CERN is given the possibility to develop advanced technologies which will contribute to succeed in improving the understanding of nature.

Those developments generally exceed the industrial know-how and once developed for CERN, they can be transferred either to industry,

or to society. This is known as Technology Transfer (TT).

In the context of TT, projects can be generated with non High Energy Physics (HEP) partners, in which CERN can contribute and give its know-how (for example in the fields of accelerator, magnets and cryogenic systems). For industrial transfers, patents can then be deposited.

Alternatively, projects can be started with CERN contributing by developing or improving technologies to be further used in HEP (imaging systems using new photodetectors, or new scintillators for example). Currently as CERN is looking forward to upgrade the LHC toward a Super-LHC (SLHC) with 10 times higher luminosity, the second point is particularly important.

The most popular example of TT is the development of the internet in Europe which originates from the interconnection of CERN internal computer systems to improve in communication. Another reference of TT project is Medipix [Medipix] demonstrating that HEP can be a driving force in the development of detector technologies. Medipix is a collaboration of several institutes in which CERN develops the electronics of a pixel detector to be used for X-ray imaging. In this case, CERN gives its competencies and experience in electronics design and hybrid detector development.

As CERN is specialized in accelerators and detector systems, medical imaging projects using various kinds of detectors can particularly benefit from the transfer of technology.

In this context, CERN has collaborated to the BioCare project [BioCare], funded by the European Union sixth framework program (FP6) for research and development. BioCare is the starting point of the work presented here, and prior to describe the goals of this project, a brief introduction to the medical imaging techniques and trends is necessary.

1.3 Medical imaging

Medical imaging refers to the techniques and processes used to image internal structure of the human body for clinical purposes (medical procedures to diagnose or examine disease) or medical science (study of anatomy and physiology).

In its wide sense, it is part of biological imaging and incorporates, in a non exclusive list, radiography, photoacoustic imaging, endoscopy, thermography, electron microscopy, ultrasound etc. This section focuses on 3 different imaging techniques: Positron Emission Tomography (PET),

Computed Tomography (CT) and Magnetic Resonance Imaging (MRI).

1.3.1 PET and TOF-PET

PET is a nuclear medicine imaging technique which produces a three-dimensional image of functional processes in the body. Figure 1.2 illustrates the functioning of this medical examination.

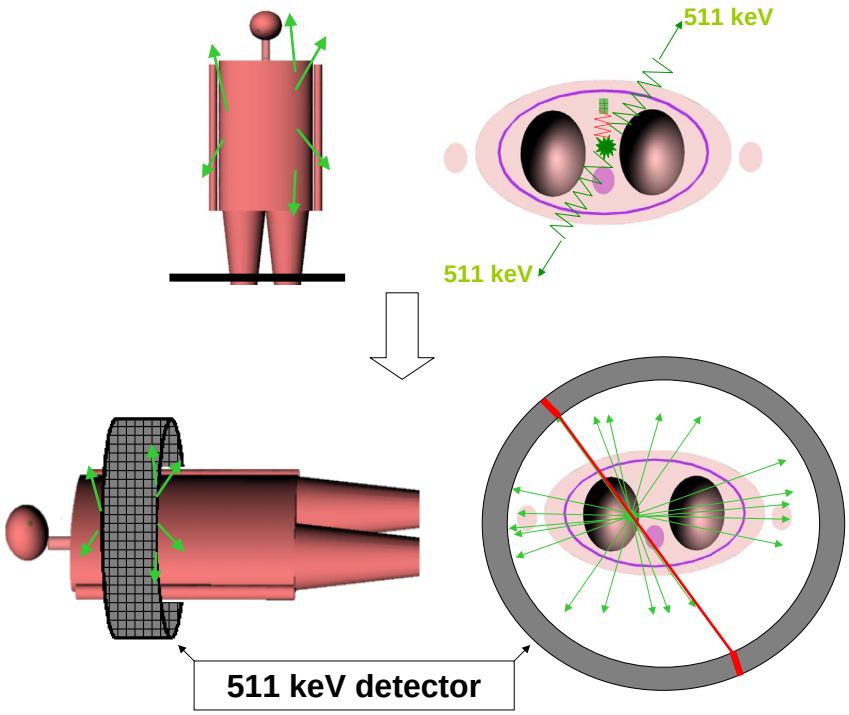

Figure 1.2: Schematic of a PET examination. top left: patient injected FDG, emitting 511keV γ-rays. Top right: slice view of the patient, positron emission and annihilation. Bottom left: patient going through the PET scanner. Bottom right: examination of patient slice, illustration of LOR intersections.

A radiotracer is injected in the body of a patient, usually fluorodeoxyglucose (FDG): a glucose molecule labeled with a radioactive β^+ marker, with a half lifetime of about 120 minutes. The glucose is accumulated in the cells of the body as a function of their metabolic activity where it emits positrons. A positron is the antiparticle of the electron, it will travel a short distance (in the order of 2 mm) before annihilating with an electron. This electron-positron annihilation is followed by the emission of 2 γ-rays of 511 keV, directed at 180^o from each other, as shown on the top right part of Figure 1.2. As different cells in the whole body (and in particular the cancer cells) consume this glucose, those parts of the body

then become emitters of γ-rays, as shown on the top left part of Figure 1.2.

It should be noted that other radiotracers more specific to certain parts of the body (for example brain) do exist and are used.

Within a certain time after the radiotracer injection, the patient is placed in the PET scanner. The PET detector head has the shape of a ring comprising several thousands of γ-ray detectors elements, as shown on the bottom left part of Figure 1.2. A γ-ray detector is usually composed of a scintillator, a photodetector and then the readout electronics. Those different devices are discussed in chapter 2. When 2 gamma-rays are detected in a tight time window, they are supposed to originate from the same e^+/e^- annihilation. The annihilation has thus occurred along a line called Line Of Response (LOR), represented by the two detectors points and shown in red on the bottom right part of Figure 1.2.

If the information of one LOR is usually not enough, the intersection of 2 LORs gives an emission point, and the intersection of a high number of LOR indicates a region of high density of positron annihilation, i.e. where FDG is accumulated, as shown on the bottom right part of Figure 1.2.

A PET scanner consists of multiple rings of detectors so that there are two approaches to reconstruct images from LOR information: the 2D reconstruction and the 3D reconstruction [Alessio 06].

The 2D reconstruction, historically the first one, consists of treating each ring as a separate entity, so that only coincidences within a ring plane are detected. The image of a volumetric object is done by repeating the 2D acquisition for multiple slices, and stack them together to form a three dimensional image.

The 3D reconstruction allows coincidences to be detected between rings as well as within rings, and then reconstruct the entire volume together. 3D techniques have better sensitivity than 2D as more coincidences are detected and used. The images show less noise, nevertheless they are more sensitive to the effects of γ-ray scatter and random coincidences, they also require 10^3 times more computer resources.

Cancer cells have a high reproduction rate which makes tumor with a high metabolic activity where the glucose concentration is high. In a healthy body, the cells which consume more glucose are well identified in the brain, heart, kidney, liver etc. A high localized emission of positron in any other places in the body will indicate cancer cells. The Figure 1.3 shows the kind of picture obtained after the full reconstruction of a

patient slice.

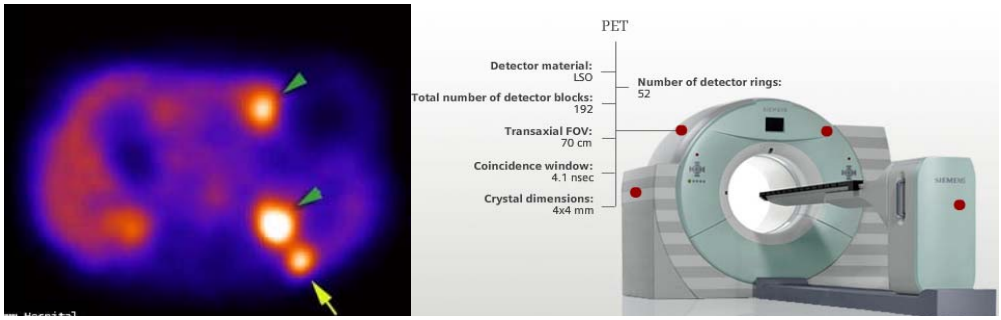

Figure 1.3: Left:PET Image. Right: Siemens PET Scanner.

The highlighted parts, shown by arrows show regions of high cell metabolic activity. The precision of PET image is of 3 mm, limited by the size of crystals , by the non linearity of pair production or by the positron range before annihilation. This does not permit to localize precisely the unhealthy tissues in the patient's anatomy. A technique named Time Of Flight (TOF) was proposed to improve the image contrast and background rejection. It consists of measuring precisely the time of arrival of the γ-rays reaching the detectors. In coincidence, it permits to localize where the positron has annihilated along the LOR which then improves the image contrast. This technique will further be described in chapter 2.1.3.

The time precision of a TOF-PET system is a key feature as it determines the accuracy of the positron annihilation position along the LOR. On the market, the first TOF PET scanner was developed by the Philips Company. It is called "Gemini TF" (True Flight) and the γ-ray detectors have a coincidence time precision of 585 ps FWHM [Surti 07], which permits to place the emission point on a LOR of about 1 m with a precision of 8.7 cm. This is obtained with LYSO scintillators mounted on PhotoMultiplier Tubes (PMTs).

1.3.2 Computed Tomography (CT)

Computed tomography (CT) is a diagnostic tool which uses X-ray to obtain cross-sectional, morphological pictures of the body. The CT analysis displays these pictures as detailed images of organs, bones, and other tissues.

As shown on the left part of Figure 1.4, an X-ray source is mounted on a ring, opposite to the detector. The patient is installed in the center of the ring, ready to be scanned slice by slice. For each slice, the detector

and x-ray source rotate around the patient. The X-rays will be sensed by the detector which will produce an image with a contrast corresponding to the absorption of the X-rays in the body, as shown on the left part of Figure 1.4.

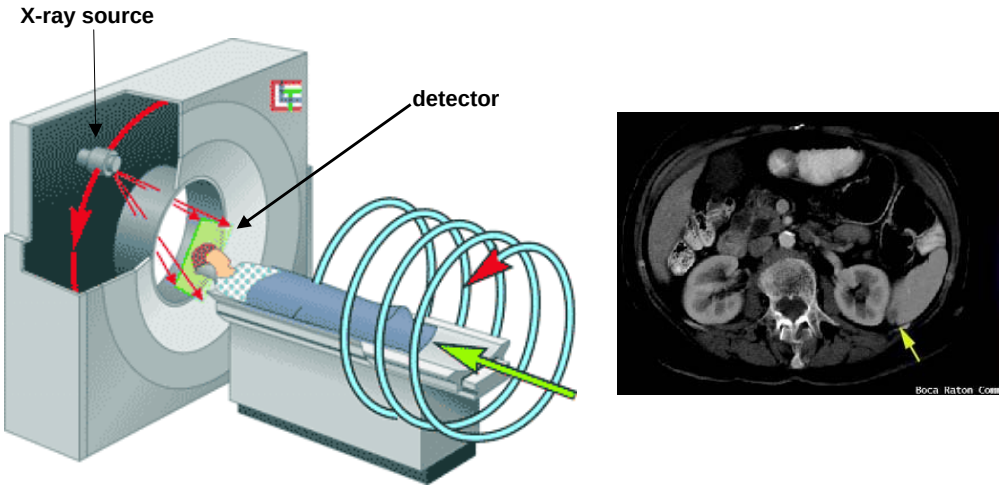

Figure 1.4: Left: CT scanner. Right: CT image.

This technique permits to obtain pictures with precision better than 1 mm. Moreover, to highlight some particular organs, contrast materials can be used.

The main drawback of this technique is that the patient will generally receive an important radiation dose, 50 to 100 times a standard X-ray radiography.

1.3.3 MRI

Magnetic resonance imaging (MRI) is a technique used commonly for imaging the soft structures of the body. Unlike CT, it uses no ionizing radiation. The patient lies inside a large, cylinder-shaped magnetic tube, which can be pulsed in the order of 1 T and Radio waves in the order of 1 T are generated. The magnetic field forces the nuclei of the body into an excited state. As they move back to their ground state, nuclei specific radio waves are emitted. The imager detects these waves and produces an anatomical picture of the patient.

MRI provides much higher contrast between the different soft tissues of the body than computed tomography (CT) does, making it especially useful in neurological (brain), musculoskeletal and cardiovascular imaging.

1.3.4 Dual modality

CT and MRI are used to make precise, 3 dimensional, anatomic images showing the positions of different tissues and bones in the body. The obtained images do not show the metabolic activity of tissues. It is therefore important to complement the anatomical image with a functional image of a PET scanner.

By combining two imaging modalities, an unprecedented accuracy in the delineation of the tumor on a background of normal tissue anatomy is achieved, as shown on Figure 1.5. The main problem is the difference in the organs positions between the two snapshots because of patient motion such as heart beating, breathing, digestion etc.

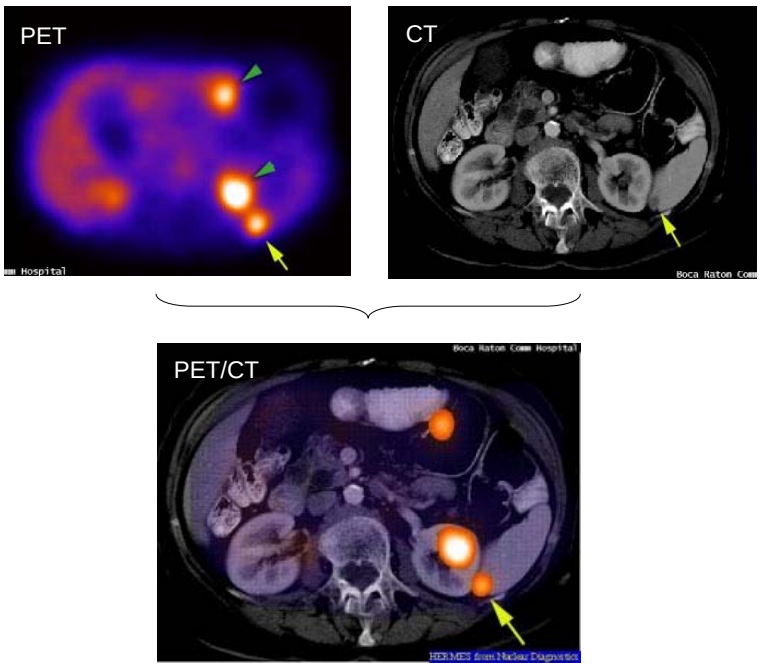

Figure 1.5: Superimposition of PET and CT images.

Scanners currently used in hospitals offer a double examination in the same unit. The PET scan and the CT or MRI scan of a same patient slice are done at some seconds of interval and the patient only has a single cession in the scanner. This way, problems of image fusion are reduced, but not fully solved. An improved solution would be to build the two images not successively but at the same time. The problem is that no detector exists to detect the radiations used in both modalities with the same efficiency.

The preference between CT and MRI for the delivery of the anatomic picture is currently discussed among the physician community [Zaidi 07].

Historically dual modality scanners based on CT were the first used, providing greatly improved images. The combination of PET and MRI was impossible because of the high magnetic field disturbing the photomultipliers. Today the developments in solid state photodetectors have lead to the possibility of implementing MRI scanners with PET. The use of MRI seems to grow more and more popular as the patient receives no dose. Moreover, from a medical point of view, the anatomical data derived from CT are not as complete as that obtained with MRI. Therefore future developments might see the emergence of PET/MRI dual modality.

1.4 BioCare

The European BioCare project is focused on developing new techniques and approaches to increase the sensitivity and specificity of existing tumor imaging techniques as well as introducing more systematic and adaptive approaches based on high-quality tumor imaging [BioCare]. The first objectives of the project are to improve and speed up the implementation of PET-CT imaging in cancer management. The second objectives are to develop new European intellectual property to improve tumor imaging by more specific tumor tracers. They will result in considerably increased resolution, sensitivity and specificity in tumor detection.

The BioCare project is subdivided into 3 major activities in which 21 European institutes participate:

1. **detection system development**: the instrumentation part. Research is done on the design of detectors for whole body PET systems with a high intrinsic resolution. The possibility of integrating a PET-CT device with a radiation therapy unit is investigated as well as the possibility to develop a hybrid detector system, i.e. which could detect both X-rays for CT, and γ-rays for PET.

2. **clinical validation and oncological implementation**: aims to use PET through therapy to characterize the efficiency of treatments. The evolution of cancers and the sensitivity of tumors are studied in vivo to optimize the planning of radiotherapy and chemotherapy

3. **New tracer development**: fluorodeoxyglucose (FDG) is not tumor specific, as all regions with an increased metabolic rate will

show an elevated glucose uptake. Research is done on more specific tumor markers allowing an even more accurate imaging.

The work presented in this thesis addresses the characterization of such potential dual mode detector systems

A very important characteristic of this project is the collaboration between scientists from the different fields of physics, biology and medicine.

CERN collaborates in the BioCare consortium's first activity, applying his know-how in detector systems of high timing precision.

A PET detector system is composed of a scintillator, a photodetector and the readout electronics, this combination will be further explained in chapter 2. The scintillator and photodetector currently used in PET scanners are Lutetium oxyorthosilicate (LSO) and PhotoMultiplier Tubes (PMTs), associated to form a detector module as shown in Figure 1.6

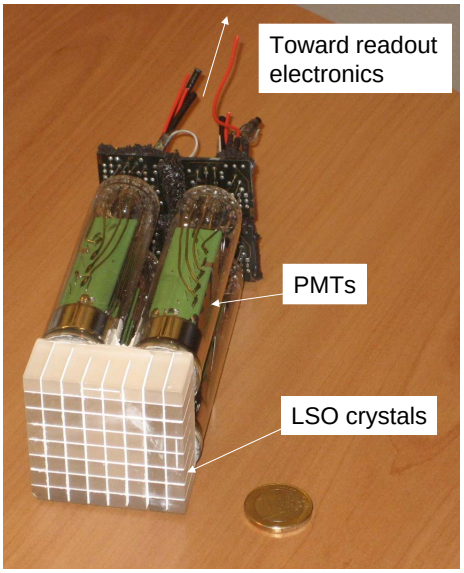

Figure 1.6: Detector module currently used in Geneva hospital PET scanners (from Siemens).

This kind of photodetector takes a lot of space and is expensive. One of the goals of the BioCare project is to replace these PMTs by silicon photodetectors such as Avalanche PhotoDiodes (APDs), without compromising in efficiency, i.e. with comparable energy and time resolution. The advantages of the APDs over the PMTs are mainly their low cost and small size, which facilitates their integration into PET scanner. This is explained in more details in chapter 2.4.3.

It is at this point and in the context of its technology transfer that CERN had the opportunity to apply its competence in time resolved electronics, for example the one developed for the ALICE experiment, to

biomedical imaging. Therefore commercial scintillators and photodetectors are used together with the NINO chip in order to build a prototype of PET detector and determine its performances for such an application. The objectives are also to evaluate the different factors limiting the performance, such as timing performance of the full detector system. The possibility to build a hybrid detector, which can detect both 511 keV γ-rays in PET and 50-100 keV X-rays in CT in a same unit, is also studied. The challenges imposed by this project set the basics of the work presented in this thesis.

1.5 Objectives and content of the work

The Characterization of time resolved photodetector systems for Positron Emission Tomography implies different areas of study.

The first aim is to build a suitable detector system for PET imaging. Its characterization in terms of energy resolution and time precision should be established. The same detector will also be characterized for CT detection to assess the potential for dual mode applications with the same detector head.

A second objective is to gain on in depth understanding of the mechanisms of timing, which will be studied in detail for the whole detector chain and for each component in order to establish the different limiting processes and factors influencing the timing precision and to improve their understanding. This necessarily implies a detailed study of the different elements constituting the whole detector system.

A third objective is to study of the performances of different photodetectors , in order to estimate the potential of each system to be integrated in a PET machine or in a combined PET-CT apparatus.

The study of the performance of Avalanche PhotoDiodes (APDs) photodetectors was part of the BioCare objectives, and the success in the development of a suitable PET detector system with good timing characteristics has encouraged repeating the experiment with different photodetectors.

A new photodetector was characterized: the Silicon PhotoMultiplier (SiPM). This photodetector finds increasing interest in the scientific community, offering better characteristics in terms of gain and of single photon sensitivity.

This device was tested and characterized to estimate its potential for the readout of the NINO chip, aiming to insert it in a TOF-PET detector

system, permitting this way to overcome the timing limits of the APD. For this purpose and specifically for the detection of LSO photons in PET, upgraded readout electronics has been developed in order to couple this photodetector to the NINO chip.

Finally, this work wants to demonstrate the viability of the CERN readout technique adapted for the first time to medical imaging purposes within the BioCare project. Moreover, by using different photodetectors such as SiPMs and MCPs, one can show the possibility to enlarge the domain of applications of the NINO chip to many other experiments where time resolved detector systems are needed such as fluorescence spectroscopy or Cerenkov detection.

The Layout of the work is organized in different chapters described in the following:

Chapter 2 aims to describe the functioning of each part of a PET detector system, i.e. the electronics, the scintillator and the photodetector. In particular, their timing characteristics will be studied. The choices made for the scintillator and the photodetector for PET detectors will be justified.

Chapter 3 presents the results obtained in the context of the BioCare project with a detector system composed of the CERN electronics reading out a LSO scintillator and an Avalanche PhotoDiode (APD). A setup with 2 such detector systems in coincidence was built and the performance in terms of energy and time resolution is shown. A detailed analysis identifies the contribution of each detector element on the time precision .

Chapter 4 then addresses the characterization of a new photodetector appearing on the market: the SiPM. In the context of a scientific collaboration with CERN, ST Microelectronics (STM) supplied the SiPM in this work. The possibility of connecting to the electronics is studied in order to build a PET detector based on this technology. The results in terms of photodetector characterization mainly focuses on the highest achievable time resolution.

Chapter 5 aims to present a novel photodetection technology built in collaboration with the Institute of MicroTechnology (IMT) of Neuchatel : the MicroChannel Plate (MCP) made of hydrogenated amorphous sili-

con (a-Si:H). First characterizations on prototype structures were done in order to show the multiplication of electrons in the channels.

Chapter 6 presents the discussion of the results which forms the core of this thesis and the conclusions which can be drawn from this work.

1.6 Contributions of this work to the research field

In the last years an increasing interest was shown in the fields of PET detector systems and Photodetectors, and work performed by other authors is considered in the following chapters. This PhD thesis contributes to the research field with the following elements:

- The analysis of the photons propagation time in a scintillator was done. If a similar approach was shown in [Achenbach 07] for long plastic scintillators of 1 m, the calculation was applied to the case of LSO of size $2 \times 2 \times 10\ mm^3$.

- A study of the statistics of photon production in scintillators was done, based on [Post 50, Lynch 66]. The equations were developped in order to calculate the limit time precision achievable in a detector system, due to this only statistics. The particular case of LSO was studied.

- The time over threshold technique was applied for the first time to PET experiment. The detector system developed shows an energy resolution of 16% and a coincidence time resolution of 1.6 ns FWHM [Powolny 08]. Those results are comparable to the one obtained in [Pichler 04, McCallum 05, Pepin 04].

- A detailed analysis of the time resolution measured was done. The contribution of the different elements of the detector system were extracted [Powolny 08, Moses 79, Casey 03].

- The presence of a high terminal capacitance intrinsic to the SiPM was shown to shape the output current signal. This one explains the differences of SiPM pulse height obtained with samples of $1 \times 1\ mm^2$ and of $3 \times 3\ mm^2$.

- The SiPM signal in the case of LSO photons detection was calculated, showing a good agreement with the measurements presented in [Spanoudaki 07, Kim 09, Karakash 06].
- The first generation of a-Si:H MCP was characterized, showing an increase of current generated by incoming photons in the MCP pores.

Chapter 2

Detection principle

For photons of energy 511 keV involved in Positron Emission Tomography imaging, the electromagnetic radiation does not offer a direct conversion from ionization to charge signal in most photodetectors. This energy is nearly invisible to most of the material employed for photodetection and scintillators have to be used. Scintillators permit an indirect detection where the radiation energy is first transformed into light of a different (lower) energy and then sensed by a photodetector.

The different detector systems presented in this thesis are composed of 3 components put together: a scintillator converting photons of high energy into visible light, a photodetector converting the light absorbed into a measurable electrical signal and the readout electronics analyzing the signal as shown in Figure 2.1.

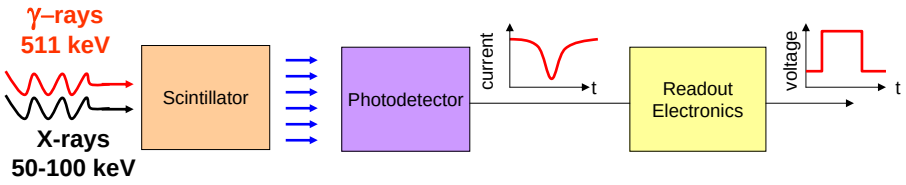

Figure 2.1: schematic of a detector system.

After presenting some general properties and definitions, this chapter will describe the different elements of the detector system. First it will focus on the readout electronics originally developed for high energy physics and transferred to biomedical application. Then the scintillators will be described, giving an overview of the timing limits that this device imposes. Finally the photodetectors used during the thesis will be described.

2.1 Properties and definitions

This section aims to give general key definitions for detector systems such as energy resolution and time resolution. The mechanisms of the interaction of photons with matter will be detailed as this represents the basics of radiation detection.

2.1.1 Interaction of photon with matter

When a photon interacts with matter, three ionization processes may happen: the photoelectric effect, the Compton effect and the electron/positron pair production.

The photoelectric effect is a quantum electronic phenomenon in which the energy from the electromagnetic radiation is fully transferred to one electron which is ejected from its bound shell. The ejected electron then ionises the surrounding electrons of the medium until it loses its energy. The maximum kinetic energy of the electron is E_{max}:

$$E_{max} = \frac{hc}{\lambda} - W \tag{2.1}$$

Where h is the Planck constant, c is the speed of light in vacuum, λ is the photon wavelength and W is the work function: the minimum energy required to emit one electron. It has different definitions whether the photoelectric effect is internal (the electron remains confined in the matter) or external (the electron escapes from the surface of the matter).

In the case of the external effect, if the energy of a radiation illuminating a material in vacuum is high enough, the excited electron can escape over the potential barrier of the surface of the material and be liberated in vacuum as a free electron. The work function is the energy difference between the Fermi level and the vacuum level. For Cesium, the lowest value of W is 2 eV.

In contrast with external effect, the effect in semiconductors is different as the ejected electron remains in the matter, but is released from the valence band to the conduction band.

The Compton effect is an elastic collision between an incoming photon and an electron of the matter. A part of the photon energy E' is absorbed by the electron which is emitted. This electron goes on to create ionisation in the medium. The photon is scattered with an angle θ from its initial direction as shown in Figure 2.2.

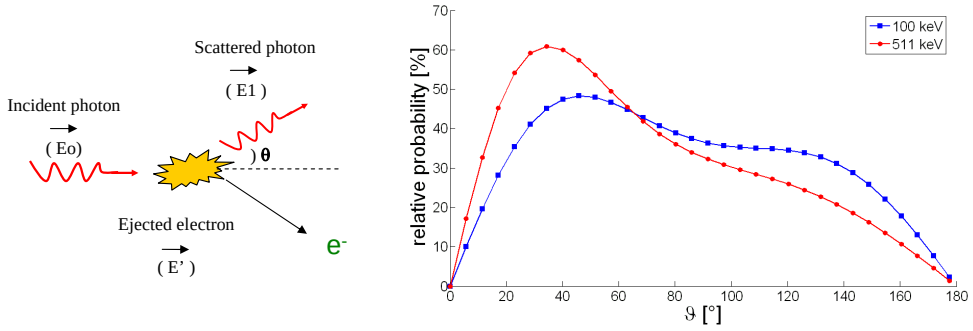

Figure 2.2: Left: Compton interaction schematic. Right: relative probability of scattering angle for Compton interaction of 511 keV and 100 keV radiations.

The energy of the scattered photon E_1 is defined by the following equation.

$$E_1 = \frac{E_0}{1 + \frac{E_0}{m \cdot c^2} \cdot (1 - cos\theta)} \tag{2.2}$$

With E_0 the energy of the incident radiation, m the mass of the electron, c the speed of light in vacuum and θ the scattering angle.

The energy E' absorbed in the matter is then: E'=E_0-E_1. It depends strongly on the scattering angle which can vary from 0 to π . E' is maximum for E_1 minimum, hence for θ=π. In this last particular case the photon is backscattered.

The probability of Compton scattering per atom of the scintillator depends on the number of electrons available as scattering targets and therefore increases linearly with Z. The angular distribution of scattered radiation is described by the Klein-Nishina formula [Knoll 00] for the differential scattering cross section $d\sigma/d\Omega$.

$$\frac{d\sigma}{d\Omega} = Zr_0^2 \left(\frac{1}{1 + \alpha\,(1 - cos\theta)} \right)^2 \left(\frac{1 + cos^2\theta}{2} \right) \times \left(1 + \frac{\alpha^2\,(1 - cos\theta)^2}{(1 + cos^2\theta)\,[1 + \alpha\,(1 - cos\theta)]} \right) \tag{2.3}$$

With $\alpha = E_0/mc^2$ and r_0 the classical electron radius.

This distribution can be plotted for $E_0 = 511\ keV$ ($\alpha = 1$) and $E_0 =$

100 keV (energies used in PET and CT), with $r_0^2 = 7.94.10^{-26}\ cm^2$ and with $d\Omega = 2\pi sin\theta d\theta$. The probability P_{scatt} of scattering between 0 and π becomes:

$$P_{scatt} = \frac{\frac{d\sigma}{d\Omega}}{\int_{4\pi} \frac{d\sigma}{d\Omega} d\Omega} = \frac{\frac{d\sigma}{d\theta}.2\pi sin(\theta)}{\int_0^{\pi} \frac{d\sigma}{d\theta} 2\pi sin\theta d\theta} \tag{2.4}$$

It shows greater probability for θ comprised between 0 and $\pi/2$, i.e. for forward scattering as shown on the right part of Figure 2.2.

Pair production effect only happens when the incident electromagnetic radiation energy E_0 is greater than 1.022 MeV. The interaction with the medium leads to the creation of an electron/positron pair. The positron has an electric charge of +e, and the same mass as the electron.

As a consequence the positron annihilates with another electron of the medium, generating the emission of two γ-ray photons with an angle of π and each one with an energy of 511 keV. These two γ-rays can then either be absorbed by the medium or be lost if they escape from the medium. The incident energy E_0 is then: $E_0 = 511\ keV + 511\ keV + E_2$ with E_2 the remaining energy. Assuming that E_2 is always detected by the crystal, three different energies can be detected :E_0 if no γ-ray escapes the medium, $E_0 - 511\ keV$ if one γ-ray escapes the medium and $E_0 - 1022\ keV$ if the two γ-rays escape.

These three effects occur with different probabilities, depending on the atomic number Z of the matter and on the energy of the photons involved. The Figure 2.3 shows the dominant interaction mechanism as a function of the photon energy and of the atomic number [Knoll 00].

For the LSO scintillator used in this thesis, the effective atomic number is Z=65. For incident γ-rays of 511 keV, the interaction will occur through photoelectric and Compton effect with comparable probabilities (see Figure 2.3). For visible light (between 1 eV and 4 eV) interacting in Silicon detectors which Z=14, the photoelectric effect highly dominates.

In the case on the interaction of a large number of photons with an energy E_0, and if every of these three processes happen, the resulting histogram of the energy deposited in the medium has the profile shown in Figure 2.4, which highly depends on the medium atomic number.

As shown in Figure 2.3, only 1 or 2 effects can at the same time have significant contribution. Figure 2.4 only illustrates the different contributions to the histogram.

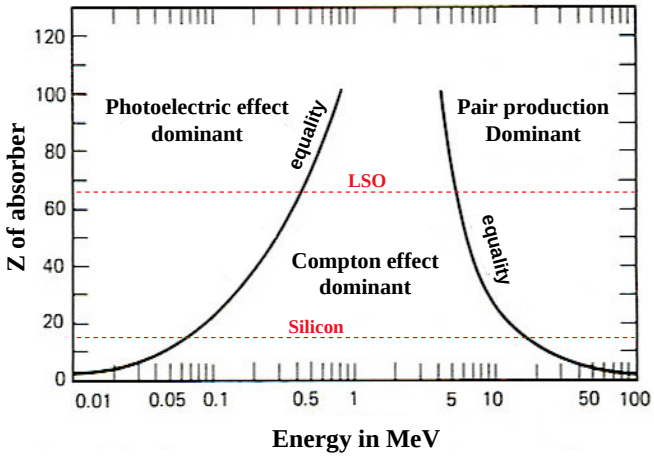

Figure 2.3: atomic number Z vs. Energy.

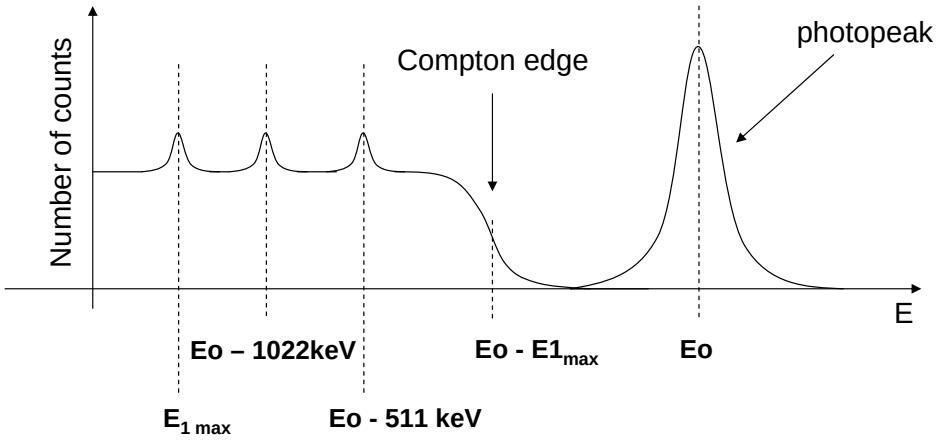

Figure 2.4: Energy histogram of a particle interacting with matter through the three processes.

A Gaussian peak can be observed, centered at an energy of E_0 resulting from the photoelectric absorption of the electromagnetic radiation. It is called the photopeak and is the only relevant one to determine the energy of the incoming photon. The Compton scattering leads to the detection of energies from 0 to $E_0 - E_{1max}$ with E_{1max} the energy of the backscattered photon. The profile in this range of energies is called the Compton continuum and its extremity is the Compton edge at $E_0 - E_{1max}$. Superimposed on the Compton continuum the peaks coming from the annihilation process can be seen: the annihilation peaks centered at $E_0 - 511\ keV$ and $E_0 - 1022\ keV$. Additionally there are also probabilities to detect photons coming from the Compton interaction with the environmental matter. The backscattered photons have higher geometrical probabilities

to interact with the scintillator which leads to a peak centered at E_{1max} called the backscatter peak.

From these three interaction principles, with any given energy (from a radioactive source for example) it is possible to fully interpret the position of the peaks in an energy histogram.

2.1.2 Energy resolution

This very important property of a detector system can be characterized by its response H (such as a pulse height or a pulse area) to a monoenergetic source of radiation. In the cases of the photoelectric effect, as a detector system is not ideal, the histogram of this response H will show a distribution around the photopeak, centered at the average value H_0. The width of this peak tells about the ability of the detector system to give a stable response from event to event for a same energy deposited.

The energy resolution R, as shown in Figure 2.5, is defined by the ratio of the Full Width at Half Maximum (FWHM) of the peak by the average value of H (minus the pedestal).

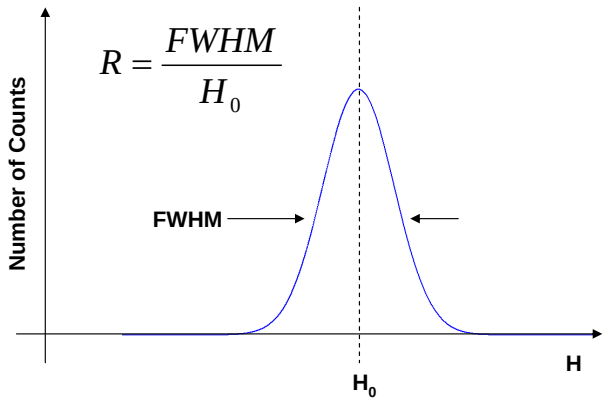

Figure 2.5: Energy resolution (pedestal at 0)

The smaller the value of R, the better the detector system is able to distinguish between two radiations whose energies are close to each other. The rule states that two energies are detectable if they are separated by more than one FWHM.

There are various sources contributing to the fluctuations of H in a given detector for example electronics noise. These contributions have to be identified and reduced to a minimum.

The different sources of fluctuations in the detector system chain will combine to give the overall resolution, and it is sometimes possible to measure each contribution independently. From statistical theory, the overall response function will tend to be a Gaussian distribution, even if individual fluctuations are characterized by distributions of different shapes. The overall FWHM $(\text{FWHM})_{overall}$ in this condition will be the quadratic sum of each independent individual source of fluctuation.

As an example, in the detector system presented in this thesis and composed of a scintillator, a photodetector and an electronic readout, every piece of the chain will add its respective fluctuations $(FWHM)_{scint}$, $(FWHM)_{PD}$ and $(FWHM)_{elec}$ to the overall.

$$(FWHM)^2_{overall} = (FWHM)^2_{scint} + (FWHM)^2_{PD} + (FWHM)^2_{elec} \quad (2.5)$$

2.1.3 Time resolution

For time resolution, the parameter observed is the time of response (or delay) of the detector system. A histogram of this delay will show a distribution forming a peak, centered at the average delay t_0. The time resolution is usually defined as the FWHM of this distribution which will tend to be a Gaussian such as for energy resolution. It should be noted that $FWHM = 2.35\sigma$ with σ being the standard deviation. The fluctuations at the origin of this distribution have contributions from every part of the detector chain so that the overall time resolution of a detector system can be expressed as the quadratic sum of each individual source of fluctuation.

One of the goals of the work presented here is to identify all the relevant sources of timing fluctuation in a studied detector system, and try to find their intrinsic limits for a PET system. The goal is to detect two γ-rays of 511 keV emitted at 180° from each other. If the time precision for the PET scanner has to be optimum, the figure of merit is the coincidence time precision, i.e. the ability to establish the difference of time arrival of the two γ-rays. In general, the time resolution of a PET scanner is expressed as:

$$\begin{aligned} (FWHM)^2_{coincidence} &= (FWHM)^2_{det1} + (FWHM)^2_{det2} \\ (FWHM)_{coincidence} &= \sqrt{2} \times (FWHM)_{det} \end{aligned} \quad (2.6)$$

The smaller the resolution, the better the detector system is able to

distinguish between the arrival times of the two photons. Two photons are identified if their time of arrival is separated by more than one FWHM.

In Time Of Flight (TOF) PET systems, the time precision is such that the difference of time arrival tells where the emission of the two γ-rays has occurred along the line of response. As the speed of these γ-rays nearly equals the speed of light in vacuum (c=3.10^8 $m.s^{-1}$) and the minimum time difference $\Delta t \geq FWHM$, the precision of the emission point on the line of response Δx is:

$$\Delta x = \frac{1}{2}(\Delta t)c \tag{2.7}$$

As an example, if the time resolution of the system is of 100 ps, the uncertainty on the emission point is $\Delta x = 15\ mm$.

2.2 Readout electronics developed at CERN for fast detection

To read out photodetectors in TOF PET and CT applications, circuits developed at CERN have been chosen considering their excellent timing properties: the NINO chip and the HPTDC both originally designed for high energy physics. For some photodetectors such as APDs, the output signal is too low to be directly read out by the NINO circuit, and hence a preamplifier has to be used. Among the different preamplifiers developed in the microelectronics group at CERN, the FEDC05 preamplifier was chosen.

2.2.1 NINO

The NINO chip [Anghinolfi 04] is an ultra fast front end preamplifier discriminator which has been developed for the ALICE [ALICE] Time Of Flight (TOF) detector. The chip has been designed in a 0.25 μm CMOS technology and its dimensions are 2 x 4 mm^2. The layout of the chip is shown in Figure 2.6.

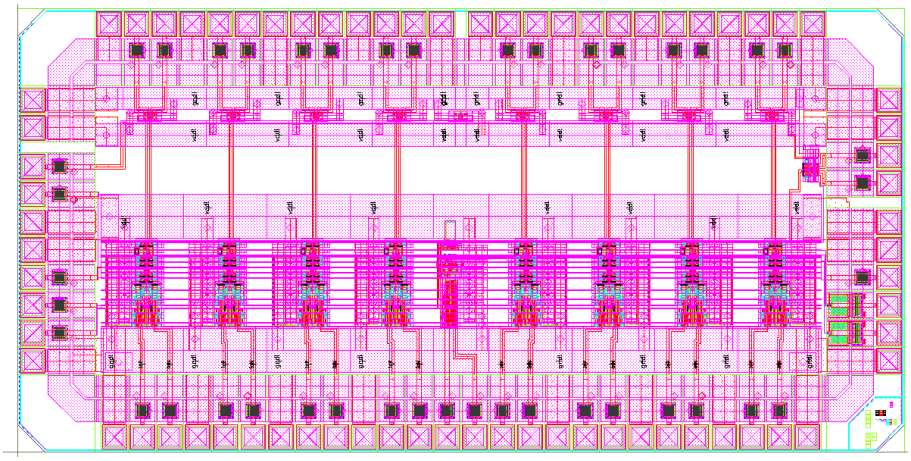

Figure 2.6: Layout of the NINO chip

The chip consists of 8 channels, each of which exhibits less than 1 ns peaking time (time needed to reach the highest voltage value) and is designed fully differential for better immunity against noise.

The circuit schematic and the different stages of the channel will be first presented. The NINO circuit principle will then be explained by looking at the different steps of signal processing inside one channel.

NINO architecture

Each channel comprises an input stage followed by 4 identical cascaded differential amplifiers in series and by an output driver. A functional block diagram of the circuit is shown in Figure 2.7.

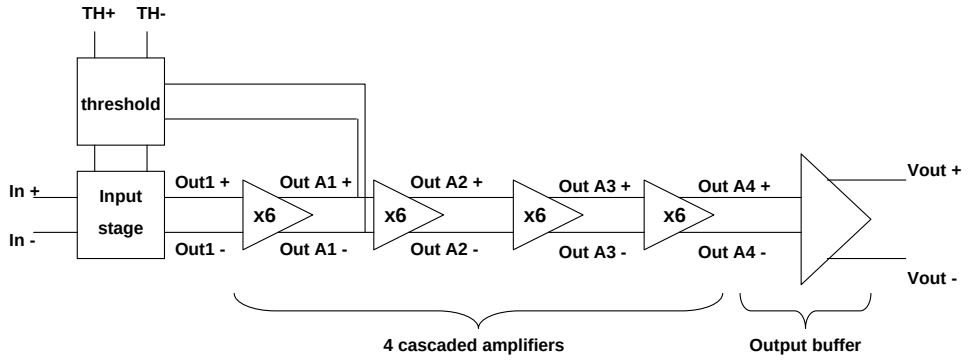

Figure 2.7: Block diagram of one NINO channel

The input stage is a transimpedance amplifier chosen for fast signal processing. As shown on the left part of Figure 2.8, it is based on a balanced common gate configuration and has a dedicated circuit to optimize the input impedance externally.

This schematic can be separated into 4 blocks:

1. The first block is a current source which sets the total current I_{tot} into each branch of the circuit.

2. The second block is a cascode common gate differential circuit which permits to provide a low input resistance on the differential inputs In+ and In- of the channel. This input resistance is determined by the transconductance g_m of the common gate transistors M_1 and M_4. These transistors are moreover biased in weak inversion so that their g_m (and then the channel input resistance) are determined by their drain current, i.e. by the total current I_{tot} flowing in each branch and set by the block 1. The input resistance R_{in} of the channel can therefore be estimated by:

$$R_{in} \approx \frac{1}{g_m} \approx \frac{n.V_T}{I_{tot}} \tag{2.8}$$

Where V_T is 25.6 mV at room temperature and n varies between 1 and 3. A high total current thus leads to a low input resistance.

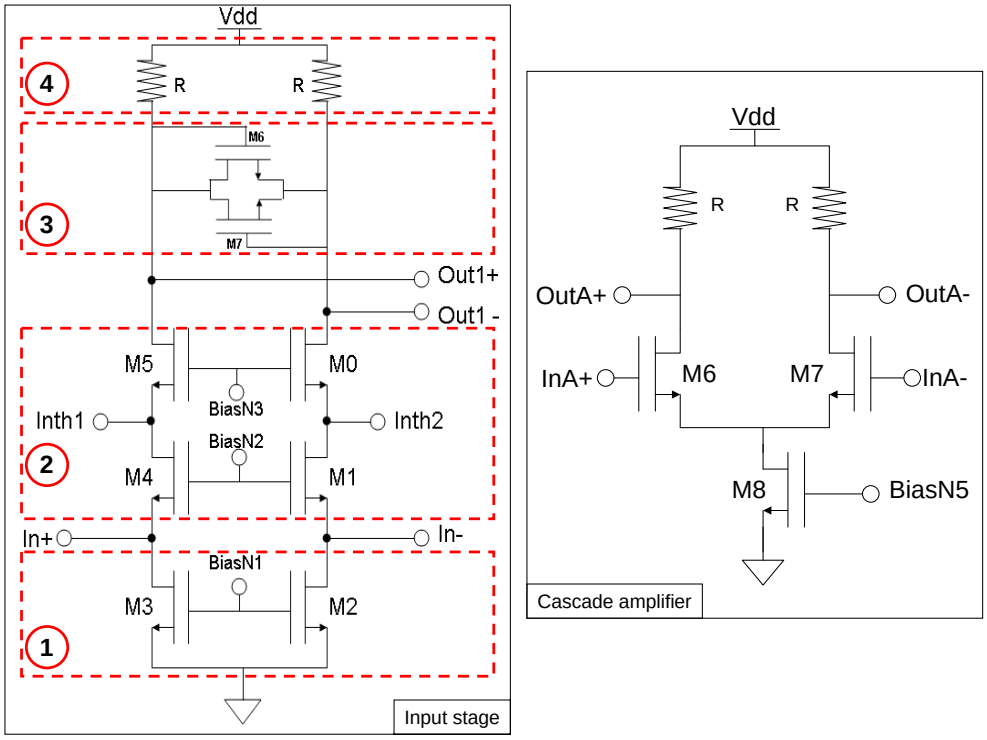

Figure 2.8: Right: NINO input stage schematic, Left: NINO amplification stage schematic

As an example, an input resistance of about 50 Ω can be obtained with a current of 1 mA. Such low resistance permits to achieve a high speed readout (and therefore good time resolution) even with high input loading capacitances C_{in} in the order of 10 pF (the input pole is given by $R_{in}.C_{in}$). Moreover, low input resistance permits to decrease the cross talk and to lower reflections in the connection lines.

As this resistance is determined by the total current I_{tot}, a dedicated complex biasing circuit (which will not be detailed in this thesis) was developed to set this current for all channels. It comprises a resistance R_{ext} which has to be mounted externally from the circuit. Depending on this external resistor value, a certain current I_{tot} is copied by current mirrors from the biasing circuit to all the channels (by bias voltage BiasN1). Transistor sizing was done in such a way that the bias current I_{tot} will lead to a g_m of the common gate transistors equal to $1/R_{ext}$. In other words, the developed biasing technique permits to control the input resistance R_{in} of each channel only with one external resistor and $R_{in} \approx R_{ext}$.

3. The third block is a diode connection whose role is to limit the differential output voltage signal of the first stage in case of too large input signal.

4. The fourth block consists of two passive resistors R which sense the current and convert it into a voltage. The DC values output voltages Out1- and Out1+ are determined by V_{dd}, the resistance value and the current flowing through it. The output voltage is given on each branch as :

$$\begin{aligned} V_{Out1^-} &= V_{dd} - R(I_{tot} - Inth1) \\ V_{Out1^+} &= V_{dd} - R(I_{tot} - Inth2) \end{aligned} \tag{2.9}$$

   Inth1 and Inth2 are two currents injected by the threshold block which permit to have differential current flowing in the resistance of each branch, and then different DC voltages. This offset will act like a threshold for the following cascade amplifiers.

   The gain in the current to voltage conversion is given by the resistance R so that the output voltage increase ΔV_{Out1^+} with respect to the current increase ΔI_{In+} is:

$$\Delta V_{Out1^+} = R(\Delta I_{In+}) \tag{2.10}$$

   Respectively in the othe branch:

$$\Delta V_{Out1^-} = R(\Delta I_{In-}) \tag{2.11}$$

   The absence of feedback makes this architecture stable and well suited for high speed processing.

The cascade amplifiers are simple differential voltage amplifiers with a gain of 6 and a roll of linearity at -3 dB above 500 MHz. They permit to amplify and then saturate the voltage signal in order to obtain a square pulse with a width corresponding to the total input charge. Their schematic is shown on the right side of Figure 2.8.

The voltage difference between the inputs InA+ and InA- is amplified to OutA+ and OutA-. Four stages of this amplifier are required to saturate the voltage signal, leading to a square pulse.

The threshold of the discriminator is controlled by a voltage difference applied externally. This difference determines the currents Inth1 and Inth2 and then control the DC voltage difference $(OUT1+) - (OUT1-)$, acting like a threshold voltage. This block is placed on the feedback path from the first amplifier stage to the input stage, which permits to compensate for a mismatch between the input stage branches.

It is possible to send a single ended signal into one of the two NINO inputs, the other branch will act as a discriminator threshold as long as the two signals intersect each other, as shown in Figure 2.9.

The output driver is a differential circuit compatible with Low Voltage Differential Signaling (LVDS).

This channel configuration has been optimized for high timing precision as low as 10 ps rms time jitter (representing fluctuations on the measured delay). The output pulse width can be used to do charge measurement as well as time walk correction, this last one being a slewing of the delay imposed by the technique employed and described thereafter.

NINO signal processing

In the applications presented here the different signals from the photodetectors are all single ended and have to be sent into the proper input of NINO: if the value of $(Th+) - (Th-)$ is positive, a positive current pulse must be sent into the positive input, where the DC level OUT1+ is decreased by the threshold stage.

As an example of the NINO functioning, the Figures 2.9, 2.10 and 2.11 show the different steps of signal processing for a single ended positive current pulse sent to the input.

The left part of Figure 2.9 shows a current pulse sent into the positive input of NINO. The right part of this Figure shows the corresponding outputs of the input stage Out1+ and Out1-.

These voltages are injected into the four amplification stages. The outputs of these stages are shown in Figure 2.10.

It is possible from this last simulation to observe the progressive amplification and saturation of the signal, going with an increase of the DC levels. The voltages OutA4+ and OutA4- are then sent to the driver which outputs Out+ and Out- are shown in Figure 2.11.

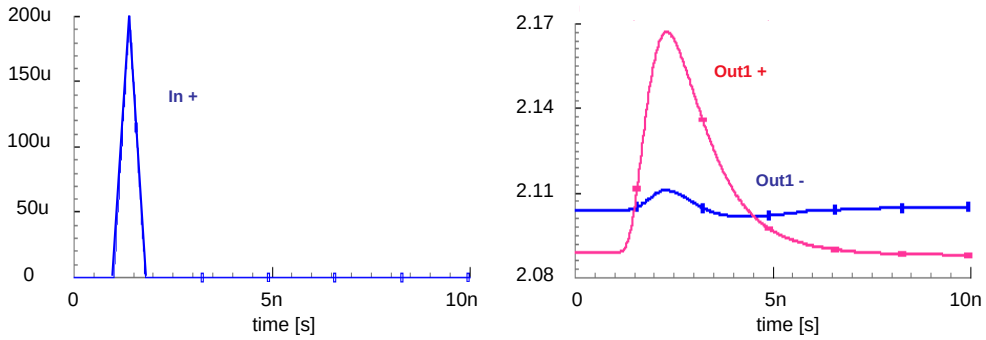

Figure 2.9: input current signal and outputs "out+" and "out-" of the NINO input stage

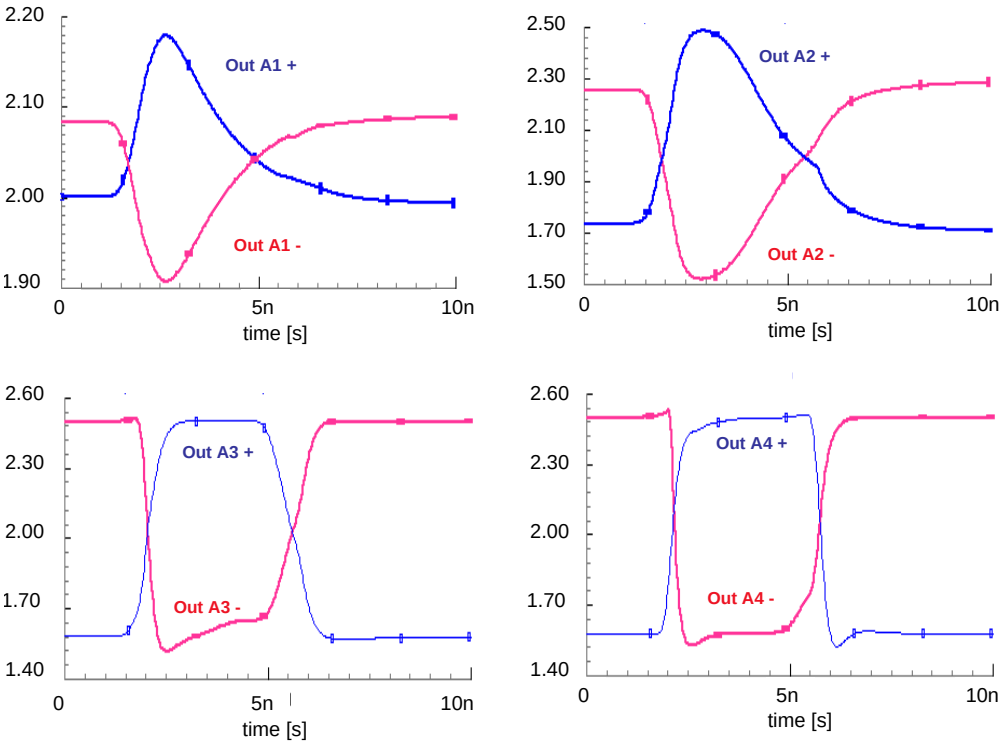

Figure 2.10: Output of the four amplification stages.

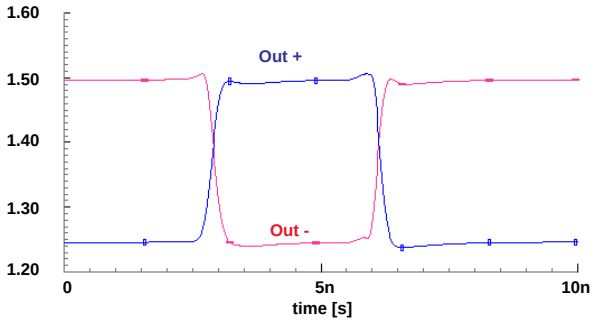

Figure 2.11: Output signal of NINO

In order to give a simple explanation of the functioning of this chip one can say that NINO uses the "time over threshold" technique. The pulse width can be approximated by the intersection of Out+ with Out-. In the real case a delay is added by the electronic chain as well as a pulse duration offset. The Figure 2.12 shows the principle of the chip functioning for different input signals.

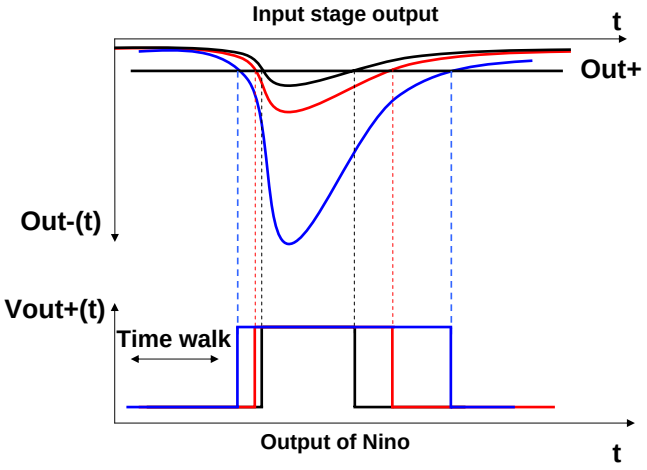

Figure 2.12: Illustration of the time over threshold technique used by NINO.

The dominant feature of this technique is its very good timing characteristics: the time jitter on the front edge of the NINO output signal has been measured down to 10 ps FWHM [Anghinolfi 04, Lapington 08]. Inherent to this method, two effects can be observed. First, the pulse width is not a linear function of the input charge. A calibration has to be applied by simulation and measurement in order to retrieve the input charge from the output pulse width. Second, the leading edge time of the NINO output pulse varies as a function of the charge. The delay from the input signal leading edge to the NINO output signal leading edge is called time walk and it varies as a function of the input charge. The time walk variations are known from the pulse width information and from the calibration, they can thus be corrected for.

The time precision of NINO is given by the time jitter. The jitter is the timing uncertainty of the output signal leading edge. Jitter typically follows a Gaussian distribution. The jitter at the output of NINO is governed by electronic noise. The instantaneous signal level produced at the input of NINO is affected by the electronic noise σ_e. This noise can be visualized by an envelope surrounding the signal. It is represented in gray in Figure 2.13. This makes the time of threshold crossing fluctuate.

The electronic time jitter σ_j is then given in a first approximation by the ratio of the input signal noise σ_e and its rising edge slope (dV/dt) at the NINO threshold crossing [Spieler 05]:

$$\sigma_j = \frac{\sigma_e}{(dV/dt)_{threshold}} \tag{2.12}$$

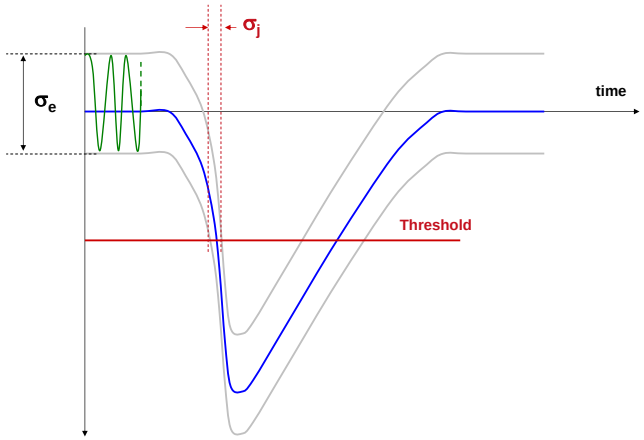

Figure 2.13: Jitter generated by electronic noise.

2.2.2 FEDC05

The FEDC05 front-end circuit [Kaplon 05], implemented in a 0.25 μm CMOS technology, is a low-noise preamplifier designed for the readout of silicon strip detectors used in the ATLAS experiment [ATLAS] at CERN. The layout of this chip is shown in Figure 2.14.

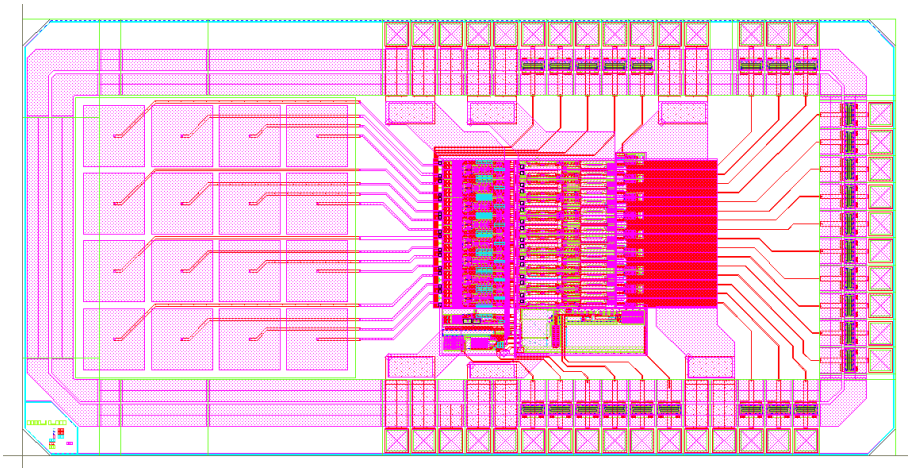

Figure 2.14: Layout of the FEDC05 chip.

The chip contains 16 channels, each of which comprises a fast transconductance preamplifier, with an active feedback loop and an output buffer, as shown in Figure 2.15.

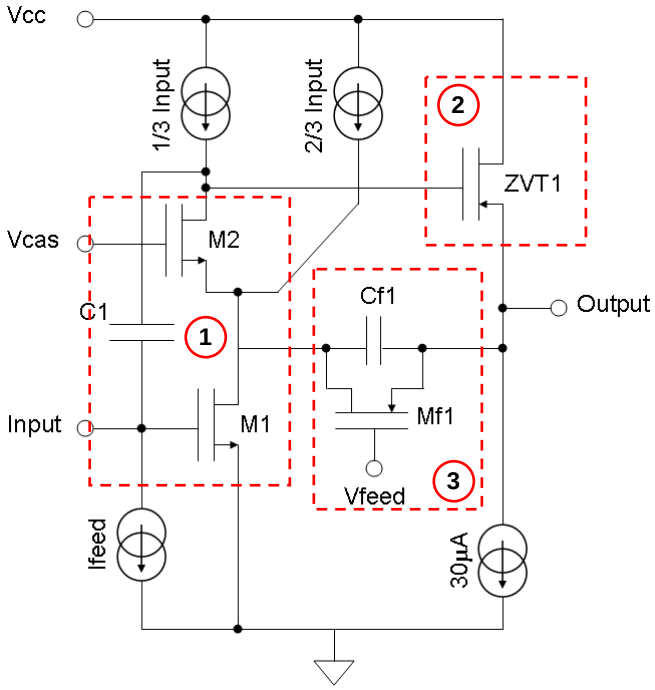

Figure 2.15: Schematic of the FEDC05 chip.

This schematic is composed of 3 parts:

1. The first part is a transconductance amplifier made of two cascoded transistors NMOS M1 and M2, and biased by current mirrors represented here by current sources.

2. The second part is the output buffer, composed of a common drain PMOS ZVT1. This configuration is also called source follower and its role is to copy the voltage signal, adapting the output impedance for compatibility with following electronics.

3. The third part is the active feedback circuit. Its principle is detailed in [Jarron 96]. The transistor PMOS Mf1 is placed in the feedback path of the cascode stage instead of a conventional feedback resistor. For a bias current of 0.8 μA, the transconductance is about 8 μS, i.e. a resistance of about 120 kΩ. The main advantage of this technique is the strong reduction of the parasitic capacitance compared to resistive feedback in the technology used. On the other hand if the noise performance of the active feedback is worse than in passive

feedback, it can be kept at an acceptable level by a proper choice of the feedback current.

An example of the functioning of the FEDC05 can be given by sending a voltage step of 100 mV through a 100 fF test capacitance integrated in the circuit. The corresponding impulse response is shown in Figure 2.16.

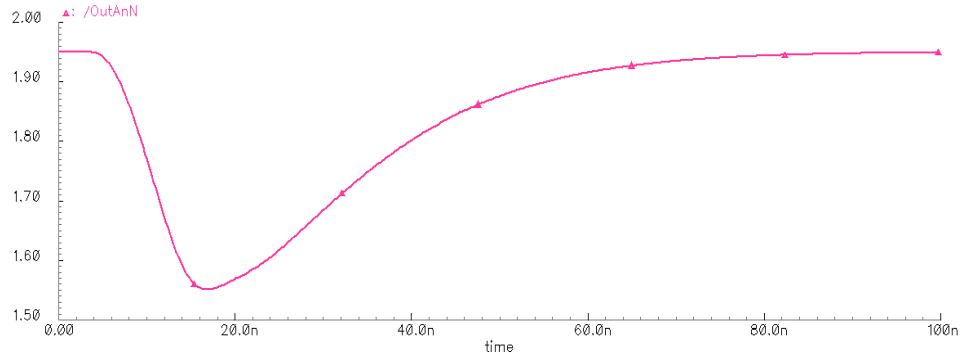

Figure 2.16: Simulation of the FEDC05 impulse response for a 10 fC charge.

In the nominal conditions presented in [Kaplon 05], the peaking time is 13 ns, the parallel noise is about 400 electrons equivalent noise charge (ENC) and the gain is of 4 mV/fC. For scintillator and avalanche photodiode readout in PET application, different biasing conditions were used. A full calibration of this chip will be presented in chapter 3.

2.2.3 High Precision Time to Digital Converter (HPTDC)

TDCs are used to record with high precision and in a digital form, the time of transition of sporadic pulses. They are used extensively in high energy physics experiments with time precision from 250 ps for most of the LHC experiments down to 25 ps for highest required time precision. One of its representatives is the High Performance Time to Digital Converter (HPTDC), developed at CERN [Christiansen 04]. Historically, HPTDCs were needed for the ALICE TOF detector to perform the readout of NINO. For reasons of cost saving a single HPTDC has been developed in a 0.25 μm CMOS technology with high flexibility to be used for both projects, with the result that it can also be used for many other applications such as [Lapington 08]. The layout of this chip is shown in Figure 2.17

The HPTDC is based on a Delay locked loop (DLL) and on a Phase lock loop (PLL). In a single channel, the input signal will be either 0

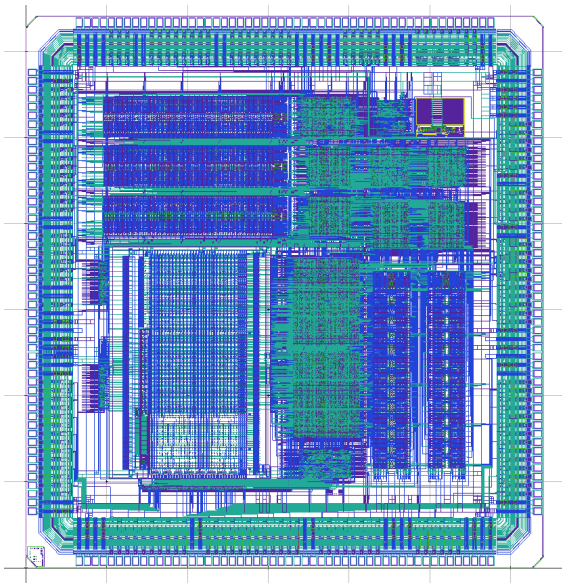

Figure 2.17: Layout of the HPTDC.

for low state, either 1 for high state. A hit controller outputs a square pulse for every transition of 0 to 1 or 1 to 0, it determines when a time digitization must be performed. At this moment the state of the DLL is stored in hit registers and then transferred into a buffer. The number of PLL cycles and the DLL state (a 32 bits word) will tell the time of the event with a precision of T_{DLL}.

The value of the bin size T_{DLL} can be chosen from $\approx$ 100 ps to $\approx$ 780 ps by choosing the PLL period to send into the DLL as a reference. These values are reported in the Table 2.1.

Frequency [MHz]	T_{PLL} [ns]	T_{DLL} [ps]
40	25	780
80	12.5	390
160	6.25	195
320	3.125	97.5

Table 2.1: Achievable clock period

In the very high resolution mode, 4 channels are used as 1 single very high resolution channel. RC delay lines are inserted in front of each hit controller as seen in Figure 2.18, in order to delay the signal of $T_{DLL}/4$, i.e. of 25 ps.

This way, if the channels 1, 2 and 3 detect the signal hit at time t_N and if the channel 3 detects the signal at t_{N+1}, the real time of arrival of

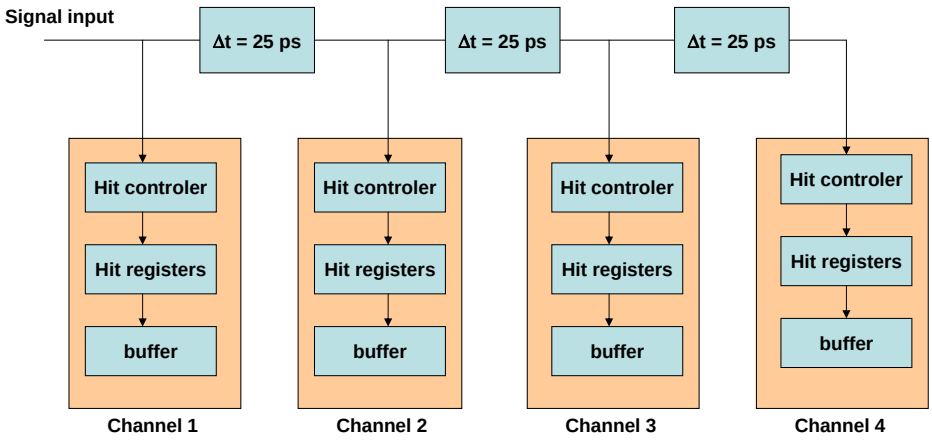

Figure 2.18: Schematic of the HPTDC architecture.

the hit is $T_N + 3 \times 25\ ps$.

2.3 Scintillators

A scintillator can be defined as a wavelength shifter [Lecoq 05]. It converts the energy (or wavelength) of an incident particle or energetic photon (UV, X-rays or γ-rays) into a number of photons of much lower energy (or longer wavelength) in the visible or near visible range, which can be easily detected with photodetectors.

This section aims to recall the theory of light emission needed for medical application, with a focus on the LSO crystals used and an analysis of the timing characteristics imposed by this scintillator.

2.3.1 Scintillation Principle

A scintillator is usually an ionic crystal with simple energy structure. The mechanisms described here focus on the case of an inorganic lattice doped with a rare earth element which transition band levels are within the matrix band-gap.

The mechanism of light emission in this kind of scintillator can be described in 5 different steps [Pédrini 05, Weber 04], shown in Figure 2.19 using the electronic band structure of the crystal. The time scale is represented on the abscissa and the energy on the ordinate. The valence band and the conduction band separated by the band gap are represented.

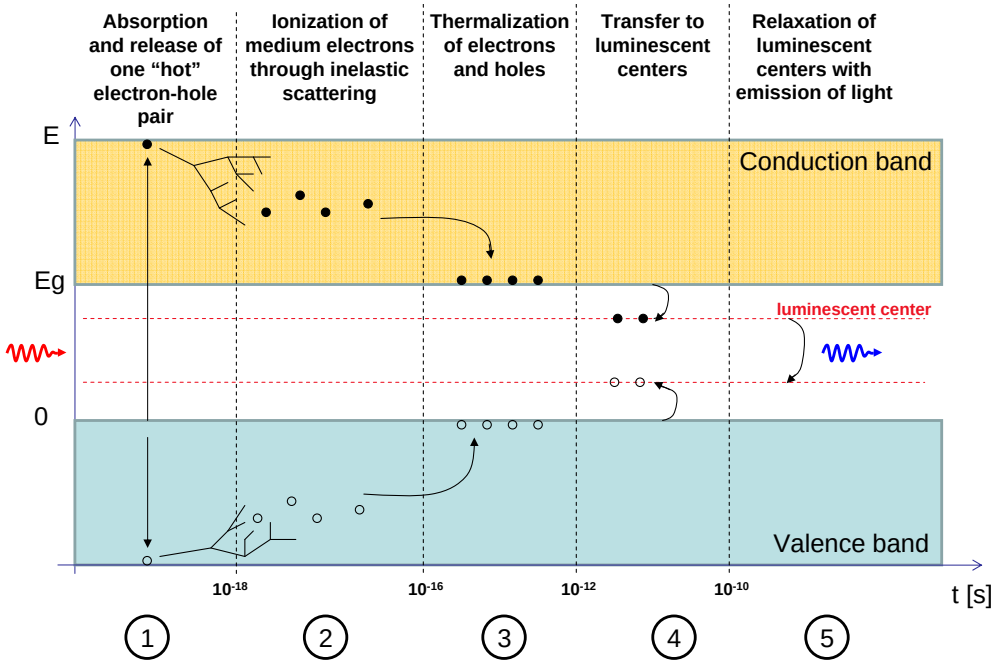

Figure 2.19: Schematic of the scintillator mechanism.

The first step is the absorption of high energy radiation through one of the three processes described formerly in 2.1.1, generating one energetic primary electron-hole pair.

The second step is the relaxation of this pair through inelastic electron-electron scattering and Auger processes, leading to the excitation of surrounding electrons in the medium. The duration of this stage is estimated at 10^{-18}s [Lecoq 05].

The third step is the thermalization of the secondary electrons and holes by intra-band transition and electron-phonon relaxation. At the end of this step which lasts 10^{-16} s, the electrons are at the bottom of the conduction band and the holes at the top of the valence band.

Those three first steps are responsible for the intrinsic rise time of the scintillation light, this rise time being much shorter than most of the detectors time precision.

During the fourth step, 10^{-12} s, various processes may happen. For example the electron-hole pairs may recombine through non radiative processes, or they might be trapped by defects or impurities in the crystal, or even more interestingly trapped by the luminescent center of the rare earth present in the crystal lattice.

The fifth and last step is the recombination of electron-hole pairs from the luminescent center, leading to the emission of luminescent photons. This mechanism can have a duration from 10^{-9} s to some seconds depending on the radiative transition involved. It is responsible for the decay time of the scintillator.

In order to fully characterize the scintillation light, the decay time and the light yield have to be known. These characteristics determine the scintillator light output for a given high energy radiation interacting with the medium. It should be noted that some scintillators have both a fast and a slow decay time because of a plurality of luminescent centers in the band-gap. The decay time τ is the signature of the radiative relaxation of the luminescent centers. Once the luminescent centers are occupied with all the electron-hole pairs, the photon emission can be approximated by a decreasing exponential as a function of time, with a time constant τ.

The light yield Y is defined by the amount of photons emitted by a scintillator per unit energy deposited by an ionizing particle. It is usually expressed in number of photons per MeV (or keV).

$$Y = \frac{E_\gamma}{E_{e-h}} SQ \tag{2.13}$$

E_γ is the energy of the high energy radiation, E_{e-h} the energy needed for the formation of one electron-hole pair in the medium, S is the efficiency of the energy transfer of thermalized states to the excited states of the luminescent centers and Q is the quantum yield of the intra-center luminescence.

2.3.2 LSO crystals

Comparative studies have been done for different scintillators [Lecomte 98]. The Table 2.2 shows important parameters attributed to different scintillators. Qualitatively, the best scintillator has the highest light yield, the shortest decay time, the highest density and the highest effective atomic number Z.

	NaI	BGO	GSO	LSO	YSO
Decay time (fast-slow) [ns]	230	60-300	60-600	40	42
Peak emission [nm]	410	480	430	420	420
Density $[g.cm^{-3}]$	3.67	7.13	6.71	7.35	4.5
Effective Z	50	73	58	65	35
Light output vs. NaI	100	15	20	75	25

Table 2.2: Comparison of different scintillators

The scintillator which is the best compromise between all the mentioned parameters is LSO. Its name stands for lutetium oxyorthosilicate: $Lu_2(SiO_4)O$. It consists of a matrix of silicate crystal mixed with the Lutetium rare earth. This crystal is doped with cerium rare earth and in this case we speak of cerium doped lutetium oxyorthosilicate: $Lu_2(SiO_4)O : Ce$ [Melcher 91, Suzuki 93]. In case of Ce^{3+} the luminescent centers are the 4f and 5d bands, present in the band-gap of the LSO.

LSO is widely used for PET and other applications because of its high density of 7.4 g.cm^{-3}, its light emission centered at 420 nm and its 40 ns decay time. The light emission spectrum of the LSO is shown in Figure 2.20.

The wavelength is centered at 420 nm and the FWHM of the spectral distribution is of about 50 nm, from 400 nm to 450 nm, with 68% of the photons produced in this range.

Its light yield is about 27 photons/keV in horizontal position and of about 16 photons/keV in vertical position in the case of crystal dimensions

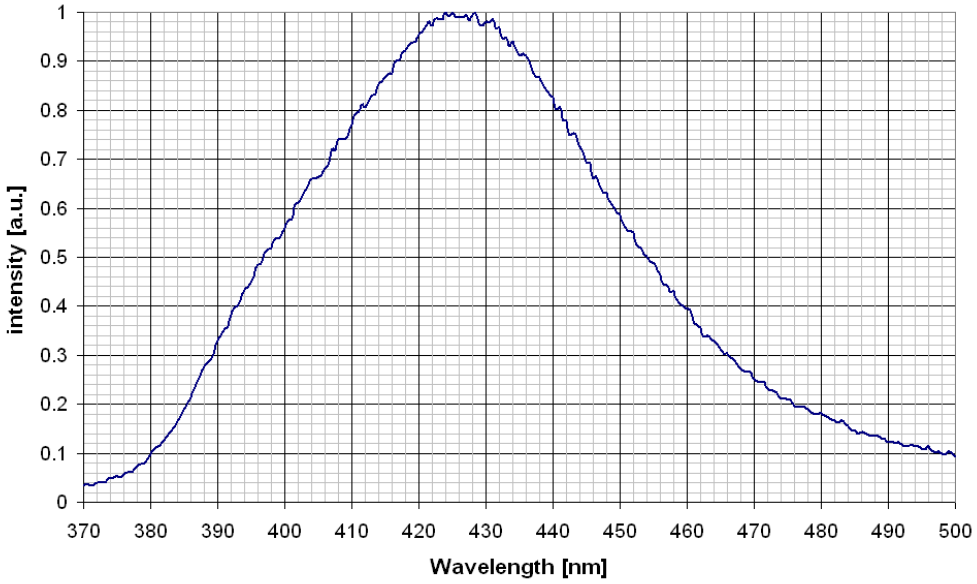

Figure 2.20: Light emission spectra of the LSO.

of $2 \times 2 \times 10\ mm^3$. The rise time of the light emission function is in the order of a hundred of ps, and is neglected for the moment so that the scintillation light can be modeled by the function y. For the case of a scintillator producing on the average R photoelectrons per excitation and decaying exponentially with a time constant τ, the light signal y(t) is :

$$\begin{aligned} y(t) &= Ae^{-\frac{t}{\tau}} \\ with \int_0^{+\infty} y(t)dt &= R = A\tau \end{aligned} \tag{2.14}$$

With A the maximum photon emission rate. The shape of the light intensity as a function of time is presented on the left part of Figure 2.21, for a decay time of τ=40 ns and R=2200, representing the fraction of photons actually sensed by the photodetector.

The average number of photoelectrons created between t_0 and t is then given by the function f:

$$\begin{aligned} f(t) = \int_0^t y(t)dt &= -A\tau e^{-\frac{t}{\tau}} + A\tau \\ f(t) &= A\tau\left(1 - e^{-\frac{t}{\tau}}\right) \\ \boxed{f(t) &= R\left(1 - e^{-\frac{t}{\tau}}\right)} \end{aligned} \tag{2.15}$$

For R=2200 and τ=40 ns, the number of emitted photons as a function of time is shown on the right part of Figure 2.21. From the function f,

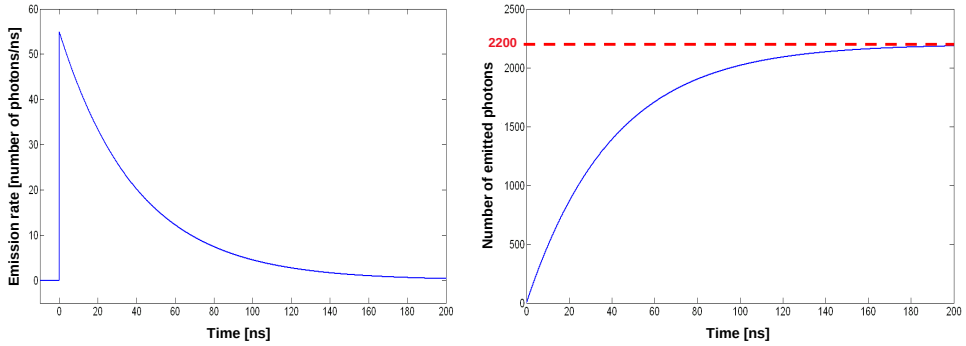

Figure 2.21: Left: Light intensity as a function of time. Right: number of emitted photons as a function of time.

it is possible to find out the average time t_N at which the N^{th} photon is emitted:

$$\begin{aligned} N = \int_0^{t_N} y(t)dt = -A\tau e^{-\frac{t_N}{\tau}} + A\tau \\ N = R\left(1 - e^{-\frac{t_N}{\tau}}\right) \\ \boxed{t_N = -\tau ln\left(1 - \frac{N}{R}\right)} \end{aligned} \tag{2.16}$$

The LSO is radioactive because it contains with the abundant ^{175}Lu, 2.59% of the isotope of the ^{176}Lu which is a γ emitter at 306 keV. For a 2 x 2 x 10 mm^3 crystal this corresponds following the calculation in the Appendix A to an activity of $\approx$ 13 Bq. Depending on the radioactive source strength used in our tests, the ^{176}Lu may show up as a background in the energy spectra.

2.3.3 Scintillation Timing

To improve PET systems, a solution is to measure the Time of Flight of the gamma rays. This way, the readout time precision has to be improved to some hundreds of picoseconds or less. This thesis focuses on the limits of the timing resolution of a detector systems but it is also important to consider the different contributions to the time precision which are intrinsic to the scintillator. These are studied and are explained in this section. The time variation inherent to the rising edge of LSO light production is discussed as well as the mechanisms of light propagation in the scintillator and the statistics of photoelectron production.

2.3.3.1 Rise time precision

The rise time doesn't appear in the light intensity equation 2.14. However, scintillation light in LSO is not produced instantaneously but rather within the order of 100 ps, leading to time jitter contributing to the total time precision. In order to improve the performance of TOF PET systems, this contribution shouldn't be neglected anymore. Nevertheless the characterization of this rise time is difficult because even PMT based detector systems are still comparatively slow. Only a photodetection system based on MCPs could allow such studies as this photodetector is currently the fastest

2.3.3.2 Light propagation in the scintillator

It is considered that the photons are created from an incident radiation, through the photoelectric effect which is the one relevant in timing measurements. Then the photons travel inside the scintillator which is acting as a light guide towards the photodetector.

Since photons are emitted isotropicly during the scintillation process, the time of propagation is not uniform and induces timing fluctuations.

In LSO, the photoabsorption coefficient μ for 511keV photons is $\mu_{511} = 0.28\ cm^{-1}$, as shown in Figure 2.22 [XCOM].

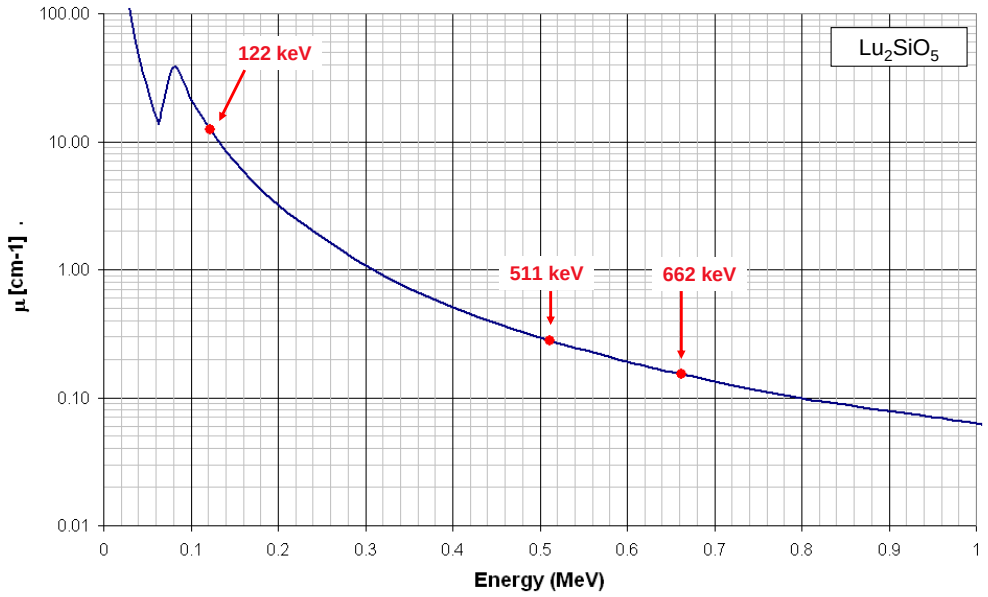

Figure 2.22: Absorption coefficient of LSO in the energy range of PET and CT.

The attenuation in photon flux is described as:

$$I = I_0 e^{-\mu_{511} x} \tag{2.17}$$

With I_0 the initial photon flux entering the LSO, and I the flux after absorption in x cm. This means that a LSO scintillator of 1 cm length has 25 % chance to absorb a γ-ray of 511 KeV.

In this case, an incident photon can interact anywhere in the crystal, with a probability exponentially decreasing with the interaction depth.

As mentioned in 2.3.1, when the interaction takes place, the photon transfers all its energy to one electron. While relaxing, this electron will ionize the surrounding electrons of the matter through inelastic collisions. The volume in which surrounding electrons are ionized is characterized by the radius r in μm given by the Kanaya and Okayama formula [Kayama 72, Dapor 92]. It corresponds as well to the sphere radius from which photons will be emitted.

$$r = \frac{2.7610^{-2} A E_0^{1.67}}{\rho Z^{0.89}} = 174 \ \mu m \tag{2.18}$$

With E_0 the initial photon energy ($E_0 = 511 \ keV$), Z the effective atomic number ($Z_{LSO} = 65$), ρ the density of the crystal ($\rho_{LSO} = 7.4 \ g.cm^{-3}$) and A the atomic weight of the LSO ($A_{LSO} = 57.25 \ g.mol^{-1}$).

A schematic shown in Figure 2.23 shows the absorption of a gamma-ray of 511 keV in the LSO scintillator of length L and of width l, the depth of interaction is x_0. The volume of photon emission is represented by a dashed circle. From this volume of radius r, photons are emitted isotropicly, so that any emission angle θ with respect to the x-axis is possible. Because of the crystal geometry, a right-angled parallelepiped, the system is symmetric in x so that the study can be limited to angles from 0 to π. The LSO crystal is coupled to the detector with silicon grease (SiG), meaning that the position of the crystal on the detector is not well determined as well as the quantity of grease used. For this reason the study presented here is limited to the time propagation into the crystal. The photon can only be detected if it reaches the silicon grease region presented in 2.23. A mismatch between the crystal and the photodetector (fill factor), quantum efficiency and reflections can lead to a loss of photons. These effects are discussed in chapter 3.

The propagation time t_{propag} of a photon emitted at x_0 is given by the ratio of its path length over its speed. The speed of light in a medium is c/n, with c the speed of light in vacuum and n the refraction index of the medium ($n_{LSO} = 1.85$ at 420 nm). The propagation path length is

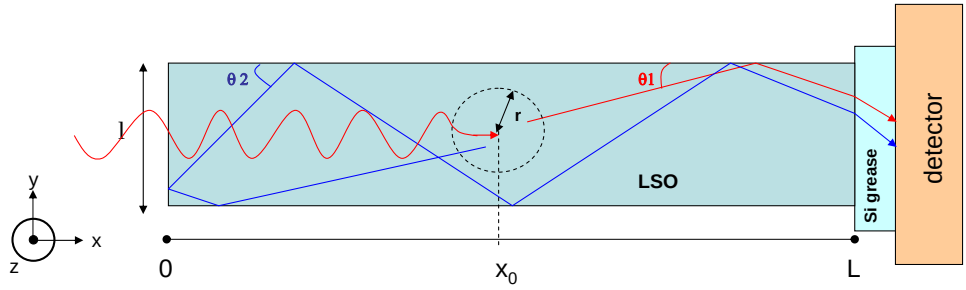

Figure 2.23: Schematic of the light emission mechanism in the crystal.

given by the ratio of the axial length over the cosine of the emission angle [Achenbach 07]. The axial length is defined here as the projection of the photon path over the x axis.

$$t_{propag} = \frac{axial\ length}{cos\theta} \times \frac{n}{c} \tag{2.19}$$

Two cases appear:

$$\begin{aligned} for\ 0 \leq \theta < \frac{\pi}{2} \quad &\rightarrow \quad t_{propag} = \frac{(L - x_0)n}{c.cos\theta} \\ for\ \frac{\pi}{2} < \theta \leq \pi \quad &\rightarrow \quad t_{propag} = \frac{(L + x_0)n}{c.cos\theta} \end{aligned} \tag{2.20}$$

The propagation time depends of x_0, L, θ and n. This propagation time's limit becomes infinite for $\theta \rightarrow \frac{\pi}{2}$, but the reflections rules do not permit the total propagation of photons over a certain angle which can be defined by the Fresnel equations [Saleh 07]. Those equations define the reflection coefficient.

As shown in Figure 2.24 for a photo flux composed of N photons, for light incident with an angle β_i from the perpendicular on the interface of two media of different indices, a fraction R will be reflected with the same angle and a fraction (1-R) will be refracted with an angle β_t.

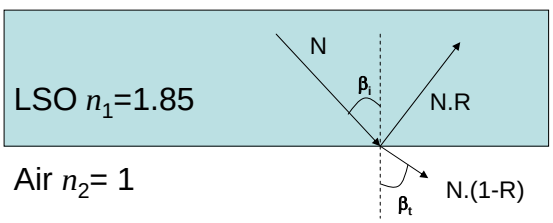

Figure 2.24: Reflection and refraction at the interface scintillator / air.

The polarization of light might be of importance, light polarized in parallel will have a coefficient R_P, and light polarized in perpendicular a

coefficient R_S. In the case presented here, the light is not polarized so that the reflection coefficient R is the average of R_P and R_S which are given by the Fresnel equation:

$$\begin{aligned} R &= \frac{R_S + R_P}{2} \\ with\ R_S &= \left[\frac{n_1 cos(\beta_i) - n_2 cos(\beta_t)}{n_1 cos(\beta_i) + n_2 cos(\beta_t)}\right]^2 \\ and\ R_P &= \left[\frac{n_1 cos(\beta_t) - n_2 cos(\beta_i)}{n_1 cos(\beta_t) + n_2 cos(\beta_i)}\right]^2 \end{aligned} \tag{2.21}$$

According to the Snell-Descartes law:

$$\begin{aligned} n_1 sin(\beta_i) &= n_2 sin(\beta_t) \\ \beta_t &= Arcsin\left(\frac{n_1}{n_2} sin(\beta_i)\right) \end{aligned} \tag{2.22}$$

As $n_1 > n_2$, there is a critical angle β_c from which the light is totally reflected. R, R_S and R_P are plotted in Figure 2.25

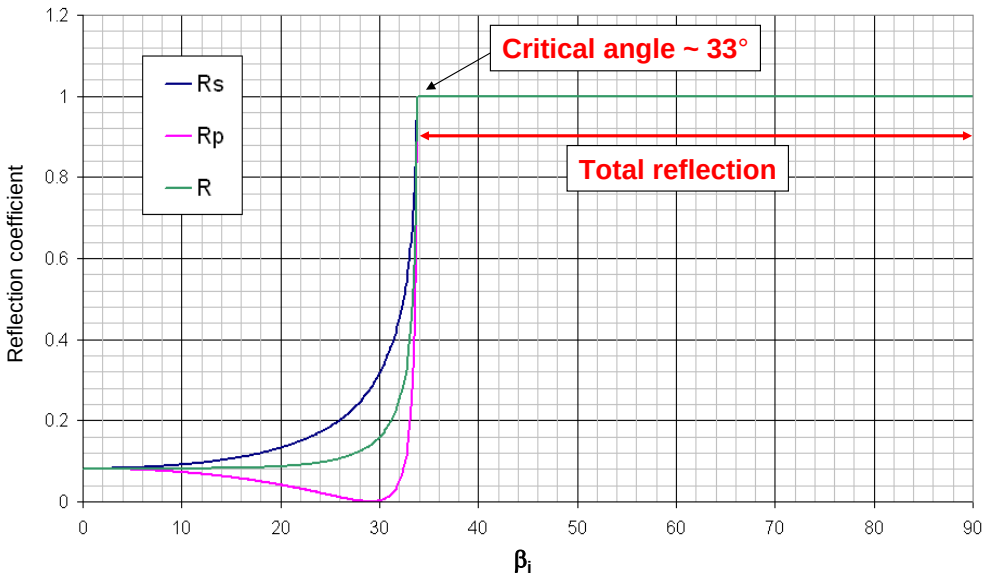

Figure 2.25: Reflection coefficient versus the incident angle β_i .

For a single photon, R describes the probability to be reflected. For $0 < \beta < \beta_c$, R increases from 0.2 to 1 with a very steep slope close to β_c. It is clear from this study that only photons emitted with angles larger than β_c can be reflected.

Since in the case presented here the photons are produced in the LSO crystal with $n_{LSO} = 1.85$, two interfaces have to be considered: the interface of LSO with air ($n_{Air} = 1$), and the interface of LSO with silicon

grease ($n_{SiG} = 1.4$) [Marlow 04].

Due to the different index of refraction of air and silicon grease, the critical angle is different at each interface.

$$\begin{aligned} \beta_{c\ LSO/air} &= 33\ ^\circ \\ \beta_{c\ LSO/SiG} &= 49\ ^\circ \end{aligned} \tag{2.23}$$

We consider in first approximation that:
at the interface LSO/air any photon is totally reflected for $\beta_i > 33\ ^\circ$
at the interface LSO/air any photon is transmitted in the air for $\beta_i < 33\ ^\circ$
at the interface LSO/SiG any photon is totally reflected for $\beta_i > 49\ ^\circ$
at the interface LSO/SiG any photon is transmitted toward the detector for $\beta_i < 49\ ^\circ$.

The angle of photoemission θ is always given through the x axis so that:
If the interface is parallel to (x,y) or (x,z) the incident angle is $\pi/2 - \theta$,
If the interface is parallel to (y,z) the incident angle is θ.

The figure 2.26 shows from the photoemission origin, the angles leading to the transmission into the silicon grease and those leading to the loss of the photon.

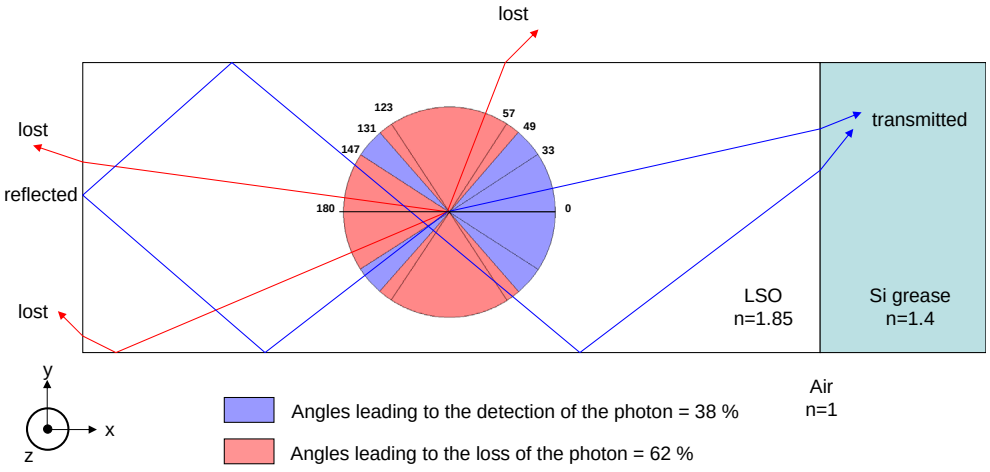

Figure 2.26: Schematic of the angles probabilities leading to the transmission of the emitted photon to the Silicon grease in contact with the detector.

- $0° < \theta < 49°$ the photon is reflected at the LSO/air interface and transmitted in the SiG. It can be detected.

- $49° < \theta < 57°$ the photon is reflected on both interfaces. It is lost for the detection.
- $57° < \theta < 123°$ the photon is transmitted through the LSO/air interface. It is lost for the detection.
- $123° < \theta < 131°$ the photon is reflected on both interfaces. It is lost for the detection.
- $131° < \theta < 147°$the photon is reflected at the LSO/air interface and transmitted in the SiG. It can be detected.
- $147° < \theta < 180°$ the photon is transmitted through the LSO/air interface. It is lost for the detection.

Once the photon transmitted to the SiG, as $n_{SiG} \leq n_{Si}$, the photon has high possibilities to be transmitted to the silicon detector.

Coming back to the timing, the contribution from reflection on the time jitter can be estimated. A focus is done on the worst case. The minimum propagation time is obtained for an emission point at x_0=L, with an angle $\theta = 0$ so that $t_{prop\ min} = 0$. The maximum propagation time is given for x_0=L and $\theta = 131°$ (or 237°). The photon path length in this extreme case is of 3.67 cm. The maximum variation on propagation time is then given by:

$$\Delta t_{max} = t_{prop\ max} - t_{prop\ min} = \frac{2Ln}{c.\,|cos(131)|} = 188\ ps \tag{2.24}$$

This value represents the largest variation possible, or the Gaussian maximum width, i.e. $\Delta t_{max} = 6\ \sigma$. With σ the standard deviation of the propagation time contribution $\sigma_{prop} = 32\ ps\ and\ FWHM = 75\ ps$. It is the uncertainty on the time arrival of each photon in the silicon grease once emitted.

At 420 nm the optical absorption coefficient of LSO has been calculated at 0.027 cm^{-1} [Kronberger 08], meaning that after 3.67 cm, 90 % of the photons are transmitted. Nevertheless, as shown in 2.3.2, the LSO also emits photons at wavelengths $\leq 400\ nm$. In this range, the absorption constant reaches $\geq 0.2\ cm^{-1}$ so that half the photons are absorbed in a thickness of $\leq 4\ cm$. In other words, the number of detectable photons depends on the depth of interaction: longer crystals will emit fewer photons.

Moreover, in order to increase the light yield, scintillators are usually wrapped with Teflon. As this wrapping is done by hand, the interface to be considered is LSO/air. The difference is that at 420 nm, 95% of the photons which would escape the LSO are then reinjected in the crystal. This reflection is diffuse at 95% and specular at 5% so that the angle at which the photons are reinjected will mostly vary from 0 to π. This makes the model presented here more complex. Simulations and measurements have been performed in [Kronberger 08] to show that the wrapping with Teflon increases the light yield with nearly a factor 2.

2.3.3.3 statistics of photoelectron production

The time resolution achievable with slowly decaying scintillators such as LSO is limited primarily by the statistics of photon production converted in electrons in a detector [Post 50]. The time resolution imposed by this effect alone has been calculated by Post and Schiff in 1950.

Their work is dealing with the limitation in resolving time that arises from fluctuation in the emission, transmission and collection of scintillation photons. In order to use their formulas, some assumptions have to be clarified. Following the excitation of the scintillator by an energetic event:

- the photodetector multiplies the primary photoelectrons without time spread. In these conditions only the contribution of the scintillator is taken into account in the time precision, not the one of the photodetector.

- the electrons resulting from the multiplication in the photodetector are fed into a discriminator which gives a signal only if a minimum of Q primary photoelectrons are accumulated. A signal is triggered only if a minimum of Q photoelectrons is sensed which is exactly the case of the NINO chip. Note that time precision contribution from the readout electronics is not discussed in their work.

- $f(t)$ is the average number of photoelectrons emitted between t_0=0 (time of the initial excitation) and t, and that f(0)=0.

The probability $P(Q,t)$that Q photoelectrons are sensed between 0 and t is given by the Poisson distribution:

$$P(Q,t) = [f(t)]^Q e^{-f(t)}/Q! \tag{2.25}$$

In the case of a scintillator the light signal y(t) is given by the equation 2.14. The average number of photoelectrons created between t_0 and t is then given by the function f(t), as mentioned chapter 2.3.2, in equation 2.15. This last formula can be inserted into the formula 2.25 which can now be written:

$$P(Q,t) = \frac{R^Q \times \left(1 - e^{-\frac{t}{\tau}}\right)^Q \times e^{-R\left(1-e^{-\frac{t}{\tau}}\right)}}{(Q)!} \tag{2.26}$$

The maximum of this probability is given for $\frac{dP}{dt} = 0$, leading to the time t_{max} at which the Q^{th} electron has the highest probability to be emitted, or the number Q of the photoelectron emitted at this time :

$$\begin{aligned} t_{max} &= -\tau ln(1 - \frac{Q}{R}) \\ Q &= R(1 - e^{\frac{-t_{max}}{\tau}}) \end{aligned} \tag{2.27}$$

Which is an equivalent form to equations 2.16.

The Probability that the Q^{th} photoelectron is detected between t and t+dt has been shown to be the probability that $(Q-1)^{th}$ photons are detected at time t, multiplied by the probability that the Q^{th} photon is detected between t and t+dt [Westcott 48, Knoll 00]:

$$W(Q,t).dt = P(Q-1,t) \times \frac{df}{dt}.dt \tag{2.28}$$

the total probability being for infinite time:

$$\int_0^\infty W(Q,t).dt \tag{2.29}$$

By replacing the function f from equation 2.15, this probability becomes:

$$W(Q,t).dt = \frac{R^Q \times \left(1 - e^{-\frac{t}{\tau}}\right)^{Q-1} \times e^{-R\left(1-e^{-\frac{t}{\tau}}\right)-\frac{t}{\tau}}}{\tau(Q-1)!}.dt \tag{2.30}$$

with W(Q,t) the density of probability that the Q^{th} photoelectron is detected between t and t+dt, in other words the probability per time interval dt. The derivative of this equation is:

$$\begin{aligned} \frac{dW}{dt} = &\frac{e^{-\left(1-e^{-\frac{t}{\tau}}\right)R-\frac{2t}{\tau}} (Q-1) R^2 \left(R\left(1-e^{-\frac{t}{\tau}}\right)\right)^{Q-2}}{\tau^2(Q-1)!} \\ &+\frac{e^{-\left(1-e^{-\frac{t}{\tau}}\right)R-\frac{t}{\tau}} R \left(R\left(1-e^{-\frac{t}{\tau}}\right)\right)^{Q-1} \left(-\frac{1}{\tau} - \frac{e^{-\frac{t}{\tau}}R}{\tau}\right)}{\tau(Q-1)!} \end{aligned} \tag{2.31}$$

The density of probability is maximum for $\frac{dW}{dt} = 0$, leading to t_Q: the most probable interval in which the Q^{th} photon is detected, in other words t_Q represents the **time precision** [Lynch 66, Wright 06].

$$Q = R(1 - e^{\frac{-t_Q}{\tau}}) + e^{+\frac{t_Q}{\tau}}$$
$$t_Q = \tau ln\left(\frac{1}{2}\left(Q - R + \sqrt{(Q-R)^2 + 4R}\right)\right) \quad (2.32)$$

The time precision can be calculated through 3 parameters: R the total number of photoelectrons generated per excitation of the scintillator, Q the photoelectron number on which the discriminator is triggering the signal, τ the decay time of the scintillator.

It is interesting to see from this formula that the time precision from the statistics of scintillation depends on the decay time. If the fast rise time of the scintillation light plays a major role to detect the first photons, the decay time also plays a role.

In order to determine the influence of each parameter, W(Q,t) can be plotted as a function of time. If two parameters out of three are fixed, and if the third parameter is varying, a trend can be found. Figure 2.27 shows the graphs for R = 2200 photoelectrons and τ = 40 ns, with Q varying from 1 to 20. The time precision is the maximum of W(Q,t). This Figure shows that the time precision is minimum for Q minimum. For Q=1, which is the reference measurement, the time precision is 0.

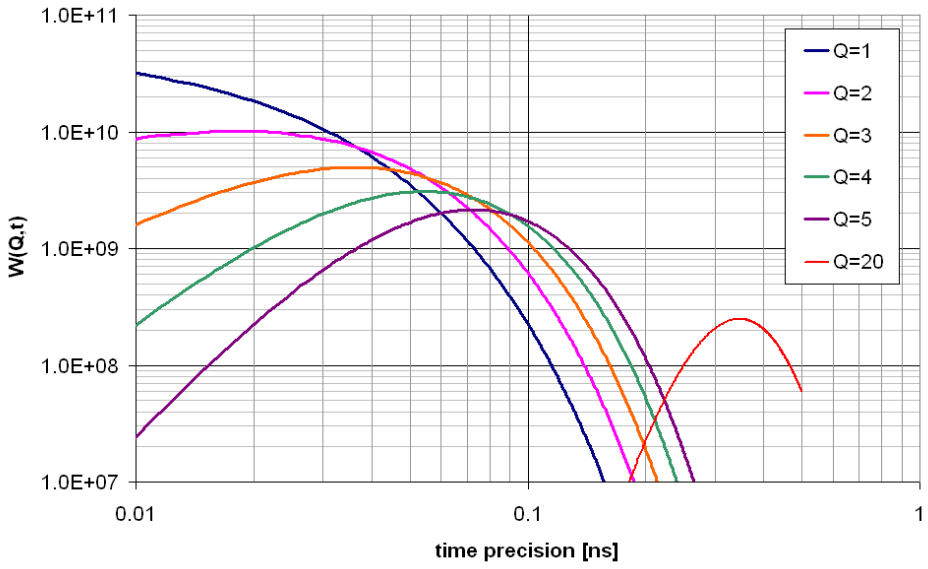

Figure 2.27: Time precision as a function of Q varying from 1 to 20 in LSO (R=2200 and τ=40 ns) .

Figure 2.28 shows the graphs for R = 2200 photoelectrons and Q = 5, with τ varying from 5 ns to 100 ns. This Figure shows that the time precision is minimum for τ minimum. In the case of LSO, $\tau = 40\ ns$, the

time precision achievable while triggering on the 5^{th} photon out of 2200 is of 75 ps.

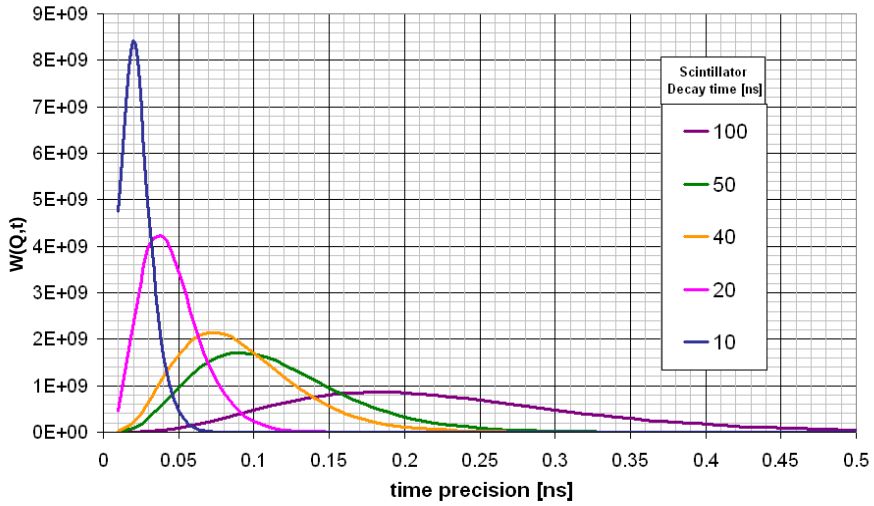

Figure 2.28: Time precision as a function of τ varying from 10 ns to 100 ns in LSO (R=2200 and Q=5).

Figure 2.29 shows the graphs for $\tau = 40$ ns and Q = 5, with R varying from 800 pe to 2200 pe. This Figure shows that the time precision is minimum when R is maximum. It is impossible to achieve a time precision of less than 100 ps with less than 1500 photons detected if Q=5.

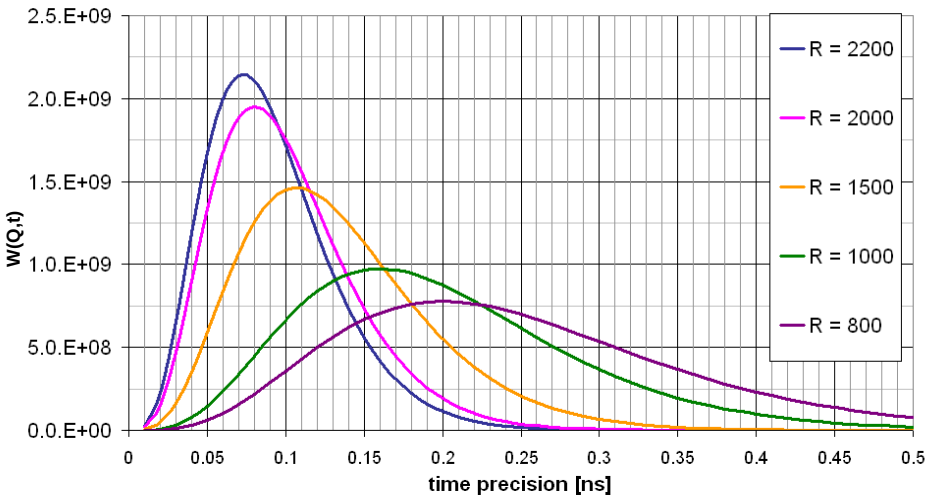

Figure 2.29: Time precision as a function of R varying from 800 p.e. to 2200 p.e. in LSO ($\tau = 40$ ns and Q = 5).

2.3.3.4 Conclusion

The time precision achievable with a scintillator such as LSO has 3 main limitations:

1. One from the intrinsic rise time of light production in the scintillator estimated at some 10 ps.

2. One from the time of light propagation in the crystal: $\sigma_{propag} \approx 75\ ps$. One could improve on this by reducing the scintillator length, however with a trade off loosing in detector sensitivity because of shorter absorption length.

3. One owing to the statistical nature of photon production: σ_{phot}. This one can be improved by using different scintillators with higher light yield and shorter time constant. However the choice of a scintillator is generally a compromise between these two values and LSO is at the moment the optimal choice. Nevertheless the minimum time precision can be reached only if the photodetector coupled to the crystal is able to detect the first photoelectrons.

Each of these limitations constitutes the total time precision intrinsic to the scintillator σ_{scint}:

$$\sigma_{scint} = \sqrt{\sigma_{rise}^2 + \sigma_{propag}^2 + \sigma_{phot}^2} \tag{2.33}$$

In the case of $\sigma_{rise} = 20\ ps$, $\sigma_{propag} = 75\ ps$ and $\sigma_{phot} = 18\ ps$ (Q=2, R=2200 and τ=40 ns), the limit time precision achievable with a LSO scintillator is $\sigma_{scint} = 80\ ps$, highly dominated by the fluctuations in propagation time.

2.4 Photodetectors

The aim of a photodetector is to convert the energy of absorbed photons into a measurable electrical signal. A photon has no rest mass, no charge, and its energy E_{Phot} and momentum p_{Phot} are :

$$E_{Phot} = \frac{hc}{\lambda} \quad p_{Phot} = \frac{h}{\lambda} \tag{2.34}$$

With h being the Planck's constant, c the speed of light in vacuum and λ the wavelength.

The Photodetectors described in this document are based on the photoelectric effect (see chap. 2.1.1) and can be divided into 3 main categories:

- The Vacuum photodetectors: in which photons interact through external photoelectric effect and in which electrons are multiplied through secondary emission under a high electric field. In this category one finds the PhotoMultiplier Tubes (PMT) and the Micro Channel Plates (MCP)
- The solid state photodetectors : in which photons interact through internal photoelectric effect in a semiconductor. Electrons are multiplied through the impact ionization mechanism, under an electric field of 10^6 V/m. In this category we will find the photodiodes, the Avalanche PhotoDiodes (APD) and the Silicon PhotoMultipliers (SiPM).
- The hybrid photodetectors combining solid state and vacuum photodetectors. In this category we will find Hybrid PhotoDetector (HPD), Hybrid Avalanche PhotoDetector (HAPD), Hybrid phototube with luminescent screen etc...

The key characteristics of photodetectors are quantum efficiency as a function of the wavelength QE(λ), geometry, operating voltage (from 30 V for SiPM to 3000 V for PMTs), gain M (M=1 for a photodiode, M=10^2 for an APD, M=10^6 for a PMT), noise and time resolution.

This chapter aims to describe the photodetectors used with the CERN electronics in my experimental work.

2.4.1 Vacuum photodetectors

Prior to describing different photodetectors, some general definitions and mechanisms of vacuum are presented.

2.4.1.1 Main mechanisms

Photoemission

In vacuum photodetectors, electrons have to escape the matter after being excited by a radiation. In this case the photoelectric effect is external as described in 2.1.1 and one can speak of photoemission to characterize the photoelectric effect.

Secondary emission

The secondary emission is the mechanism behind the electron multiplication in most vacuum photodetectors. It is based on the emission of secondary electrons from a solid in vacuum caused by the impact under a high electric field of primary electrons. Depending on the material used as a target, the secondary emission efficiency is defined by the yield δ. It represents the number of secondary electrons emitted per incident electron.

This process can be described as follows. Under an electric field, a primary electron excites other electrons in the matter, which are then emitted radially. These secondary electrons which move toward the interface solid-vacuum are undergoing elastic and inelastic collisions. Then, if they still have a minimum energy corresponding to the surface work function W, the electrons escape over the surface barrier into the vacuum.

Even if secondary electrons are generated along the primary electron path, only these electrons that originate less than 50 nm can escape from the material into vacuum [Wittke].

2.4.1.2 Photomultiplier tubes (PMT) [Knoll 00]

Photomultiplier tubes are the most common light amplifiers used with scintillators. They have the ability to convert a single light quantum into a measurable electric signal without adding a blurring noise. This chapter is describing their functioning principle and exhibits their main characteristics.

Principle:

Photomultipliers are constructed from a glass vacuum tube which in-

tegrates an entrance window, a photocathode, several dynodes, and an anode. Incident photons impinge on the photocathode material which is a very thin deposit on the entry window of the device, where electrons are generated through the external photoelectric effect. These electrons are transported by the accelerating field of the focusing electrode toward the dynodes chain, where electrons are then multiplied by the process of secondary emission.

Each dynode is biased at a more positive voltage than the previous one to create step by step an accelerating electric field. The electrons leave the photocathode, having the energy of the incoming photon (minus the work function of the photocathode). As they move toward the first dynode they are accelerated by the electric field, which increases their energy. On striking the first dynode, more low energy electrons are emitted with a yield δ and these, in turn, are accelerated toward the next dynode. The geometry of the dynode chain is such that a cascade occurs with an ever-increasing number of electrons being produced at each stage. At the end of this multiplication process, the anode collects all the electrons and the accumulated charge results in a sharp current pulse indicating the arrival of a photon at the photocathode. A schematic of the principle is shown in Figure 2.30.

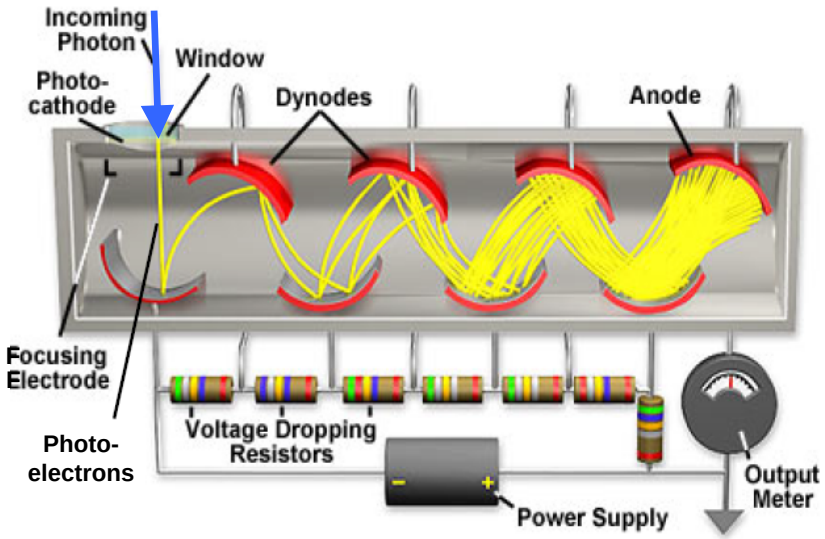

Figure 2.30: Principle schematic of the PMT.

Entrance Window

The window transmittance depends on the wavelength of the incident

radiation as seen on the left part of Figure 2.31 [Musienko]. Its constituting material has to be carefully chosen from the radiation to detect.

Photocathode and Quantum efficiency (QE)

The photocathode is a cathode emitting electrons when illuminated. The number of emitted electrons per photon is called the Quantum Efficiency (QE). The QE is a function of the wavelength and it strongly depends on the material used for the photocathode as seen on the right part of Figure 2.31. The main weakness of the PMT resides in their low QE: ≤ 0.25 for bialkali photocathodes in commercial PMTs. Nevertheless new material is tested for photocathodes such as GaAsP [Suyama 04] or ultra bialkali [pani 08], which could provide QE in the order of 0.5 at 500 nm.

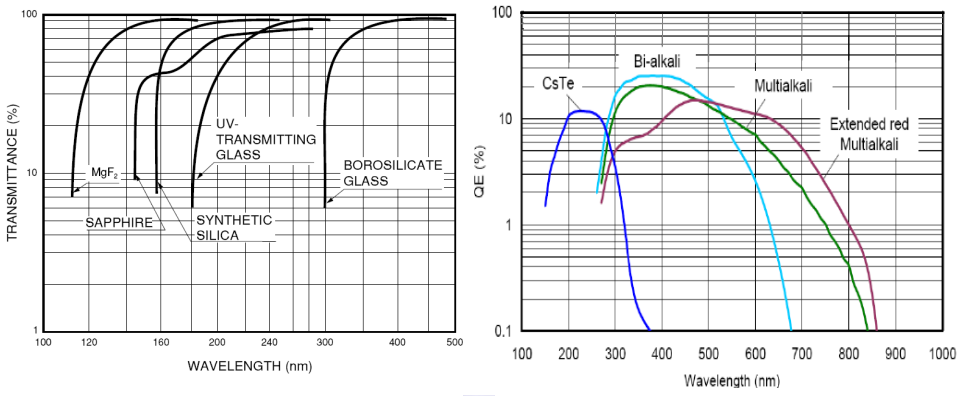

Figure 2.31: Left part: transmission coefficient as a function of the wavelength for different window material. Right: Quantum efficiency as a function of the wavelength for different photocathode material.

Dynodes

The dynodes are the electrodes where secondary emission occurs. The Figure 2.32 from [Hamamatsu] shows the secondary emission yield for different dynode materials used as a function of the accelerating voltage for the primary electrons.

Linearity

The electron multiplication factor or gain in PMTs is constant from 1 initial photoelectron to many thousands. Nevertheless a saturation effect

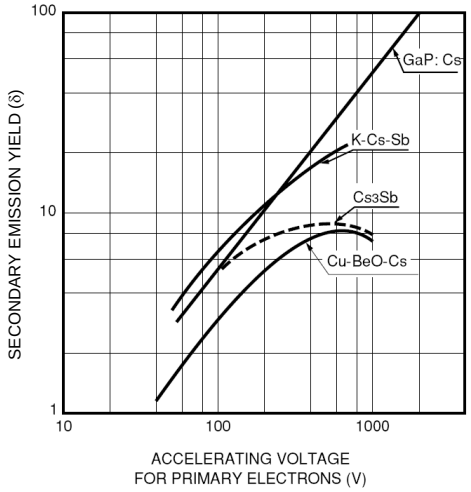

Figure 2.32: Secondary emission yield δ for different materials as a function of the accelerating voltage for the primary electrons.

occurs in case of large numbers of photoelectrons generating a space charge between the last dynode and the anode. The buildup of space charge affects the accelerating field which degrades the anode collection efficiency.

Noise

In a PMT, the most significant source of random noise results from the spontaneous emission of a thermal electron at the photocathode, called thermal noise. The resulting pulse corresponds then to a single photoelectron pulse, and it is impossible to make the difference between a single photoelectron pulse and thermal noise. Those thermal electrons are produced with a rate which depends on the photocathode area and material, and on the temperature. To minimize this noise, PMTs with small photocathode area should be used. The material of this photocathode should also be chosen among the most "quiet" such as bialkali which emits electrons at a typical rate of $10^2 - 10^4$ $electrons.cm^{-2}.s^{-1}$ at room temperature. In case of a dark rate of 10^3 $electrons.s^{-1}$, or 1 electron emitted every ms on average, the probability that a thermal electron contributes to a signal with a length of approximately of 100 ns is very low, in the order of 10^{-4}.

Another source of noise in a PMT is afterpulsing. Afterpulses are satellite pulses which follow a true signal pulse after a short delay. The emission of light from the last dynode (during the electron emission) can find a way back to the photocathode and then generate the emission

of electrons. These electrons will generate a current pulse delayed by the transit time. This pulse amplitude is generally the size of a single photoelectron

Pulse timing properties

The transit time in a PMT is the average time difference between the arrival of a photon at the photocathode and the collection of the subsequent secondary electrons at the anode. From different PMTs, this transit time can vary from 10 ns to 50 ns.

This transit time, if it was constant, would just add a fixed delay. The variation of the transit time called transit time spread determines the width of the pulse of electrons arriving at the anode of the tube as shown in Figure 2.33.

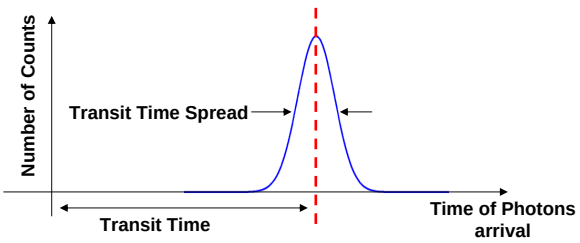

Figure 2.33: Histogram of the arrival time of photons at the anode of a PMT. The Transit Time as well as the Transit Time Spread is shown.

As the time required for photoemission in the photocathode or for secondary emission from the dynodes is far below a hundred of picoseconds, the critical point for timing properties is the region between the photocathode and the first dynode. This region can be quite large compared to the inter dynode distance. The difference in path of an electron leaving the center of the photocathode and another at the edge is a dominant factor.

Let's assume that an electron leaves the photocathode at point A and goes to the first dynode at point B. An electric field is created when a voltage difference $V_A - V_B$ is applied. The total energy E of the electron is a sum of its kinetic energy K and of its potential energy P. The conservation of the energy tells that the total energy at A E_A is the same as the total energy in B E_B so that we have $E_B - E_A = 0$. In this case,

$$\begin{aligned} E_B - E_A = K_B - K_A + P_B - P_A = 0 \\ P_B - P_A = -(K_B - K_A) \end{aligned} \tag{2.35}$$

$K = 1/2mv^2$ and P=qV, with v the speed of the electron, V the voltage applied, m the mass of the electron and q the charge of the electron. The speed of the electron at point A and B is respectively v_A and v_B, so that:

$$\begin{aligned} \frac{1}{2}mv_B^2 - \frac{1}{2}mv_A^2 = q(V_B - V_A) = q\Delta V \\ v_B = \sqrt{\frac{2(q\Delta V + 1/2mv_A^2)}{m}} \end{aligned} \tag{2.36}$$

Independently, if a charged particle is set free in an electric field and in vacuum at point A, it is accelerated by a force proportional to the electric field and charge on the particle. Moreover, if the velocity remains small compared to the velocity of light, this force can also be described by the particle mass and its acceleration:

$$\vec{F} = e\ \vec{E} = m\ \vec{a} \tag{2.37}$$

The velocity of this charged particle at time t can thus be expressed as:

$$\vec{v}\ (t) = \int \vec{a}\ dt = \frac{e\ \vec{E}}{m}.t + \vec{v_A} \tag{2.38}$$

With $\vec{v_A}$ its initial speed. This particle reaches the point B at time $t = t_{total}$, with a speed v_B.

$$\begin{aligned} v_B = v(t_{total}) = \frac{eE}{m}.t_{total} + v_A \\ t_{total} = [v_B - v_A]\ \frac{m}{eE} \end{aligned} \tag{2.39}$$

The electric field E is:

$$E = \frac{\Delta V}{d} \tag{2.40}$$

With d the distance separating point A and point B and ΔV the electrodes voltage difference. Replacing v_B by equation 2.36, the time required for the electron to go from point A to point B is:

$$t_{total} = \left[\sqrt{\frac{2(q\Delta V + 1/2mv_A^2)}{m}} - v_A\right] \frac{md}{e\Delta V} \tag{2.41}$$

For $\Delta V = 200\ V$, $v_A = 0$, $m = 9.109\ 10^{-31}\ kg$ and $e = 1.602\ 10^{-19}\ C$, $v_B = 8.38\ 10^6\ m/s$. If an electron path is greater of Δd from another, the difference of time propagation between the two will then be Δt_{total}:

$$\Delta t_{total} = \left[\sqrt{\frac{2(q\Delta V + 1/2mv_A^2)}{m}} - v_A \right] \frac{m\Delta d}{e\Delta V} \approx 2.38\ 10^{-7}.\Delta d \qquad (2.42)$$

For $\Delta d = 1\ mm$, $\Delta t_{total} = 238\ ps$.

From this it is also obvious that the second important point is the difference of initial velocity v_A between these two electrons. This value will increase if the initial speed is lower for the electron whose path is larger.

If the situation above represents the worst case (the extremity of the Gaussian), then the standard deviation of the TTS σ_{TTS} issue from the difference in path length is $\sigma_{TTS} = 238/6 = 40\ ps$

In order to minimize this difference of path length, the photocathode is often designed spherical. However, the glass window can be kept flat for better coupling with scintillators. The design of the dynodes can also vary in order to speed up the interdynode transit time. Several structures exist, they are shown in Figure 2.34.

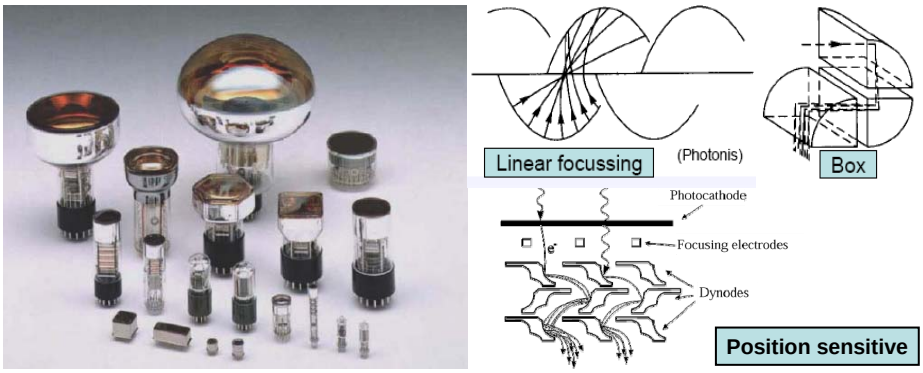

Figure 2.34: different existing PMTs (left) and different dynodes structures(right)

It should be mentioned that a larger number of photoelectrons leads to smaller fluctuations and hence transit time spread will improve with $\frac{1}{\sqrt{N_{pe}}}$

PMT used in the study

Three PMTs have been used in the study: one from Photonis, the XP 2020 Q, and 2 from Hamamatsu, the H6533. Their respective datasheets are given in Appendix B

2.4.1.3 MCP

A micro-channel plate (MCP) is a planar component used for direct detection of particles (electrons or ions) and radiation (ultraviolet radiation and X-rays). This photodetector is a glass plate with high resistivity layer through which micro channels or pores are etched. A schematic of its working principle is shown in Figure 2.35. Each pore is a continuous-dynode electron multiplier, in which the multiplication takes place under the presence of a strong electric field. Its dimensions are usually characterized by its diameter d (few μm) and length L, with a ratio $\alpha = \frac{L}{d}$ usually in the order of 40 to 100. For light detection, the MCP is encapsulated in a vacuum tube and uses an entrance window and a photocathode, similarly to PMTs).

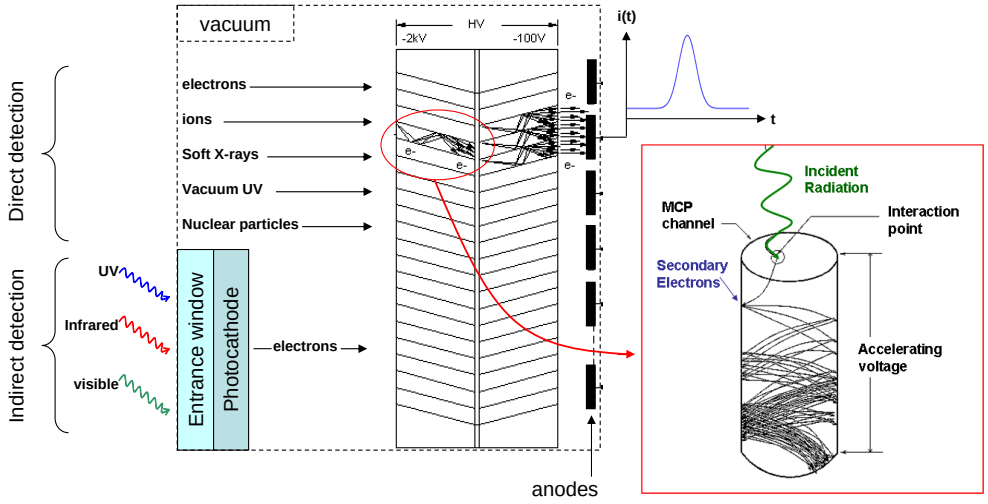

Figure 2.35: Schematic of the MCP

The structure presented is called chevron stacked: 2 MCPs are put together with channels sloping at small angles (between 5 an 20 degrees). The angles limit ion feedback effects. The use of two consecutive MCPs permits to reduce the space charge effects and then to reach higher gains [Wiza 79]. The channel matrix is usually fabricated from lead glass on which a semiconducting layer is deposited to optimize secondary emission and to render the channel wall semiconducting. The MCP thickness is in the order of 1 mm.

Due to the angle, a particle or photon that enters one of the pores is channeled to hit the wall of the pore. The impact starts a cascade of secondary electrons that propagates through the channel, which amplifies the original signal by several orders of magnitude depending on the electric field strength and the geometry of the micro-channel plate. In the

case presented here, a gain of up to 10^4 per MCP can be achieved. The electrons exit the channels on the opposite side where they are themselves detected by additional means, often simply metal anodes measuring the total current.

Due to the high speed of electrons in vacuum (see chapter 2.4.1.2) and the short path they have to travel (MCPs are some mm thin), this device is the fastest known for photodetection.

The left part of the Figure 2.35 shows that MCPs may be used for direct or indirect detection. They can detect directly and with sufficient quantum efficiency electrons with energies from 0.2 keV to 50 keV, positive ions (H^+, He^+, A^+) with energies from 0.5 keV to 200 keV, UV radiations between 30 nm and 150 nm and even soft X-rays with detection efficiency ≤ 10 % [Wiza 79].

In the case of indirect detection the same photocathodes and entrance windows than PMTs' are used and their choice is a function of the radiation wavelength to detect. The interaction of photons with the photocathode will generate electrons which will reach the MCP.

After the cascade, the microchannel takes time to recover before it can detect another signal. As explained for the samples used in [Wiza 79], the associated resistance and capacitance per channel are respectively of about $3\ 10^{14}\ \Omega$ and $4\ 10^{-16}\ F$. After a channel is fired, the charge in its wall must be replenished. Because of the exponential nature of the multiplication along the channel, most of the charge is depleted from the last 20 % of the channel length. This means that an effective channel capacitance of $C_C = 8\ 10^{-17}\ F$ has to be recharged through a $R_C = 3\ 10^{14}\ \Omega$ channel resistance leading to a time constant of $R_C.C_C = 24\ ms$: a relatively long dead time.

CERN is also collaborating in a project where MCPs are used [Lapington 08]. The goal is to readout MCPs with the NINO chip and the HPTDC for an application in fluorescence spectroscopy. In this project, a time precision of 10 ps on the detection of 1 photoelectron is targeted.

2.4.2 Solid state photodetectors

Advances in semiconductor photodiodes have led to the progressive replacement of PMTs with solid state devices in some applications. Solid state photodetectors are used because of higher quantum efficiency and hence a potentially better energy resolution. Moreover they have lower power consumption and a more compact size. Photodiodes are also much

less sensitive to magnetic fields and can therefore be used in experiments where high magnetic fields (B) are used as for example LHC experiments (B=4 T) or MRI scanners (B=1 T). Because of the short distance over which the carriers have to move in these devices, their time response starts to compete with that of the PMT so that they can be used in timing experiments.

In this chapter, three kinds of solid state photodetectors are studied: the photodiode, the Avalanche PhotoDiode (APD) and the Silicon PhotoMultipliers (SiPM). These are PN junction silicon diodes on which increasing reverse bias is applied.

The region of operation of each detector is shown on a typical diode reverse biased I(V) plot in Figure 2.36.

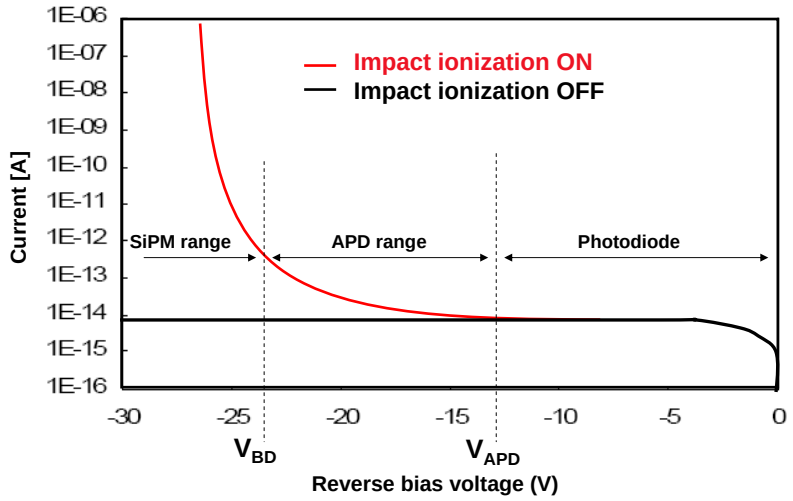

Figure 2.36: Current of a diode as a function of the reverse bias

Photodiodes are structures operated at low reverse bias below the avalanche region. The current flowing remains low.

APDs work in a range of intermediate reverse voltages where the multiplication process is linear. Impact ionization triggers avalanche process so that the current flow will increase.

SiPMs work for higher reverse voltages. The electric field is high enough so that the avalanche process becomes self sustained. Each photon triggers a Geiger mode avalanche.

2.4.2.1 Photodiodes

Between 1 eV and 5 eV, the most probable interaction process is the photoelectric effect as shown in Figure 2.3.

The absorption of such photon by a semiconductor leads to the generation of one electron-hole pair. The electron is in the conduction band and the hole in the valence band. As shown in Figure 2.37, the electric field E assures the separation of electrons and holes and their transport to respectively the cathode and the anode.

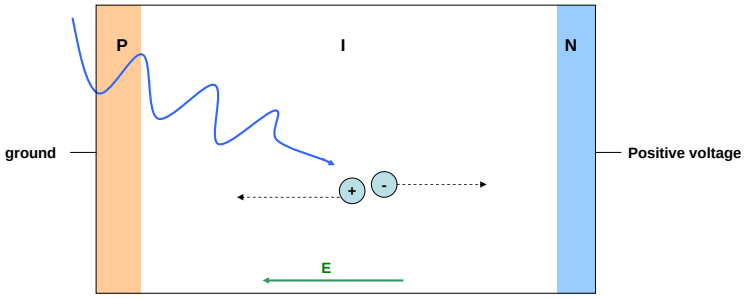

Figure 2.37: mechanism of carrier generation and collection in a photodiode

Signal generation

Photodiodes have a linear response. The interaction of N photons will generate N electron/hole pairs. Each electron/hole pair generated is separated and drifts under the electric field. This motion induces a current I on the detector electrodes, as described by the Ramo theorem extended to semiconductors [Ramo 39, Cavalleri 71]:

$$\begin{aligned} I &= \pm qN\ \vec{v}_{drift}\ .\ \vec{E}_W \\ with\ \vec{v}_{drift} &= \pm\mu\ \vec{E} \end{aligned} \tag{2.43}$$

μ is the carrier mobility and $\vec{E}$ is the electric field. $\vec{v}_{drift}$ is the carrier velocity, negative for electrons and positive for holes, q is the elementary charge of the electron, and N the number of carriers. $\vec{E}_W$ is the weighting field and is a measure of the electrostatic coupling between the moving carrier and the sensing electrode

Quantum Efficiency (QE) in a solid state photodetector

QE is the probability that a single photon incident on the photodetector will generate a photocarrier pair that contributes to the detector current [Saleh 07]. $0 \leq QE \leq 1$. Actually, not all the photons will contribute to the current generation, some of them will be reflected at the

detector surface, some of them will not be absorbed if the depth of the detector is shorter than the attenuation coefficient or some of them will recombine at the surface of the detector where the recombination centers are abundant.

$$QE = (1 - R).\epsilon.[1 - exp(-\alpha.d)] \tag{2.44}$$

R is the reflection coefficient mentioned in chapter 2.3.3.2. In order to minimize the effect of this parameter, special coating should be used. This parameter sometimes has to be considered separately from the QE given by the manufacturers. It varies with the technique used to do the measurement.

ϵ represents the fraction of photons which will not interact at the surface of the detector in the P or N layer where the electron hole pairs will immediately recombine due to the abundance of recombination centers. This parameter can be increased closer to 1 by careful design of the device minimizing the doped regions and then by careful material growth so that impurities are not too abundant in the depleted region.

$[1 - e^{-\alpha.d}]$ represents the fraction of the photon flux which will be absorbed in the active depth of the semiconductor which thickness is d:

$$\frac{\int_0^d e^{-\alpha x} dx}{\int_0^\infty e^{-\alpha x} dx} = [1 - exp(-\alpha.d)] \tag{2.45}$$

The Quantum efficiency is a function of the wavelength λ as the attenuation coefficient is also a function of λ. If the radiation wavelength is lower than the bandgap of the material λ_g the material becomes transparent to the radiation.

2.4.2.2 Avalanche mechanism [Saleh 07]

In order to increase the current at the output of a solid state photodetector, the mechanism of avalanche of electrons is used. A high electric field of approximately 10^5 V/cm is applied between the cathode and the anode of a photodiode. The charge carriers created by photoelectric effect are accelerated and their kinetic energy is increased. In a material, unlike vacuum, acceleration is constantly interrupted by random collisions which decrease the carrier acquired energy. These competing processes cause the carriers to reach an average saturation velocity. If the acquired energy gets larger than the energy needed to create an electron/hole pair, a second electron / hole pair can be generated at the next collision through

the process of impact ionization. Under the electric field the two carriers will be separated and accelerated to impact ionize and so on. This will generate an avalanche of carriers.

The gain can be defined as the charge induced by the movement of all the avalanche carriers divided by the charge of the first carrier(s) generating this avalanche.

Impact ionization is characterized by the ionization coefficient of electrons α_e and of holes α_h. They represent the probability to impact-ionize per unit length, expressed in cm^{-1}. Then $1/\alpha_e$ and $1/\alpha_h$ represent the average distance between two consecutive ionizations. This ionization coefficient increases with the electric field because of larger acceleration and decreases with increasing temperature because of thermal agitation which make the collisions more frequent. In ideal case these electric field and temperature are fixed. The ionization ratio k is an important parameter which permit to characterize the avalanche quality: $k = \frac{\alpha_h}{\alpha_e}$.

If $k << 1$ in a semiconductor, most of the ionization is made by electrons. The avalanche is then essentially done from the P side to the N side of the diode.

If $k \approx 1$, electrons and holes both ionize with the same probability. The holes moving toward the P side will generate electrons which will move to the N side. These electrons will generate further holes and so on. Although this process increases the gain, this situation presents different drawbacks: first as the process is random, this increases also the noise of the gain, second it is time consuming, being undesirable for the application and third it is unstable and can generate an avalanche breakdown.

An avalanche breakdown occurs when the avalanche mechanism is not controlled anymore.

2.4.2.3 Avalanche PhotoDiode (APD)

An APD is a strongly reverse-biased photodiode with typically $4\ 10^5\ V/cm$ electric field allowing impact ionization and then avalanche process as described before.

On one hand the geometry of the APD should maximize the photon absorption, and on another hand the multiplication region should be kept thin to minimize the localized uncontrolled avalanche breakdown. It is therefore necessary to separate the absorption region from the multiplication region. A widely chosen example of device is a P+-i-P-N+ diode where the intrinsic region is quite large for a better photon absorption,

and where the p-n+ junction is thin, as shown in Figure 2.38.

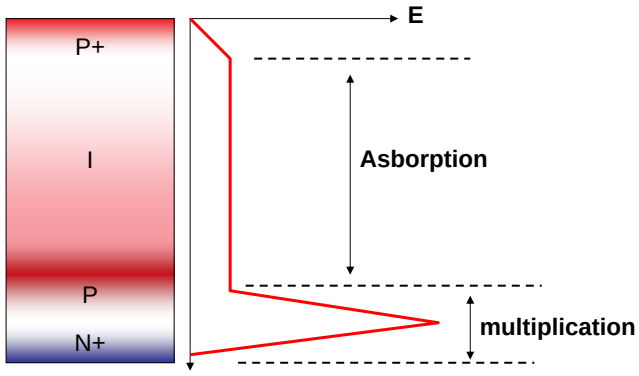

Figure 2.38: PIPN junction with its electric field profile

In this type of structure, holes drift toward the p+ layer where they will recombine and the electrons toward the p-n+ junction where they will be accelerated and will impact-ionize. In order to decrease the avalanche breakdown probability and random noise and time consumption, only one type of carrier should impact-ionize, not both. Most of the time electrons are chosen because of larger velocity in silicon but a device using holes might also work.

Excess noise factor (F)

The gain mechanism generates excess noise that arises from the randomness of the multiplication process. The excess noise factor F is a measure of the avalanche gain fluctuation and is defined by:

$$\left(\frac{\sigma}{E}\right)^2 = \frac{F}{N} \tag{2.46}$$

With N the total number of photoelectrons. Random fluctuations of the distance traversed by carriers between successive ionizing collisions give rise to fluctuations in the total number of secondary generated carriers. If we consider the gain M of the APD and σ_M the variation of the gain , the excess noise factor is:

$$F = 1 + \frac{\sigma_M^2}{M^2} \tag{2.47}$$

According to the model developed by Mc Intyre [McIntyre 66], the excess noise factor is a function of the ratio $k = \alpha_h/\alpha_e$

$$F = kM + (2 - \frac{1}{M})(1 - k) \tag{2.48}$$

Hamamatsu S8550

The APD chosen to be part of the detector system in this study is the Hamamatsu S8550. It is a 32 channels matrix APD used for example in PET detectors [Varella 07]. Each channel is $1.6 \times 1.6\ mm^2$, at 390 V the gain of the APD is around 175 and at 420 nm, the APD quantum efficiency is 75 %. The datasheet of this APD is given in Appendix B. Details of gain measurements are given in chapter 3

Time resolution

A complete study of the timing resolution obtained with APDs is also done in chapter 3

2.4.2.4 Silicon PhotoMultiplier (SiPM)

The advantages of the SiPM over the APD is its significantly higher gain (10^6) which permits single photon detection and limits the excess noise factor due to the geiger process used.

Principle

A SiPM is a matrix of Single Photon Avalanche Diodes (SPADs) with a common output (anode or cathode). A SPAD is a cell of small size (typically $50 \times 50\mu m^2$) usually built as a PIPN junction diode (such as the APDs) in series with a resistance in the order of 1 $M\Omega$. What makes it different from the APDs is that it is biased over the breakdown voltage.

In such conditions, the interaction of photons with the diode will lead to the flow of a large current into the diode. This current comes from the uncontrolled multiplication of carriers in the PN junction in geiger mode. As the impact ionization mechanism is self sustained over the breakdown voltage, the detector only needs the first photocarriers to trigger an uncontrolled avalanche. The first carriers can be produced by the interaction of a single photoelectron in the diode as well as by the interaction of several photoelectrons. A SPAD is then sensitive to the interaction of a single photoelectron.

The only way to stop the current flow is to reduce the bias on the diode below the breakdown voltage to stop the uncontrolled impact ionization process. That is the role of the serial resistance R_Q which will quench the diode current. As shown in Figure 2.39, the diode, resistance and bias are represented on the left part. The current I and the bias of the diode V_{diode} are represented on the right part as a function of time.

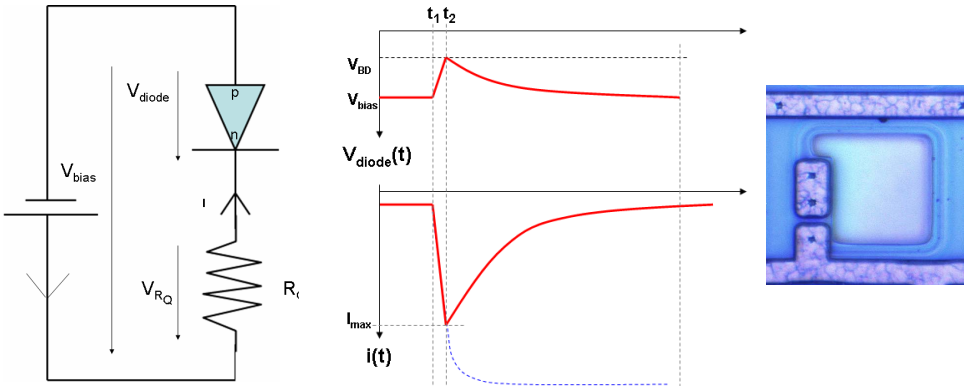

Figure 2.39: Left: schematic of a SPAD cell. Center: mechanism of signal formation as a function of time. Right: picture of a SPAD

The voltage on the diode V_{diode} is defined by:

$$V_{diode} = V_{bias} - R_Q.I \tag{2.49}$$

The formation of the signal may be seen into 5 steps:

1. The current is considered zero so that $V_{diode} = V_{bias}$. A photon interacts with the diode at t_1.

2. the current increases and starts to be in the order of the μA. The capacitance of the diode C_{diode} is charged with the time constant $\tau_r = R_S.C_{diode}$. For a resistance value in the order of the $M\Omega$, R.I is of some volts and the bias of the diode decreases until it reaches the value V_{BD}.

3. At t_2, $V_{diode} = V_{BD}$ and the mechanism of uncontrolled carrier multiplication stops, the avalanche is quenched.

4. After t_2 the capacitance of the diode C_{diode} will discharge into the quenching resistance and the serial resistance with a time constant $\tau_f = (R_S + R_Q).C_{diode}$.

5. After a recovery time of $5\tau_f$, the current is zero again so that the cell is ready for the next photon(s) detection.

This is a first order approximation of signal formation to understand the device principle. In a real SiPM there are parasitic capacitances and resistances whose electronic model is not well established yet. This comes from the great variety of companies supplying SiPM (Zecotec, Hamamatsu, SensL, Photonique, F.B.K. etc.) each of which using a different technology, leading to different signal shapes. A comparative study of SiPMs can be found in [Dinu 08].

Nevertheless it is very important to understand that the shape of the current signal depends only on the circuit elements and not on the number of photons involved in the trigger of the signal.

In a SiPM, SPADs are put together in parallel to form a matrix. Each element is independent and should give the same signal when fired by a photon. The output of the SiPM is then the sum of all the SPADs signals piled up. The current response given by one fired cell is triggered by one photoelectron. It is called the single photoelectron response. If N photoelectrons fire N cells at the same time, the current response will be N times the single photoelectron response. As an example, if the maximum pulse height of the SiPM output is measured with few photons sent to the SiPM, a histogram of the pulse height (measured during the thesis) is produced and is shown in Figure 2.40. The number of SPADs determines the dynamic range and the SiPM size (typically $1 \times 1\ mm^2$ or $3 \times 3\ mm^2$) determines the spatial resolution.

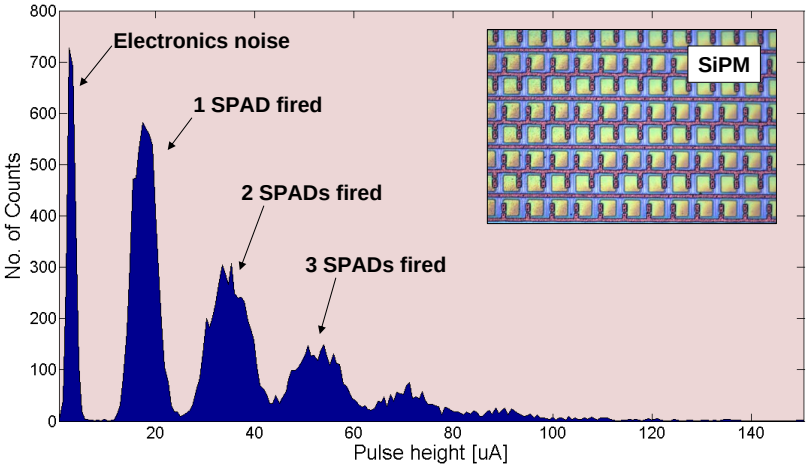

Figure 2.40: Histogram of the current pulse height for some photoelectrons sent to the SiPM. Top right: picture of the SPADs in parallel in the SiPM

The variation of the single photoelectron response is Gaussian and its FWHM increases with $\sqrt{n}$ with n the number of fired cells.

SPAD Gain

The gain can be expressed as the total charge delivered by one SPAD divided by the charge of one electron:

$$G = \frac{\int i(t)dt}{q_e} = \frac{(V_{bias} - V_{BD}).C_{diode}}{q_e} \tag{2.50}$$

Noise

Like in PMTs the main source of noise in a SiPM is due to the random generation of thermal electrons in the biased diode. These carriers will trigger an avalanche leading to a current signal of the same characteristics than a single photon signal. The emission rate of these thermal electrons depends on the overvoltage applied and on the temperature and on the number of SPADS in the SiPM. A frequency of 1 thermal electron emitted per microsecond (1 MHz) is reasonable compared to the dead time of a single cell of typically 100 ns. This dead time depends on the device design and varies from the different manufacturers [Dinu 08].

Another source of noise is afterpulsing. It happens when carriers are trapped during the avalanche (by defects for example) and then released some nanoseconds later, triggering a new avalanche. If the release time is less than the recovery time, then the bias on the diode is less than V_{bias} and the afterpulse signal is smaller than the single photoelectron response.

The avalanche mechanism generates light which can be absorbed by an adjacent cell and which can trigger another avalanche. Then a pulse results, which is the sum of two SPAD signals emitted at the same time, i.e. which is double. This kind of noise is called optical crosstalk. In some SiPMs, optical trenches are used to limit this effect

These three kinds of noise are presented on the scope shot in Figure 2.41. The signal shows the output of a transimpedance amplifier (a voltage) connected to the SiPM under dark conditions so that the signal can only be noise.

PhotoDetection Efficiency (PDE)

For SiPM the figure of merit is the PDE and not simply the QE.

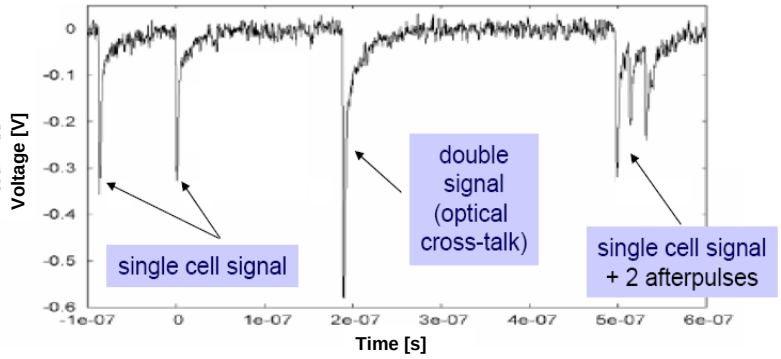

Figure 2.41: Screen shot of a SiPM placed in the dark illustrating the different kind of noise pulses

$$PDE = QE.f \tag{2.51}$$

f is the fill factor, i.e. the fraction of efficient area over the total area. In SiPM an important fraction of the total area is not efficient because of structures between the cells such as bias wires, optical trenches or guard rings. $0.3 < f < 0.8$ for Hamamatsu chips. QE is the quantum efficiency.

Usually a factor P_{01} is added to the PDE definition. It represents the probability that an electron traversing the high field region triggers an avalanche. In the case presented in this thesis, this phenomenon is already treated in the quantum efficiency definition.

The PDE is shown in Figure 2.42 as a function of the wavelength for Hamamatsu SiPM.

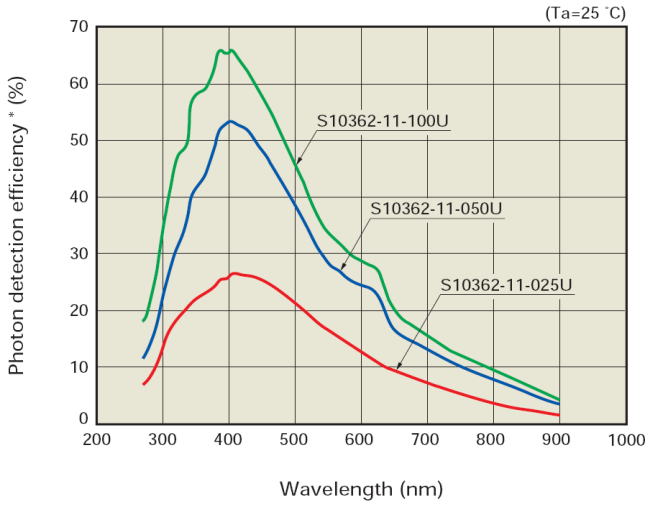

Figure 2.42: PDE as a function of the wavelength for three Hamamatsu SiPMs.

Dynamic range

The output signal of a SiPM is proportional to the number of fired cells. The number of fired cells equals the number of photoelectrons to detect N_{pe} as long as N_{pe} is smaller than the total number of cells N_{total}.

$$N_{firedcells} = N_{total}\left(1 - e^{\frac{N_{pe}}{N_{total}}}\right) \tag{2.52}$$

The Figure 2.43 taken from [Dolgoshein 06] shows the number of fired cells as a function of the number of photoelectron sent to the SiPM

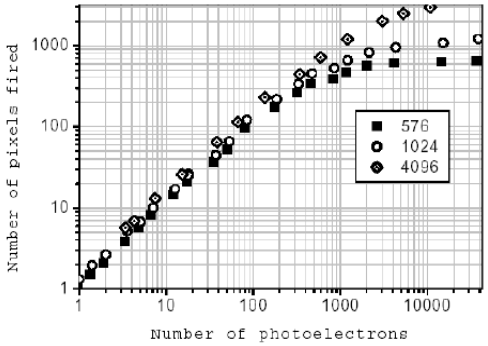

Figure 2.43: Dynamic range: number of fired pixels as a function of the number of photoelectrons sent to the SiPM

When the number of photons reaches the same order of magnitude as the number of cells, the probability that several photons hit the same cell increases. The resulting signal will remain the same whatever the number of photoelectrons, so that some of them will be lost for the detection

Time resolution

A complete study of the timing resolution obtained with SiPM is done in chapter 4

2.4.3 Overview

A comparison of the photodetectors presented in this chapter is shown on Table 2.3. It gives an overview of the different photodetectors properties, according to the results published and referenced throughout the chapter.

As a conclusion of chapter 2.3.3, the best photodetector in terms of

Table 2.3: Overview of mentioned photodetectors characteristics

		Vacuum technology		Solid state technology		
		PMT	MCP	PN, PIN	APD	SiPM
PDE	Blue	20%	20%	60%	50%	30%
	Green-yellow	40%	40%	80-90%	60-70%	50%
	Red	$\leq 6\%$	$\leq 6\%$	90-100%	80%	40%
Time precision		100ps	10ps	tens ns	few ns	$\leq 100ps$
Gain		$10^6 - 10^7$	$10^6 - 10^7$	1	200	$10^5 - 10^6$
Threshold sensitivity		1p.e.	1p.e.	100p.e.	10p.e.	1p.e.
Operation voltage		1kV	3kV	10-100V	100-500V	$\leq 100V$
Operation in magnetic field		$\leq 10^{-3}T$	Axial 2T	no sensitivity	no sensitivity	no sensitivity
Shape characteristics		sensible bulky	compact	robust, compact, mechanically rugged		

timing performance has the ability to sense the highest number of photons and to trigger on the first one.

From the table, it is clear that greater gain goes with better time precision and better threshold sensitivity. In this field the vacuum photodetectors offer the best performances. However they suffer from poorer quantum efficiency which limits the total number of detectable photons and then limits the time precision to about 100 ps. For the detectors to improve, scientific groups are working to increase the quantum efficiency of the photocathodes up to 50 % [Suyama 04, pani 08].

If solid state detectors offer a greater detection efficiency, their low gain doesn't permit to sense the first photoelectron which limits the time precision to the ns for APDs and photodiodes. The innovation in this field might come from the SiPM. Due to its higher gain it has the ability to sense the first photoelectron with a detection efficiency slightly lower than the solid state detectors.

Besides technical considerations, in medical imaging a strong improvement would be to reduce the cost of the scanner and to improve in compactness. In terms of cost, solid state photodetectors are much cheaper because of well established and large scale production in semiconductor industry. On the contrary, vacuum detectors are expensive. In this project

where only some units of each photodetector were bought the cost of one PMT H6533 is of $\approx$ 1350 euros and the cost of the SiPM is of $\approx$ 250 euros, i.e. a factor 5 difference.

Also in terms of compactness, possibilities offered by solid state detectors are much better. The volume of a SiPM is 50 times smaller than that of a PMT.

Moreover, in terms of power consumption, a PET scanner is composed of about 150 detection modules. With 4 PMTs per module this makes 600 PMTs to bias at about 2 kV. The power management in these conditions is much more delicate than for the same amount of SiPM, biased at typically 50 V.

As mentioned in chapter 1.3.4, the future improvements in medical imaging are hybrid technologies. Physicians are still discussing PET/CT or PET/MRI for the best dual mode imager in the future.

For PET/MRI, The problem of vacuum technology comes from the magnetic field in MRI ($\approx 1T$) which influences the path of electrons in vacuum and which severely degrades the electron collection efficiency in PMTs. Due to the microstructures used in MCPs, the device is less sensitive but its functioning is still limited to 2T. Solid state photodetectors are insensitive to magnetic field, giving them a higher potential for this application.

It is therefore obvious that as soon as solid state detectors can achieve good energy and time resolution, they will be the ideal component for PET/MRI imagers. From now on, photodiodes and APDs are well known devices which cannot lead to a breakthrough. The focus is made on SiPM: with an increasing number of publications every year this photodetector is the star of conferences such as IEEE NSS-MIC (nuclear science symposium and Medical Imaging) or NDIP (New Development In Photodetectors).

Chapter 3

Readout technique for PET/CT based on APD

This chapter shows the work done in the context of the European Framework Program 6 (FP6) BioCare project. The goal is to show the suitability of the readout electronics developed at CERN, i.e. the NINO chip, as a readout system in a detector head composed of a LSO crystals and an APD photodetector. In a first step each part of the detector is characterized individually. The whole detector system is then characterized in terms of energy and time resolution. Finally, the time resolution is analyzed in order to understand the contribution of each part of the detector system.

3.1 Characterization of each part of the detector system

3.1.1 LSO crystals

For different LSO crystals of 2x2 mm^2 small surface, the light yield was measured with a Photonis XP2020/Q PMT by the Crystal Clear collaboration [CrystalClear] at CERN. The scintillator is placed in vertical position, the surface of 2x2 mm^2 is coupled to the photodetector with silicon grease and the crystal is wrapped in Teflon.

The current signal from the PMT is sent to an attenuator followed by a shaper and then by an ORTEC MultiChannel Analyzer (MCA) of 8000 channels. This MCA is controlled by a MAESTRO emulation software which plots in real time the histogram of the pulse height.

The crystals are characterized with 3 different sources:

- A sodium source ^{22}Na of 2 MBq which emits positrons and in lower proportions γ-rays at 1275 keV. From the positrons annihilation, 2 γ-rays of 511 keV are emitted in coincidence.
- A Cobalt source ^{57}Co of 5 kBq which emits X-rays at 122 keV.
- A Cesium source ^{137}Cs of 800 kBq which emits γ-rays at 662 keV.

A histogram obtained with the ^{22}Na source is first shown in Figure 3.1. According to Figure 2.3 for 511 keV γ-rays, Compton and Photoelectric interactions happen in equivalent proportions. For 1275 keV, the Compton scattering will be dominant.

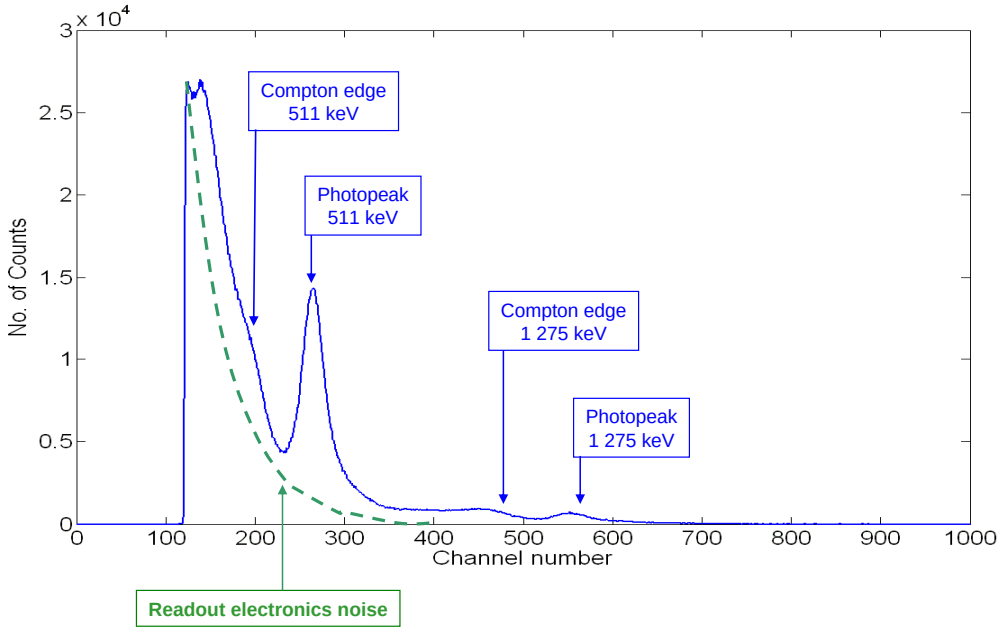

Figure 3.1: ^{22}Na spectrum obtained with crystal C1 on the Crystal Clear test Bench.

This spectrum shows the noise of the readout electronics (in dashed line), which is a Gaussian distribution cut by a low level discriminator. The center of this Gaussian (not shown on this plot) gives the pedestal. The two photopeaks of ^{22}Na are at 511 keV and at 1275 keV. The Compton plateau and Compton edge for the energy 1275 keV are clearly visible between channels 350 and 500. Fitting the photopeak regions allows to derive both the peak position of the 511 keV line, and the energy resolution. In the case presented here, the energy resolution is 16 % for the 511 keV photopeak, and 9 % for the peak at 1275 keV.

The light yield Y at 511 keV is obtained from the photopeak position PP divided by the single electron position SE, which gives the number

of photoelectrons. Corrections are applied for the attenuation A used and pedestal Ped. The single photoelectron pulse height is measured independently without attenuation (A=1). The number of photoelectrons is then divided by the quantum efficiency (QE=20%) to derive the total number of photons sent to the PMT and then by the energy of the incident radiation (E=0.511 MeV). Y is calculated at 16 085 photons/MeV. This calculation doesn't comprise the reflection factor R at the interface LSO/PMT which is estimated negligible ($R \approx 3\%$ considering a PMT entrance window of index $n_{window} = 1.5$).

$$Y = \frac{(PP - Ped).A}{(SE - Ped).1.E} \tag{3.1}$$

The Figure 3.2 shows on a same graphic the 3 spectra obtained with the 3 sources used, taking into account the attenuations used for each spectrum. The y axis is modified in order to see the photopeaks with an equivalent size.

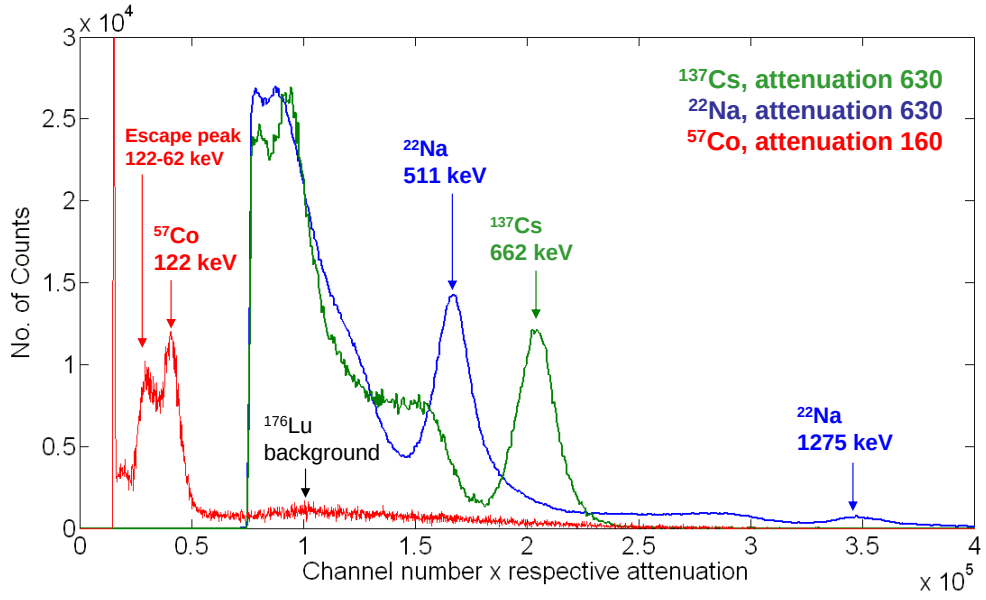

Figure 3.2: ^{57}Co, ^{22}Na and ^{137}Cs spectra obtained with crystal 1123 on the Crystal Clear test Bench.

The ^{137}Cs spectrum shows a photopeak as well as a Compton plateau and edge more pronounced than for the ^{22}Na, in good agreement with Figure 2.3. The ^{57}Co shows 2 peaks plus the 306 keV background of the ^{176}Lu. This background is present in the 3 spectra but only visible in this case as the source is weak. The peak of furthest position is the photopeak. The other is called escape peak and its energy is $122 - 62 = 60keV$.

After the photoelectric absorption of a radiation in LSO, the first hot electron can hit and excite electrons of the lutetium atom. If an electron of the first layer K_α is excited, it can either excite further electrons (ionization), either return to its normal state with the emission of an X-ray of energy 62 keV (K_α binding energy). If the X-ray is not further absorbed by the matter, the total energy detected is $E_0 - 62\ keV$.

As shown in Figure 2.22 the absorption coefficient in LSO is 30 times higher at 122 keV than at 511 keV, meaning that the interaction will take place at much shorter depth of interaction. Under this condition, X-rays have higher chances to escape the crystal. This escape peak is thus statistically better seen for 122 keV, than for 511 keV and 662 keV.

As shown in Figure 3.3 the peak position as a function of the energy can be linearly fitted.

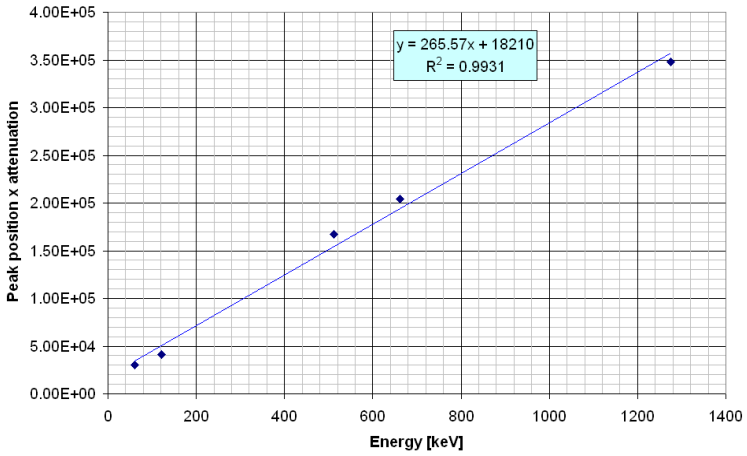

Figure 3.3: Peak position as a function of the energy.

Four different crystals were used and are listed in Table 3.1 with their dimensions and light yield obtained from 511 keV measurements.

Table 3.1: LSO crystals light yield

Crystal number	Dimensions [mm^3]	light yield [photons / MeV]
1123	2×2×10	16 100
1050	2×2×10	14 400
1807	2×2×15	19 500
LYSO	2×2×10	12 000

The light yield of LSO is usually given at 27 000 ph/MeV as it is mea-

sured in horizontal position. However in vertical position, as explained in 2.3.3.2, the depth of interaction is longer so that the photons of wavelength $< 390\ nm$ might be lost. The light yield is therefore lower.

3.1.2 APD Hamamatsu S8550

Accurate values of gain as well as the effective quantum efficiency were measured on the APD. The other characteristics are taken according to the datasheet shown in Appendix C.

Gain

Gain measurements were done for all the channels of the APD S8550. As shown on the Figure 3.4, 405 nm photons are sent continuously from a laser through an attenuator. The attenuated blue light is carried by a 80 μm diameter optical fiber to the APD via a mask. The goal of the mask is to center the light spot on the $1.6 \times 1.6\ mm^2$ APD channel.

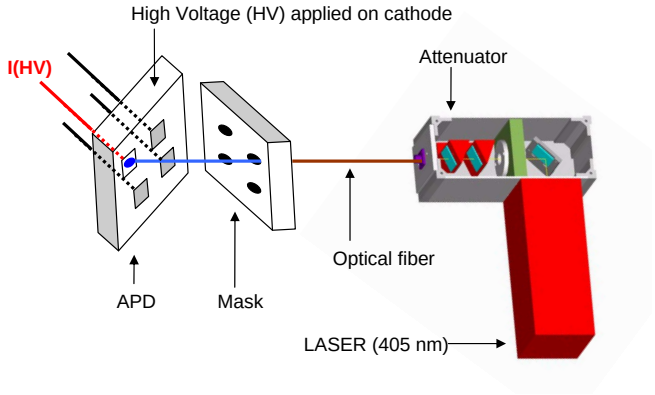

Figure 3.4: schematic of the gain measurement setup

A high-voltage source meter Keithley 2410 is used to bias the APD and measure its corresponding current. A positive voltage is applied on the common cathode and the negative one on the output of the studied channel. The current measured is then positive. The other channels are left floating.

The source meter is piloted by a Labview program which collects all the data. The whole setup is placed in a black box for dark current measurements $I_{dark}(HV)$, shown in the left part of Figure 3.5. The room temperature is stabilized at 20°. When the laser is on, the current I(HV) is measured. At low voltages, below 50 V, the gain is 1 (no impact ioniza-

tion). The APD current under 10 V voltage is then taken as a reference. The gain M is then defined as:

$$M = \frac{I(HV) - I_{dark}(HV)}{I(10\ V) - I_{dark}(10\ V)} \tag{3.2}$$

The gain of the channel E2 (in the center of the APD matrix) is shown on the right part of Figure 3.5. This channel will be used in the rest of the study.

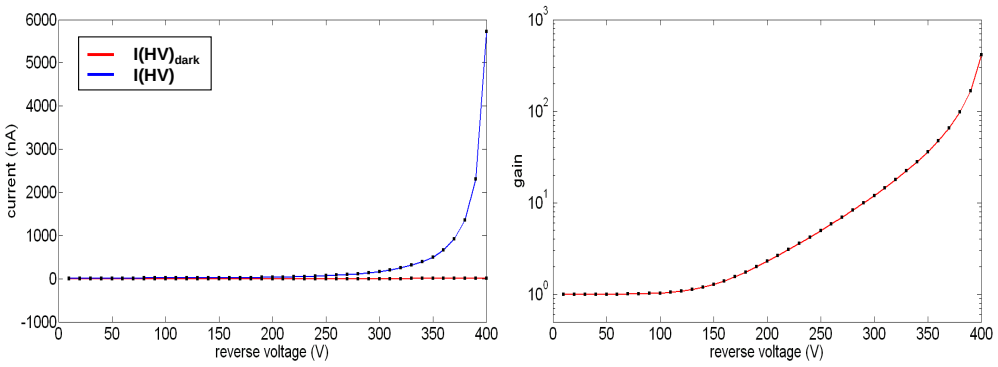

Figure 3.5: Left: I(HV) and $I_{dark}(HV)$ as a function of the reverse voltage applied. Right: gain as a function of the reverse voltage applied.

For respectively HV=380 V and HV=390 V, the gain of the APD is M=100 and M=175. At HV>400 V, the avalanche breakdown occurs and may degrade the APD. For this reason, the breakdown conditions are not reached in the presented measurements.

Quantum efficiency

As shown in Figure 3.6 taken from the datasheet, the quantum efficiency (QE) of the APD is 72 % at 420 nm. Over the full light emission spectra of LSO, the QE varies from 50 % at 370 nm to 82 % at 500 nm.

The Light Emission Spectra (LES) as a function of the wavelength is LES(λ) as shown previously in Figure 2.20. The quantum efficiency as a function of λ is QE(λ). It is assumed that 100% of the photons are emitted between 370 nm and 500 nm. The total number of emitted photons N_{tot} is:

$$N_{tot} = \int_{370}^{500} LES(\lambda) d\lambda \tag{3.3}$$

The ratio of photons emitted between 370 nm and 370.5 nm, $N_{370}^{370.5}$ is given by

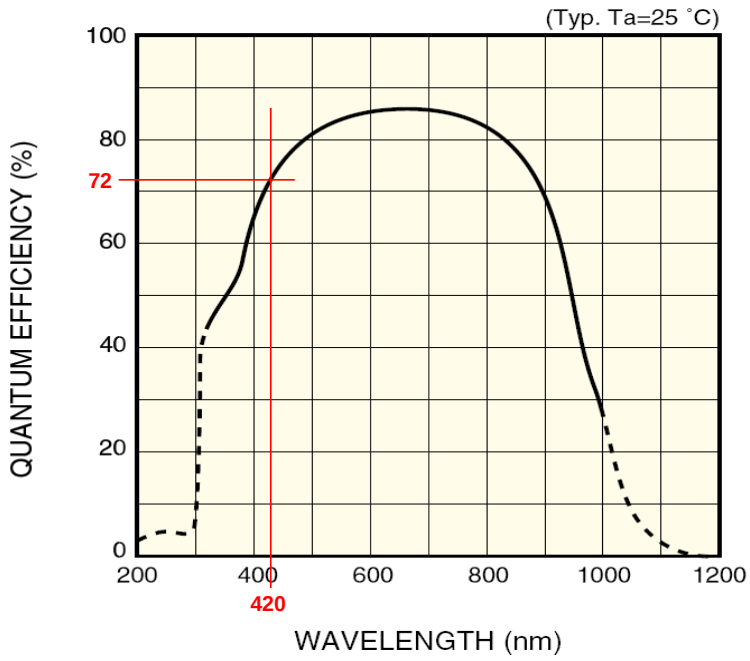

Figure 3.6: Typical Quantum efficiency as a function of the wavelength QE(λ).

$$N_{370}^{370.5} = \frac{\int_{370}^{370.5} LES(\lambda)d\lambda}{N_{tot}} \tag{3.4}$$

In this very small wavelength range, the quantum efficiency is considered constant so that the ratio of detected photons from this range is $Nd_{370}^{370.5}$:

$$Nd_{370}^{370.5} = \frac{\int_{370}^{370.5} LES(\lambda)d\lambda}{N_{tot}} \times QE(370) \tag{3.5}$$

The sum of the numbers calculated over 0.5 ns intervals, over the full LSO emission spectrum represents the effective quantum efficiency QE_{eff}.

$$QE_{eff} = \sum_{n=0}^{259} \left(\frac{\int_{370+(0.5n)}^{370+(0.5n+0.5)} LES(\lambda)d\lambda}{N_{tot}} QE(370+n) \right) = 0.72 \tag{3.6}$$

The effective quantum efficiency is then of 72%, indeed the same as QE(420 nm).

3.1.3 Calibration of the electronics

This section explains the behavior of the electronics system composed of the FEDC05 chip coupled to the NINO chip. The charges are expressed in number of electrons instead of Coulombs, with 6240 electrons$\approx 1\ fC$.

In first approximation, for an incident radiation of 511 keV (PET conditions), with a LSO light yield of 16 photons/keV, a fill factor $f = \frac{1.6^2}{2^2} = 0.64$ (size ratio between APD active area and LSO crystal) and an APD quantum efficiency of 72 %, the number of detected photons (or photoelectrons [p.e.]) N is:

$$N = 511 \times 16 \times 0.72 \times 0.64 = 3790\ p.e. \tag{3.7}$$

For an APD gain of M=175, the number of electrons N_e at the output of the APD is $N_e = 3790 \times 175 \approx 6.62\ 10^5\ electrons$, which corresponds to a charge of 106 fC. As the current signal of the APD follows the 40 ns decay constant of the LSO, the maximum amplitude is about 2.6 μA:

$$I_{max} = \frac{Q}{\tau} = \frac{1.06\ 10^{-13}}{40\ 10^{-9}} \approx 2.6\ 10^{-6}\ A \tag{3.8}$$

This value of current is below the NINO lower threshold limit so that it is impossible to detect radiations which energies are in the PET and CT range.

The NINO chip can therefore not be used directly to readout the APD and a preamplifier has to be used. The FEDC05 was chosen and its calibration is presented, before to study its performance while connected to the NINO chip.

FEDC05 calibration

The calibration of the FEDC05 was done by injecting 2 different test signals. The first signal type is obtained by applying a voltage step into a 100 fF test capacitance integrated in the preamplifier input. The second input signal shape is generated to closely reproduce the waveform of the signal given by the APD coupled to a LSO scintillator. It is generated by applying a voltage step into a CR filter with $C = 1.8\ pF$, $R = 20\ k\Omega$ and $C \times R = 36\ ns$ as shown in Figure 3.7. This configuration is possible as the input resistance of the FEDC05 is very low, so that it can be considered as a fictive mass. This signal is defined as an LSO-like signal.

The output of the preamplifier shown in Figure 3.7 is a scope shot of

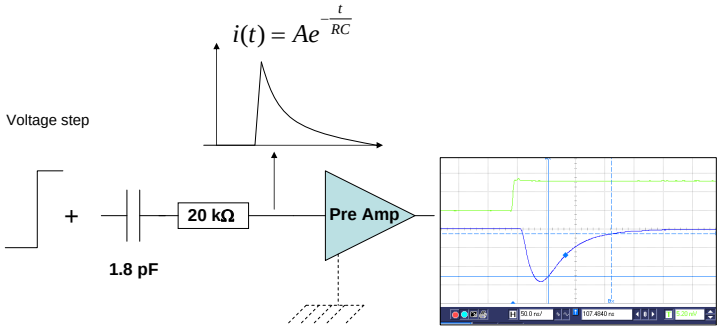

Figure 3.7: Schematic of the LSO-like signal generation.

the FEDC05 signal. The Figure 3.8 shows the measured response curves of the FEDC05 amplifier to both the test and LSO-like signals (points) and compares them with HSPICE simulations (lines). Despite a small deviation of the simulations from the data, HSPICE confirms the measurement for both kinds of input charges.

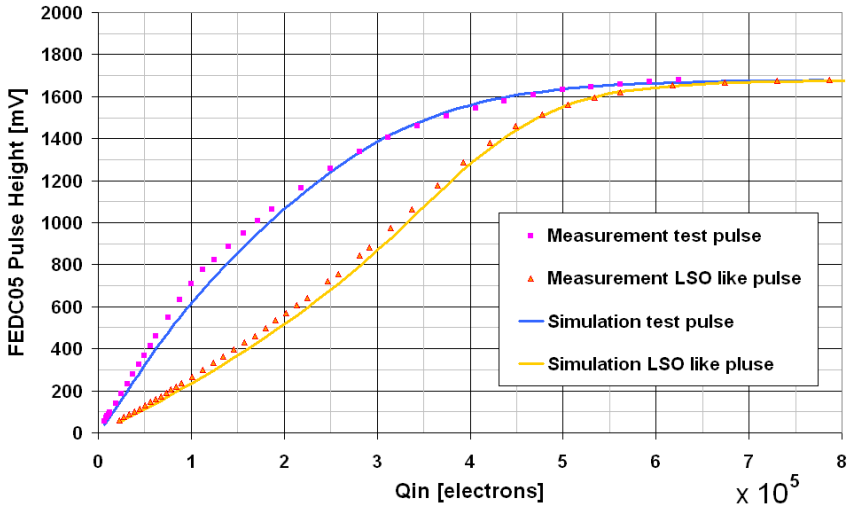

Figure 3.8: Simulation and measurements of the FEDC05 pulse height as a function of the input charge for LSO pulses and test pulses.

The non linearity of the calibration curves accounts for a saturation effect in the FEDC05, limiting the maximum signal height but increasing the pulse width with the input signal. The top plot of Figure 3.10 shows increasing LSO-like input charges injected in the electronics, from 1.1 10^5 (idex=10) to 11 10^5 electrons (idex=100) with steps of 1.1 10^5 electrons. The middle plot shows the corresponding FEDC05 output pulse which height is progressively saturating, going with an increase of the signal width.

One can see from Figure 3.8 that for input charges below 10^5 electrons

the amplifier response to a test pulse is approximately linear in pulse height. For higher charges, i.e. between 10^5 and 5 10^5 electrons, the pulse height progressively saturates, while the pulse width increases with the input charge. For input charges above 5 10^5 electrons the amplifier output is fully saturated with the pulse width increasing almost linearly.

On the other hand, for LSO-like input pulses, the amplifier response in terms of pulse height remains quasi-linear over a longer range, i.e. for charges up to 4 10^5 electrons. Beyond that, similar saturation effects and increases of pulse width occur as for the test pulses as shown on the simulations presented in Figure 3.10.

Figure 3.9 shows measurement of the FEDC05 output pulse area (in nanovolts second) as a function of the input charge for test pulses and LSO-like pulses.

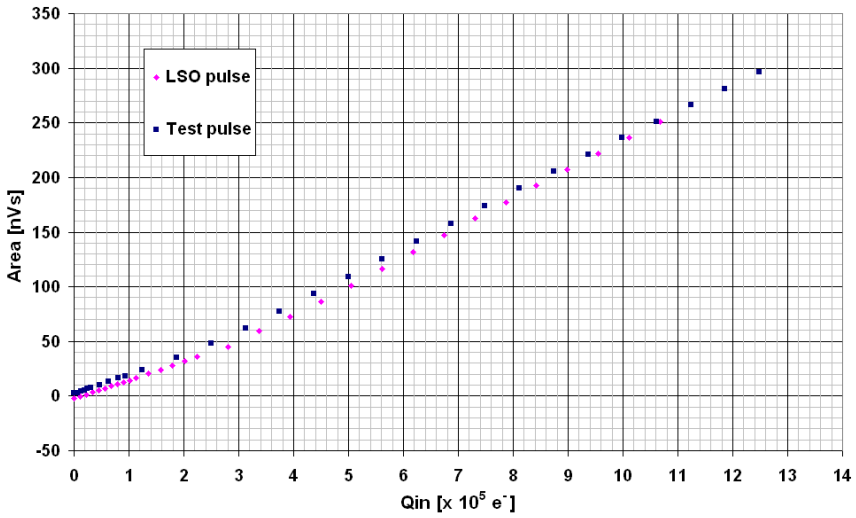

Figure 3.9: Measurements of the FEDC05 pulse area as a function of the input charge for LSO pulses and test pulses.

The area is nearly the same for test input charges or LSO-like input charges. The output signal of the amplifier has an area that is varying with the input charge. Two regions can be distinguished: a first one corresponding to the linear mode of the FEDC05, and a second one corresponding to the saturated mode, each one with different linear slope.

As a conclusion, the saturation of the FEDC05 output pulse height is not a problem as it goes with an increase of the pulse width. This way the total input charge is sensed and can be transferred toward the NINO chip. Moreover, considering the time over threshold technique used by the NINO, this effect permits to have a good charge discrimination for more than 4 10^5 electrons. Without saturation, the NINO output pulse

width would increase toward a limit imposed by the input pulse shape.

FEDC05+NINO calibration

As explained formerly in 2.2, both FEDC05 and NINO accept a current at the input and deliver a voltage at the output. It is thus impossible to directly connect the FEDC05 to the NINO. An interface composed of a resistance in series with a capacitance is interconnected between the two chips. A 4 $k\Omega$ resistance ensures the voltage to current conversion and a 1 nF capacitance ensures the decoupling between the two chips as well as the offset removal. The resistance value chosen is a trade off between the signal height and the noise which should be kept at low level so that it is not sensed by the NINO threshold.

The electronic system is calibrated with LSO-like input signals in order to match realistic conditions as with a LSO scintillator. The electronic system comprises both the FEDC05 and NINO chips mounted on an external PCB and connected via the RC interface described above. Figure 3.10 shows simulations of increasing LSO-like injected charges, the corresponding FEDC05 output pulses and the corresponding NINO output pulses.

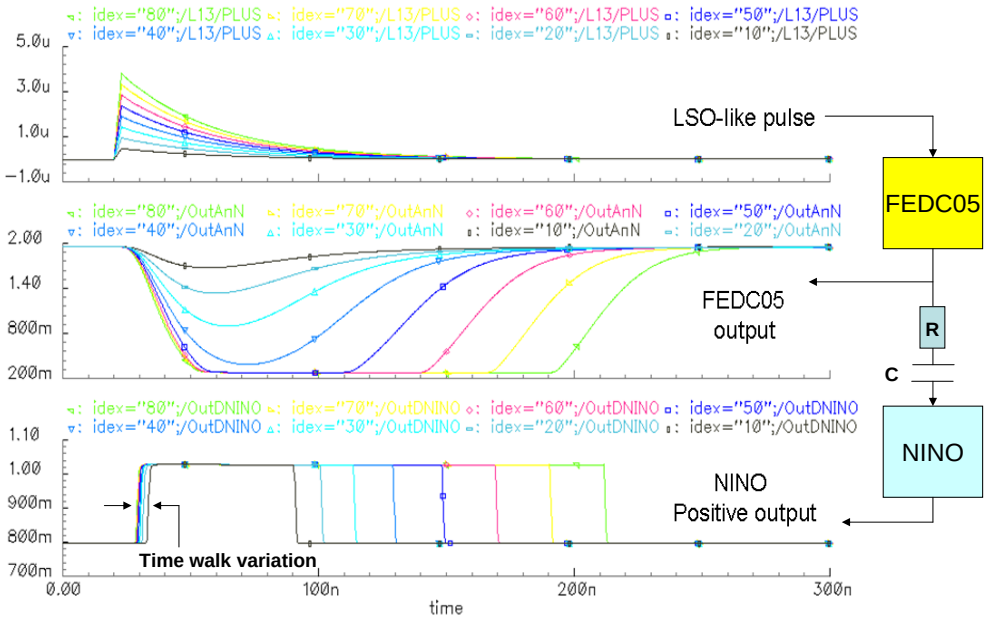

Figure 3.10: Simulation of the FEDC05 and NINO output pulses as a function of increasing LSO pulses.

The response of the combined FEDC05+NINO system to equivalent input charges ranging from 0.5 10^5 to 8 10^5 electrons, is a non-linear

relationship between pulse width (NINO output) and input charge. This is shown in Figure 3.11. The SPICE simulation of the system response shows an overall good concordance with measurements. The non-linearity is a feature of the NINO stage.

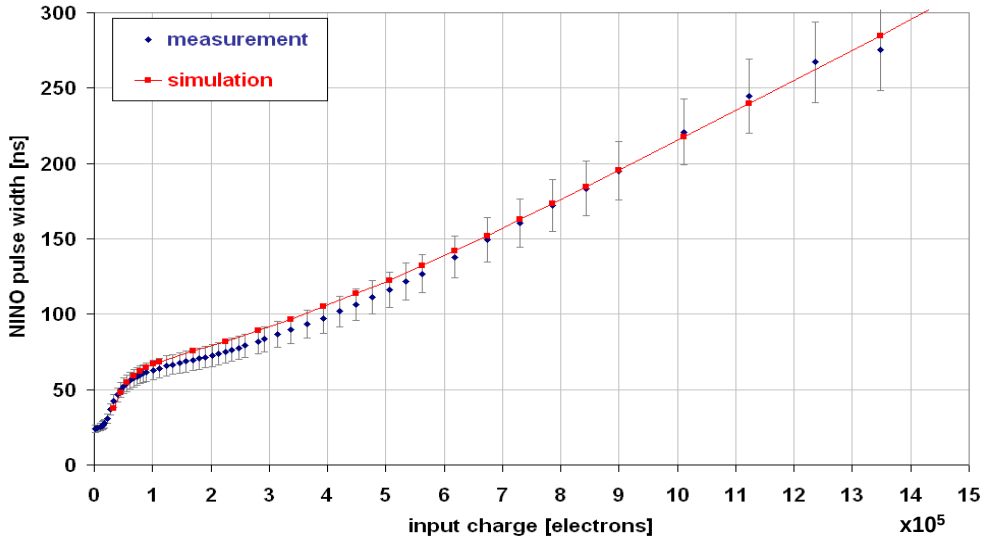

Figure 3.11: Simulation and measurements of the NINO pulse width as a function of the input charge for LSO pulses.

The time over threshold technique, however, implies that pulse discrimination of input signals necessarily leads to variations in time walk. Here time walk is understood as the time lag (or delay) between the initial γ interaction with the crystal and the leading edge of the NINO output signal. Time walk can easily be simulated and tabulated as a function of input charge. The Figure 3.11 thus allows plotting the time walk variation as a function of the pulse width (or as a function of the input charge), as shown in Figure 3.12.

The largest variations of time walk occur for pulse widths smaller than 150 ns with a maximum slope of 250 ps per nanosecond of pulse width variation. On the Figure 3.11, 150 ns represents an input charge of 7 10^5 electrons, which is above the 511 keV events calculated at 6.6 10^5 electrons with an APD gain M=175. It is therefore necessary to correct the time walk variation in order to have the best possible time resolution.

As a conclusion, this calibration permits from a pulse width measured at the output of NINO, to retrieve the corresponding charge injected at the input of the FEDC05. Moreover, it permits from the same pulse width measurement to know the time walk variation and to correct for it in timing analysis.

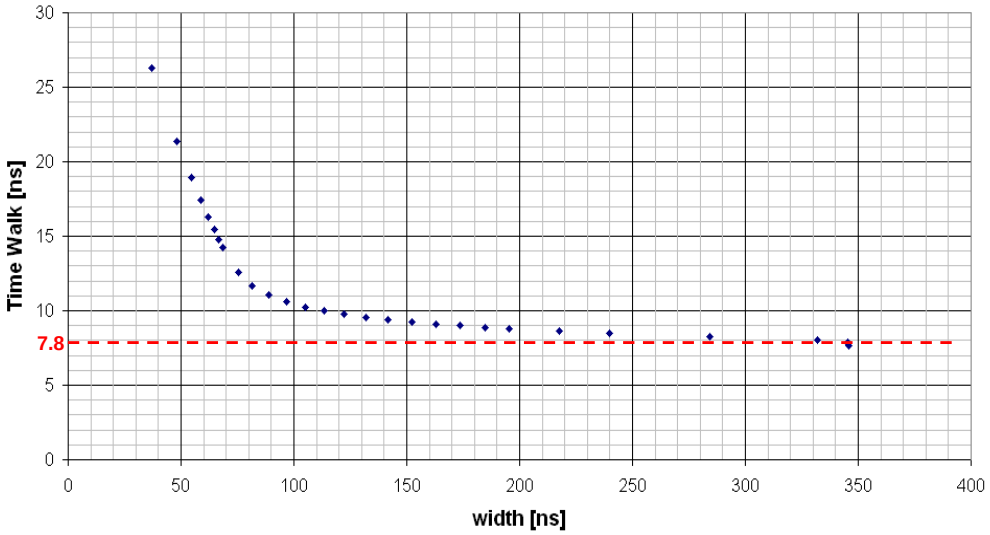

Figure 3.12: Simulation of time walk.

3.2 Characterization of the full system

In this chapter, two detection methods are exposed to X and γ photons and compared in terms of energy and time resolution. The first one, widely used [Moses 79, Moszynski 03, CrystalClear], is called the PMT based method and is presented in chapter 3.1.1. The second one is the time based readout technique, adapted for medical imaging for the first time, and composed of the APD S8550 coupled to the LSO scintillating crystals. The readout electronics comprise the FEDC05 chip coupled to the NINO chip via the RC interface. In the two cases, the same scintillators are used. The LSO crystals are polished on all faces, wrapped with Teflon tape and mounted vertically (γ rays incident on the small crystal face) onto the photodetectors with optical grease, as shown in Figure 3.13.

3.2.1 Energy resolution

This section aims to show how the energy resolution is calculated, before to compare the different possibilities of detector systems and to conclude about the optimum configuration.

3.2.1.1 Energy resolution calculation method

The PMT is connected to a Multi Channel Analyzer (MCA) for all reference measurements and the APD is read out with the FEDC05 alone or with the FEDC05+NINO associated. The performance of the APD based system is compared to that of the PMT based system. The interest

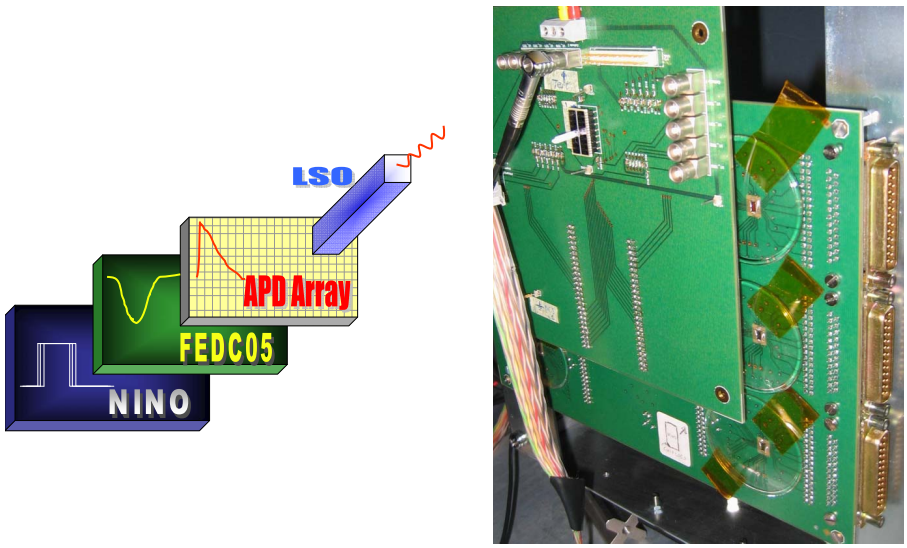

Figure 3.13: Schematic and picture of the full photodetector system.

in measuring directly the FEDC05 in terms of output charge is that its response is a linear function of the input charges. The three radioactive sources of ^{57}Co, ^{22}Na and ^{137}Cs described in 3.1.1, were used allowing to determine linearity and energy resolution over an energy range between 122 keV and 1275 keV.

First, spectra are obtained with FEDC05 alone, measuring its output pulse area. Second, the FEDC05+NINO readout is studied.

FEDC05 alone

Figure 3.14 shows typical energy spectra of ^{22}Na, ^{57}Co and ^{137}Cs radioactive sources taken with the APD detector head and the FEDC05 preamplifier. The FEDC05 output pulse area is measured by a LeCroy scope which directly builds the histogram of the response. The ADP gain is either M=100 (HV=380 V) or M=175 (HV=390 V). The crystal used is the 1123.

Like in chapter 3.1.1, the ^{137}Cs spectrum shows a photopeak as well as a Compton plateau and edge. The ^{22}Na spectra show 2 photopeaks at 511 keV and 1275 keV, each one associated with the Compton continuum and edges. The ^{57}Co spectra shows the photopeak, the escape peak and the background of the ^{176}Lu.

In order to retrieve from the pulse area the corresponding equivalent input charge at the input of the FEDC05, a Look Up Table (LUT) is built from the calibration measurements as shown in Figure 3.15.

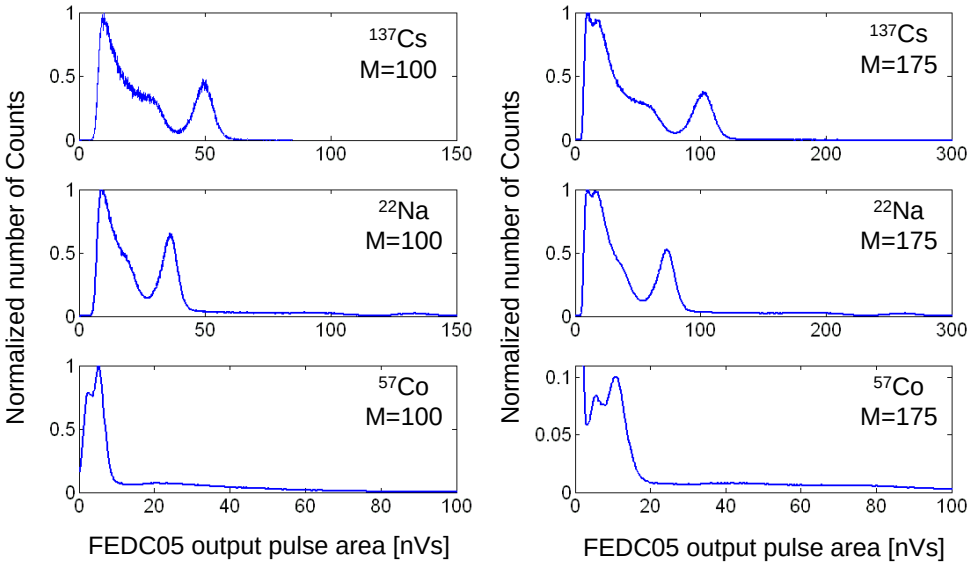

Figure 3.14: Histograms of FEDC05 output pulse area for ^{22}Na, ^{57}Co and ^{137}Cs radioactive sources at gain M=100 and M=175.

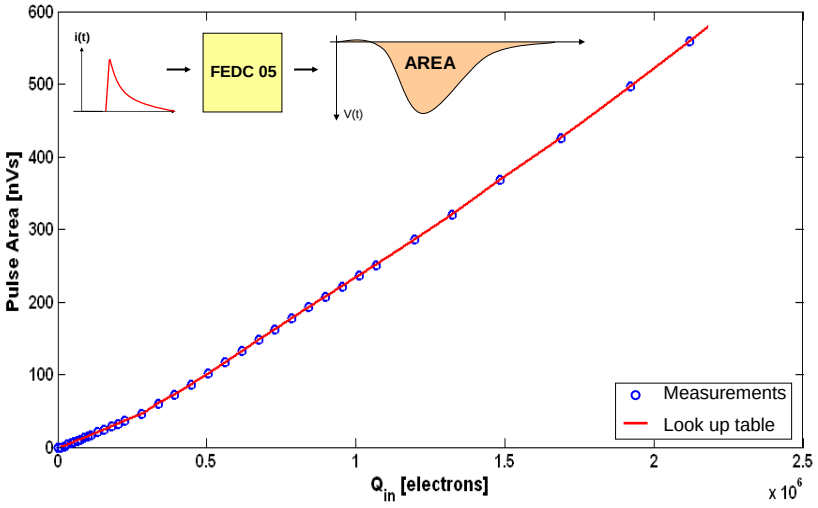

Figure 3.15: Look up table based on the measurements of the FEDC05 output pulse area as a function of the input charge for LSO-like pulses

By extrapolation between the measurements, a table of very thin step (10^{-3} nVs) associates areas from 0 nVs to 550 nVs to respectively charges from 0 to 2.5 10^6 electrons. When an area is measured , a Matlab program finds in the LUT the same value with a precision of 10^{-3} nVs and replaces it by the corresponding input charge. This way, the spectrum is rescaled with an x axis in number of electrons as shown in Figure 3.16.

As an example, the spectrum of ^{22}Na at gain M=175 is analyzed (right part of Figure 3.16 in the middle). This histogram is composed of two

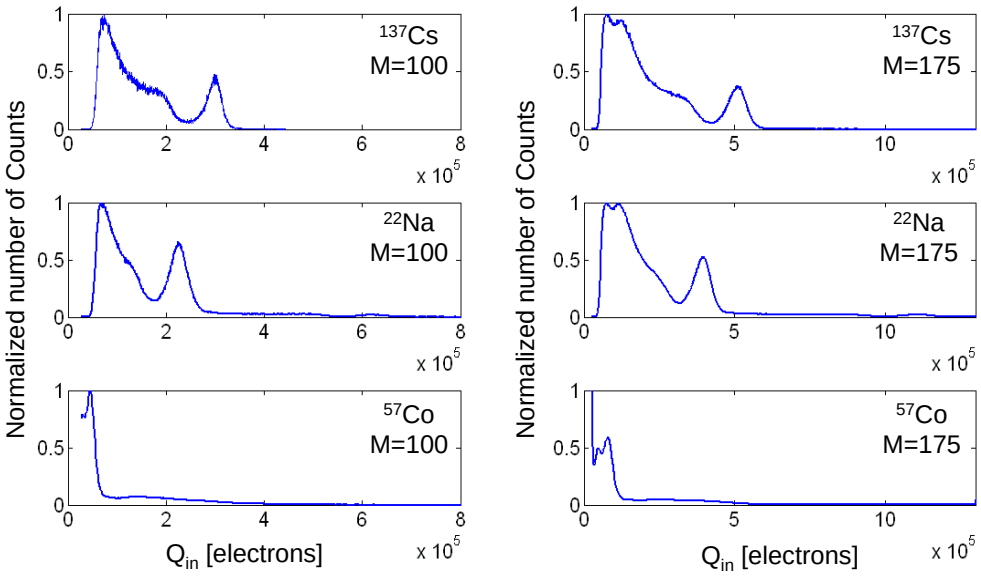

Figure 3.16: Histograms of FEDC05 output pulse rescaled in equivalent input charge (number of electrons) for ^{22}Na, ^{57}Co and ^{137}Cs radioactive sources at gain M=100 and M=175.

photopeaks: one for the 511 keV photons and the other for the 1275 keV photons. Each photopeak is associated to a backscatter peak, a Compton plateau and a Compton edge.

Therefore the photopeak region for 511 keV photons can be interpreted as the sum of 3 equations: a Gaussian equation for the photopeak (parameters a_1, b_1 and c_1), an equation that takes into account the Compton edge (parameters a_2, b_2 and c_2), and a constant which stands for the Compton plateau of the second 1275 keV peak (parameter c_3).

$$y(x) = a_1.exp\left[-\frac{(x-b_1)}{c_1}\right]^2 + a_2.\frac{1}{exp\left[\frac{x-b_2}{c2}\right]+1} + c_3 \qquad (3.9)$$

A first coarse Gaussian fit is applied on the photopeak to extract its center. The center is at $E_0 = 393\ 400\ electrons$. The value of the Compton edge is then calculated through the formula 2.2 in chapter 2.1.1. In this case, $E_0 = 511\ keV$, $E_1 \approx 340\ keV$ and $(E_0 - E_1)/E0 = 2/3$. The Compton edge should then be at $393\ 400 \times 2/3 \approx 262\ 000$ electrons. The fit is then forced at $b_1 = 393\ 400$ and $b_2 = 262\ 000$

The Full Width at Half maximum of the peak is $FWHM = 2.35 \times c_1/\sqrt{2}$. The application of this fit in the photopeak region, between 2.5 10^5 and 6 10^5 electrons, shows very good correlation factor ($R^2 > 90\%$) which permits to extract the parameters of the Gaussian as shown in Figure 3.17.

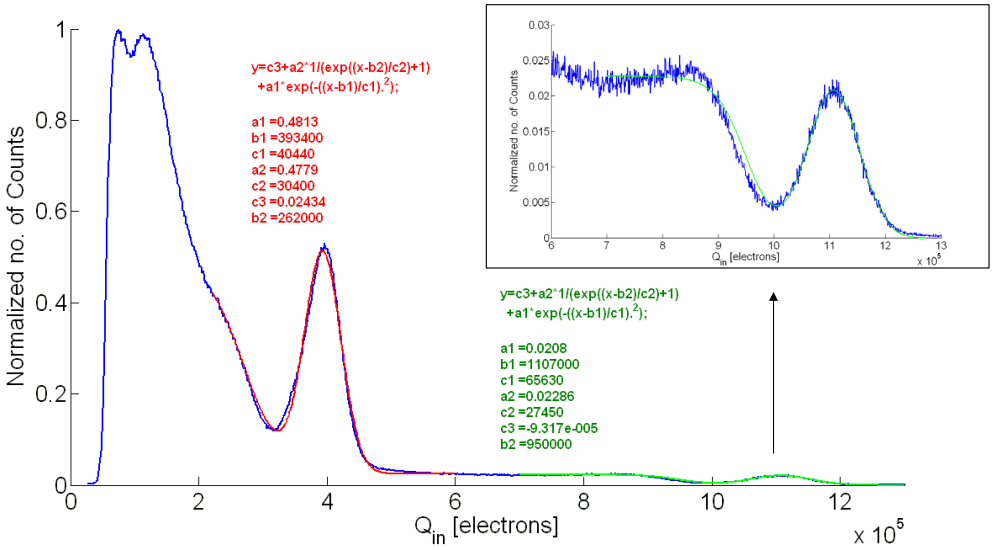

Figure 3.17: ^{22}Na spectrum obtained from APD based method, with crystal 1123 and using the FEDC05 chip alone. The top right plot is a zoom of the 1275 keV region.

The energy resolution was found to be 17 % for the 511 keV photopeak, and 10 % for the peak at 1275 keV.

The same method was applied to all the histograms of Figure 3.16 and the Energy resolution calculations are shown and discussed in section 3.2.1.2.

FEDC05+NINO readout

The detection system is now changed: the output of the FEDC05 is sent to the NINO chip via the RC interface. The NINO output pulse width is measured by a LeCroy scope which directly builds the histogram of this pulse duration. The APD gain is either M=100 (HV=380 V) or M=175 (HV=390 V). Figure 3.18 shows typical energy spectra of ^{22}Na, ^{57}Co and ^{137}Cs radioactive sources taken with the APD detector head and the FEDC05+NINO electronics.

The non linearity of the time over threshold technique used by the NINO chip makes the direct recognition of the Compton events more delicate. The spectra have to be rescaled before to identify their shape. Here again, a look up table is built from the measurement calibration as shown in Figure 3.19. When a pulse width is measured, a Matlab program finds in the LUT the same value with a precision of 10^{-3} ns and replaces it by the corresponding input charge. From previous measurements, the equivalent charges corresponding to CT and PET conditions are shown

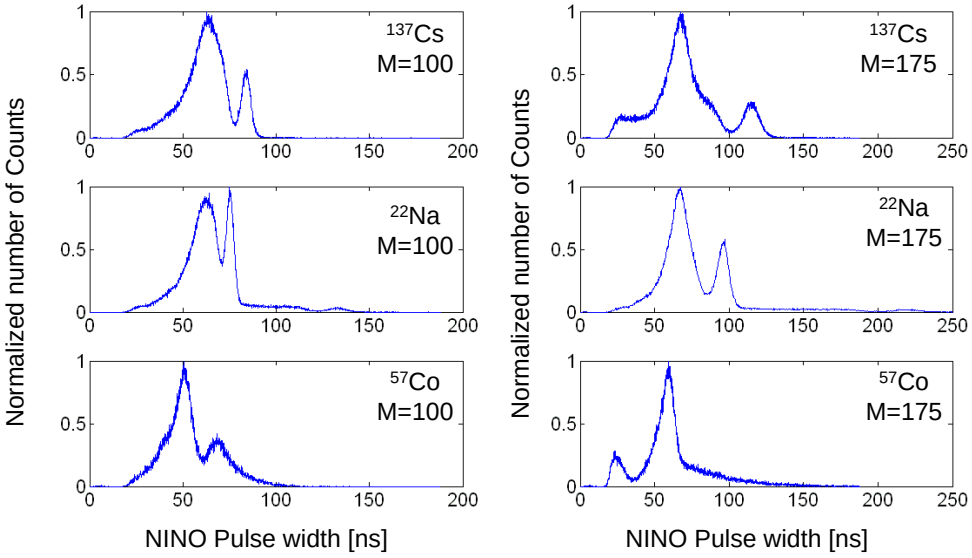

Figure 3.18: Histograms of NINO output pulse width for ^{22}Na, ^{57}Co and ^{137}Cs radioactive sources at gain M=100 and M=175, with crystal 1123.

in case of a gain M=175.

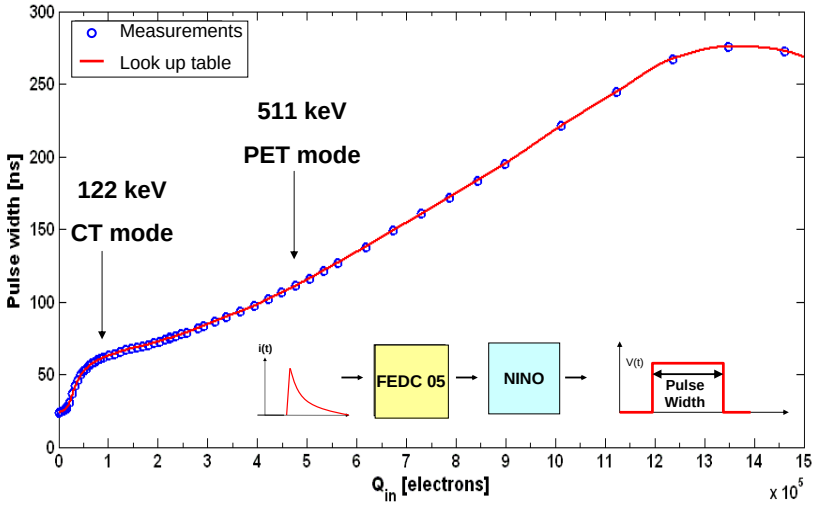

Figure 3.19: Look up table based on the measurements of the NINO pulse width as a function of the input charge for LSO-like pulses.

The spectra are rescaled with an x axis in number of electrons as shown in Figure 3.20.

For 662 keV and 511 keV the photopeaks are still visible, but the Compton continuum and Compton edges are melted in a high peak at 10^5 and 1.5 10^5 electrons for respectively M=100 and M=175. A coarse Gaussian fit applied on the photopeaks allows to extract their center Q_0 in terms of input charge. The positions of the big peaks correspond to

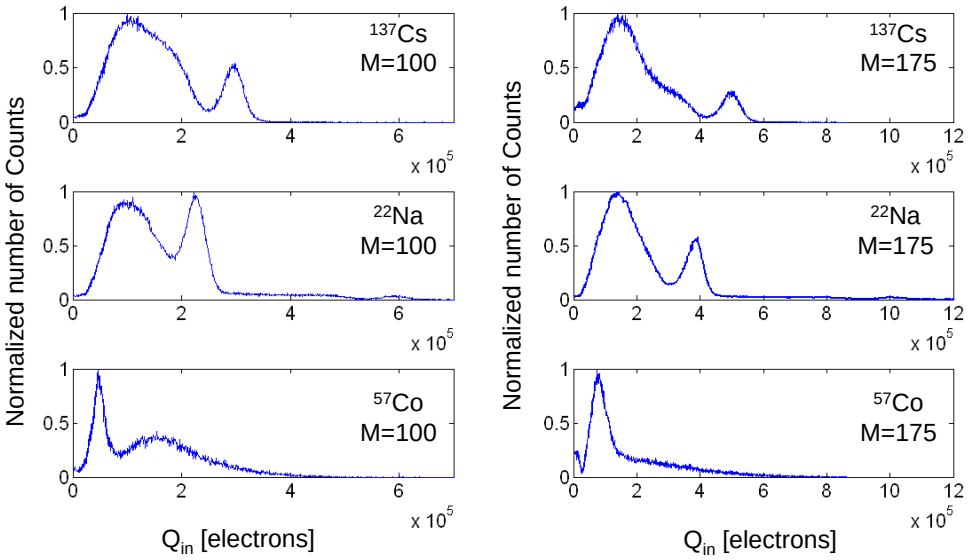

Figure 3.20: Histograms of NINO output pulse rescaled in equivalent input charge (number of electrons) for ^{22}Na, ^{57}Co and ^{137}Cs radioactive sources at gain M=100 and M=175, using crystal 1123.

the backscatter events calculated from Q_0 with the equation 2.2. The 1275 keV photopeak and Compton plateau are clearly visible at charges higher than 4.5 10^5 electrons. The ^{57}Co spectra shows only one photopeak plus the background of the ^{176}Lu. The escape peak is not distinguished.

With this method using the FEDC05+NINO readout, the same measurements are done with the other crystals described in chapter 3.1.1. The rough spectra and rescaled spectra are shown in Appendix C. As an example, the spectrum of ^{22}Na at gain M=175 is analyzed (right part of Figure 3.20 in the middle). The same fit is applied and the result is shown in Figure 3.21.

The energy resolution is calculated at 16% for 511 keV and 10% for 1275 keV.

3.2.1.2 Results and interpretation

The energy resolution is now used as the parameter to compare the different possible setup configurations. The best detector system is the one which shows the best (lowest) energy resolution.

The detector system studied can be composed of 2 different readout electronics, the APD can be driven at various gains and 4 different scintillating crystals can be used. Each time, the 3 radioactive sources are used in order to do comparisons on a wider energy range (from 122 keV

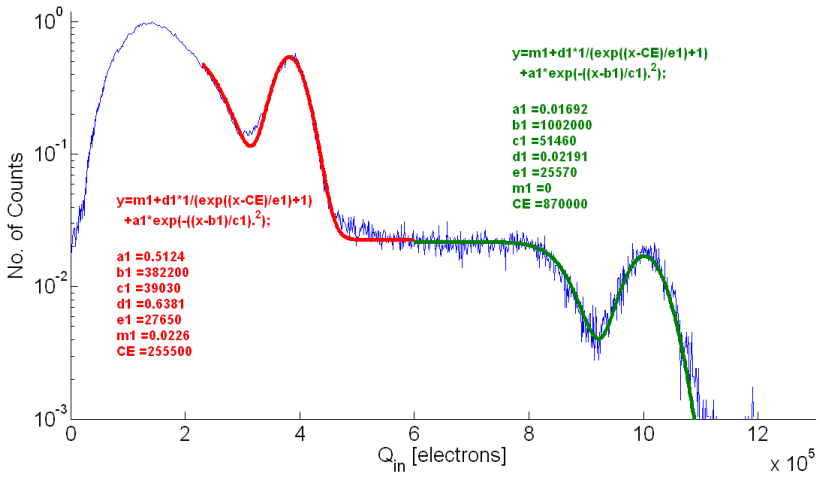

Figure 3.21: Fit of the 511 keV region (left) and 1275 keV region (right).

to 1275 keV). This makes a too high number of spectra to analyze and to compare. The study presented in this chapter permits to select through 3 steps the optimal detector combination, which performances are always compared with that of the PMT+MCA method presented in 3.1.1.

Two readout electronics were used, employing the FEDC05 chip alone or together with the NINO chip. The first comparison of these 2 methods with same crystals and at 2 different gains permits to understand the influence of the time over threshold technique on the energy resolution.

A second study, consists of measuring the energy resolutions of the detector, using the 4 different scintillators, and of concluding about the one that best suits the application.

At last, a comparison of the energy resolution will be performed at different APD gains in order to select the optimal one.

Influence of the NINO readout technique on the energy resolution

The rescaled spectra obtained from FEDC05 alone or FEDC05+NINO readout in chapter 3.2.1.1 are superimposed in Figure 3.22.

If the peak position of the 511 keV line are nearly the same after rescaling, a difference of position is seen on the 1275 keV photopeak. The same measurements were performed at gain M=100. The results of photopeak position as a function of the energy is shown in Figure 3.23.

Except for the 1275 keV line at gain M=175, the results are comparable. The rescaling of spectra through two different look up tables show the same results, meaning that the use of the NINO chip doesn't affect the

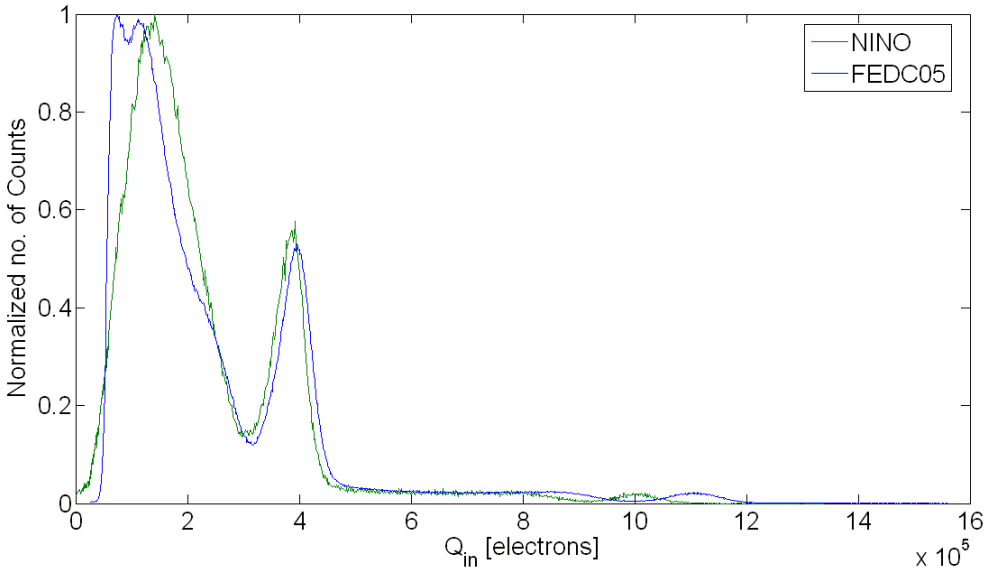

Figure 3.22: Rescaled spectra of ^{22}Na source obtained from FEDC05 output pulse area and from NINO output pulse width.

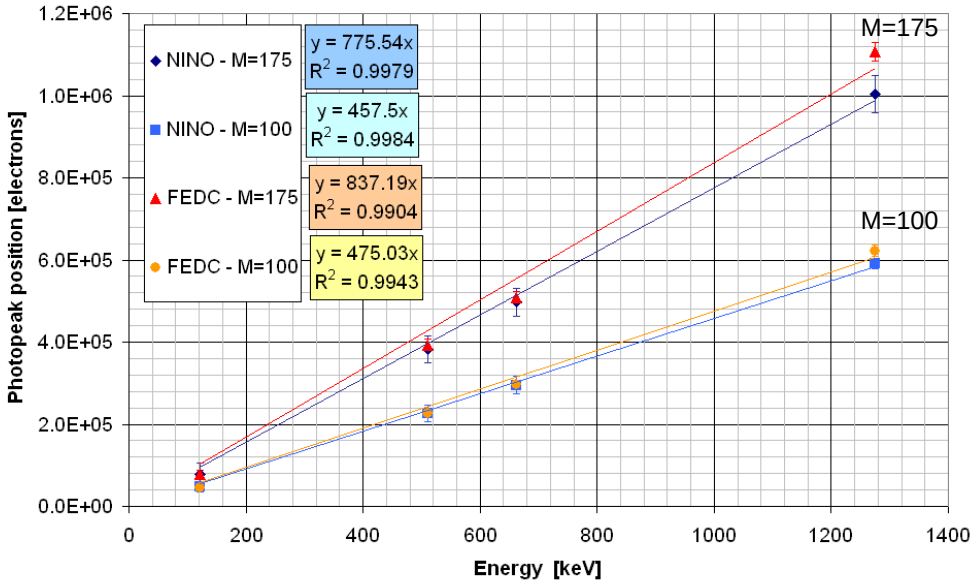

Figure 3.23: Photopeak position after rescaling as a function of the energy for FEDC05 alone and FEDC05+NINO readout electronics, at gain M=100 and M=175 .

photopeak position in the 2 cases of gain M=100 or M=175: the charge information is conserved.

From the fits the photodetection efficiency PDE of the APD can be calculated. The slopes are of $\approx$ 800 electrons/keV at gain M=175, which means that the number of primary photoelectrons N_{pe} in the APD is $N_{pe} \approx 800/175 = 4.5$ photoelectrons/keV or 4500 photoelectrons/MeV.

The same way, at gain M=100, the slope is of $\approx$ 460 electrons/keV, leading to Npe=4600 photoelectrons/MeV. Similar results were found in [Kapusta 03]. As the scintillator light yield was measured at 16100 photons/MeV on the PMT test bench, the PDE is:

$$PDE = \frac{4500}{16100} = 0.28 \tag{3.10}$$

This PDE is understood as the product of the quantum efficiency QE with the fill factor f and with the efficiency coefficient e.

$$PDE = QE.f.e = 0.72 \times 0.64 \times e = 0.46e = 0.28 \tag{3.11}$$

This factor e=61% means that 39% of the photons are lost through another process. A possible explication for this is the optical coupling, as the APD is enclosed in a package and protected with a transparent window, identified as Epoxy. This Epoxy has a high refractive index (1.57 at 430 nm) [Montecchi 01]. Its surface is not flat and can induce a loss of photons at the interface LSO/Epoxy [Kapusta 03] and then a degradation of the reflection coefficient which was neglected in equation 3.11.

Figure 3.24 shows the energy resolution obtained with the 2 readout techniques, with the crystal 1123 at gain M=100 and M=175. The results are compared with the one of the PMT based method calculated from chapter 3.1.1 and using the same crystal.

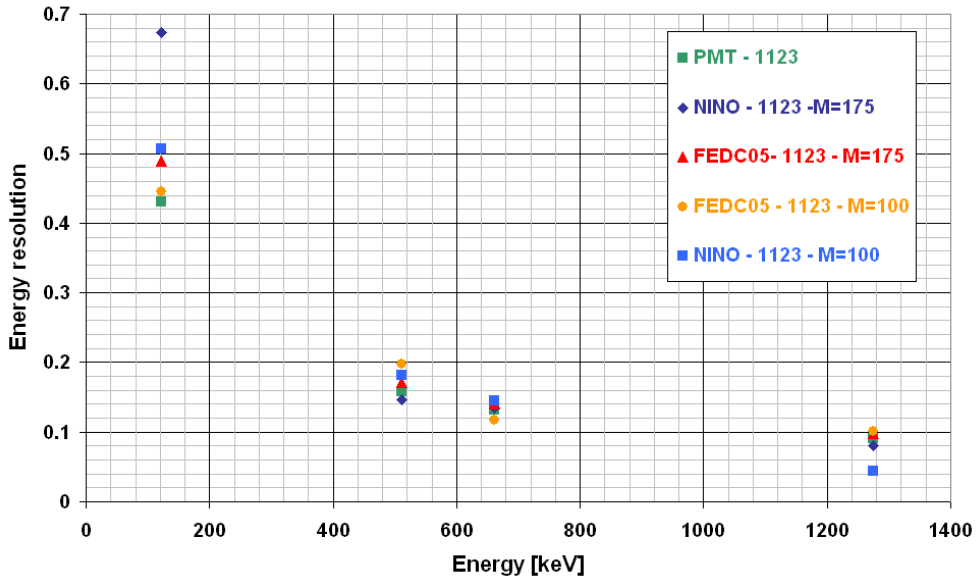

Figure 3.24: Energy resolution as a function of the energy for both PMT and APD based systems.

The energy resolutions obtained with both methods are very close from each other. It confirms that the Time Over Threshold (TOT) technique of NINO doesn't degrade the energy resolution at 511 keV, 662 keV and 1275 keV.

The NINO readout is less sensitive to 122 keV radiations compared to the PMT based method. The energy resolution obtained from NINO suffers from the impossibility to separate the 122 keV peak from the escape peak at 60 keV. This comes from the calibration strong non linearity in the region $< 2\ 10^5$ electrons.

Influence of the scintillator

The Peak position and energy resolution are calculated from the spectra shown in Appendix C, using the 3 same sources, the FEDC05+NINO readout, and the APD at gains M=100 and M=175. The Figures C.1, C.2, C.3, C.4, C.5 and C.6 show the pulse width spectra, and the spectra rescaled in equivalent input charge for respectively the crystals 1050, 1807 and LYSO.

The photopeak positions are plotted as a function of the energy in the Figure 3.25, for an APD gain M=175. The same plots at gain M=100 are shown in Appendix C, in Figure C.7.

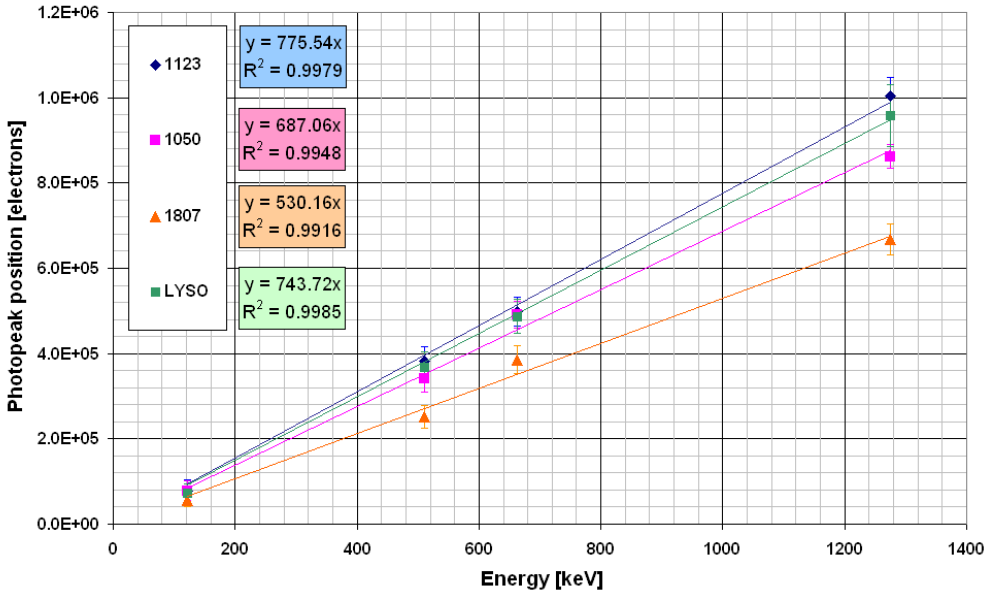

Figure 3.25: Photopeak positions as a function of the energy for the 4 crystals studied, at gain M=175.

The number of primary photoelectrons is proportional to the slope. It

is calculated through the linear fits such as in previous section.

At gain M=175, the crystals 1807 and 1050 give the lowest number of electrons, respectively 3000 and 3900 photoelectrons/keV at the input of the APD. The crystal 1123 and LYSO give the largest number of electrons, respectively 4500 and 4250 photoelectrons/keV. As the same readout technique is used for the 4 crystals, this number is either due to poorer light yield, either to mounting problem as this mounting is done by hand. As shown in 3.1.1, on Table 3.1 the highest light yield is obtained for the crystal 1807, which is in total contradiction with the results obtained here.

At gain M=100, the results shown in Figure C.7 show more reasonable results compared to the light yield previously measured. The crystal 1123 gives the highest number of electrons, followed by the crystals 1050, LYSO and then 1807. There might be a problem with this 1807 crystal which seems to have a significantly worse light yield compared to measurements made from the PMT based setup.

The energy resolution is calculated from rescaled spectra shown in 3.20, C.2, C.4 and C.6. The results are then plotted as a function of the energy in Figure 3.26, at gain M=175.

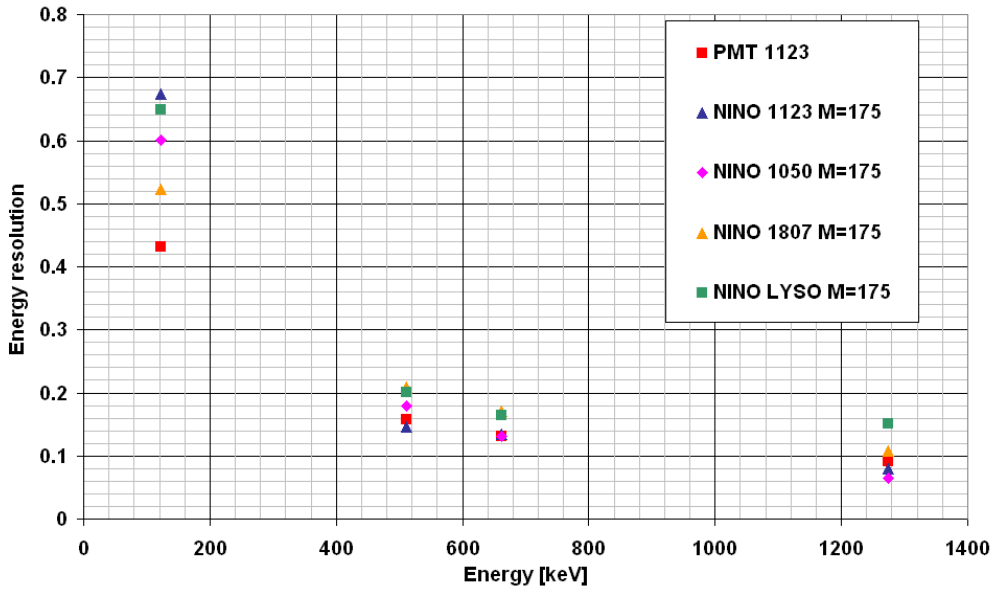

Figure 3.26: Energy resolution as a function of the energy for the 4 crystals studied, at gain M=175.

At 122 keV, the best energy resolution is obtained with the PMT readout. Nevertheless, at 511 keV, 662 keV and 1275 keV, the results with different readout are similar. These results are confirmed at gain

M=100, as shown on the Figure C.8.

The crystal 1123 was chosen as it comes from a series of 5 crystals with similar light yield. These will then be prefered for timing measurements in the coincidence setup.

Influence of the APD gain

The APD based setup is now read out with the FEDC05+NINO and the LSO scintillator 1123. In order to understand the impact of the gain on the energy resolution, this one is set at M=57, 68, 82, 100, 132, 175, 201 and 227.

Figure 3.27 shows the histograms of the NINO output pulse width with the APD biased at these gains.

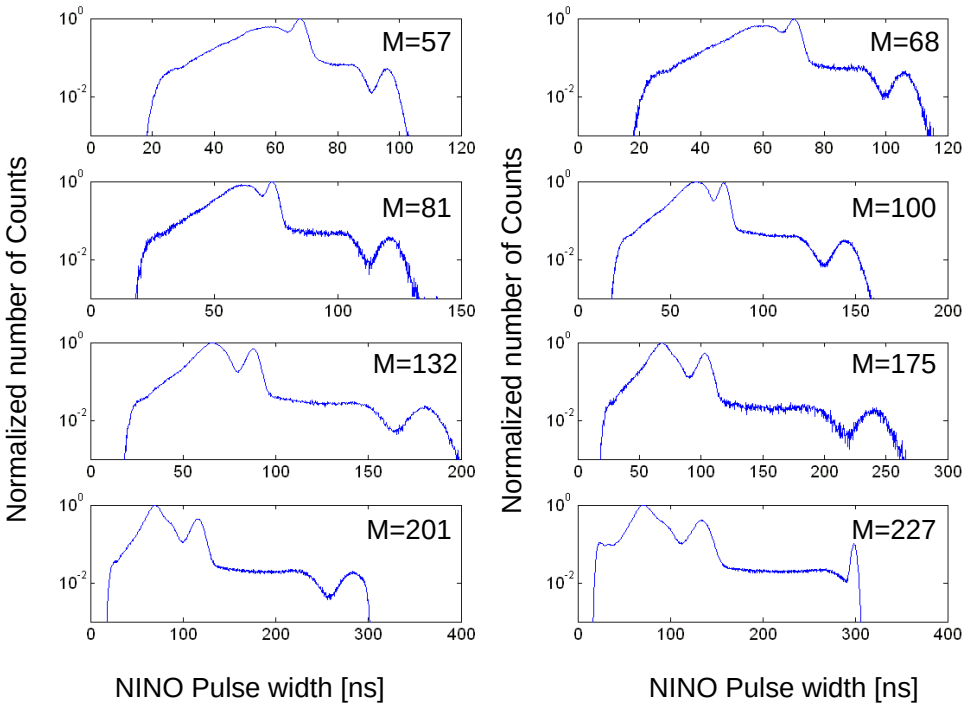

Figure 3.27: Histograms of NINO output pulse width for ^{22}Na radioactive source at gains from M=57 to M=227, with the crystal 1123.

As the gain increases, the photopeak position of the 511 keV line is shifted from 68 ns to 130 ns. The 1275 keV photopeak moves from 100 ns to 250 ns for gain M=57 to M=175. For higher gains the peak is in the saturation region of NINO.

The spectra are rescaled and shown in Figure 3.28.

The same series of measurements are done with the ^{57}Co source. The corresponding plots are shown in Appendix C, in Figures C.9 and C.10.

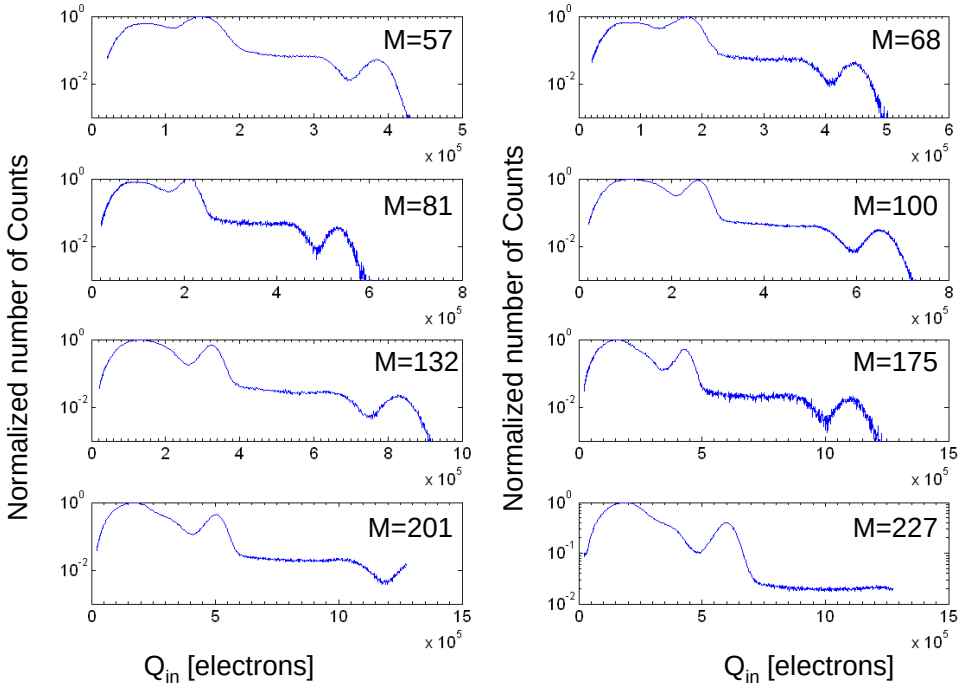

Figure 3.28: Histograms of NINO output pulse width normalized in equivalent input charge for ^{22}Na radioactive source at gains from M=57 to M=227, with the crystal 1123.

At 122 keV, the plots show that for gain M<175, the noise cannot be seen, which makes impossible to determine if the escape peak is present or not. For this reason the energy resolution is not calculated in this range.

As shown in Figure 3.29, the peak positions is a linear function of the APD gain.

The energy resolution is then plotted as a function of the APD gain for 122 keV, 511 keV and 1275 keV in Figure 3.30.

For γ-rays of 511 keV, for M<100, the energy resolution is degraded as the photopeaks are placed in the most non linear region of the NINO calibration, i.e. $<2\ 10^5$ electrons. The energy resolution is calculated at values between 16 % and 20 % for higher gains, with the best one at M=175.

For γ-rays of 1275 keV, the energy resolution is constant at $\approx 10\%$ as the peaks are always placed at positions $> 2\ 10^5$ electrons.

For X-rays of 122 keV, the peaks are always placed in the non linear region which makes the energy resolution either impossible to calculate because of insufficient gain, either degraded because of the impossibility to separate the escape peak from the photopeak.

The gain M=175 is the best compromise as it allows to have a good

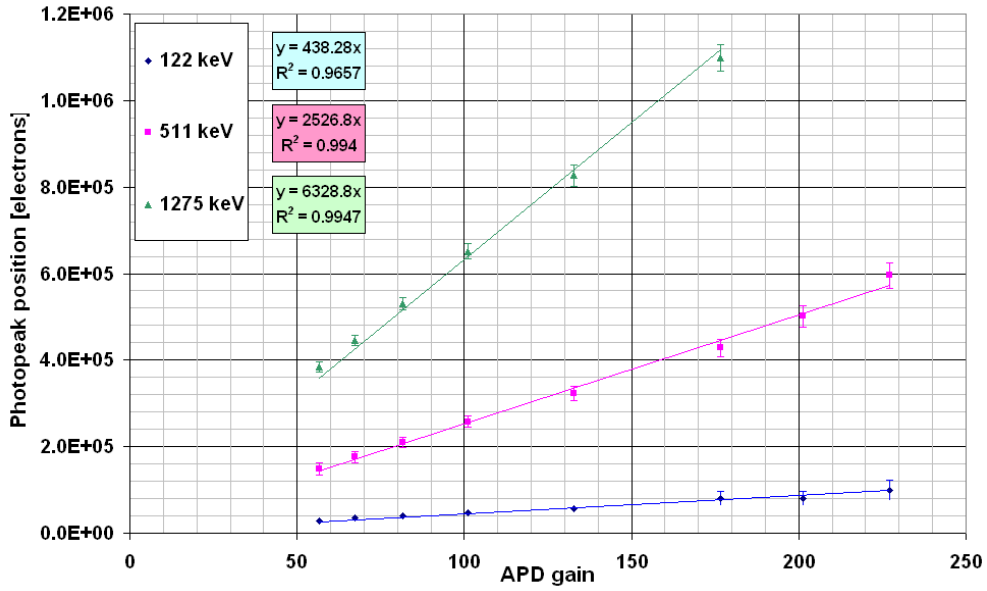

Figure 3.29: Photopeak position as a function of the gain.

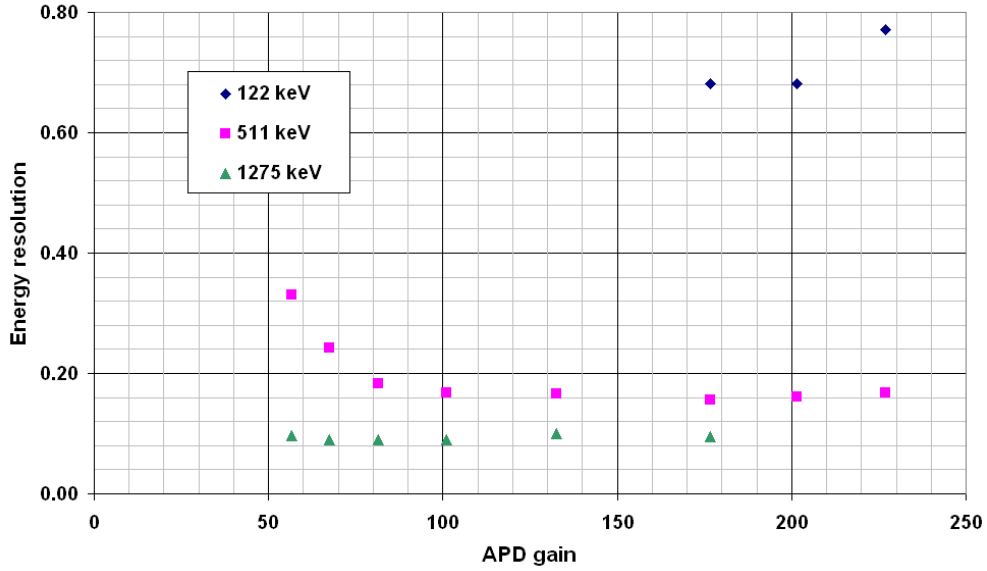

Figure 3.30: Energy resolution vs. APD gain.

energy resolution on the 511 keV and 1275 keV line. Moreover, it is the minimum gain at which the energy resolution can be calculated for 122 keV X-rays.

3.2.2 Time resolution [Powolny 08]

3.2.2.1 Time resolution measurements

The viability of the time-based readout system was shown to provide an energy resolution comparable to PMT-based system. The technique must now also be evaluated in terms of timing performance. Timing is especially important in PET scanners for which image contrast depends of the background rejection determined by timing precision. This requires high precision coincidence measurements between the two opposite detector heads. In the case of time precision better than 500 ps, the selection of events can be done via TOF measurement. In the following the timing performance of the chosen APD-based system will be evaluated. Figure of merit for this type of performance is defined as coincidence time resolution, also called time jitter.

The most commonly used standard for photon detection with highest timing precision is the PMT with its nanosecond rise time. The photodetector Hamamatsu S6533 PMT has thus been chosen as a reference. It has a rise time of 0.7 ns and a transit time spread of 0.16 ns FWHM. This PMT has a diameter of 25 mm and contains ten dynode stages and a bialkali photocathode, as shown in Appendix B.

Two PMTs are mounted back-to-back, and a ^{22}Na source is installed in between. Figure 3.31 shows a schematic of the setup. Each PMT has one LSO crystal of $2 \times 2 \times 10\ mm^3$ mounted in the center of its entrance window coupled with silicon grease. A Constant Fraction Discriminator (CFD) is connected to each PMT output.

The role of the CFD is to output a square pulse of 50 ns when a signal comes at the input. A low level threshold is set externally to define the CFD signal sensitivity. The coincidence measurements with this setup are free of time walk. The CFD outputs, are read out and processed by a fast digital oscilloscope, a technique commonly used for this type of measurements [Moses 99].

In the following the coincidence time resolution is defined as the variation of the delay between the two front edges of the CFD outputs. One of the CFD outputs is also chosen to form a gate. A fixed delay of 2 ns is added to the other CFD output. Events are gated in such a way that the arrival of collinear photons must fall into a 50 ns window. Other events are rejected.

A histogram of the two PMT-CFDs' arrival time difference is shown in Figure 3.32.

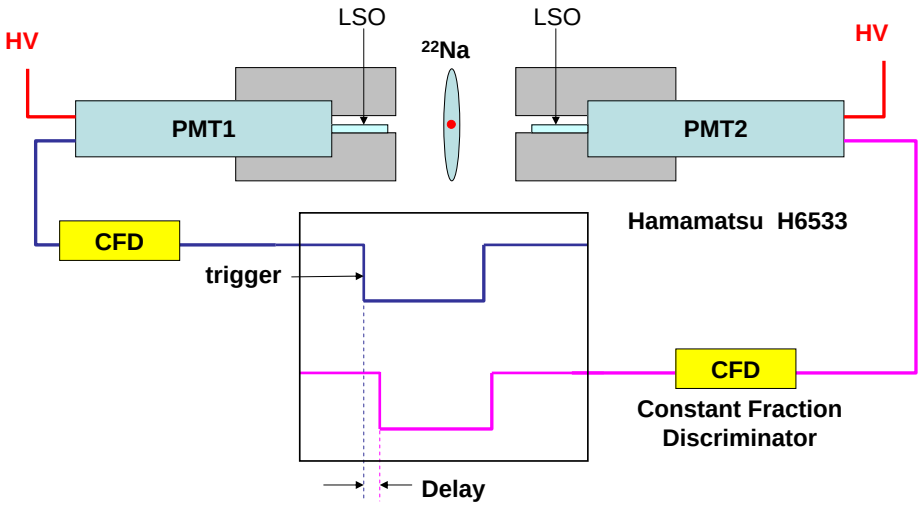

Figure 3.31: Schematic of the PMT based coincidence setup.

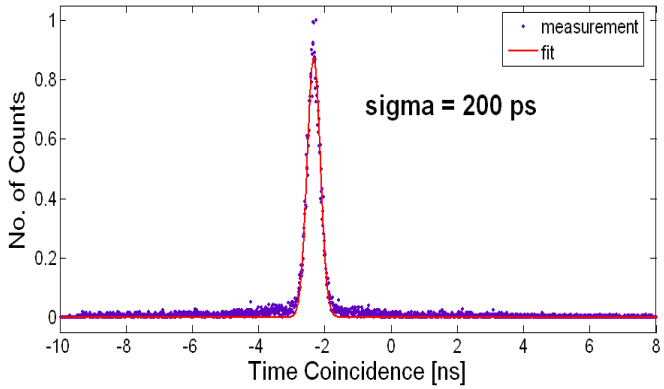

Figure 3.32: Time coincidence histogram of the two reference PMTs in coincidence.

The distribution is fitted with a Gaussian having a FWHM close to 500 ps FWHM (200 ps rms).

In the new setup shown in Figure 3.33 one of the PMT-CFD detector heads was replaced with the APD-FEDC05-NINO detector system. In this arrangement, the time difference from the coincidence measurements is made between the CFD front edge and the NINO leading edge, the latter not being free of time walk. Therefore, for each event, the pulse width information of NINO needs to be corrected for time walk.

Figure 3.34 (2) shows what happens if one plots the delay versus the corresponding pulse width of the NINO chain output. This leads to a typical scatter plot in which timing and energy information are correlated. This type of plot permits to illustrate the results and is used throughout

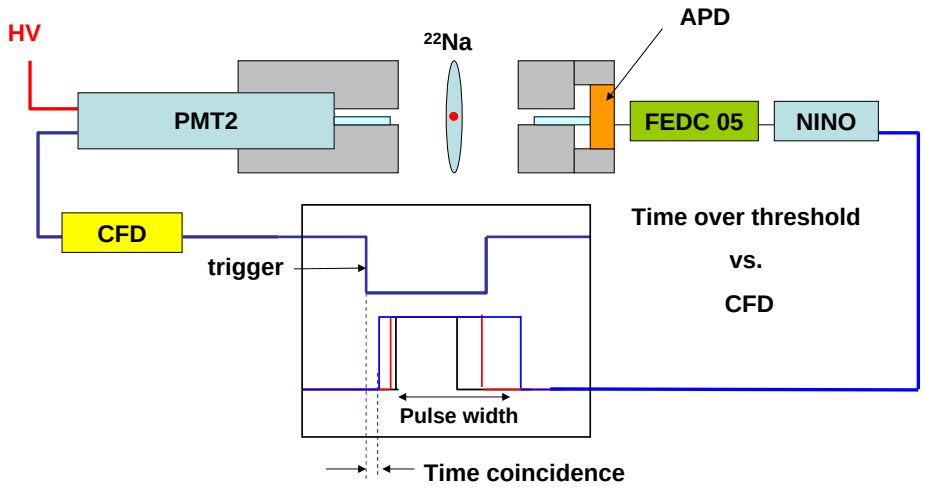

Figure 3.33: Schematic of the time coincidence measurement setup composed of 2 PMT based detector systems.

this thesis. If the delay versus pulse width data are projected on the horizontal axis of the scatter graph one extracts the energy spectrum of the detected correlated events (Figure 3.34 (3)). The 1275 keV line produced by non-correlated photons is not present in the spectrum. On the other hand, projecting the data on the vertical axis reproduces the associated delay histogram from coincident γ rays (Figure 3.34 (1)).

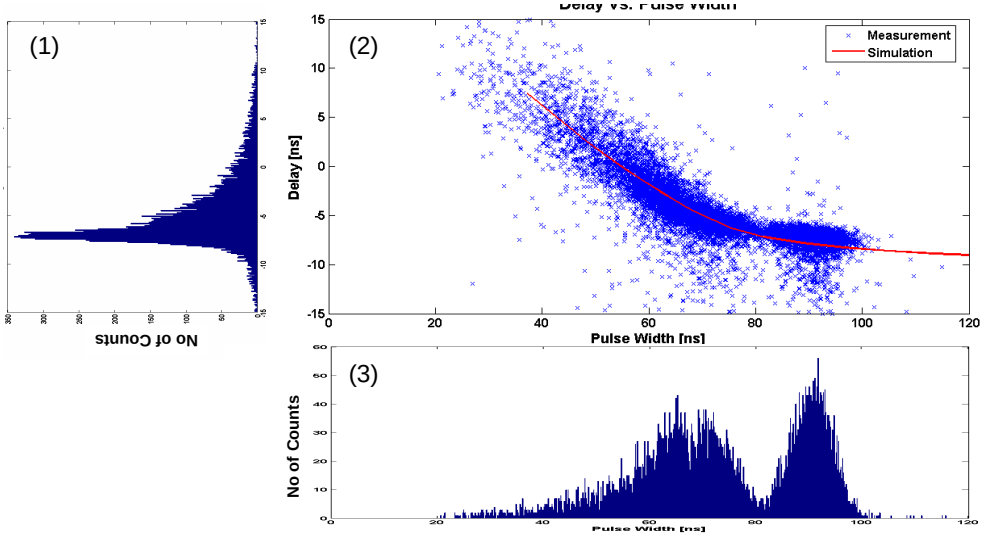

Figure 3.34: Correlation of pulse width and delay for coincident photons from ^{22}Na in a PMT vs. APD setup (2). The projections yield the corresponding energy spectrum (3) and delay spectrum (1).

The time-energy scatter graph also contains the time walk information, increasing toward lower energies, here expressed in terms of pulse width. The previously simulated time walk relation as a function of input charge

or energy (see Figure 3.12) is superimposed on the data and shown as a continuous line. The vertical offset is due to cable delays. A good fit is clearly seen between the measurements and the simulations so that time walk correction can be applied to the measured data.

What is also seen from the delay histogram (vertical projection) is the effect of time walk spreading the distribution toward larger delays. Thus, the necessity to remove the effect of time walk by applying, event-by-event, the proper corrections.

Only events around the 511 keV photopeak were selected (between 80 ns and 100 ns), leading to the delay spectra shown in Figure 3.35 (1). The Compton and backscatter events are thus eliminated from the timing events. The time walk corrections, in the form of a look-up table, were derived from the simulations described in Chapter 3.1.3 and shown previously in Figure 3.12.

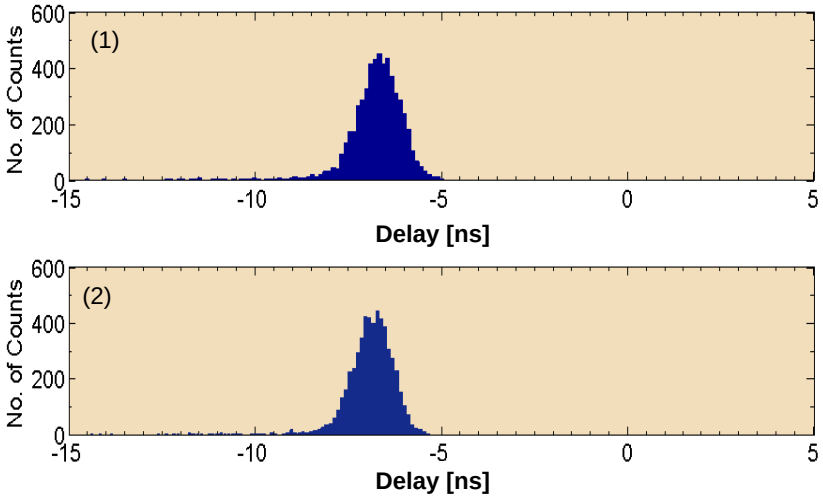

Figure 3.35: Coincidence time spectra of PMT vs. APD detection systems. top: spectrum after selection of photopeak events, bottom: spectrum further refined with time walk correction.

The delay spectrum, now time walk corrected and constrained to the photopeak, is shown in Figure 3.36.

From the fit of the nearly Gaussian distribution shown in Figure 3.36, the standard deviation σ_{TD} is calculated at 500 ps. σ_{TD} correspond to the quadratic sum of the individual time resolution of the PMT setup σ_{PMT} and of the APD+NINO system σ_{APD}, hence given as:

$$\sigma_{TD} = \sqrt{\sigma_{APD}^2 + \sigma_{PMT}^2} \tag{3.12}$$

From the previously made reference measurements in which two iden-

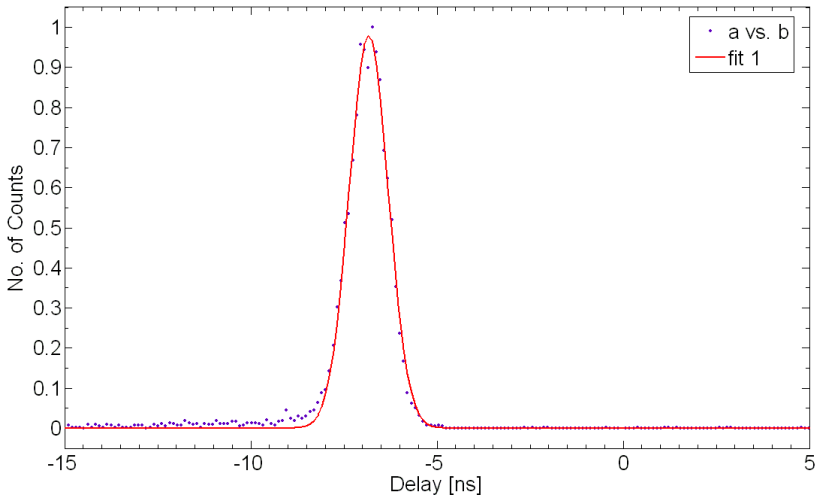

Figure 3.36: delay histogram from the PMT vs. APD measurement. The spectrum is corrected from time walk in NINO and constrained to events in the photopeak region .

tical PMTs were used the intrinsic single PMT time resolution σ_{PMT} can be extracted:

$$\sigma_{PMT} = \frac{200}{\sqrt{2}} = 141\ ps\ rms \tag{3.13}$$

This number matches the value of the transit time spread (TTS=160 ps) given by the Hamamatsu datasheet. Replacing PMT in 3.12 with the expression 3.13 gives the intrinsic APD+NINO time resolution R_{APD}:

$$\begin{gathered} \sigma_{APD} = 480\ ps\ rms \\ or\ R_{APD} = 1.13\ ns\ FWHM \end{gathered} \tag{3.14}$$

The objective is to show how the timing performance of an all-APD-based system compares with high speed PMT detectors in PET. Therefore the coincidence setup was modified in order to accommodate two APD detectors mounted back to back, running both with the FEDC05+NINO readout, as shown in Figure 3.37.

A second APD based detector system is built and calibrated like the first one described in 3.1.3. The results are shown in Appendix D and demonstrate a similar behavior to that of the first APD based detector system.

No CFD but only leading edge discrimination is used, implying that both coincidence signals are smeared out by time walk variations.

Thus, the pulse width and time stamp of both APD detectors are recorded. The principle of measurement is the same as before, except

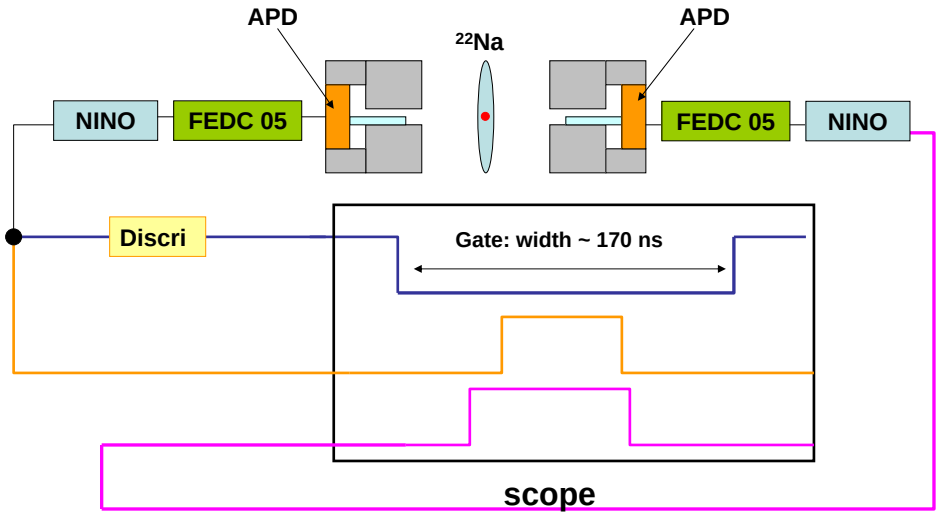

Figure 3.37: Schematic of the time coincidence measurement setup composed of 2 APD based detector systems.

that one of the NINO output signals is used to generate a gate of 170 ns through a discriminator.

To account for the intrinsic time jitter of the gate itself, two delay measurements are done, recording the time between the front edge of the gate and each leading edge of the two NINO outputs. Subtraction of the two time intervals then results to coincidence time difference between the two APD+NINO outputs, independent of the gate.

In Figure 3.38 it is shown how the raw coincidence time spectrum of an APD system improves by applying successively photopeak selection and time walk corrections on each signal output (from top to bottom).

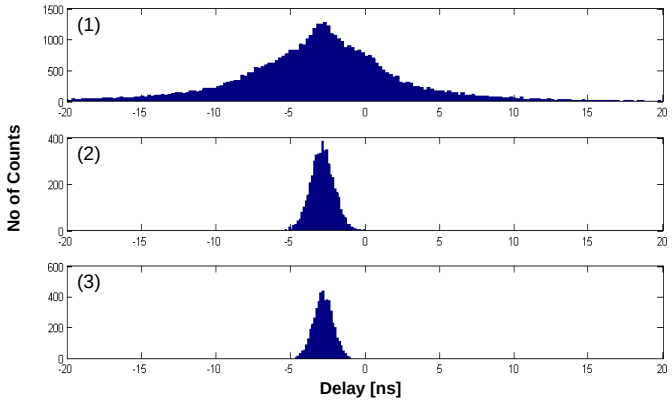

Figure 3.38: Coincidence time spectra of a double APD based detector system. top: raw spectrum, middle: spectrum after selection of photopeak events, bottom: spectrum after further refined by time walk correction on the remaining data sample .

The bottom spectrum of Figure 3.38 is fitted with a Gaussian and shown separately in Figure 3.39.

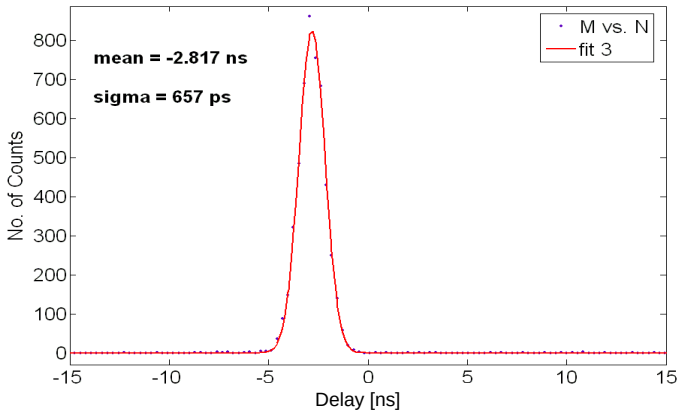

Figure 3.39: Fit of the refined time coincidence spectrum of two APD detectors .

From the fit, the standard deviation system of the dual APD setup is found to be $\sigma_{system} = 660\ ps$, in other words the coincidence time precision is $R_{system} = 1.6\ ns$ FWHM. This result proves our earlier measurements with a single APD detector correct, since

$$\sigma_{system} = \sqrt{\sigma_{APD1}^2 + \sigma_{APD2}^2} \approx \sqrt{2(480\ ps)^2} = 680\ ps \\ or\ R_{system} = 1.6\ ns\ FWHM \tag{3.15}$$

Despite data correction and refinement, some 'fake' coincidence events are still left in the data sample, some coincidence measurements were done at a larger distance from the source. Table 3.2 is a summary of our results and shows three geometric scenari for three different detector combinations (PMT1/PMT2, PMT1/APD1 and PMT1/APD2). Zero distance denotes closest spacing between detector and source, whereas "5-10 cm" describes an asymmetric arrangement where one detector is 5 cm and the other 10 cm away from the source. This distance increase has the effect to decrease the detection solid angle and thus to make fake coincidence events less probable.

The results in Table 3.2 show that different detector-source distances have little influence on the achievable time resolution. It can hence be concluded that the intrinsic time resolution R_{APD} of the APD-FEDC05-NINO readout is:

$$R_{APD} \leq 1.2\ ns\ FWHM \tag{3.16}$$

Table 3.2: Coincidence measurements with different detector configuration

Distance source/detector [cm]			0	5	5-10
PMT vs. PMT		σ [ns]	0.2	0.19	0.19
		FWHM [ns]	0.46	0.44	0.44
PMT vs. APD	intrinsic APD1	σ [ns]	0.43	0.45	0.45
		FWHM [ns]	1.01	1.06	1.05
	intrinsic APD2	σ [ns]	0.43	0.45	0.45
		FWHM [ns]	1.13	1.13	1.14

or for the combined dual APD system, a time resolution R_{system}:

$$R_{system} \leq 1.6\ ns\ FWHM \tag{3.17}$$

From [Pichler 04], [McCallum 05], [Pepin 04], it turns out that our time based approach of reading and processing coincident photon data from an APD circuit is comparable to classical methods where APD signals are digitized with ADCs. However, timing resolution of the order of 1 ns is relatively poor compared to the potential time resolution of the electronic circuits used in this study. It is thus worthwhile to investigate the different sources of time jitter that contribute to the overall system time resolution to determine the bottleneck limiting the timing performances.

3.2.2.2 Interpretation of the results

In an approach similar to [Casey 03], the overall timing uncertainty is factorized into three parts corresponding to the three detector components in our system, each contributing to time jitter: first the scintillating crystal, second the APD photodetector, and third the electronic circuit. Statistically, the total time jitter $\sigma_{j\ total}$ can then be expressed as the quadratic sum of the three contributions:

$$\sigma_{j\ total} = \sqrt{\sigma^2_{j\ crystal} + \sigma^2_{j\ APD} + \sigma^2_{j\ elec}} \tag{3.18}$$

where $\sigma_{j\ crystal}$ denotes time jitter issue from the scintillating crystal, $\sigma_{j\ APD}$ the time jitter of the current signal at the APD output for any light input signal, and $\sigma_{j\ elec}$ the time jitter at the electronic readout output for any input current. Note that the index j used in the equations

describes timing variations in order to make a difference with σ the usual standard deviation or electronics noise.

Considering the electronic part of the detector alone, the time precision is governed by the electronic noise. In fact, the instantaneous signal level produced at the output of FEDC05 is governed by noise σ_e. This makes the time of threshold crossing fluctuate. The electronic time jitter $\sigma_{j\ elec}$ is then given by the ratio of the amplifier noise σ_e and the signal slope (dV/dt) delivered within the rise time of the amplifier at the discriminator threshold crossing (also denoted as slope to noise ratio) [Spieler 05] :

$$\sigma_{j\ elec} = \sigma_e \times \left(\frac{dV}{dt}\right)^{-1}_{threshold} \tag{3.19}$$

This time jitter is measured by injecting test charges at the input of the amplifier (FEDC05) and by measuring the corresponding signal delays at the output of NINO, as shown in Figure 3.40 (1). Since input or detector capacitances influence front-end noise, our measurements were made with the fully biased APD array coupled to the FEDC05 amplifier. This leads to approximately 10 pF at the input of FEDC05.

In addition, the APD dark current also adds to the noise at the input of the amplifier. Thus, $\sigma_{j\ 1}$ is a convolution of the intrinsic amplifier front-end noise $\sigma_{j\ elec}$ and the noise contributions from the biased APD dark current $\sigma_{j\ dark}$.

The electronic time jitter $\sigma_{j\ 1}$, measured under these conditions, is plotted in Figure 3.41. One should note that the steep decline in time jitter for low input charges and its asymptotic behavior for charges higher than 2 10^5 electrons is only a consequence of the previously described output signal behavior of FEDC05. It was shown then that the output signal of FEDC05 rapidly rises with increasing input charge and then gradually reaches full saturation (with increasing pulse length) where the pulse rise time, however, does not increase anymore, i.e. the slope dV/dt is constant.

APD signal amplification through avalanche processes underlies gain fluctuations also leading to time variations of the output signals. To test this mechanism and its influence on time jitter, laser light bursts of a defined number of photons of 410 nm were sent onto the APD window, as shown in Figure 3.40 (2). The resulting time jitter $\sigma_{j\ 2}$, also shown in Figure 3.41, is now a convolution of the time variations produced by the avalanche mechanism of the APD and the electronic time jitter $\sigma_{j\ 1}$

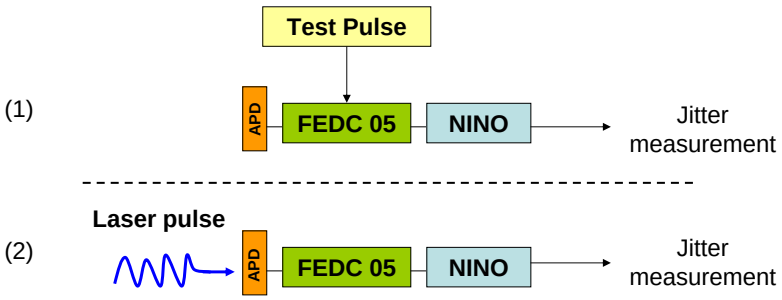

Figure 3.40: Schematic of the 2 setups used for the determination of $\sigma_{j\ 1}$ and $\sigma_{j\ 2}$.

described above:

$$\sigma_{j\ 2} = \sqrt{\sigma^2_{j\ APD} + \sigma^2_{j\ elec} + \sigma^2_{j\ dark}} \tag{3.20}$$

The overall system time jitter, $\sigma_{j\ total}$, including all contributions, plus the jitter induced by the non uniform light production of the scintillating crystal, was measured with 511 keV γ-rays from ^{22}Na and is also shown in Figure 3.41, as a single point only.

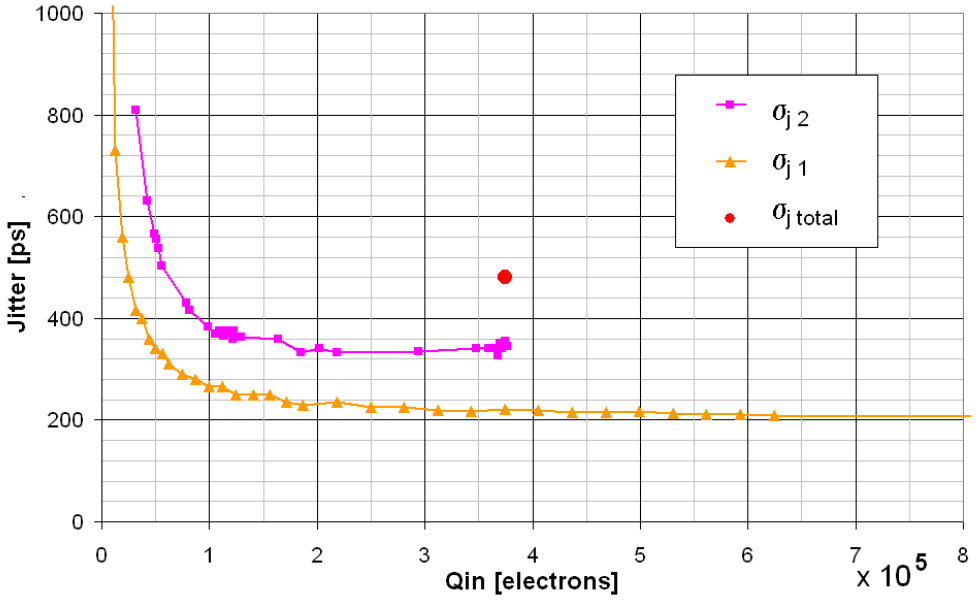

Figure 3.41: Time precision as a function of the charge.

The individual jitter contributions in equation 3.18 is only done on the charge equivalent to the 511 keV photopeak, i.e. 3.8 10^5 electrons, which is common to all three measurements. Hence, this is the only region where the three effects of jitter can be deconvoluted.

From SPICE, and using the nominal input charge of 3.8 10^5 electrons, the signal rise of the FEDC05 output signal at threshold crossing was determined at dV/dt=33 mV/ns, and the equivalent noise voltage was measured as σ_e=6 mV. Thus, from 3.19 is derived:

$$\sigma_{j\ elec} = \sigma_e \times \left(\frac{dV}{dt}\right)^{-1}_{threshold} = 6/(33) = 0.180\ ns\ rms \tag{3.21}$$

The measured asymptotic value of $\sigma_{j\ 1}$ shown in Figure 3.41 is:

$$\sigma_{j\ 1} = 220\ ps\ rms \tag{3.22}$$

The impact of dark current on the time precision should then be of $\sqrt{220^2 - 180^2} = 120\ ps$, but the precise value of this contribution is not measured in more details in this thesis.

The jitter attributed to the APD amplification mechanism is extracted from Figure 3.41 where $\sigma_{j\ 2} = 340\ ps\ rms$. Using expression 3.20, APD jitter becomes:

$$\sigma_{j\ APD} = 230\ ps\ rms \tag{3.23}$$

Finally, the crystal jitter $\sigma_{j\ crystal}$ can be estimated by making use of equation 3.18 and expressions 3.22 and 3.23 knowing that the overall system jitter was measured as 480 ps with 511 keV photons from ^{22}Na:

$$\sigma_{j\ crystal} = 340\ ps\ rms \tag{3.24}$$

The total time jitter, its components, and their relative contribution to the total are summarized in Table 3.3.

Table 3.3: LSO crystals light yield

Contribution	Electronics	APD	Crystal	Total
σ_{jitter} [ps] rms	220	230	340	480
%	20	30	50	100

As mentioned in chapter 2.3.3, the time resolution from the scintillator has contributions from the propagation of photons in the scintillator, from the fluctuations in the LSO signal rise time and from the mechanism of photon production. Theorical calculations of the time resolution due to the propagation of photons in the crystal have lead to $\sigma_{prop} \approx 32\ ps$ (see

section 2.3.3.2), which is negligible compared to the 340 ps obtained. The fluctuations in the LSO signal rise time, even if not well characterized, shouldn't have a contribution higher than 100 ps, hence also negligible in a quadratic sum. Therefore the main contribution might come from the mechanism of photon production in the crystal. Knowing the LSO time constant $\tau = 40\ ns$ and the number of primary photoelectrons detected R=2200, the maximum photoelectron number Q on which the detection is triggered can be calculated from equation 2.32 in chapter 2.3.3.3, by replacing t_Q by 340 ps.

$$Q = R(1 - e^{\frac{-t_Q}{\tau}}) + e^{+\frac{t_Q}{\tau}} \approx 20\ photoelectrons \tag{3.25}$$

In other words, the detection system has to wait for the 20^{th} photoelectron before to give a response.

The results demonstrate that the noise of the electronics developed at CERN, combined with the noise induced by the APD dark current, is 20% of the total jitter. Non uniformities in avalanche amplification inside the APD account for 30% of the total jitter. The effect is explained by the excess noise factor (ENF) in the APD, which describes the variation of electron multiplication during the avalanche process. The final contribution of 50% to the system time jitter is seen to be due to a combination of two effects: It is not only associated with the Poisson-like light production in the crystal within the 40 ns decay time, but also by the lacking gain of the APD making the system insensitive to fewer than 20 photoelectrons. The better time resolution of PMTs (140 ps) comes from the single photon detection which exhibits a lower timing uncertainty than the 20 electrons threshold of the APD

3.3 Conclusion

It was shown that in terms of energy resolution a full time based readout technique for PET based on high speed and low noise electronics, is comparable to classical readout methods. The energy resolution in CT operation is degraded because of the system non linearity for signals of less than 10^5 electrons. This prevents from distinguishing the escape peak from the photopeak at 122 keV.

The detector system presented in this chapter offers numerous advantages over standard architectures, such as higher reliability, simplicity, and easier system integration. This has a direct and positive impact on

spatial resolution and cost when highly segmented or pixilated photon detectors are chosen for tomographs.

However, timing precision is limited by the use of APDs coupled to standard scintillators. In the case of LSO, a widely used crystal in medical imaging, the time resolution with the Hamamatsu S8550 APD is limited to 1.6 ns FWHM. The analysis of timing has shown that the electronics contributes to 20% of the total time resolution, the APD contribution constitutes 30% and the contribution of LSO is of 50% as the system is not sensitive to less than 20 photoelectrons.

These results suggest other and new choices of photodetectors than PMTs, offering the advantages of solid state integrability together with higher gain. Silicon PhotoMultipliers (SiPM) are such possibilities whose signal could be sensed by the NINO discriminator directly, i.e. without an additional amplifier in the chain. Such an approach would further simplify the readout architecture and system integration, and finally overcome the inherently large timing fluctuations imposed by LSO-APD detector heads.

Chapter 4

Characterization of Silicon PhotoMultipliers for PET detector system

Silicon PhotoMultipliers (SiPM) are recent photodetectors (patent submitted in 1996 [Sadygov 96]). They have all the advantages of solid state devices like for example small size, low cost, insensitivity to magnetic field, together with sub-nanosecond rise time and single photon sensitivity, these latter being only achieved until now with vacuum photodetectors.

SiPM exhibit very good timing characteristics and could substantially improve the performances of PET detector system, for example in adding the TOF information to the detection of 2 collinear photons.

The objective of this study is to assess the timing resolution obtainable by a TOF-PET detector system, using LSO scintillator coupled to SiPM photosensors and a readout based on CERN electronics.

In this context, a scientific collaboration was established between ST Microelectronics Catania (STM) and CERN: STM developed and supplied prototypes of SiPM which were then tested and characterized at CERN with the high speed electronics developed for the LHC experiments. Commercial SiPMs from Hamamatsu called Multi Pixel Photo-Counters (MPPC) were also investigated with the same electronics, as a comparison.

As shown previously in chapter 2.3.3.3, the ability to detect the first photoelectrons is crucial to obtain the best possible time resolution. Therefore a part of this study aims at testing the SiPM analog characteristics for single photon detection and the readout of it by the NINO chip.

The output current signal of the SiPM is first described before its

response to the detection of photons emitted by a LSO crystal is calculated. Then a presentation of the setup developed at CERN for the measurements is done and at last, the characterization of the STM and Hamamatsu SiPMs are shown.

4.1 Discussion about the SiPM current signal in the case of single photon detection

As the SiPM current signal is the sum of individual SPAD signals, the first and crucial point is to understand the SPAD signal shape, also called single photoelectron response as this one is activated by one single photon. In a first approximation, the SPAD response is a decreasing exponential whose time constant τ_{RC} depends on the SPAD technology: e.g. the quenching resistance, the diode capacitance and the load resistance. This shape is more complex because of parasitic resistances and capacitances involved, as shown in electronics models of the SiPM given by [Corsi 07, Cova 07, Pavlov 05, Corsi 06].

The signal is thus composed of a fast rise time and of at least 2 decay time constants: a fast one (of some nanoseconds) and a slow one (in the order of 100 ns). These parameters strongly depend on the technology used by the manufacturer. Some examples of pulse shape for single photoelectron response are presented in Figure 4.1 with SiPMs from Zecotek [Zecotek], Hamamatsu (MPPC) [Hamamatsu], Photonique (SSPM) [Photonique] and FBK [FBK]. Those plots are taken from [Dinu 08] where the SiPMs are readout with a transimpedance amplifier which schematic is not precisely described. Since this is to show the different pulse shapes and not the pulse height, arbitrary units on the ordinate were chosen.

The SPAD response to single photon detection shows in every case a fast rise time below 2 ns. The signal fall time varies with the manufacturer, e.g. it is longer for Hamamatsu cells, from 10 ns to 50 ns. The presence of 2 decay components is best seen for SiPM from FBK with a fast first decay of less than 10 ns and a longer one in the order of 50 ns. The SiPM current signals from Photonique and Zecotek show a single decay time of less than 10 ns, but a second decay component could be covered by the electronics noise or by inappropriate scope settings.

The SiPM device size and its number of SPADs is also of importance

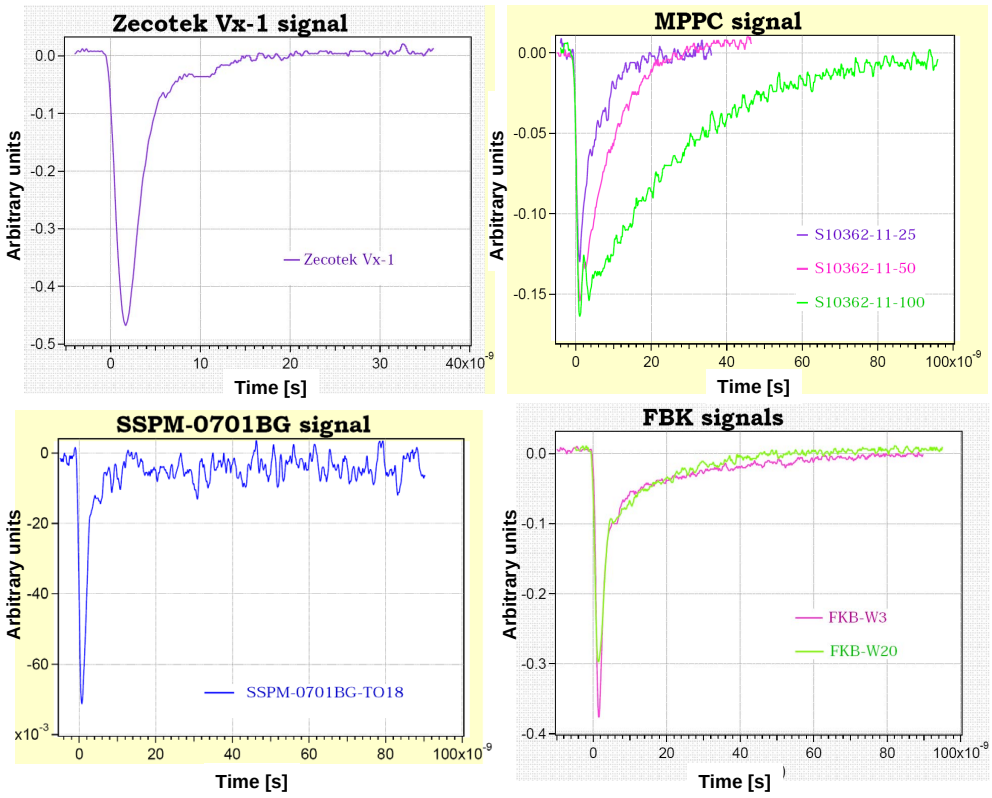

Figure 4.1: SiPM output signal shape for different manufacturers.

for the current signal shape as the total load capacitance (or terminal capacitance), corresponding to the sum of each diode capacitance and parasitic capacitance, can be from some tens of pico Farads for $1 \times 1\ mm^2$ SiPMs of 400 cells, to some hundreds of pico Farads for $3 \times 3\ mm^2$ SiPMs, composed of 3600 cells. As shown in Figure 4.2, this capacitance in parallel with a load resistance (scope load resistance or preamplifier input impedance) shapes the signals.

A fast current signal $i_1(t)$ simulates the SPAD currant response with a pulse height of 34 μA, and a fall time of $\approx 5\ ns$. The current actually seen on the scope $i_2(t)$ depends on the terminal capacitance in parallel with the 2 resistances of 50 Ω. As clearly seen, the terminal capacitance C_T has a high influence on pulse height and pulse rise time, degrading substantially the timing performance of the device.

The only way to overcome this effect is to reduce the input resistance of the readout electronics. For Hamamatsu cells, this terminal capacitance is given at 35 pF for $1 \times 1\ mm^2$ SiPMs and at 320 pF for $3 \times 3\ mm^2$ structures. For STM cells, these values are not known, but are expected to be in the same order of magnitude.

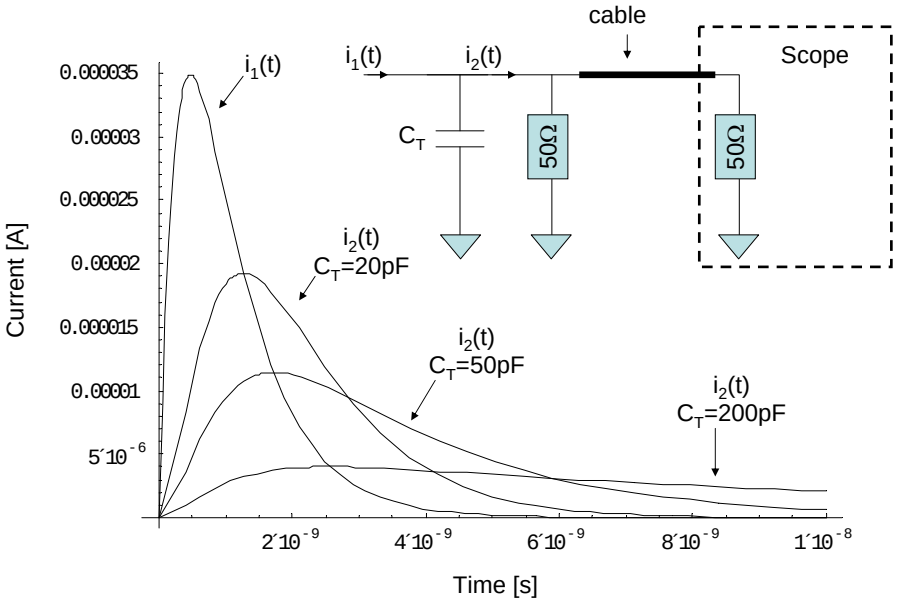

Figure 4.2: SiPM output signal shape for different manufacturers.

4.2 Detection of photons emitted by a scintillator

This section aims to model the SiPM output current shape when it is reading out the light from a scintillator such as LSO. Unlike PMTs and APDs, the SiPM is not simply a photoelectron multiplier, so that the pulse shape will not exactly reproduce the LSO light decay time constant $\tau_{LSO} = 40\ ns$.

As mentioned before in chapter 2.3.2 in equation 2.16, all the photons from the LSO do not arrive at the same time. The n^{th} photon out of n_{total} arrives at a time t_n defined by:

$$t_n = -\tau_{LSO} ln \left[1 - \frac{n}{n_{total}}\right] \tag{4.1}$$

Whatever the SPAD response $I_{SPAD}(t)$ is, the SiPM signal will be the sum of the individual SPAD responses triggered at time t_n, defined as $I_{SiPM}(t)$:

$$I_{SiPM}(t) = \sum_{n=0}^{n_{total}} I_{SPAD}(t - t_n) \tag{4.2}$$

For a SPAD signal modeled as a decreasing exponential with maximum height I_0 and of time constant τ_{RC}, the SPAD response can be written as:

$$I_{SPAD}(t-t_n) = I_0.exp\left(-\frac{t-t_n}{\tau_{RC}}\right) \times H\left(t-t_n\right) \tag{4.3}$$

With H(t) the Heaviside function (or unit step function). The total signal can then be described by 4 parameters: τ_{LSO}, τ_{RC}, n_{total} and I_0.

$$I_{SiPM}(t) = I_0 \sum_{n=0}^{n_{total}} exp\left(-\frac{t-\tau_{LSO} ln\left[1-\frac{n}{n_{total}}\right]}{\tau_{RC}}\right) \times H\left(t-\tau_{LSO} ln\left[1-\frac{n}{n_{total}}\right]\right) \tag{4.4}$$

Assuming that $\tau_{LSO} = 40\ ns$, $\tau_{RC} = 5\ ns$, $n_{total} = 2000$ photons detected and $I_0 = 34\ \mu A$, the signal $I_{SiPM}(t)$ can be plotted as a function of time as shown in Figure 4.3.

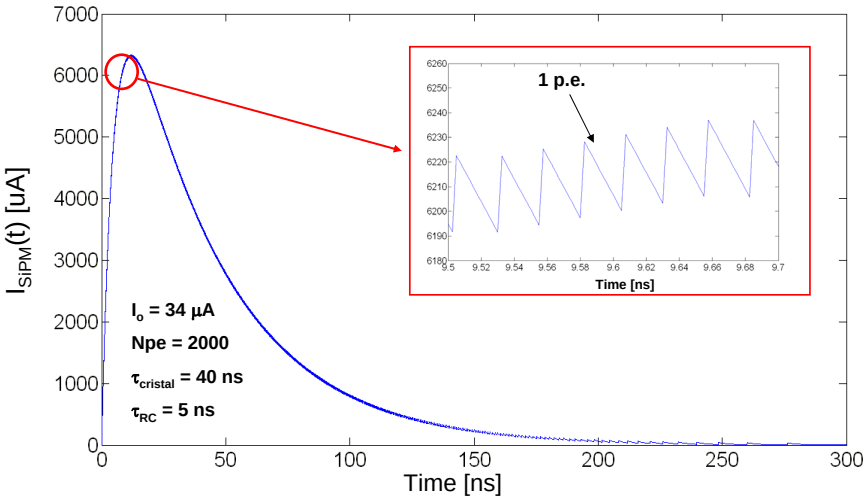

Figure 4.3: SiPM output signal for LSO photons detection.

The total current peaks at 20 ns, with a maximum amplitude of 6.3 mA.

Note that this model considers that each photon is detected in a single and separate SPAD. However, if a photon hits an already fired cell, no more current will be induced in that cell (saturation effect) so that the calculated current signal from equation 4.4 is a maximum. The equation above explains the measurements obtained when a SiPM and a LSO crystal are coupled in a detector system such as in the work presented in [Spanoudaki 07, Kim 09]

The LSO crystals have a light yield of 16100 photons/MeV. Considering that the PDE is $\approx$ 25% at 420 nm (given by the Hamamatsu datasheet), only $\approx$2000 photons should be detected. In order to avoid

saturation effect, a SiPM of at least 4000 cells (2 times more than the number of photons to be detected) over 2×2 or 3×3 mm^2 should be used. Currently, the maximum number of cells given by Hamamatsu SiPM is 14400 (pixel size of 25×25 μm^2, total size of 3×3 mm^2) which is sufficient to cover the needed dynamic range.

4.3 Description of the measurement setup

Because of the large gain of the SiPM ($10^5 - 10^6$, see chapter 2.4.2.4), no further amplification is needed. The typical maximum current I_0 for an individual cell is ≈ 35 μA which is above the minimum threshold of NINO. However, when the input currents are too high, the NINO output pulse width saturates. The NINO circuit is not appropriate to readout total currents higher than 1 mA. A way of decreasing too high signal has been found. It permits on one hand to detect the first photoelectron in order to maintain good timing characteristics, and on another hand to avoid the saturation of the NINO. The technique consists of a high pass capacitive filter, serving as an interface with NINO and shown in Figure 4.4. As a consequence, one maintains the high sensitivity to the detection of single photoelectron, important for good timing characteristics, and at the same time avoids the saturation of the NINO circuit.

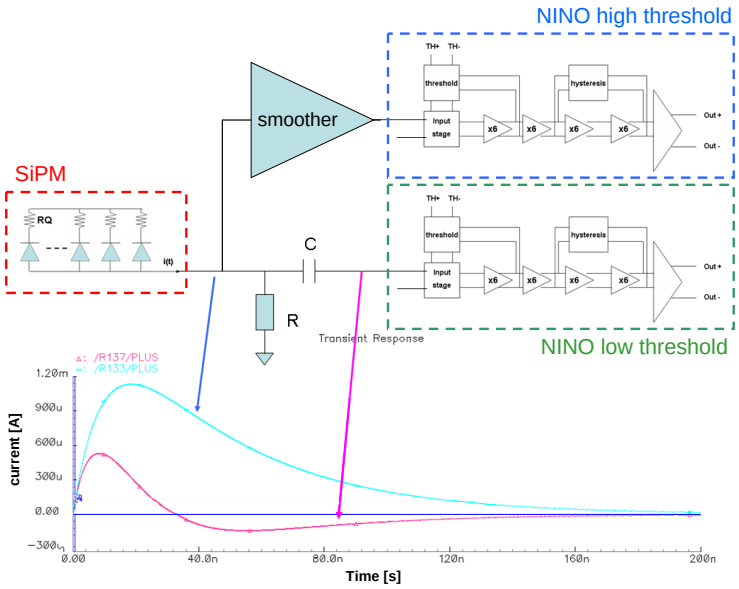

Figure 4.4: Schematic and simulation of the capacitive filter behavior.

The filtered signal (in red) follows the SiPM signal (in blue) during the first nanosecond. It is then attenuated by the filter. Despite the at-

tenuation of the signal, it is still possible to detect the first photoelectron emitted in the first 100 ps, albeit with a possible loss in the energy resolution. In order to retrieve both good timing and higher energy resolution, one could think of a second single path in which the signal goes through a smoothing circuit and is read out by a separate NINO channel with a higher threshold to get good energy resolution. This way the fast component of the signal can be used by NINO to determine the time stamp with a low threshold, while the smoother circuit permits integrate a part of the charge to determine the energy.

A test board shown in Figure 4.5 was developed to characterize both the analog SiPM current signal and the combined SiPM+NINO readout.

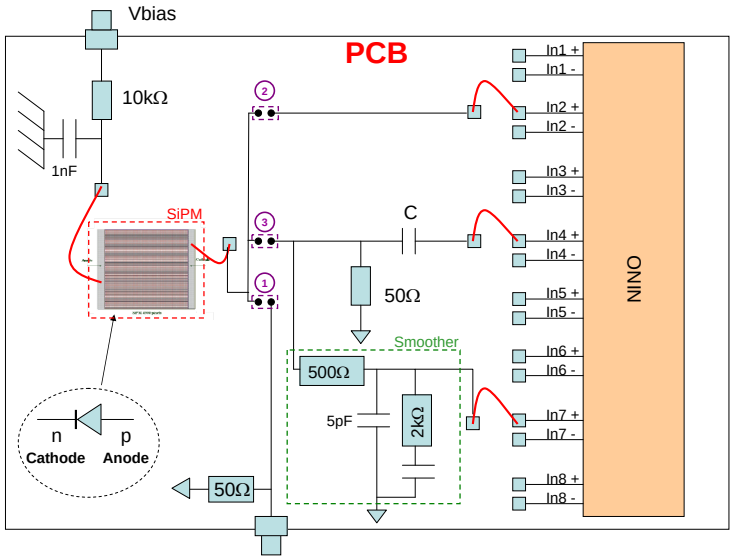

Figure 4.5: Schematic of the SiPM test board.

There are 3 possibilities of connecting the output of the SiPM to the Printed Circuit Board (PCB) via jumpers:

1. The direct readout of the SiPM current output is done through a load resistance of 50Ω to avoid reflections in cables.

2. The SiPM current signal is injected into the NINO chip. The input impedance of NINO can be set between 20 Ω and 200 Ω.

3. in case of too high current signal (scintillator case), the SiPM output is sent to the capacitive filter in parallel with the smoother circuit.

In order to test the photodetector, a laser system provided by a PicoQuant PDL 800-B picoseconds pulse generator is used [PicoQuant]. Two laser head can be used: one emitting photons at 405 nm (blue), the other

emitting photons at 660 nm (red). The laser pulses have a FWHM of 50 ps. In this case all the photons are sent with a spread much shorter than the photodetector's rise time. It is thus possible to consider that they arrive "at the same time" at the photosensor.

The laser intensity (LI) can be varied with a potentiometer allowing a dynamic range of 1 to 1000. Note that the number of photons emitted by the laser is not a linear function of the LI. Moreover, this system offers an external trigger, generating a square pulse whose leading edge corresponds to the time of photon emission. It is used as a time reference in all timing measurements.

The SiPM readout test board is installed into a black box, in a laboratory where the temperature is stabilized to 20^oC. The chosen SiPM is aligned with the laser beam, the whole apparatus being mounted onto a rail with micrometer positioning setup. Figure 4.6 shows the board on which the SiPM and the NINO chip are bonded (top right and top left). At high light intensity, the laser spot can be observed on the SiPM structure as shown in the bottom right picture. A close up of the SiPM structure is also shown in the bottom left picture, with the wire connecting the device to the PCB.

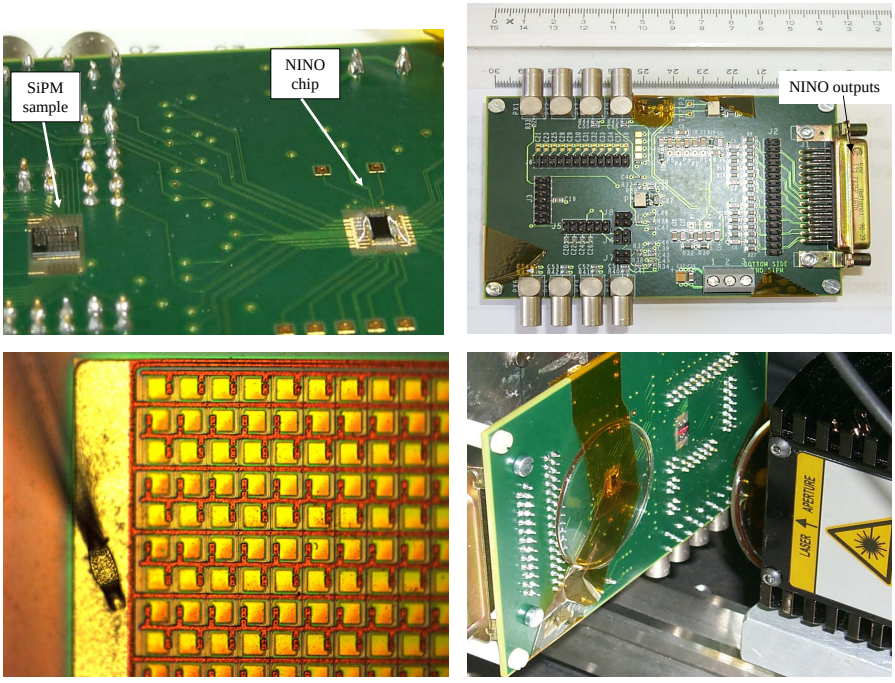

Figure 4.6: Pictures of the setup.

4.4 Measurements

In the context of the scientific collaboration between STM and CERN, several samples of SiPM were developed by STM, with their main characteristics presented in table 4.1. Commercial SiPMs from Hamamatsu were also used as cross reference. They were chosen because they are already used in many experiments [Kim 09, Vinke 09, Bolle 09].

	STM		Hamamatsu	
active area [mm^2]	1×1	3.5×3.5	1×1	3×3
number of pixels	400	3600	100	3600
pitch [μm^2]	50	58	100	50
optical trench	yes	yes	no	no
fill factor %	40	48	78.5	61.5
peak sensitivity wavelength [nm]	420	420	440	440
breakdown voltage [V]	30	30	69	69
PDE	13% [Bonanno 09]	no data	61.5% (20%[Bonanno 09])	50%
package	no	no	yes	yes

Table 4.1: Overview of SiPM characteristics

4.4.1 STM 1×1 mm^2

4.4.1.1 I(V) measurements

A positive voltage from 0V to 40V is applied on the SiPM common cathode by a Keithley 2410 voltage source (reverse bias). The current is measured through this same instrument and plotted in Figure 4.7.

The avalanche breakdown occurs clearly at a bias of 30 V, showing a steep increase of the dark current.

To measure the forward current, a negative voltage is applied to the cathode from 0 V to 4 V. The current delivered is positive and much higher, as shown of Figure 4.8.

For a bias above 3.5 V on the diodes, a high conductivity is observed so that the resistance seen by the voltage source is defined by all the quenching resistances in parallel. The slope of the forward I(V) is calculated at 247 $\mu A/V$ so that the quenching resistance R_Q is given by:

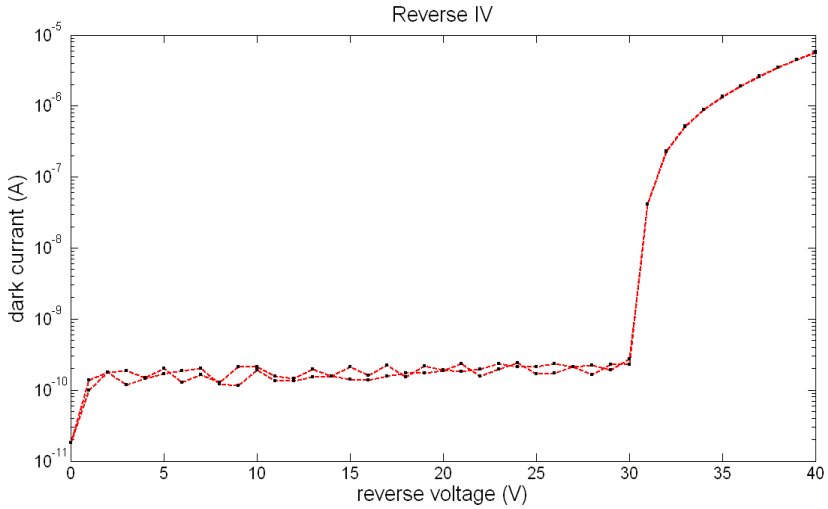

Figure 4.7: Dark current as a function of the reverse voltage.

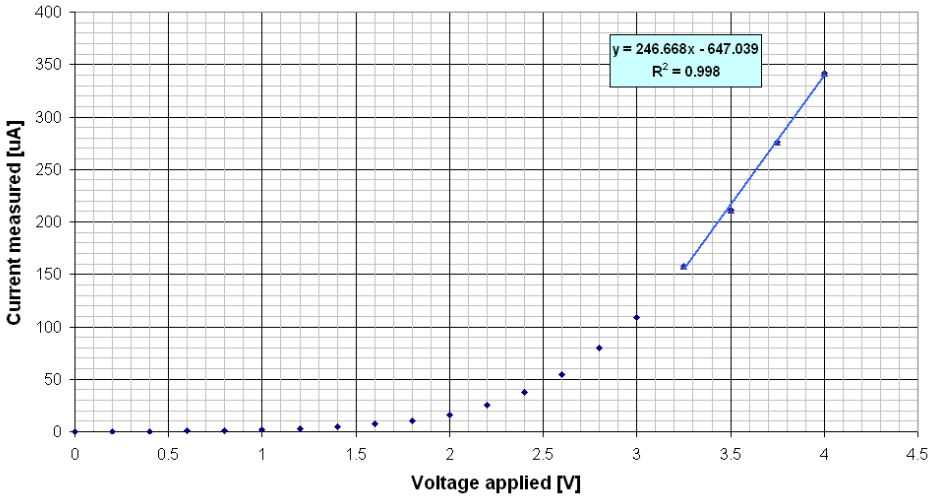

Figure 4.8: Dark current as a function of the forward voltage.

$$\frac{R_Q}{N_{cell}} = \frac{dV}{dI} = 4.05\ k\Omega \tag{4.5}$$

As the number of cells is $N_{cell} = 400$, the value of the quenching resistance is $R_Q = 1.62\ M\Omega$.

4.4.1.2 Analog response study

On the PCB, the jumper is set on position 1 so as to study the analog response of the SiPM. The SiPM is biased according to the schematic shown in Figure 4.9. Without amplification, the noise observed on the scope is about 2 mV into 50 Ω, or about 40 μA. The value of the single photoelectron response is about 35 μA at 33 V, marginally visible without

amplification. A fast broadband Hewlet Packard amplifier with a bandwidth from 5 MHz to 1.3 GHz is then interfaced between the SiPM and the scope in order to amplify the signal by 26 dB (amplification ×20) and is connected to the oscilloscope (LeCroy Wavepro 7100). The PicoQuant laser setup illuminates samples with laser pulses of 50ps FWHM. The variation in light intensity (LI) between 0 to 1000 arbitrary units (a.u.) permits to send from few to thousands of photons.

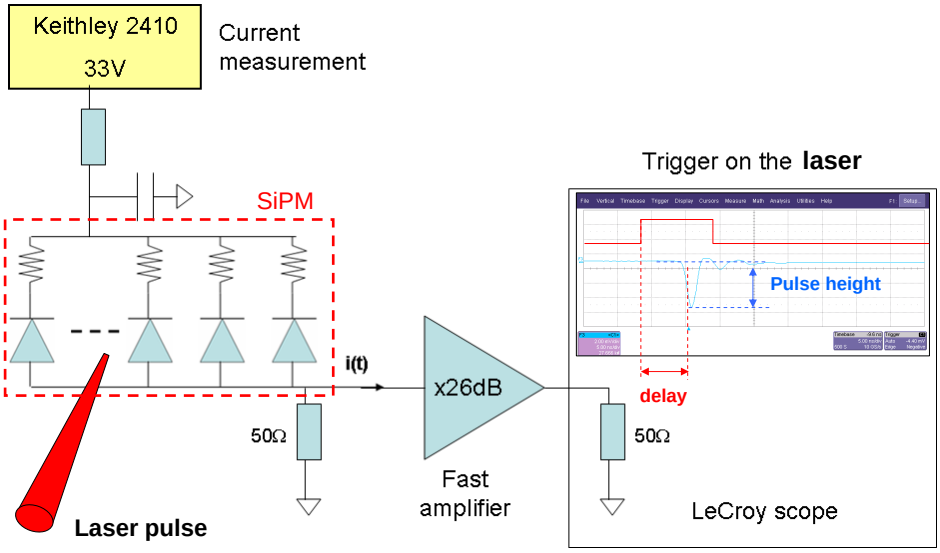

Figure 4.9: Schematic of the analog setup.

In dark conditions, the signals observed from the SiPM correspond to the generation of thermal carriers in the SPADs, triggering an avalanche and then a single SPAD response. This defines the single photoelectron response.

The single photoelectron response shows both very fast rise and fall time in the order of 1 ns each, as shown in Figure 4.10. The frequency of these pulses is of $\approx 1\ MHz$, i.e. a dark count rate of 10^6 counts/s.

It should be noted that the signal measured is already shaped by the terminal capacitance in parallel with the 50 Ω load resistance of the amplifier.

The laser light impinging on the SiPM is kept at a low level so that for each pulse, between 0 and 5 photons are sent at the same time (LI=89/1000). On the scope, the trigger is set on the laser pulse and the SiPM signal is observed. The delay between the trigger and the output signal leading edge is measured for each pulse as well as the SiPM output pulse height according to the scheme shown in Figure 4.9.

The delay is plotted as a function of the pulse height as shown in

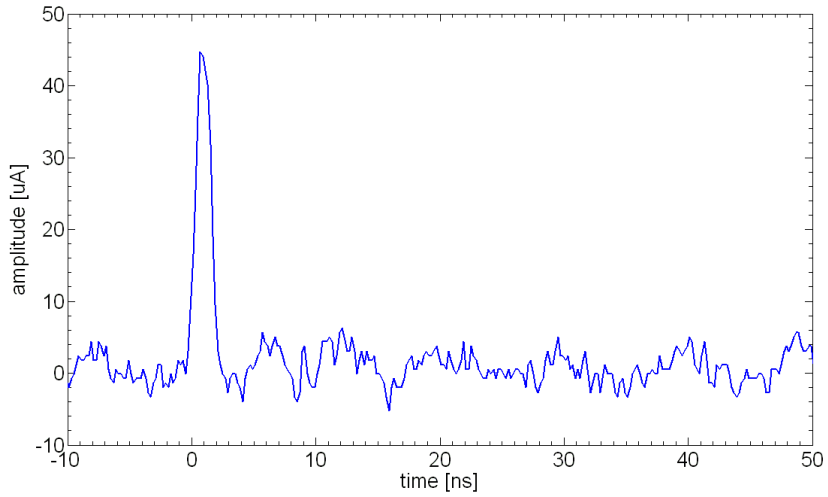

Figure 4.10: Scope shot of the single photoelectron signal.

the scatter plot of Figure 4.11 (2). Figure 4.11 (3) then represents its projection on the x-axis, i.e. the pulse height histogram, and Figure 4.11 (1) shows its projection on the y-axis, i.e. the histogram of the delay (in a log scale).

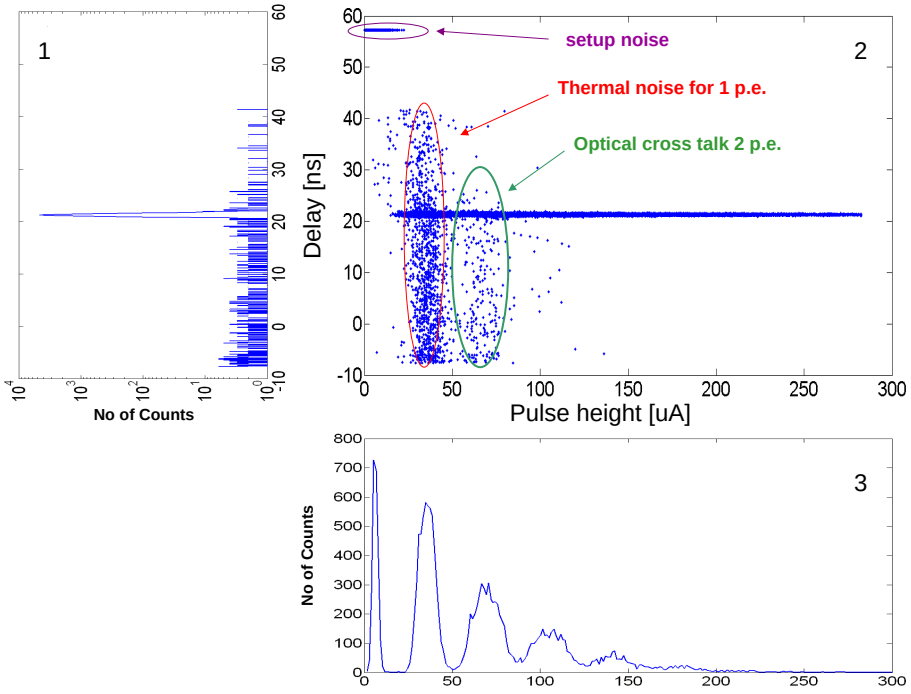

Figure 4.11: (1) delay spectrum, (2)Delay vs. Pulse height spectrum, (3) Pulse height spectrum.

Nearly all of the measured signals have a delay of 21.3 ns from the trigger, meaning that the SiPM signal is generated by the laser pulse. In addition, 3 different regions can be observed:

- Uncorrelated events in the range of 1 photon. They are due to thermal noise and their distribution is random.
- Uncorrelated pulses in the range of 2 photons. They are due to thermal noise triggering a neighboring SPAD (cross talk). These events are rare because of the optical trenches around the SPADs.
- On the top left corner one can see the noise of the setup.

The most populated region corresponds to delays between 20.5 ns and 22 ns, as shown in Figure 4.12 (2), and represents the signals generated by the laser photons.

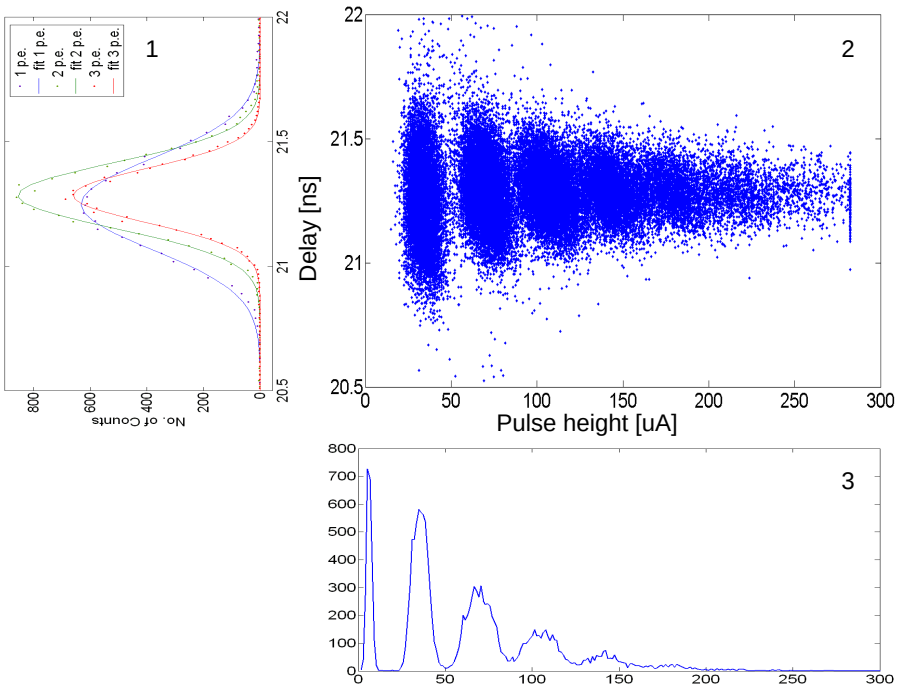

Figure 4.12: (1) delay spectrum, (2)Delay vs. Pulse height spectrum, (3) Pulse height spectrum. A close up is done on the most populated area

The single photoelectron response varies from 26 μA to 50 μA. A selection of data in this pulse height interval permits to obtain the corresponding delay histogram, plotted in blue in Figure 4.12 (1). The same method is used to isolate timing from 2 and 3 photoelectrons, respectively in green and red.

The delay histograms are shown in Figure 4.13 for biases of 33V and 35V.

The time precision on the detection of a single photon is of 180 ps, the contribution of the laser trigger to the total jitter is estimated to

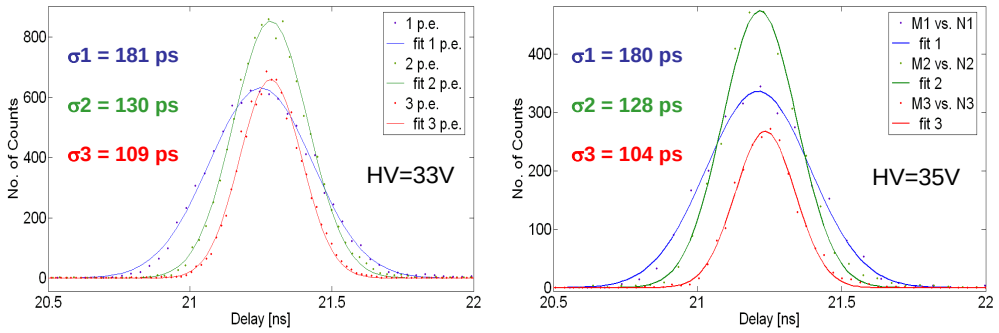

Figure 4.13: Time resolution on the detection of 1, 2, and 3 photoelectrons, at bias of 33 V (left) and 35 V (right).

be about 10 ps, thus negligible. The average delay corresponding to 1 detected photon is slightly shifted to lower values. The time precision on the detection of 2 and 3 photons is 130 ps and 109 ps, respectively. These values don't change for an increased overvoltage of 5 V.

Prior to concluding on these timing results, an analysis of the pulse height histogram shown in Figure 4.12 (3) is made. A 5-Gaussian fit is applied to the histogram shown in Figure 4.14, to extract the parameters corresponding to the noise and the signal generated by 1, 2, 3 and 4 activated SPADs.

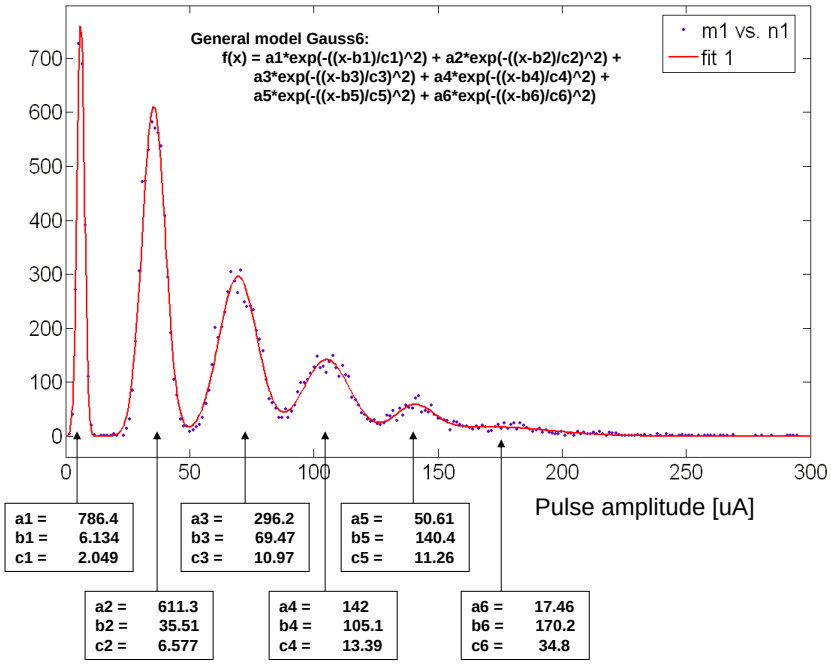

Figure 4.14: SiPM output Pulse height spectrum on which a sum of 5 Gaussians fit was applied.

It should be noted that the pedestal noise close to 0 has a FWHM

much smaller than the random fluctuations of the photoelectron peaks. This means that the variations in SPAD responses are larger than the electronics noise. The signal corresponding to a single photon detected, at a bias of 33 V, has a current amplitude of 35 μA. The signal corresponding to 2 photons detected has current amplitude of $2 \times 35 \approx 70$ μA, and accordingly $3 \times 35 \approx 105$ μA for 3 photons detected.

This information is important to understand the results on time precision presented. The jitter for 1 detected photon $\sigma_{j\ 1}$ is:

$$\sigma_{j\ 1} = \frac{\sigma_e}{(dI/dt)_{50\%}} \tag{4.6}$$

with σ_e being the electronic noise and dI/dt the slope of the current signal leading edge at 50% of the total height. Figure 4.14 shows that the fluctuations of the signal amplitude $\sigma_{I_{SPAD}}$ are 3 times higher than the electronic noise ($c2 > 3 \times C1$) so that it is the dominant source of fluctuations. Since the timing measurements are referenced to half of the pulse height, these fluctuations will have an influence on the timing precision. Equation 4.6 thus becomes:

$$\sigma_{j\ 1} = \frac{\sqrt{\sigma_e^2 + \sigma_{I_{SPAD}}^2}}{dI/dt} \approx \frac{\sigma_{I_{SPAD}}}{dI/dt} \tag{4.7}$$

With $\sigma_{I_{SPAD}} = c2/\sqrt{2} = 4.6\ \mu A$, $\frac{dI}{dt} = \frac{35\ \mu A}{1\ ns}$ shown in Figure 4.10, the jitter becomes $\sigma_{j\ 1} = 130\ ps$, in fair agreement with 180 ps considering an uncertainty in the peaking time between 1 ns and 1.5 ns. When n photons are detected, the SiPM output current signal is n times that of the single photon, and the slope is n times steeper. Since the fluctuations are Gaussian, the different $\sigma_{I_{SPAD}}$ are summed quadraticly, so that they follow a $\sqrt{n}$ rule: $\sigma_{n \times I_{SPAD}} = \sqrt{n} \times \sigma_{I_{SPAD}}$. The jitter corresponding to the detection of n photons $\sigma_{j\ n}$ is:

$$\sigma_{j\ n} = \frac{\sqrt{n} \times \sigma_{I_{SPAD}}}{n \times dI/dt} = \frac{1}{\sqrt{n}} \times \sigma_{j\ 1} \tag{4.8}$$

Based on these arguments, the measurements shown in Figure 4.13 are well matched by equation 4.8, i.e. $\sigma_{j\ 2} = \sigma_{j\ 1}/\sqrt{2} = 130\ ps$ compared to 130 ps measured, and for 3 photons, $\sigma_{j\ 3} = \sigma_{j\ 1}/\sqrt{3} = 104\ ps$ as compared to 109 ps measured

In the case of the results presented in Figure 4.13, $\sigma_{j\ 1} = 180\ ps$, it can be observed that for 2 photons detected, $\sigma_{j\ 2} = \sigma_{j\ 1}/\sqrt{2} = 130\ ps$ and for 3 photons detected, $\sigma_{j\ 3} = \sigma_{j\ 1}/\sqrt{3} = 105\ ps$.

This agreement is now checked for a higher number of photons detected. A calibration of the laser intensity is done at higher optical power (higher number of photons) to increase the SiPM signal. Now, the signal is observed directly on the scope without amplifier, because it would saturate for input currents higher than 2 mA.

The increase of light intensity exhibits a weak signal tail, visible just after the signal peak, decaying over 800 ns, as shown in Figure 4.15. This second decay time is due to the recharge of the SPAD capacitance through the quenching resistance, after the SPADs avalanches have been quenched. For 1 photon detected, this tail is completely masked by the electronic noise, and becomes only visible for more than 5 activated SPADs with maximum scope sensitivity settings. The height of this tail is at about 1/10 of the maximum pulse height.

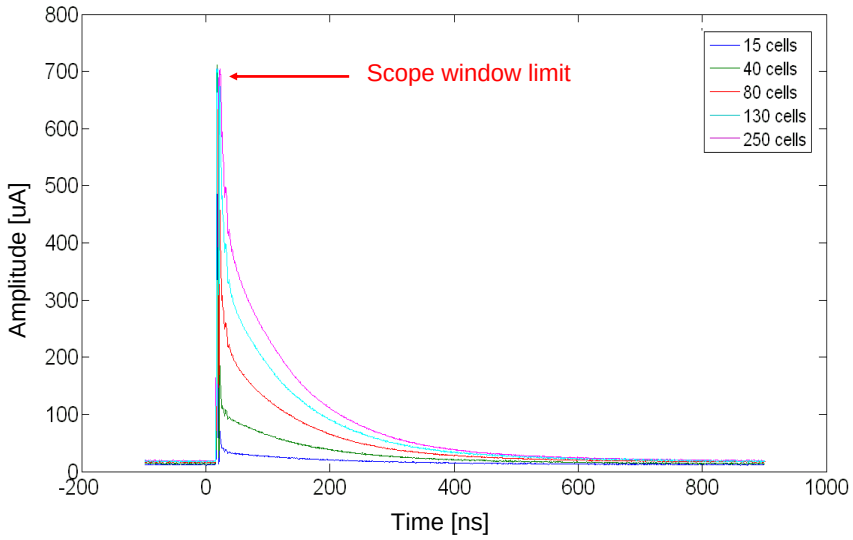

Figure 4.15: SiPM output signal for a different number of fired cells. The scope settings are optimized to focus on the signal tail.

The second decay component of the signal of 150 ns becomes visible as an increasing number of SPADs is activated by the laser. The signal amplitude (in μA) is measured as a function of the laser intensity. To calibrate the number of SPADs triggered by the laser, the current pulse amplitude obtained has to be divided by the current pulse amplitude given by a single SPAD excitation, i.e. 35 μA. Note that at high LI, The SPAD response to the number of photons detected approaches a Gaussian shape envelope, which center is used to determine the number of photoelectrons Npe. Npe is plotted on the Figure 4.16 versus the laser intensity.

The saturation effect appears from about 270 photons detected. The laser is now calibrated, meaning that the value of LI can be associated with

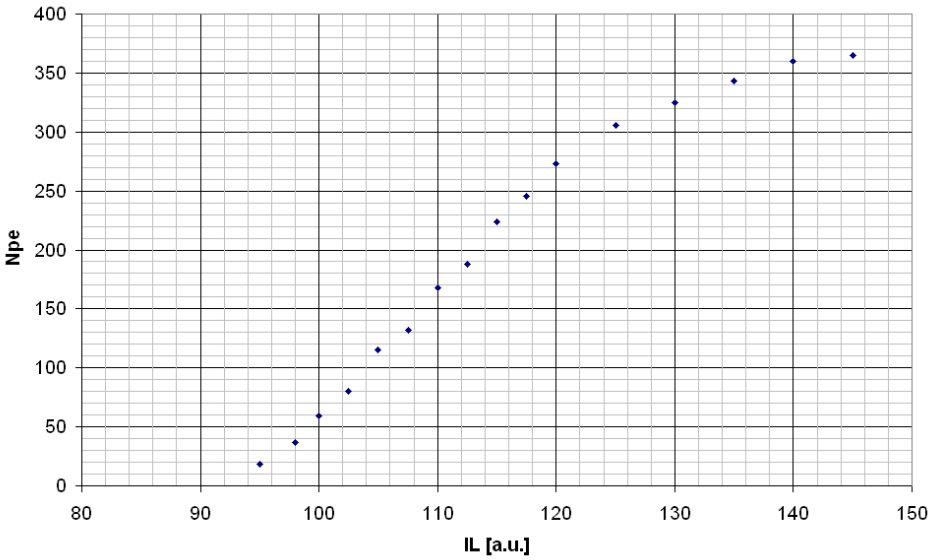

Figure 4.16: Minimum number of detected photoelectrons as a function of the laser light intensity.

the number of photons detected by the SiPM. The timing measurement is done by measuring the delay variation (or jitter), as a function of Npe. The result is shown in Figure 4.17.

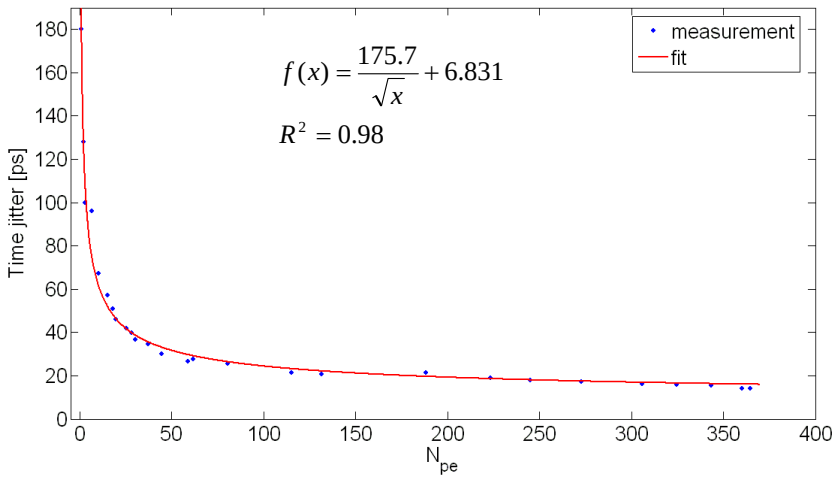

Figure 4.17: Time resolution as a function of the number of detected photons.

The measurements can be well fitted by a function varying with $1/\sqrt{N_{pe}}$, as explained in equation 4.8. The constant term of the fit equation stands for the residual timing limit, given by the jitter of the laser pulse generator.

4.4.1.3 Readout with NINO

In the following measurements, the current signal from the SiPM is directly read out by NINO as shown in the schematic of Figure 4.18. The NINO output is a square pulse whose width is a function of the injected charge.

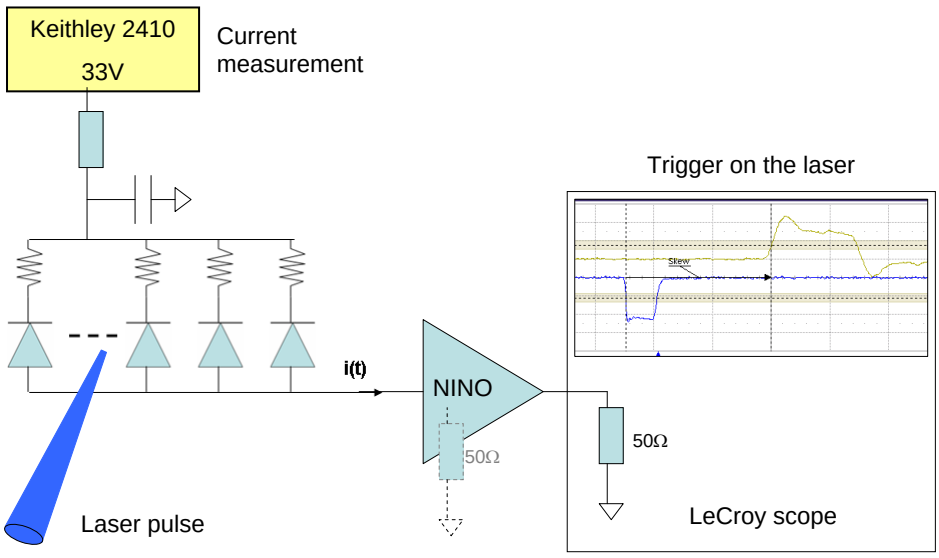

Figure 4.18: Schematic of the setup using the NINO chip.

The histogram of the NINO pulse width is shown in Figure 4.19 and exhibits a clear separation of one detected photon event from multi detected photon events different from what was obtained with analog measurement. This difference is explained by the non-linear characteristics of NINO at low level.

There is no pedestal noise since signals are discriminated against a threshold before being recorded. There is also a good separation between multi photoelectron events up to Npe=8.

The same way as before, measurements of the delay between the trigger and the NINO output rising edge are performed. In addition, also the NINO pulse width was recorded for each event triggered. The delay is plotted versus the pulse width in a graph shown in Figure 4.20 (2). The projection of this spectrum on the x-axis shown in Figure 4.20 (3) represents the pulse width spectrum. The projection on the y-axis shown in Figure 4.20 (1) represents the delay spectrum.

This graphic shows about 300 000 events. It is polluted by events uncorrelated to the laser. Nevertheless those events are statistically very rare compared to the correlated one. A region has been singled out shown

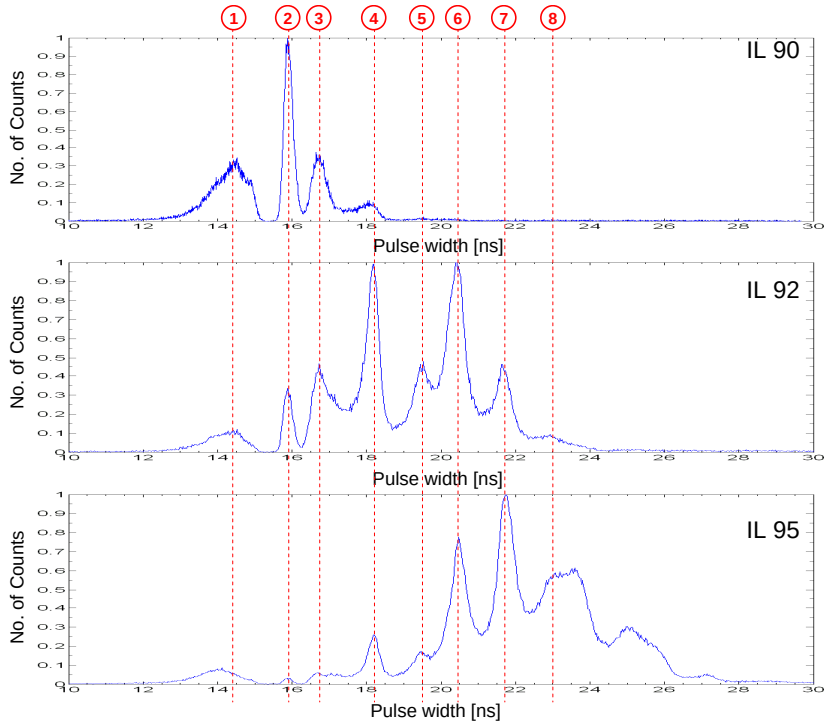

Figure 4.19: NINO output pulse width spectra for increasing laser light intensity (from top to bottom).

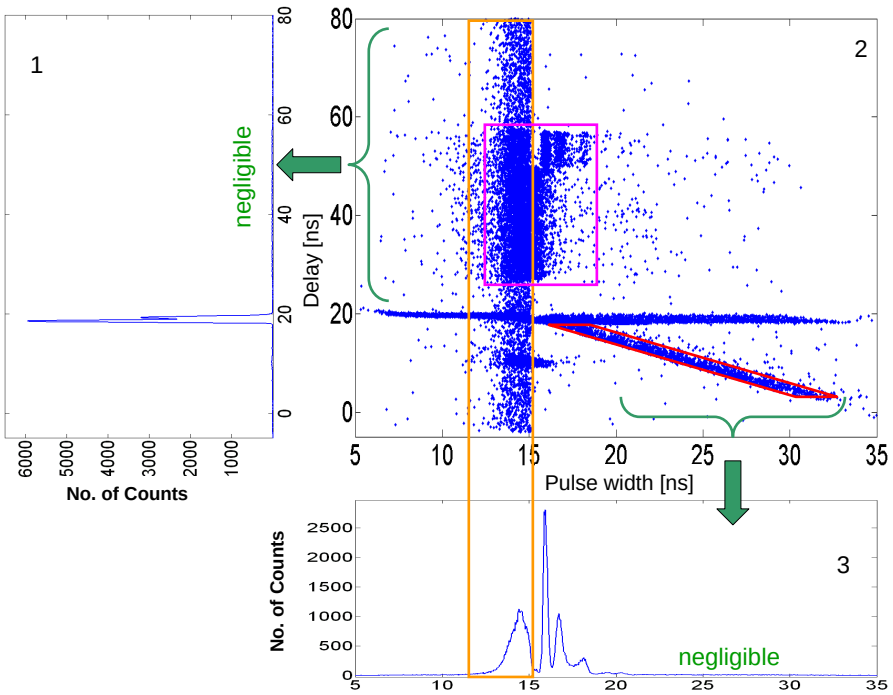

Figure 4.20: (1) delay spectrum, (2)Delay vs. Pulse width spectrum, (3) Pulse width spectrum.

by the long rectangle, indicating the region of single photon detection where pulses of same width are randomly distributed. In a similar way, the smaller square shows uncorrelated events in the region of 1, 2, 3 and 4 photons detected. Although this distribution cannot be explained as yet, it is of negligible influence despite the apparent deep coloring in the scatter plot. Another region has been highlighted, shown as a parallelogram. Also this clustering of events cannot be explained.

If one focuses on the most populated region, as shown in Figure 4.21. The selection of the regions corresponding to 1, 2, 3 and 4 photoelectrons according to the spectra in (3), permits to extract the respective delay distributions shown in blue, green, red and pink respectively.

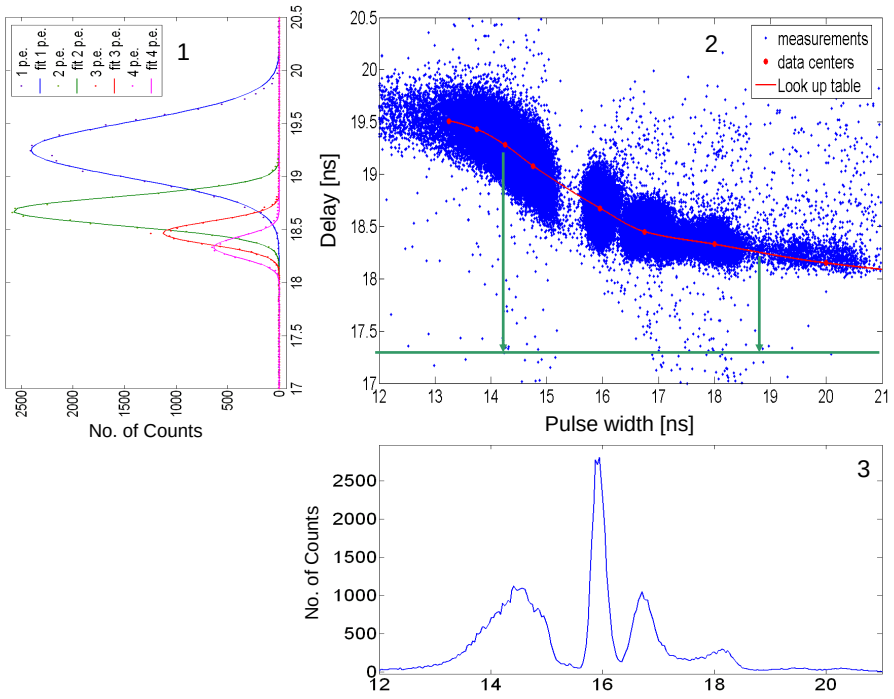

Figure 4.21: (1) delay spectrum, (2)delay vs. pulse width spectrum, (3) pulse width spectrum, with a focus on the most populated area. The center (red points) of the data clouds (blue points) are used to build the look up table (red line).

The timing precision **without time walk correction** for one detected photon is of 260 ps. It decreases to 140 ps for 2 photons detected, 123 ps for 3 photons detected and 100 ps for 4 photons detected. This Figure 4.21(2) also shows the effect of time walk as a function of the pulse width. To find an appropriate way to correct for the time walk variations, the scatter plot in this Figure is sectioned, and for each section, the center of gravity of the clustering was determined. These points are indicated in red circles and show the trend of the time walk variation as a function of

the pulse width. From this sequence of points, the look up table is derived and is represented as a red line.

The time walk correction is applied and the corrected spectra are presented in Figure 4.22. After the selection of 1, 2 and 3 photoelectrons a Gaussian fit is applied to the corresponding delays spectra and their parameters are extracted.

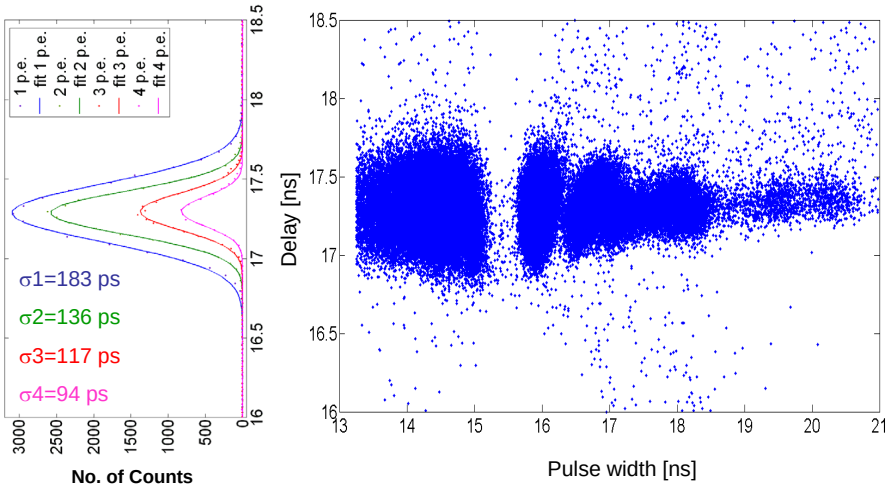

Figure 4.22: Right: delay versus Pulse width spectra after time walk correction. Left: delay distribution corresponding to 1, 2, 3 and 4 photons detected.

In Table 4.2, the peak positions are given as well as the time precision before and after time walk correction .

N_{pe}	Peak position [ns]		Time precision [ps]		
	before time walk correction	after time walk correction	before time walk correction	after time walk correction	SiPM alone
1	19.24	17.29	262	183	181
2	18.68	17.29	139	136	128
3	18.45	17.30	123	117	109

Table 4.2: Parameters of the delay histograms obtained for 1, 2, 3 and 4 photons detected. The value for the SiPM alone are also shown for comparison.

It can be seen that the time resolution benefits from the time walk correction. It is also seen that the compared values compare closely with those of the SiPM alone. This means that the contribution of the readout electronics to the time precision is negligible.

4.4.1.4 laser head 660 nm

The same series of measurements was done with the 660 nm (red) laser head. At this wavelength, the first photons are only detectable at a light intensity LI=260 instead of LI=89 for the blue laser: a larger number of photons has to be sent in order to trigger a signal in the SiPM. This shows that the PDE at 660 nm is lower than at 405 nm. The histogram of the pulse height at IL=26 is shown in Figure 4.23.

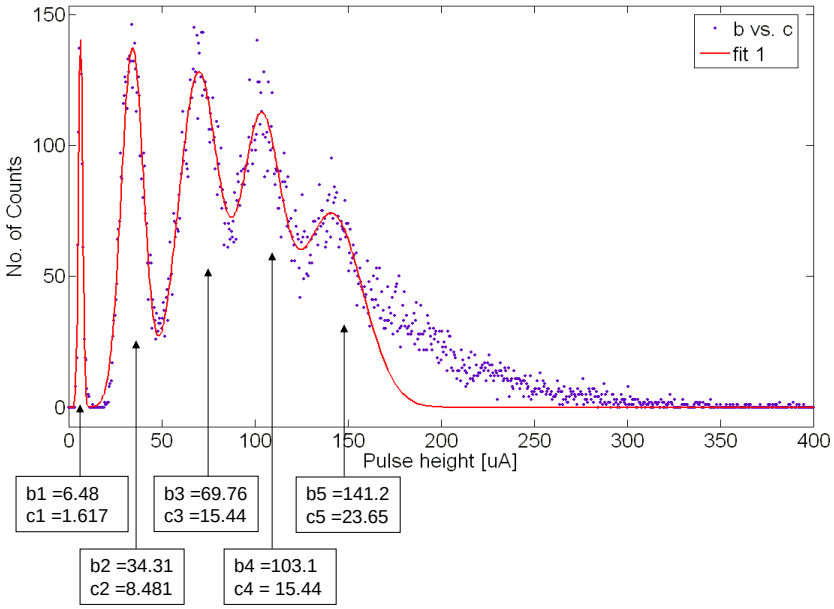

Figure 4.23: SiPM output pulse height histogram when the photodetector is exposed to 660 nm photons.

Up to 6 photons are detected. The pulse height are the same as in the measurements with the blue laser. The single photoelectron signal is 35 μA high. This is normal as the shape of the SPAD signals does not depend on the wavelength, but on the structure resistances and capacitances which have not changed.

Time resolution measurements have also been done. The left part of Figure 4.24 shows for 1, 2 and 3 photons detected the delay spectra of the analog SiPM response (top), the delay spectra of the SiPM+NINO readout without time walk correction (middle) and the delay spectra of the SiPM+NINO readout after time walk correction (bottom).

The time resolution is estimated by taking the FWHM of each spectrum. The origin of this tail is explained below.

The time resolution achieved on a single photon detection with the SiPM alone is of 600 ps FWHM. For the detection of 2 and 3 photons, it

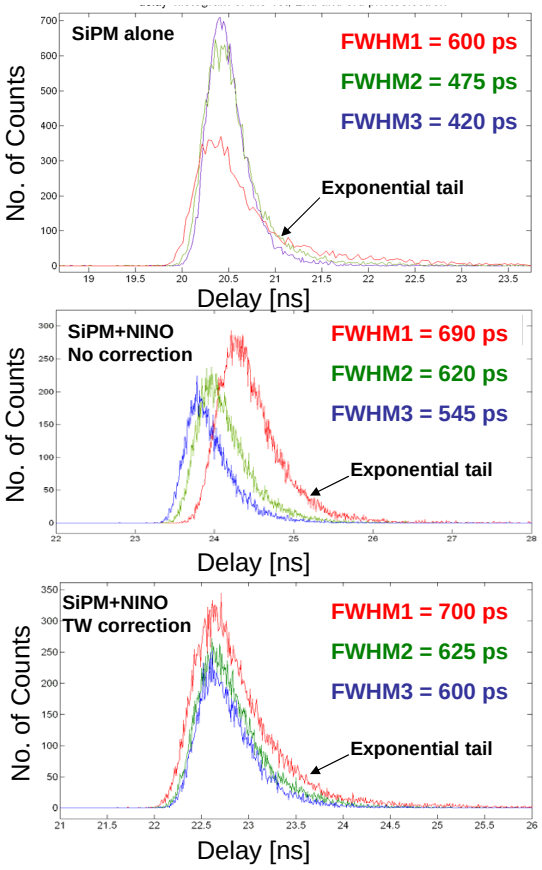

Figure 4.24: For separately 1, 2 and 3 detected photoelectrons, Top: delay spectra of the analog SiPM response, middle: delay spectra without time walk correction of the SiPM+NINO response, bottom: delay spectra corrected from time walk variation of the SiPM+NINO response.

is measured respectively at 475 ps FWHM and 420 ps FWHM. When the SiPM current signal is injected into NINO, the time resolution achieved on the NINO output pulse, after time walk correction, is of 700 ps, 625 ps and 600 ps FWHM for respectively 1, 2 and 3 photons detected.

Figure 4.25 shows a simulation of the electric field profile in the SiPM as a function of its depth, for a bias of 33 V. Two regions are distinguishable: the avalanche region from 0 to 1 μm where the electric field is the highest and the drift region from 1 μm to the end as explained in 2.4.2.3. Note that the point A of the plot is an artifact due to a mesh error in the simulations. In this region the electric field is roughly constant. The absorption of the photons $I/I_0 = e^{-\alpha x}$) is plotted, superimposed on this graphic, as a function of the silicon depth x for the 2 wavelength 405 nm and 660 nm.

At 405 nm, the absorption coefficient in silicon is $\alpha_{405} = 4.9\ 10^4 cm^{-1}$ [VirginiaSC] so that all the blue photons are absorbed in the avalanche

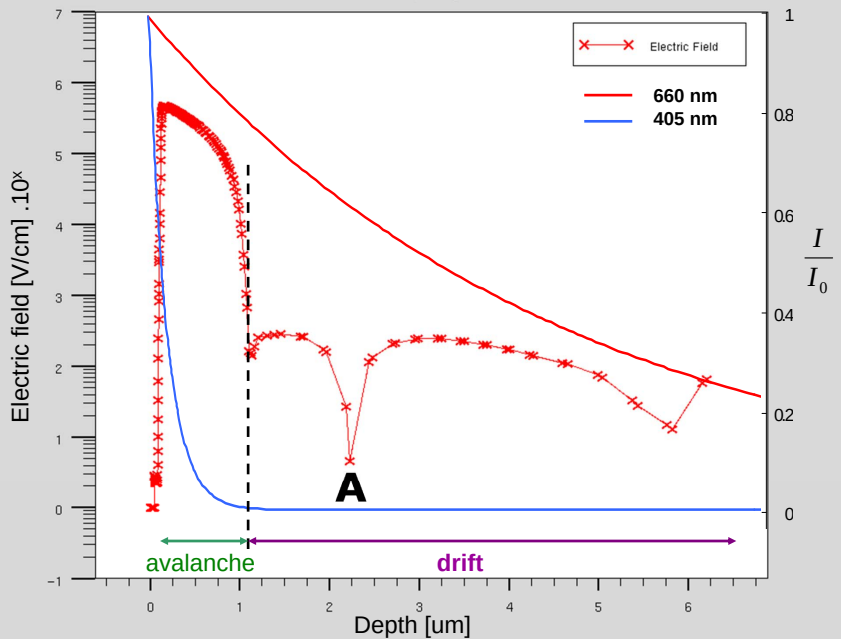

Figure 4.25: Electric field and photon absorption as a function of the SiPM depth.

region, within 1 μm. At 660 nm, the absorption coefficient in silicon is $\alpha_{660} = 2.17\ 10^3 cm^{-1}$ so that the red photons are absorbed in both the avalanche region (15 % of photons) and the drift region (60 % of photons) of the SiPM. The electron/hole pairs created in the drift region will not immediately trigger an avalanche. They first have to drift toward the avalanche region with a speed v depending on the mobility of electrons in silicon $\mu_{Si} = 1400\ cm^2 V^{-1} s^{-1}$ and on the electric field $E \approx 3\ 10^2\ V.cm^{-1}$.

$$v = \mu \times E = 420000\ cm.s^{-1} = 4.2\ \mu m.ns^{-1} \tag{4.9}$$

In other words the electrons generated in the drift region would have to drift for 240 ps per μm before they can trigger an avalanche. This additional drift time and the variations of this time depending on the depth of interaction of the photons lead to a broadening of the delay distribution and to a tail superimposed on the Gaussian delay spectra. The shape of this tail comes from the exponential nature of the absorption which leads to an exponential distribution of the drift time.

4.4.1.5 Measurements summary

As a first conclusion the timing results obtained with or without NINO, at 405 nm or 660 nm are shown in Figure 4.26.

The results obtained at 405 nm are those that should be compared with

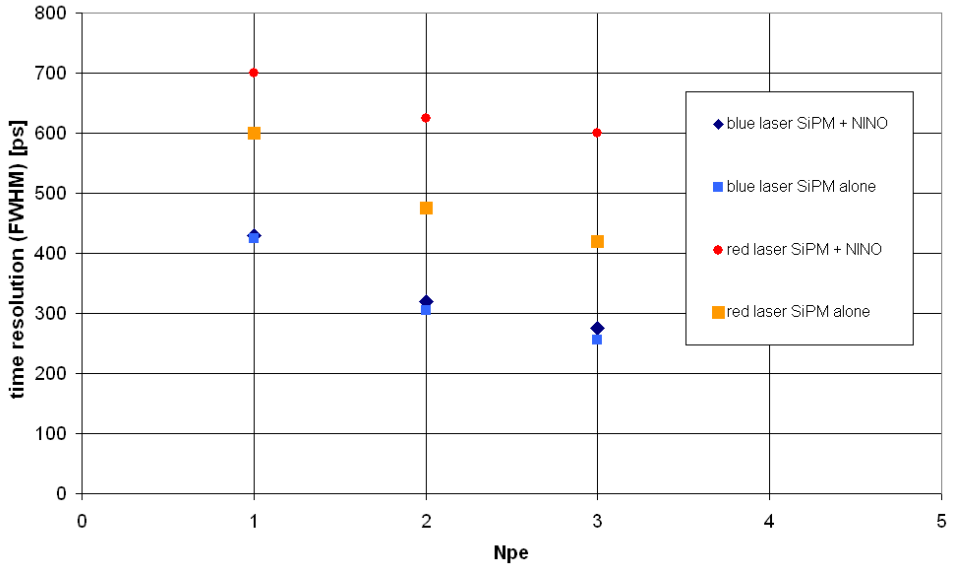

Figure 4.26: Time precision as a function of the number of photoelectrons.

LSO light (emitted at 420 nm) which is the most interesting case for the study. One can also observe that in the case of 405 nm photons, the use of NINO does not degrade the timing measurements: the detection of a single photoelectron can be achieved with the same time resolution of 420 ps FWHM whether using the SiPM alone or using the SiPM+NINO readout. In the case of 660 nm photons, the detection of a single photoelectron can be achieved with a time resolution of 600 ps FWHM using the SiPM alone and of 700 ps using the SiPM+NINO readout. This higher value in the case of SiPM+NINO readout could be explained by a non optimum time walk correction because of the tails in the delay spectra.

4.4.2 Hamamatsu $1 \times 1\ mm^2$

The same I(V) measurements as with the STM device were done with the Hamamatsu SiPM, showing a breakdown voltage of 69 V which is significantly larger than that of the STM samples. The Hamamatsu SiPM samples are biased at 69.5 V (0.5V overvoltage). A further increase of the bias would make the device unstable. The Forward I(V) measurement shows a quenching resistance of 179 kΩ

4.4.2.1 Analog measurements

The same setup and the same test methods were applied for the Hamamatsu SiPM sample of $1 \times 1\ mm^2$. As seen in Figure 4.27, the signal characteristics are largely different from those of the STM samples: the

rise time is $\approx 2.5\ ns$ and the fall time is $\approx 200\ ns$. Similarly, the signal is shaped by the SiPM terminal capacitance whose value is $C_T = 35\ pF$.

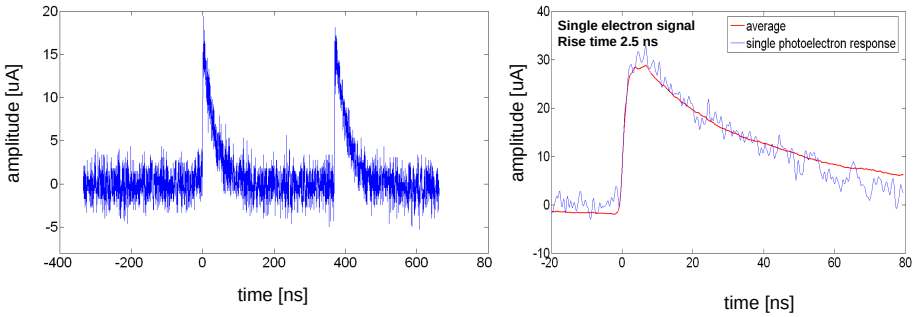

Figure 4.27: Screen shot of the Hamamatsu SiPM output signal in dark conditions. Left: two single photoelectron pulses, right: zoom on the single electron pulse (blue) and average of 1000 pulses (red).

The thermal noise frequency at the level of single photoelectrons is measured to be 1MHz, which is about the same as for the STM structures.

The histogram of the pulse height is produced with its corresponding 5-Gaussian fit, as shown in Figure 4.28.

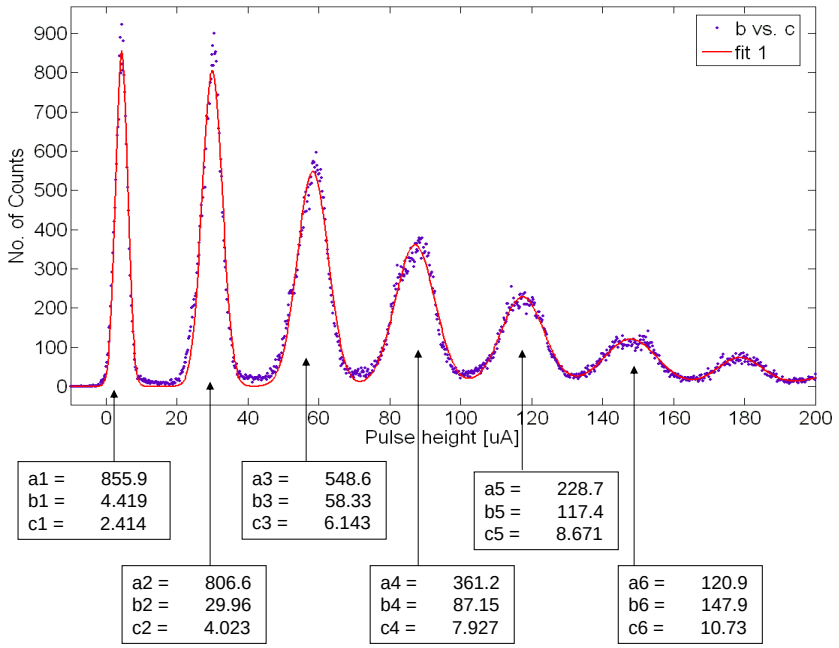

Figure 4.28: Hamamatsu SiPM output pulse height histogram. The parameters of the 7 Gaussian fit applied are shown for each peak.

The pulse height from single photoelectron response is 30 μA. It is linear with the number of photons detected.

Owing to the different signal shape, the threshold for the timing measurement was fixed over the noise, resulting in better timing precision.

This threshold is set at $6\mu A$ (1/5 of SPAD signal). This method will induce time walk variation, but the technique to overcome this problem is now well known.

Figure 4.29 shows the scatter plot of the delay versus pulse height (right). Events corresponding to 1, 2, 3, 4 and 5 photoelectrons are selected in order to determine the corresponding timing performance, as plotted on the left part of Figure 4.29.

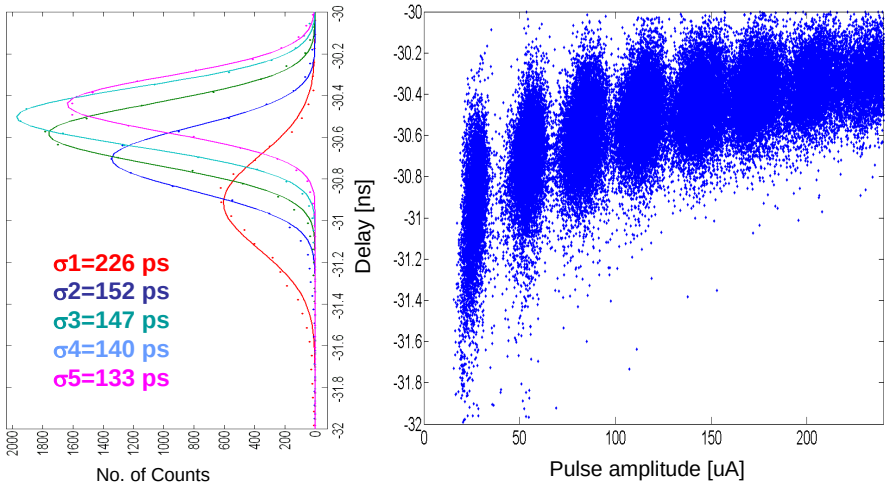

Figure 4.29: Left: delay spectrum of 1, 2, 3, 4, and 5 photoelectrons. Right: Delay vs. Pulse height scatter plot.

From the center of the delays and of the pulse heights, a look up table is built, and the data are corrected for time walk, as shown in Figure 4.30. The top part shows the uncorrected data, with the look up table superimposed in red. The bottom part of this Figure shows the corrected data

Once the time walk correction is applied, the new delay distributions corresponding to 1, 2, 3, 4 and 5 photoelectrons are fitted with Gaussians in order to derive the time precision. This is shown in Figure 4.31.

Here again, the time walk correction doesn't affect too much the time precision, except for the single photoelectron. The timing precision for the detection of a single photoelectron is 215 ps. It decreases to 151 ps rms, 145 ps rms, 137 ps rms and 132 ps rms for 2, 3, 4 and 5 photons detected respectively.

Readout with NINO

The current signal is now directly driving the NINO input (jumper

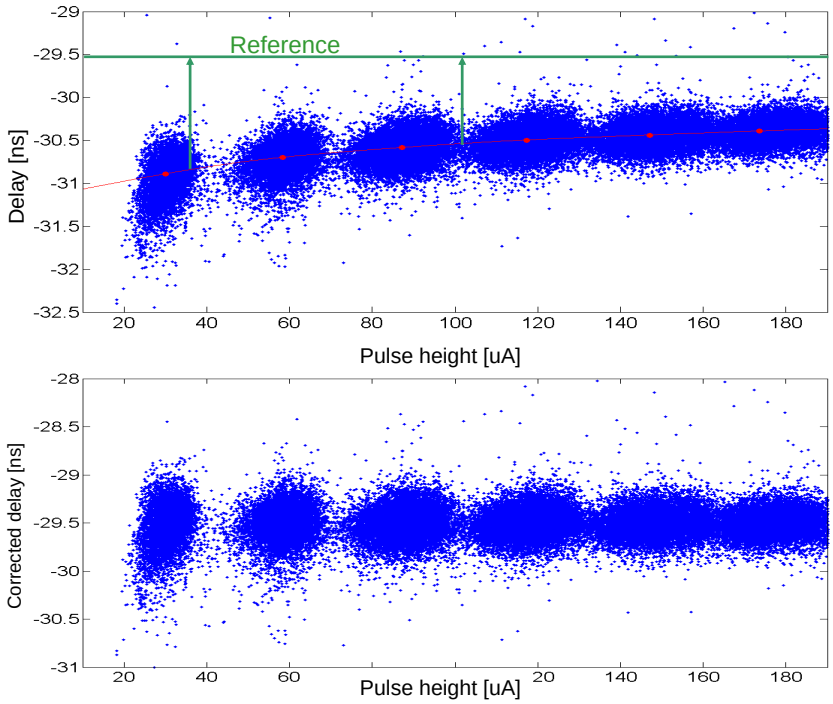

Figure 4.30: Top: time walk correction applied on the Delay versus Pulse height spectra. The center (red points) of the data clouds (blue points) are used to build the look up table (red line). Bottom: Spectra obtained after time walk correction.

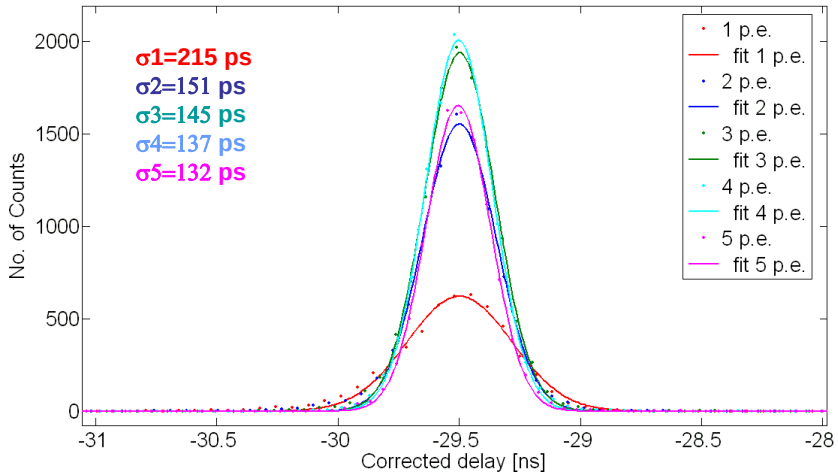

Figure 4.31: Fit of the delay histograms obtained after time walk correction.

on position 2). The Figure 4.32 shows the pulse width histogram measured at the output of NINO for the single electron response in red (dark conditions) and for the signal obtained at low laser light intensity in blue.

The data shown in Figure 4.32 exhibit an inconsistency in scale which is as yet to be explained. There is an apparent discrepancy between the

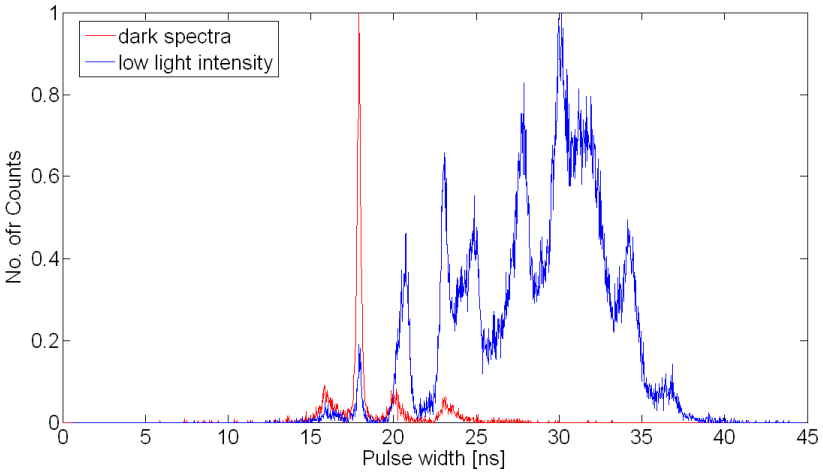

Figure 4.32: NINO output pulse width histogram in dark condition (red) and under low laser light intensity (blue).

SiPM's pulse length which is of the order of 200 ns time over threshold, and the measured pulse width clustering between 15 ns and 40 ns for up to 5 photons detected. This could be explained by a non optimal coupling between the SiPM and the NINO.

4.4.3 STM $3.5 \times 3.5\ mm^2$

The same setup is now used to perform measurements on $3.5 \times 3.5\ mm^2$ structures furnished by STM. Three different samples called A, D and E were tested without being connected to NINO, and the results are presented in this chapter. The sample A has a substrate of type P, where the cathode connection is on top of the chip and the anode connection on the backside of the sample. The quenching resistance is derived to be 1.1 $M\Omega$ and the breakdown voltage measured at 27 V. The samples D and E have a substrate of type N, where the cathode and anode connection are on top of the chip. The quenching resistances for these are respectively 650 $k\Omega$ and 250 $k\Omega$. The breakdown voltages are 28 V and 29 V, respectively.

The left part of Figure 4.33 shows the output current signal of the 3 different SiPM structures in dark conditions, biased at about 10% overvoltage.

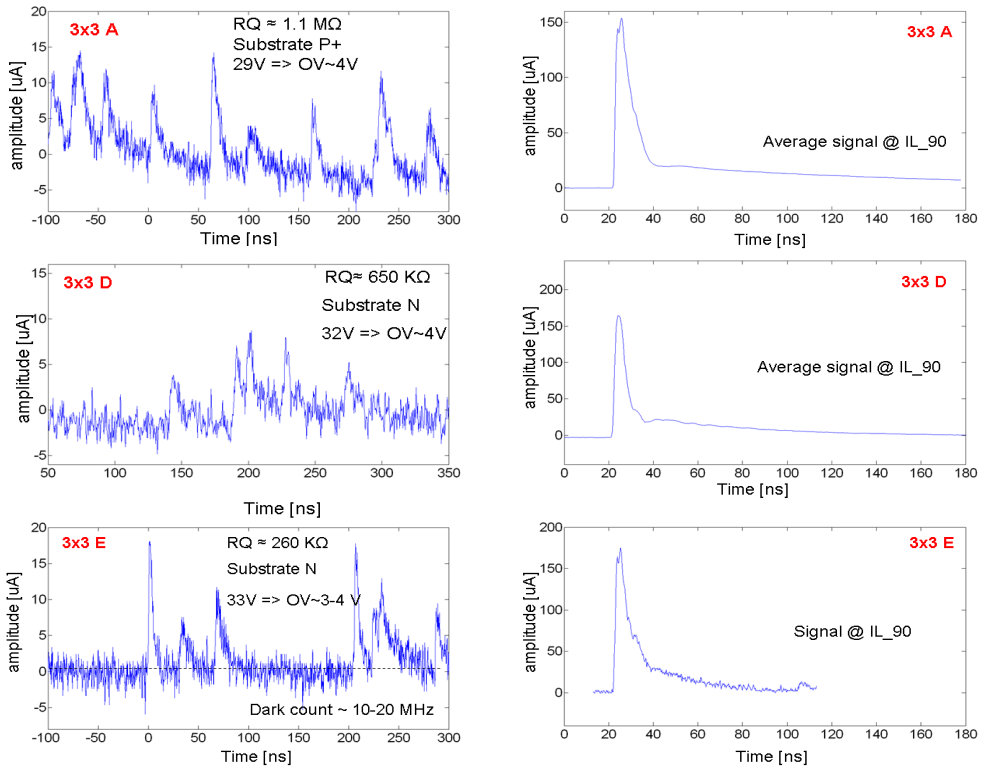

Figure 4.33: Left column: scope shot of the SiPM output current in dark conditions. right column: scope shot of the SiPM output current under low light intensity. To row: SiPM module A, middle row: SiPM module D, bottom row: SiPM module E.

All 3 samples have in common that the thermal noise rate is substantially higher, $\geq 10\ MHz$, than with the smaller structures tested before.

This effect is attributed to the higher number of SPADs in parallel in these structures. This makes a single photoelectron signal measurement very difficult.

A lower bias would decrease the thermal noise rate, but would also reduce the single photoelectron height, making it difficult to distinguish from the noise. Therefore no timing studies were made.

Nonetheless one observes a maximum amplitude of 6 μA for the single photoelectron, which is much lower than what was seen with the $1\times1\ mm^2$ samples. This is explained by the high terminal capacitance of the larger size SiPM. According to Figure 4.2, this capacitance amounts to $\geq 200\ pF$.

If the light intensity is increased so that the SiPM detects between 5 and 10 photons, a higher signal of $\approx 150\ \mu A$ can be observed, as shown on the right part of Figure 4.33. The falling edge of the signal is composed of 2 decreasing time constants: a fast one of $\approx 10\ ns$ and a slow one of $\geq 100\ ns$. The second time constant is due to the recharging of the diode capacitance through the quenching resistance [Corsi 07].

4.4.4 Hamamatsu $3 \times 3\ mm^2$

STM structures are now replaced with Hamamatsu SiPMs of $3\times3\ mm^2$ on the test board. From the I(V) measurements, the breakdown voltage was measured at 69.5V and the quenching resistance at 268 kΩ. The devices were biased at 70.5 V (1V overvoltage recommended by Hamamatsu) to find a good compromise between pulse height and stability. The device is placed in the black box and the thermal noise is observed under dark conditions. A screen shot of the output signal is shown in Figure 4.34, together with an average of 1000 of these signals (red smooth line).

As with the STM measurements, the amplitude of the pulse, is only of 6 μA, which is 5 times smaller than for the $1 \times 1\ mm^2$ samples. This is due to the high terminal capacitance of the SiPM. Nevertheless, the thermal noise is at an acceptable rate of 5 MHz, thus enabling timing measurements. The measurement of the delay versus the pulse height is shown in Figure 4.35 under low laser light intensity. The sample shows SPAD signals at a light intensity $IL \geq 85$, meaning that the PDE is higher than that of all the other samples. For STM structures, the 1st photons were detected at slightly higher light intensity IL=89.

One can see in spectra (2) and (1) that the noise region lies between -20 ns and 20 ns. This is due to the small amplitude of the pulses, as the detection level has to be set very close above the noise level in order to

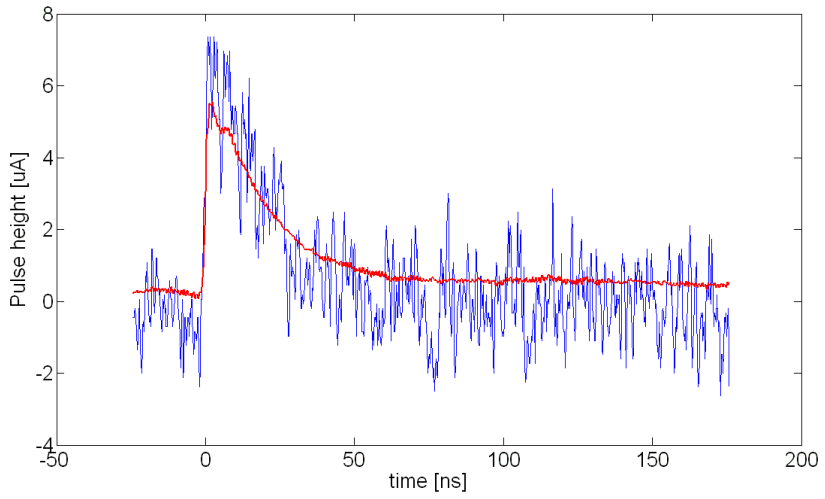

Figure 4.34: Scope shot of the Hamamatsu SiPM output signal in dark conditions, blue: single electron pulse, red: average of 1000 pulses.

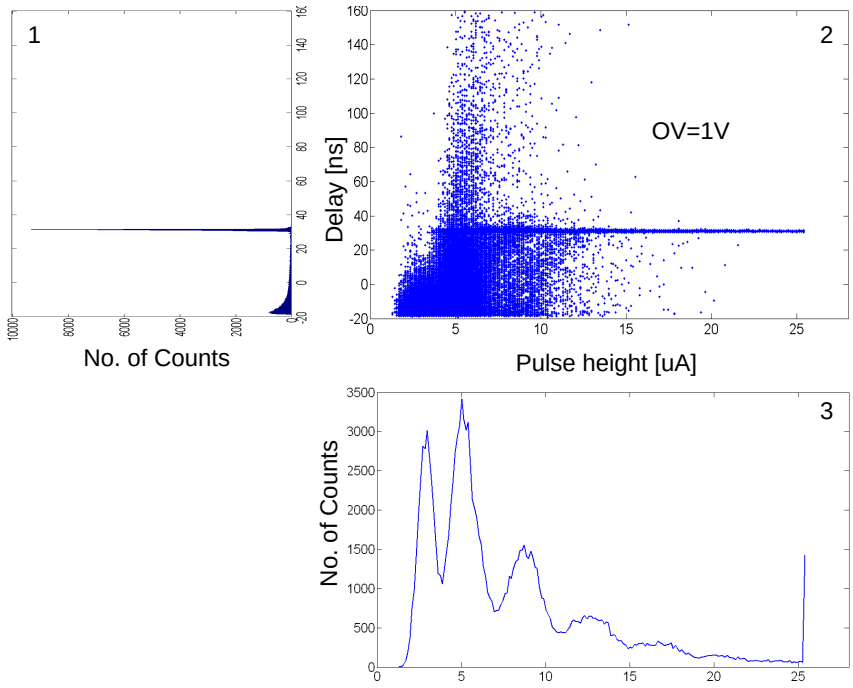

Figure 4.35: (1) delay spectrum, (2)Delay vs. Pulse height spectrum, (3) Pulse height spectrum.

detect the single photons events.

As for other measurements the thermal noise shows uncorrelated events in the range of single photoelectron (between 4 μA and 7 μA). A zoom on the most populated region, between 28 ns and 34 ns, is shown in Figure 4.36.

By selecting only the single photoelectron area from (3), the corresponding delay distribution is obtained and shown on (1). This delay

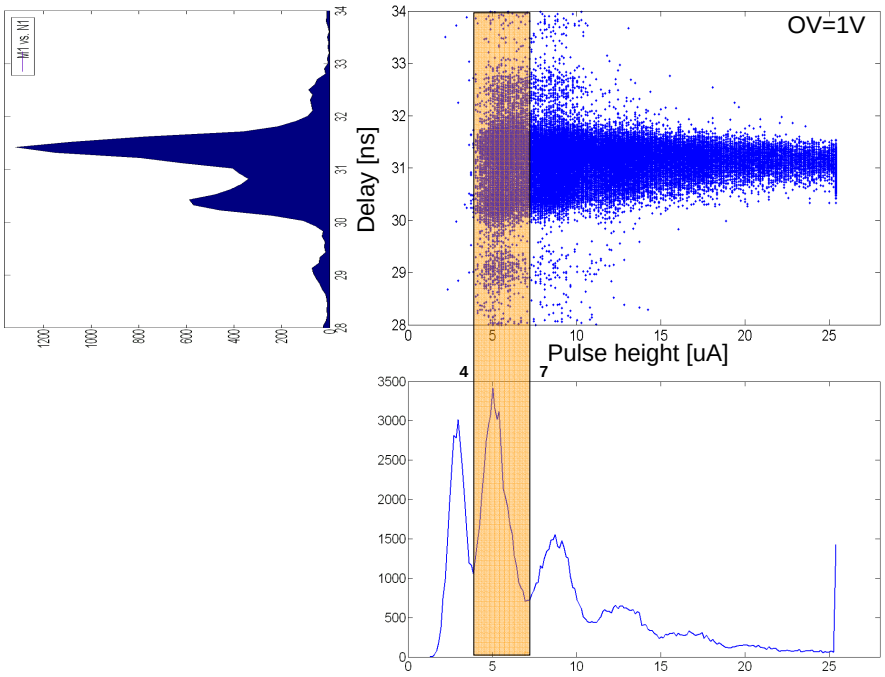

Figure 4.36: (1) delay spectrum of the single photoelectron events, (2)Delay vs. Pulse height spectrum, (3) Pulse height spectrum, with a focus on the most populated area. orange square: single photoelectron region.

distribution presents 2 main peaks, meaning that pulses of same height are triggered at 2 delays of 30.5 ns and 31.5 ns. This effect prevents from concluding about the single photoelectron time precision. It might be due to the low threshold used in the measurements.

In order to increase the single photoelectron pulse height, the overvoltage is set to 2 V. This is the limit at which the SiPM starts to become unstable. Figure 4.37 shows the delay versus pulse height scatter plot, which focused on the laser induced events, i.e. between 28 ns and 33 ns. The projection on the x-axis shown in (3) derives the pulse height spectrum. The selection of events corresponding to 1 up to 6 photoelectrons derives the corresponding delay spectra.

Here again, the delay histogram of single photoelectron events is not Gaussian, showing an unexplained shoulder. It suggests that this effect is not fully understood and requires a deeper analog study of those structures prior to connect the SiPM to the NINO chip.

In contrast, the delay distribution for 2 and more photoelectrons is Gaussian so that the time precision can be extracted by the fit. It is found to be 312 ps rms for the detection of 2 photoelectrons, decreases to about 250 ps for 3 photoelectrons, 206 ps for 4 photoelectrons and 175 ps for 5 photoelectrons. These results are much higher than the ones

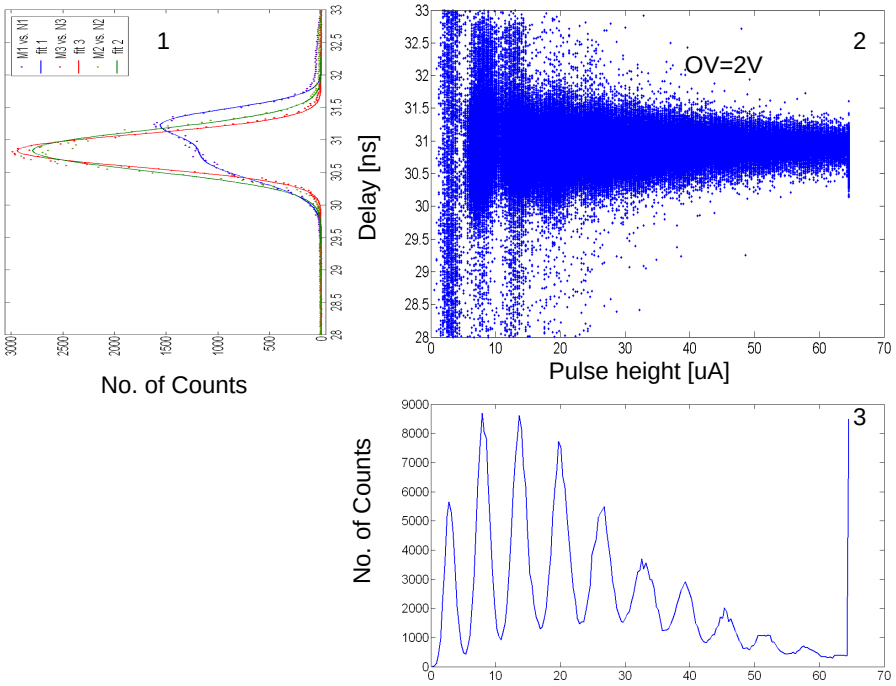

Figure 4.37: (1) delay spectrum, (2)Delay vs. Pulse height spectrum, (3) Pulse height spectrum, with a focus on the most populated area.

obtained with the $1 \times 1\ mm^2$ SiPMs. Again, this can be explained by the influence of the high terminal capacitance which decreases the rise time of the current pulse.

4.5 Conclusion and Outlook

This work has shown that the SiPM output current is shaped by its terminal capacitance when placed in parallel with the scope load resistance or with the input resistance of an amplifier. The value of this capacitance is given at 35 pF and 320 pF for Hamamatsu SiPM of respectively $1 \times 1mm^2$ and $3 \times 3mm^2$, which is high compared to the typical capacitance of the APDs of 10 pF. This terminal capacitance is not known for STM SiPMs.

This shaping is altering the timing properties of the photodetector and explains the differences in pulse height and pulse shape between the output current signals of $1 \times 1mm^2$ and $3 \times 3mm^2$ structures, regardless of the manufacturer.

Knowing the output current pulse shape of a SPAD, the SiPM output current signal was calculated for the case of photons emitted by a LSO scintillator and following the conversion of a 511 keV γ-ray. The equation of this signal has not been published before to my knowledge and permits

to visually explain the results obtained in experiments where SiPM are coupled to LSO such as in [Spanoudaki 07, Kim 09].

A test board was developed to perform measurements with SiPM alone or with SiPM read out by NINO. Using SiPM alone, these measurements have shown that with 405 nm laser single photon, a time resolution of 180 ps can be achieved for STM $1 \times 1mm^2$ SiPM alone and 215 ps for the $1 \times 1\ mm^2$ structures of Hamamatsu. Both devices show a thermal noise rate of the order of 1 MHz.

When connected to NINO, only the STM $1 \times 1mm^2$ structures give a consistent result on the time resolution, being 183 ps, whereas the equivalent $1 \times 1mm^2$ structure from Hamamatsu give non conclusive results. At least, in the case of the STM $1 \times 1mm^2$ structures, it can be said that the NINO has negligible influence on the time precision.

This suggests that there is a high potential for SiPMs in experiments where single photon detection is required with good time precision such as Cerenkov photon detection for high energy physics purposes (CEDAR project from NA62 experiment) or fluorescence spectroscopy for biological purposes (IRPICS project [Lapington 08]). In this last example, photons of different wavelength, from blue to red, are to be detected. Measurements performed with a red laser on a detector composed of a SiPM from STM read out by NINO have shown a time resolution of 328 ps rms for a single photon. This lower resolution is due to lower absorption of the red wavelength in silicon. This measurement shows the maximum limit in time resolution for fluorescence spectroscopy based on SiPM photodetectors.

The detection of a higher number n of photons shows a time resolution improving with $1/\sqrt{n}$, suggesting even better performance in the case of PET detection where 50 photons are detected within the first nanosecond.

For PET detection, where a total of 2000 photons from a LSO scintillator are to be detected, the SiPM should consist of at least 4000 cells to avoid the saturation effect. Moreover, SiPMs have to be coupled to LSO crystals which are typically $2 \times 2 \times 10\ mm^3$ or $3 \times 3 \times 10\ mm^3$. Hence, SiPM of larger size (typically $3 \times 3\ mm^2$) comprising a higher number of cells are chosen to asses the performance in PET.

These devices have higher thermal noise, of the order of 10 MHz for STM samples and about 5 MHz for Hamamatsu samples. They also have a higher terminal capacitance (320 pF for Hamamatsu cells), reducing the SPAD pulse height.

These 2 features prevent the characterization of the single photon

events for larger size STM SiPMs and hence the measurement of the time resolution at the single photoelectron level. In the case of larger Hamamatsu cells, as the thermal noise is lower, the single photon detection signal can be better separated from the noise, however still without the possibility to derive the corresponding time precision.

For PET, larger size SiPM have to be used but the device capacitance together with its high thermal noise make the detection of the first photons difficult.

A matrix of several $1 \times 1\ mm^2$ SiPM can be formed to cover the same surface as the scintillator. Read out independently, they will share the number of photons emitted by the LSO. In the case of $2 \times 2 \times 10\ mm^3$ LSO crystals, 4 $1 \times 1\ mm^2$ SiPM are required to cover the scintillator surface. Each of those will detect about 500 photons, and 15 of these during the first nanosecond. This way, even if the total number of detected photons is decreased, a time precision better than 100 ps should be obtained. The problem here is that no optimized packaging for $1 \times 1\ mm^2$ SiPM does exist to put them together without loosing space and then efficiency in the detection.

Chapter 5

Characterization of MicroChannel Plates made of Hydrogenated amorphous silicon: a-Si:H MCP

Today, MicroChannel Plates represent the fastest single photon detector available. They are made of 3 μm to 10 μm diameter micropores as shown in section 2.4.1.3, and have a shaping time of the induced current in the order of 100 ps. They are particularly useful for TOF experiments like TOF-PET, HEP experiments or time resolved spectroscopy (IRPICS project [Lapington 08]).

MCPs are usually built of lead glass covered with a semiconducting layer and an activation layer made of low work function material to get a high secondary emission production.

The main drawback of MCPs, as presented in 2.4.1.3, is the long channel recharging time after an avalanche has occurred, making the channel non usable for 1 ms. This recharging time is mainly due to high equivalent resistance per channel due to the material used.

Therefore, instead of insulating material one should use a resistive material for the MCP bulk because a lower resistivity per channel leads to shorter recharging time. To do so, MCPs with bulk material made of silicon were recently developed and characterized [Siegmund 04]. However, with the resistivity of the bulk being too low (in the order of 10^4 $\Omega.cm$) one requires an extra oxidation layer to cover the pores and the deposition of a semiconducting layer to avoid excessive leakage current, as in standard MCPs.

To overcome the limitation of existing MCPs, a new concept was proposed by CERN and the PV-lab [PV-lab] in the Institute of MicroTechnology of Neuchatel [IMT]. The idea is to use hydrogenated amorphous silicon (a-Si:H) as MCP bulk material, in which pores are etched by Deep Reactive Ion Etching (DRIE), a micromachining technique used for crystalline silicon (c-Si) microsystems. The advantage of this material is its higher resistivity compared to c-Si, being in the order of $10^{10} - 10^{12}\ \Omega.cm$

Moreover the a-Si:H is processed at low temperature and can be deposited directly on top of Application Specific Integrated Circuit (ASIC). This so-called vertical integration, shown in Figure 5.1 has the advantages of hybrid detectors without using the expensive bump bonding technology. This technique was first developed for the detection of photons in imaging devices, and then studied for the detection of particles in a collaboration of CERN with the IMT, it is called Thin Film on ASIC (TFA) technology and has been widely described in [Despeisse 06, Wyrsch 08].

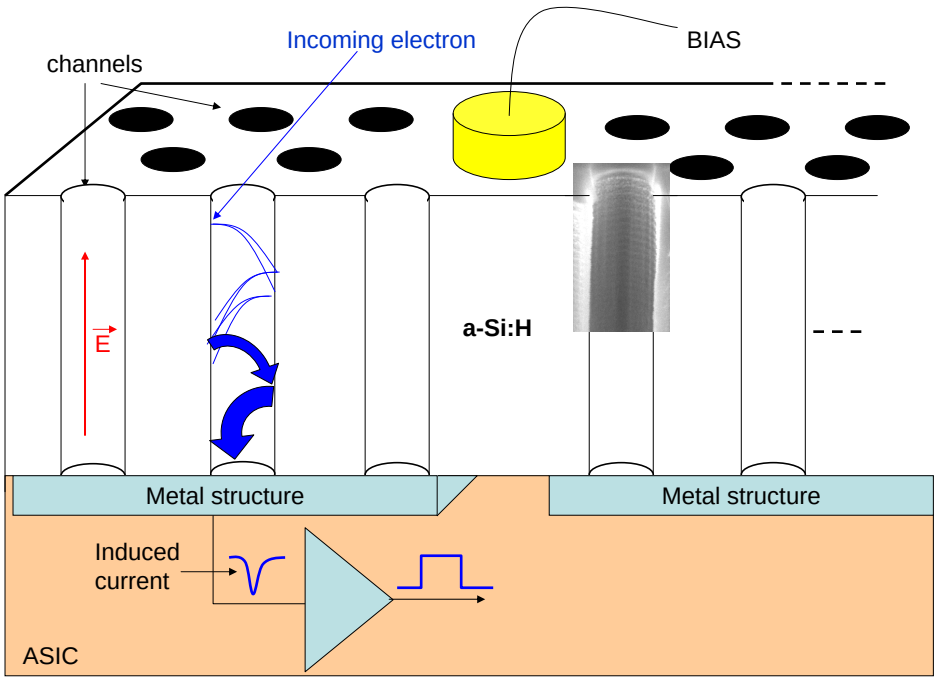

Figure 5.1: Principle of a-Si:H MCP deposited on top of ASIC.

The technological advantage of TFA technology together with the superior timing characteristics of MCP offers a high potential for a large range of experiments, including imaging and particle detection.

This chapter aims to describe the technology used to build the first a-Si:H MCPs, before to show the first results of sample characterization and conclude about the viability and improvements for such devices.

5.1 Hydrogenated amorphous silicon: a-Si:H

Hydrogenated amorphous silicon (a-Si:H) is a disordered semiconductor which still holds a short or medium range order for an atom and its nearest neighbors. Its electronic and optoelectronic properties are governed by the large defects density present in its atomic structure. In pure amorphous silicon, the typical defect density is up to $10^{19} cm^{-3}$ and prevents the use of this material in semiconducting devices. The main defects are dangling bonds resulting from broken Si-Si bonds. When amorphous silicon is deposited with hydrogen, the hydrogene passivates most of the defects so that hydrogenated amorphous silicon of good quality has a typical defect density of 2 10^{15} cm^{-3}. The hydrogen content greatly influences the structure and consequently the electronic and the optoelectronic properties. Figure 5.2 shows a comparison of the atomic structure of crystalline silicon (c-Si) and a-Si:H.

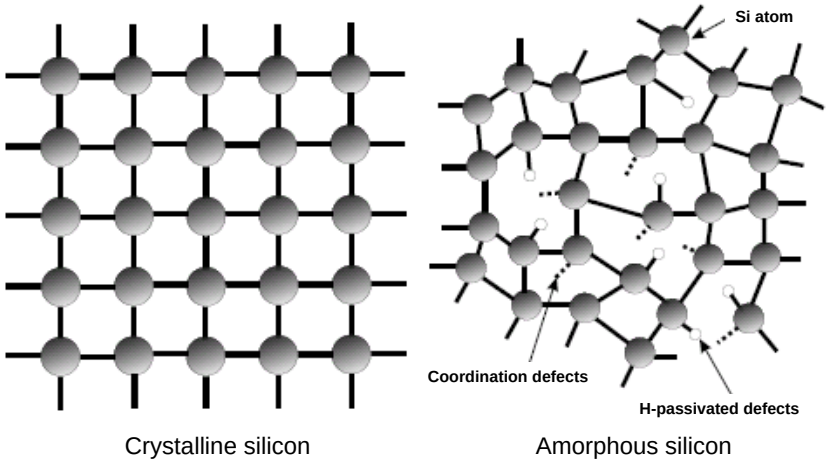

Figure 5.2: Comparison of atomic structure for c-Si and a-Si:H.

In a-Si:H, covalent bonds between the silicon atoms are similar to the bonds in crystalline silicon. The silicon atoms have on average the same number of neighbors and the same bond lengths and bond angles [Street 91].

There is a correspondence between the atomic structure and the electronic properties of a-Si:H: The disorder represented by fluctuations in atomic configuration causes fluctuations in the potential acting on an electron. As a result, the energies of the electronic states are perturbed and the band broadens [Sark 02]. In this situation, the sharp features prevalent in crystalline density of states become smeared and form band tails which extend into the forbidden gap. For this reason the sharply

defined band edges of the valence and conduction bands are smoothed in amorphous silicon. Other states in the mid-gap are due to the defects which are not saturated by hydrogen. Regardless of the structural disorder in a-Si:H, general similarities of the overall electronic properties between amorphous and crystalline silicon exist. This is caused by the similarity of the short-range atomic configuration and bonding structure in the two types of material. Table 5.1 shows the different electronic properties of crystalline and amorphous silicon.

Table 5.1: a-Si:H electronic properties

Properties		c-Si	a-Si:H
Hydrogen content [%]	C_H	0	10-20
Band gap @ 300K [eV]	E_G	1.12	1.7-1.8
Pair creation energy [eV]	E_{e-h}	3.6	4-6
Electron mobility$[cm^2.s^{-1}.V^{-1}]$	μ_e	1450	10-20
Hole mobility$[cm^2.s^{-1}.V^{-1}]$	μ_h	450	3-10
Resistivity$[\Omega.cm]$ (intrinsic)		10^5	$10^{10} - 10^{12}$

5.1.1 metastability

An important property of a-Si:H is its metastability. It means that its structure is not fixed once deposited. It has been discovered in the Staebler and Wronsky report [Staebler 77] in 1977 that prolonged exposure to light could induce large degradation of conductivity in a-Si:H. The changes are reversible through thermal annealing of samples. This is due to a complex process in the inner structure of the material which is not discussed here. The most important is that even if the detector is damaged from photons or from high radiation level, it can be "restructured" with annealing. This is not the case for crystalline silicon detectors, therefore a detector made with a-Si:H can recover its initial performance if damaged by photons or by radiations.

5.1.2 deposition

The deposition of a-Si:H is done at the IMT of Neuchatel. The method is basically a special form of Chemical Vapor Deposition (CVD) known as Very High Frequency Plasma Enhanced Chemical Vapor Deposition (VHF PECVD). Effectively, silane gas (SiH_4) is excited by a plasma at

70 MHz radio-frequency, which causes silane molecules to dissociate. Subsequently, the dissociated silicon atoms are deposited on heated substrates and form a layer. Most research and industrial reactor systems consist of two parallel electrodes in a stainless steel chamber [Sark 02]. Because it is relatively easy to deposit a-Si:H uniformly over large areas, the original parallel plate geometry with RF excitation is commonly used in industry and has not changed much over the past 2-3 decades. Material and device optimization is mostly done empirically and so-called "device quality" a-Si:H layers are made by PECVD with excellent uniformity.

The deposition process is simple and low cost. The a-Si:H can be deposited on large areas and on non flat surfaces. The challenge for MCPs is to deposit thick (80 μm) layers with low internal stress to avoid subsequent processing difficulties.

If doping elements like boron or phosphorous are introduced in the amorphous structure, p-type or n-type doping can be achieved like in crystalline silicon. It appears that the doping efficiency, which is defined as the fraction of introduced doping atoms which indeed are electrically active, is extremely low in amorphous silicon. The reason is that in crystalline silicon, the coordination number value can only be 4, but in amorphous silicon it can be between 3 and 5. Boron or phosphorous atoms can be added but their electron or hole can be trapped [Munyeme 05]. In crystalline silicon the efficiency of doping is in the order of unity, while in a-Si:H it can range from 10^{-4} to 10^{-2}. It has also been seen that doping a-Si:H drastically increases the defects density.

5.1.3 Deep Reactive Ion Etching: DRIE

DRIE is an etching process used to create deep, steep sided holes and trenches in wafers. This technique has originally been developed for micromechanical systems (MEMS) because it can fabricate 90^o walls with high aspect ratio. Therefore the DRIE technique has first been used by the SAMLAB [SAMLAB] at the IMT of Neuchatel and then transferred to the PV-LAB. It is perfectly suited to etch the MCP pores. The Figure 5.3 shows the picture of holes etched in a film of a-Si:H.

One can notice that the wall are not smooth but exhibit a wavy structure due to the DRIE process.

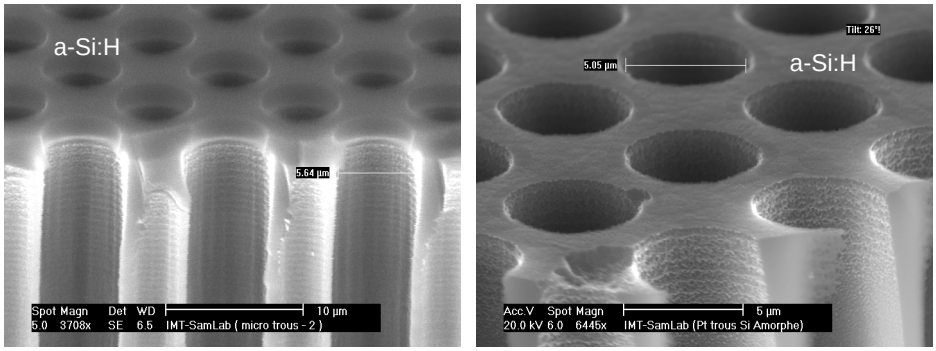

Figure 5.3: Picture of the MCP pores etched by DRIE.

5.1.4 Samples

The first prototypes of a-Si:H MCP was fabricated at the IMT of Neuchatel, the schematic of the used segmentation is shown on the left side of Figure 5.4. First, a layer of metal is deposited on a crystal silicon substrate which constitutes the anode, wires and pads for external connection (in blue). Then a 80 μm thick layer of a-Si:H is deposited on top of the anodes (orange square) followed by a thin (50 nm thick) n-doped a-Si:H layer. Then, the channels are etched via DRIE down to the anode surface.

On these samples, holes are etched through the total thickness of the a-Si:H until the anode as there is no stopping layer to indicate when the etching should stop. For this reason, many defects are present in the structures. They are due to the presence of the electrically conductive aluminum layer which gets charged as the first channels are etched through DRIE. This charging modifies the DRIE process and leads to big columnar defects which can be seen in the right part of Figure 5.4.

It should be noted that if the pores are not etched through the whole a-Si:H thickness, the impact on the induced signal is estimated be negligible in case of thin remaining layer (less than 100 nm) and large pads used (larger than 1 mm^2). An exact modeling of the induced current signal under these circumstances is very difficult and was not studied there.

Each sample is composed of 24 structures with 3 different areas. Structures 1 to 5 and 13 to 17 have a surface of 0.25 mm^2, structures 6 to 9 and 18 to 21 have a surface of 1 mm^2 and structures 10 to 12 and 22 to 24 have a surface of 4 mm^2.

Each sample is described by the diameter of the channels H in μm and by the maximum gap size separating two channels G in μm. 5 samples were developed: H2G3; H3G3; H4G3 and H5G3. These first prototypes demonstrate the technological possibility to deposit up to 80 μm of a-Si:H,

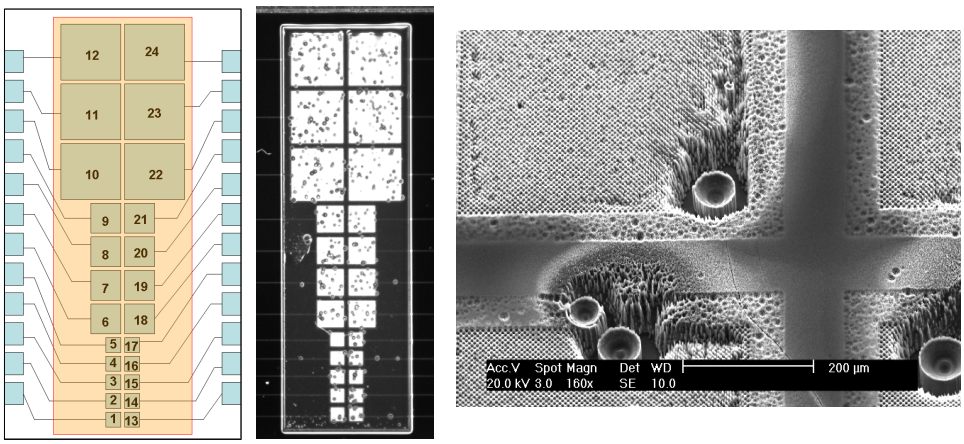

Figure 5.4: Left: layout of the structure. Middle: picture of the structure. Right: zoom on the defects with an electron microscope.

and to etch inside pores with diameters as small as 2 μm.

In order to test these structures, each sample was fixed to a glass support. Gold strips were glued on the glass and connected to the sample pads through wire bonding. A gold spot was glued on the output pads of the sample to permit wire bonding. The bias is applied through the cathode on the top of the a-Si:H layer. This mounting is shown in figure 5.5

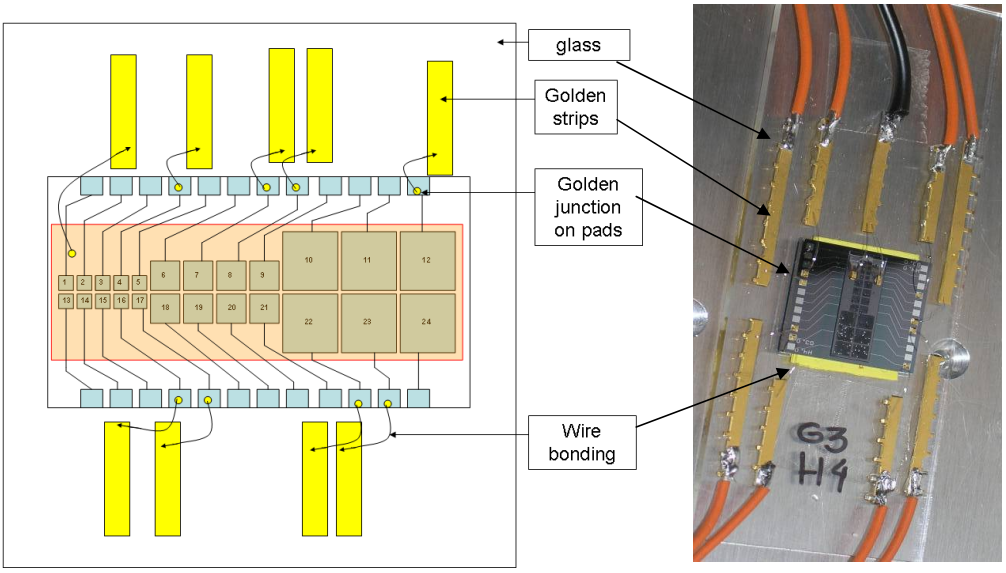

Figure 5.5: Schematic and picture of the MCP structures.

5.2 e-gun I(V) measurements

Initially, only the structures 4, 7, 8, 12, 16, 17, 22 and 23 are connected, the other structures were left floating. Cables are soldered to the gold bands to apply the bias on the structure and measure the corresponding current. A voltage from 0 to 800 V was applied and the output current of structures 4 and 8 measured with a Keithley 2410 multimeter and recorded by a Labview data acquisition program. Measurements were carried out at 10^{-6} mbars in a vacuum chamber to avoid corona effects.

An electron gun (e-gun) was set on the top of the vacuum chamber to send 10 keV electrons toward the sample. This e-gun is not fully calibrated so that the exact electron beam current and timing characteristics are not precisely known. The number of electrons sent to the sample increases with the current flowing through the beam filament. Figure 5.6 shows the MCP output current as a function of the voltage applied on the structures 4 and 8 under dark conditions and for different current values in the e-gun (i.e. different number of electrons sent).

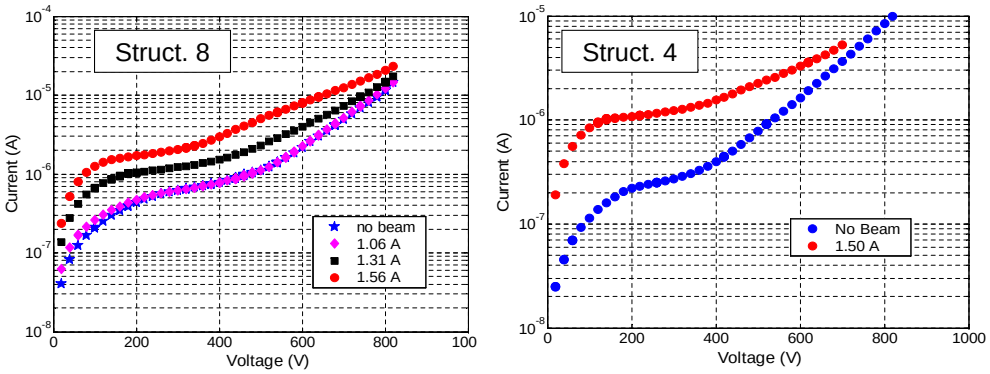

Figure 5.6: Measured current versus applied voltage on structures 8 (left) and 4 (right), for dark conditions and different levels of current sent into the electron gun.

Increasing the e-gun current, or the number of electrons sent on the sample, clearly increases the current measured on the structure. If the dark current is subtracted from the current obtained under electron beam, the current increase can be seen in Figure 5.7:

An increase of the current of some micro amperes is seen when electrons are sent on the sample. The increase of current is a linear function of the applied voltage for the structure 8, between 400 V and 800 V.

These measurements clearly demonstrate the creation of a signal in the structure caused by the 10 keV electrons from the e-gun. While this

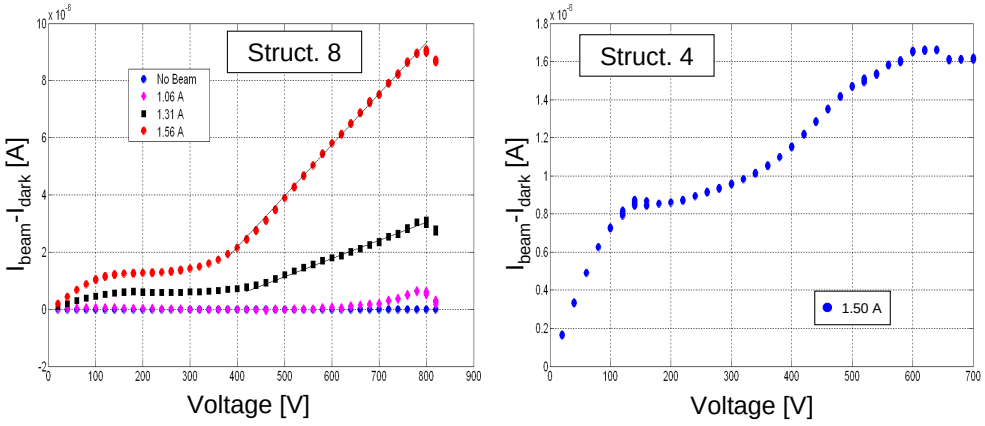

Figure 5.7: Current increase from the beam modulation.

shows a promising potential for this novel technology, a more detailed and adapted study of the structures had to be made.

5.3 Measurements done at the ESRF

Studies of the sample H4G3 were done at the European Synchrotron Radiation Facility [ESRF] in Grenoble (France), on a "Leo 1530 Gemini" Scanning Electron Microscope (SEM) from Carl ZEISS SMT. An electron microscope forms a three-dimensional image on a cathode-ray tube by moving a beam of focused electrons across an object and by reading both the electrons scattered by the object (SE1) and the secondary electrons produced by it (SE2).

The three modes of this SEM are:

- Electron-Beam-Induced Current (EBIC): gives an image of the current magnitude for a structure part hit by a scanning electron beam. The current is measured while the electron beam is scanning a selected part of the sample. It is possible to see the current value as a function of the beam position and then to see where the current increase takes place. About 20 % of the electrons incident from the SEM electron beam get backscattered from the surface and are lost.

- SE2 is the 'secondary electron' detector. This one detects secondary electrons generated by backscattered electrons as they exit the sample surface. The detector is at 45 degrees to the sample plane in order to get good contrast form surface contours. This was the mode used most to make picture of the sample surface.

- IN LENS: A detector surrounding the electron beam column detects primary electrons backscattered at an angle nearly perpendicular to the sample surface: it gives a different contrast. This is usually used at high magnifications. Since all the work was done at low magnification (×5000) compared to SEM standards, this mode was not used.

The sample is set in the vacuum chamber of the microscope, at 10^{-6} mbars, and connected to the outside instruments as shown in Figure 5.8.

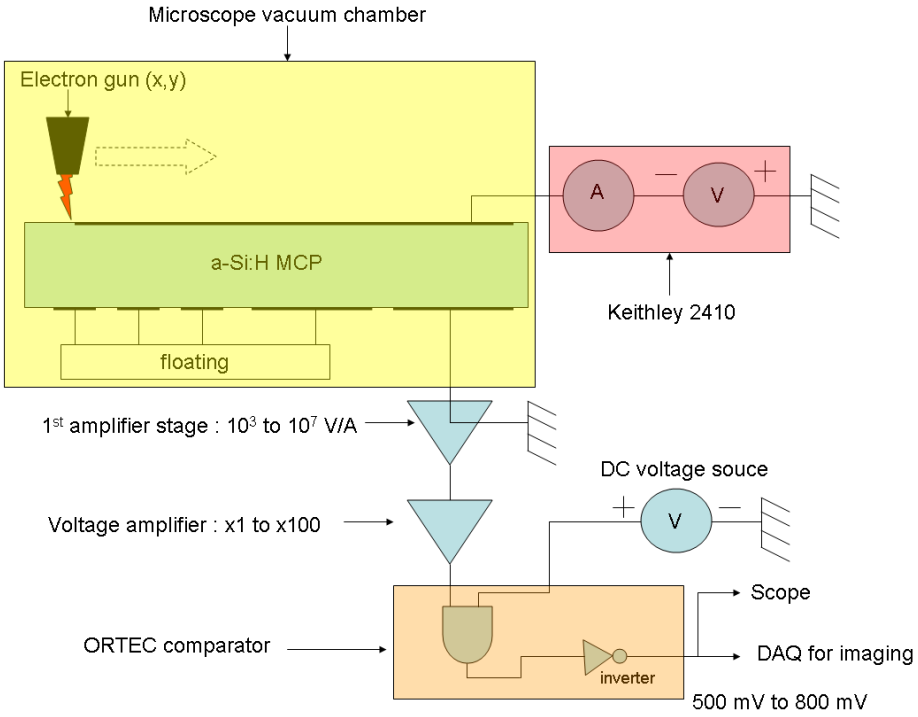

Figure 5.8: Schematic of EBIC setup.

A camera inside the chamber permits to see the sample under the electron beamer as shown in Figure 5.9.

In a first time, some pictures in SE2 mode were taken in order to have a precise description of the sample surface and the pores geometry. In a second time, tests were run in the EBIC mode to see where currents are generated in the sample when irradiated by the electron beam.

A picture of the sample in SE2 mode shows channels of 6 μm diameter instead of 4 μm and a gap of 3 μm, as shown in Figure 5.10.

Figure 5.11 shows the structures of 1 mm^2 with two different magnifications and a structure of 4 mm^2 on which damages of about 100 μm diameter are present among the 6 μm diameter channels.

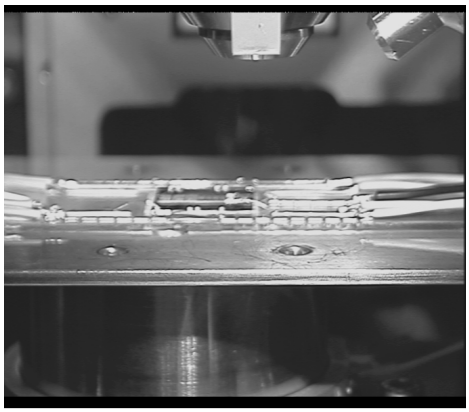

Figure 5.9: picture of the sample under the electron beamer.

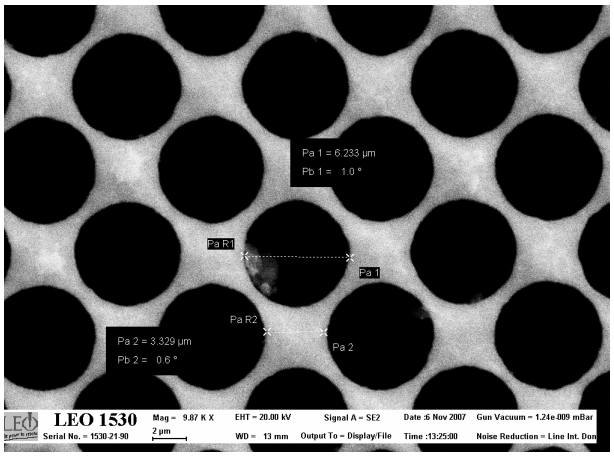

Figure 5.10: SE2 picture of the MCP channels. The diameter is 6 μm and the gap distance is 3 μm.

SEM images in EBIC mode were taken for the structure 4 of the H4G3 sample, some of the acquired images are shown in Figure 5.12. The energy of the electrons was of 30 keV, the beam aperture was set at 120 μm, which corresponds to a current of 5600 pA as defined by the ESRF calibration. This leads to about $\frac{5.6\ 10^{-9}}{1.602\ 10^{-19}} \approx 3\ 10^{10}\ electrons/s$ or 30 $electrons/ns$ sent to the sample.

On these pictures, the increase in output current generated in the structure is seen as an increase in brightness over the surface of the structure. It is thus possible to see where in the a-Si:H MCP a current is induced by interacting electrons.

From those EBIC images, some observations can be made:

- The background current I_g (no beam) of the pointed structures is high ($1\ \mu A < I_g < 30\ \mu A$) compared to the current increase ΔI under electron beam ($10\ nA < \Delta I < 100\ nA$). Hence the output

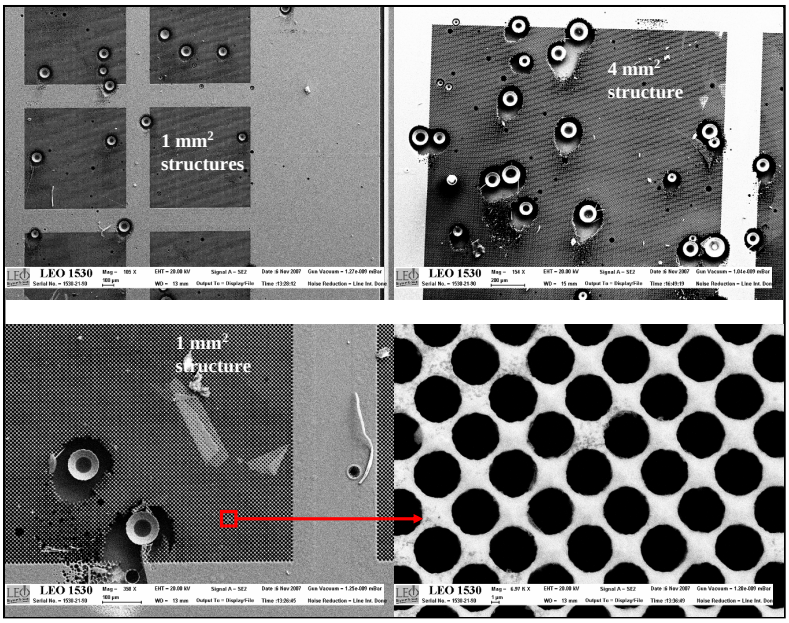

Figure 5.11: SEM picture in SE2 mode of the sample structures. 1 mm^2 structures (top left: structure 8 and bottom left: structure 7), 2 mm^2 structure 23 (top right) and channels organization (bottom right).

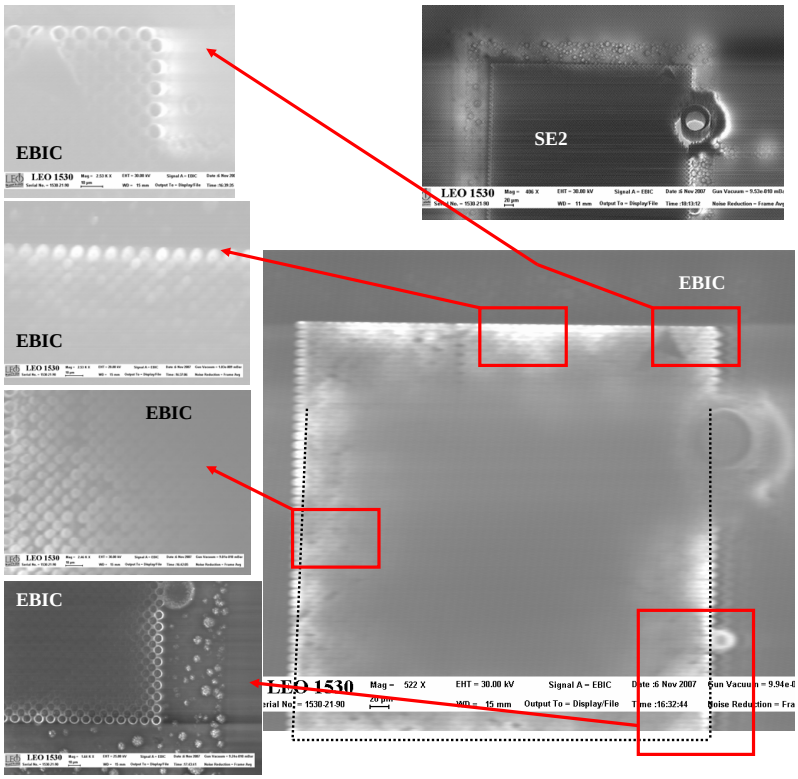

Figure 5.12: EBIC image of the structure 4 in the bottom right part (large) and in the left part. SE2 picture of the damage on the top right part. E=30 keV, beam aperture=120 μm, current=5600 pA.

voltage V_o from the transimpedance amplifier ($V_o = I_g \times 100$ [V]) was compensated with a constant voltage V_c so that $V_o - V_c \approx 0$.

In order to get good contrast on the images, the number of electrons sent by the beamer to a single hole is high. In the case of the images shown on the left part of Figure 5.12, the frame rate is fr=377 ms. It was chosen to leave enough time for the MCP channels to recharge between 2 successive images. In these pictures, the ratio of one hole area to the total scanned surface is $Sr \approx 2\ 10^{-3}$. With the intensity I=30 $electrons/ns$ sent to the sample, as 20% of the electrons are backscattered, the number of electrons N_e reaching one channel is:

$$N_e = I\ Sr\ fr\ 0.8 = 2.17\ 10^7\ electrons/pore. \tag{5.1}$$

- The brightest part of the picture coincides with the borders of the observed structure, the area outside the structure is dark. Therefore, an increase of current after electron interaction is observed in the MCP structure, which could possibly mean that a cascade of secondary electrons has occurred in the pores.

To confirm this hypothesis, a zoom was done on the structure in EBIC mode to focus on the pores only. The images obtained are shown in Figure 5.13.

It should be noted that while zooming on the pores, degradation in picture contrast can be observed. If the image is remade on the same part some 60 s later, the contrast is coming back to its original state. This might be due to a charging effect in the walls and in the bulk of the MCP. Therefore in order not to degrade the sample, the images were taken at different positions.

Maximum contrast is observed on the pores borders, and not inside the pores. This is explained as the electrons are sent perpendicularly to the surface. As shown in Figure 5.14, 3 cases are possible:

1. The electron beam hits the surface. Secondary emission of electron in vacuum is possible, but these do not reach a channel wall to generate further electrons. They are collected by the a-Si:H and do not increase the current.

2. The electron beam hits the corner of the pores so that secondary electrons are generated and trapped by the electric field, so that they can hit the pore wall to generate a cascade of further secondary electrons. In this case, an increase of signal can be measured.

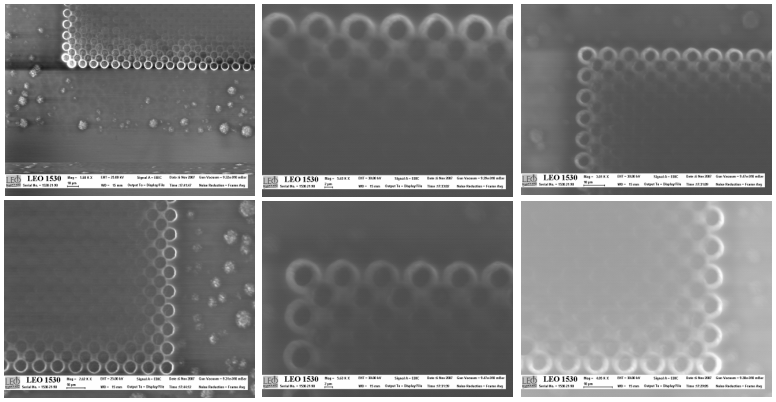

Figure 5.13: structure 4 , zoom on the border and on the inner holes with different voltage amplification and different scan speed to try to get better contrast.

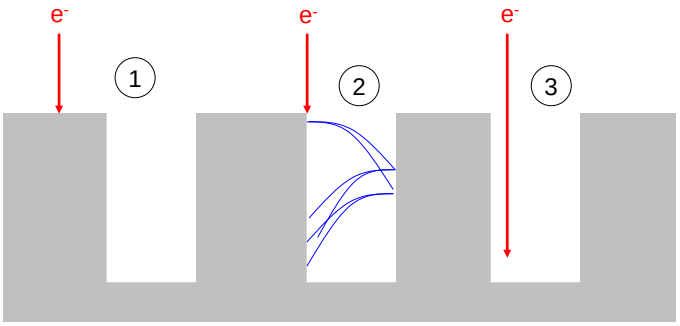

Figure 5.14: Three possibilities of electron interaction with the MCP.

3. The electron beam hits the bottom of the pore. no interaction with the walls occurs and no cascade of secondary electrons can be triggered. In this case no increase of current can be measured.

Now, the electron beam axis is angled with the sample surface normal, increasing the chances to hit the pore walls, so that an increase of current can observed for larger possibility of beam positions, even inside the pores. The EBIC pictures obtained with beam angles of 5^o and 20^o are shown in Figure 5.15.

The pictures with an angled beam impact support the hypothesis of a current increase being induced by secondary electron cascade.

However, only the pores at the extremity of the MCP structures can be observed in EBIC mode with enough contrast. No increase of signal is observed at the interior of the structures. A possible explication could be the following. The top layer of the MCPs is n-doped a-Si:H whose role is to increase the conductivity. Since the leakage current flowing through the

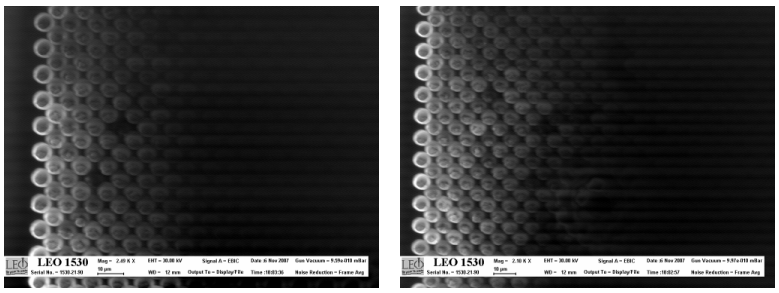

Figure 5.15: Structure 4 in EBIC mode with a beam angle of 5 degrees (left) and 20 degrees (right).

gaps of the pores perturbs the overall bias on the structure, the electric field decreases as a function of the distance from the borders as shown in Figure 5.16.

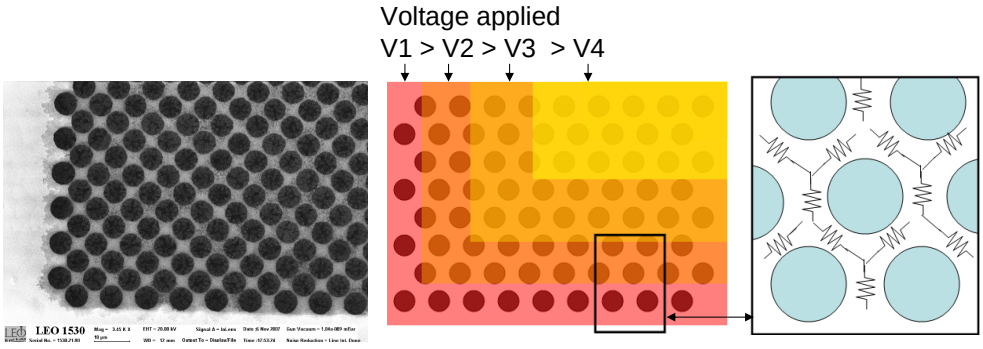

Figure 5.16: Left: picture of a MCP corner. Middle: schematic of the same MCP corner with a color representation of the bias applied on the top of the structure. Right: schematic of the top layer resistivity between holes.

In order to overcome this problem, the bias of the MCP is increased from 300 V to 450 V. The resulting pictures are shown in Figure 5.17.

The increase of voltage has a direct impact on the picture contrast, in good agreement with the measurements done with the electron gun shown in Figure 5.7. This implies that an increase of current is measured at larger distances from the structures borders, as the voltage applied increases. This reinforces the hypothesis that the resistivity of the top n-doped a-Si:H layer is too high, reducing the effective bias applied inside the structures.

in order to improve the samples, a top layer with better conductivity (like a metal layer) should be deposited on the top of the MCP, in order to establish uniform bias on the whole structures.

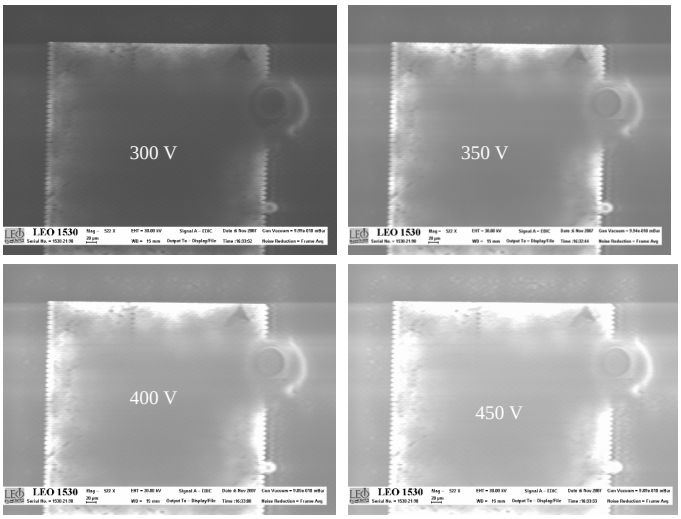

Figure 5.17: EBIC picture of structure 4, E=30 keV, beam aperture=120 μm, current=5600 pA for 300 V applied (top left), 350 V (top right), 400 V (bottom left) and 450 V (bottom right).

5.4 Conclusion and outlook

These measurements are the first ever made on the first prototypes of a-Si:H MCPs. Some promising results were obtained.

First, an increase of current measured in the MCPs is caused by the interaction of electrons sent from an e-gun at CERN.

Second, measurements in EBIC mode made at the ESRF have shown that the current increase takes place along the pores borders of the MCP rather than in the a-Si:H bulk. This support the hypothesis of secondary electrons generation through cascade mechanism inside the pores.

However those first samples have shown some flaws which need to be overcome in order to fully demonstrate the proof of concept for such a new photodetector.

The columnar damages found in the structure are suspected to cause a high increase in leakage current. This high leakage current (typically 10 μA) forced to send a higher number of electrons on the sample to distinguish a current signal. The deposition method and DRIE should be optimized in order to avoid the damages.

Moreover, there are good reasons to believe that the bias is not applied uniformly across the entire MCP surface because of too resistive n-doped top layer effectively reducing the bias away from the borders. In order to solve this problems, a thin aluminum layer (200 nm thick) has already been deposited on the MCP surface. therefore, new measurements at the ESRF are foreseen with the improved second generation of a-Si:H MCPs.

Chapter 6

Conclusion and perspectives

The work presented in this thesis was mainly motivated by the recent promising developments in solid state photodetectors. These offer high quantum efficiency, high compactness and excellent tolerance to magnetic field, properties that are not offered with vacuum photodetectors. They become widely used in various fields such as high energy physics, space applications, biotechnologies or biomedical imaging.

However, vacuum photodetectors still offer better time resolution so that their progressive replacement by solid state technology has to go with improvements in this particular domain, as required by most of the applications mentioned before.

Through the different projects and scientific collaborations in which I was involved during this thesis, I have studied the potential of detection systems based on a scintillator coupled to a photodetector and read out by fast electronics developed at CERN. The aim was to take advantage of the good timing characteristics of the electronics to assess the performances of a complete detector system based on solid state photodetectors such as APD and SiPM. The different elements of the detector system were studied, and their influence on the overall time resolution was measured.

In the following, I will draw my conclusions from my personal contributions to the work made in the different fields explored and give perspectives for future work.

PET/CT detector based on APD+NINO

The work done during my thesis was initially motivated by the development of a PET/CT detector head based on LSO and APD readout.

Another important goal was to apply the time over threshold technique

to the field of biomedical imaging and in particular to the PET/CT work in the context of the European FP6 BioCare project. This is the first time that this technique is applied to a field other than high energy physics. Because of the excellent intrinsic timing properties of the NINO chip (≤ 10 *ps* rms at 10 pF input capacitance), not only the energy resolution but also the timing potential of the new detector system could be assessed.

A test setup comprising 2 identical detector systems in coincidence was developed. Each one is composed of a LSO scintillator, an APD and the NINO readout electronics. The energy resolution for one detector was measured at 16% for 511 keV γ-rays. This is comparable to the resolution that can be obtained with PMT based systems. This means that the higher quantum efficiency of the APD compensates for its lower gain.

Conversely, the time resolution for 2 such detectors in coincidence was demonstrated to be of 1.6 ns FWHM. This is 3 times worse than what one could obtain with PMT based systems under the same conditions. In this case the contributions on the time precision of the different elements of the detector system were extracted. The relative contribution of the electronics, APD and LSO were found to account for 20%, 30% and 50% of the total time resolution, respectively.

However, the fact that the LSO crystal contributes so strongly to the time resolution is attributed to the readout mechanism of the APD. The relatively low gain of the APD prevents the photodetector from detecting fewer than 20 photoelectrons coming from the LSO whereas the PMT is sensitive to a single photon. Therefore, even with lower quantum efficiency, the PMT still offers better time precision.

This thesis has then demonstrated that the time resolution of the detector system is severely limited by the APD inability to detect single photon because of its insufficient gain. On the other hand, the contribution of the readout electronics is not a limiting factor so that the readout system could be improved by replacing the APD with its successor of still higher gain, operated in Geiger mode: the SiPM.

As far as dynamic range and energy resolution are concerned, the APD based system was also studied with 122 keV X-rays and 511 keV γ-rays, to assess its potential for combined PET-CT imaging with the same readout. Whereas the identification of 511 keV γ-rays could be done with adequate resolution, the peculiar characteristic of the FEDC05-NINO system together with the non linear response of LSO at low input charge made a determination of the resolution for the CT X-rays very

difficult.

SiPM

The high gain of the SiPM permits to directly connect the NINO chip to the photodetector, in the case where only few photons are detected. The study of a $1 \times 1\ mm^2$ SiPM has demonstrated that the time resolution of the SiPM coupled to the NINO chip is of 180 ps rms for the detection of single 405 nm photon.This measurement already shows that a detector system made of a SiPM read out by NINO has a high potential of excellent time precision at the level of 1 photon which could be used in the domain of Cerenkov light detection, fluorescence spectroscopy and TOF in PET.

In the case of PET, the response of the SiPM to LSO photons following the interaction of a 511 keV γ-ray was modeled in this work, showing a good agreement with measurements done by [Kim 09, Spanoudaki 07]. Since in this case the SiPM output current is too high to be directly read out by the NINO circuit, a differentiating circuit was developed as an interface to the effect that it decreases the total current without losing the first photons required for timing.

However, the typical size of LSO crystals ($2 \times 2\ mm^2$) together with the high number of SPAD cells required to detect the photons emitted by the LSO implies that larger size SiPM ($3 \times 3\ mm^2$) have to be used. The work done during the thesis has shown a crucial influence of the SiPM terminal capacitance, which may be as high as 320 pF for the Hamamatsu SiPM of $3 \times 3\ mm^2$. In contrast with SiPMs of smaller size, this capacitance in parallel with a load resistance (e.g. scope or NINO) is large enough to significantly increase the rise time of the SPAD signals to the extent that the timing performance of the ensemble is severely degraded. New interface electronics could permit to overcome this problem.

Timing uncertainty due to scintillation process

At least 3 different contributions to the time resolution from the scintillation process, and in particular that of LSO, were identified.

First, the rise time of the emitted light intensity in LSO following a 511 keV γ-ray conversion has an influence on the time resolution estimated to be in the order of some tens of picoseconds. This effect is usually neglected. However the measurement of this value is difficult, requiring very fast detection systems and was not pursued in this work.

Second, the different propagation paths of each generated photon in a LSO crystal of 1 cm length induce propagation time fluctuations in the time of detection. This was calculated to be 75 ps FWHM and is mainly determined by the crystal length.

Third, a detailed study of the statistics of photon production in a scintillator based on [Post 50] was done and adapted to the LSO case. This study demonstrates that the detection of the first photon emitted by the scintillator will induce a lower time jitter than any other photon detected thereafter. The minimum time resolution achievable in a detector system using a LSO crystal was calculated through 3 parameters: the total number of photons R sensed by the photodetector, the minimum number of photons Q out of R which trigger the signal, and the light decay time τ of the scintillator. Following only statistical arguments and with $\tau = 40\ ns$, R=2200 photons, jitter amounts to 18 ps rms for Q=2 and increases to 340 ps rms for Q=20.

Therefore in a detector system, the use of a scintillator implies an intrinsic limit of the achievable time resolution. This resolution could in principle be improved if one chose crystals of shorter length, with a higher light yield and shorter decay time. Typically, for LSO crystals of size $2 \times 2 \times 10\ mm^3$, this timing limit is in the order of 80 ps, highly dominated by the photons' propagation fluctuations in the crystal.

MCP

In order to further improve on time resolution, a novel photodetector was investigated for the first time: the MicroChannel Plate made of Hydrogenated amorphous Silicon (a-Si:H MCP). The use of a resistive material such as a-Si:H for the bulk of the MCP should overcome the limitations in existing MCPs, in particular the long recharging time per channel. Moreover, the possibility to deposit a-Si:H directly on top of ASIC permits to directly integrate the sensor on the readout electronics. This technology is named Thin Film on ASIC (TFA) technology and is widely described in [Despeisse 06].

The study of the first samples developed has shown that columnar defects in the structure were responsible for high leakage currents. Moreover, measurements in the Electron Beam Induced Current (EBIC) mode of a Secondary Electron Microscope (SEM) have revealed that the bias was not applied uniformly across the whole SiPM structure. This could be due to too high resistivity of the n-doped top layer of a-Si:H.

Although this technology is promising, significant improvements in the deposition and etching method should be made.

Nevertheless, it was shown in the course of my work that a current increase takes place along the borders of the MCP pores, possibly indicating the generation of a cascade of secondary electrons.

Further measurements on improved samples are required to demonstrate proof of concept of this novel technology.

Perspectives

The evolution of PET goes with improvement in time resolution, permitting to measure the time of flight of collinear photons along the LOR. In this case, one speaks of TOF-PET. If one really wants to achieve the best possible time precision, only SiPMs, PMTs or MCPs should be used in a TOF-PET system. In this thesis, it was shown that the coincidence time resolution of a PMT based detector system can reach 470 ps FWHM whereas SiPM have shown to obtain a time resolution of 580 ps FWHM [Kim 09, Spanoudaki 07]

An increasing trend in medical imaging is the construction of dual mode systems, where the metabolic information from TOF-PET is combined with the anatomic information from CT or MRI. In case of dual PET/MRI the choice of photodetector is limited to solid state detectors since only these are not sensitive to the magnetic field in MRI mode.

If timing is not an issue like in TOF-PET, APDs are still suitable devices in PET because of their high quantum efficiency and energy resolution. A remaining problem in SiPM is its high terminal capacitance, requiring improved electronics between the photodetector and the NINO in order to take advantage of the full timing potential of both devices.

Irrespective of the photodetector to be used, the time based readout was shown to be a reliable readout method as it does not compromise in energy and time resolution, and provides a simple, robust and economic solution for future scanners.

This work so far has not addressed the issue of integrating a very large number of detector channels into a concrete medical imaging system. It is within the so called IRPICS project that one will integrate a new version of NINO comprising 32 channels, with the HPTDC of 25 ps bin size to a compact, purely digital, integrated readout system.

Appendix A

calculation of the LSO crystal activity

This section aims to calculate the specific activity of a 2x2x10 mm^3 LSO crystal which radioactive element is ^{176}Lu. The calculation is taken from [Schleien 98]. The Specific Activity (SA) is the number of becquerels per unit of mass or volume. The specific activity of a carrier free isotope can be calculated as follow: if λ is the transformation constant in seconds, the number of disintegration per second is then the number of becquerels in an aggregation of N atoms.
with $N = \frac{N_a}{A}$, $\lambda = \frac{ln2}{T}$, N_a the Avogadro constant in atoms / mole, A the atomic weight in g / mole and T the half-life of the radioisotope in s.

$$SA = N\lambda = \frac{N_a}{A}.\frac{ln2}{T} = \frac{ln2 \ \times \ 6.0210^{23}}{1.19 \ 10^{18} \ \times \ 174.967} = 1998.83 \ Bq/g \quad \text{(A.1)}$$

The volumic mass of Lu_2SiO_3 is 7.41 g / cm^3.
The volume of the crystal is : $0.2 \times 0.2 \times 1 \ = \ 0.04 \ cm^3$.
The mass of the crystal is then of : $0.04 \times 7.41 \ = \ 0.296 \ g$.

The massic percentage M of the Lu in Lu_2SiO_3 is:

$$M = \frac{2M_{Lu}}{2M_{Lu} + M_{Si} + 3M_O} = \frac{2 \times 174.96}{2 \times 174.96 + 28.08 + 3 \times 16} = 82\% \quad \text{(A.2)}$$

Then the mass of Lu in the crystal is $0.296 \times 0.82 \ = \ 0.243 \ g$.
As there is 2.59 % of ^{176}Lu in the natural Lu, its mass per crystal is : $0.0259 \times 0.243 = 6.29 \ 10^{-3} \ g$

The total activity A of the crystal is then :

$$\boxed{A = 1998.83 \times 6.29\ 10^{-3} = 12.58\ Bq} \tag{A.3}$$

If this value is negligible compared to a source of some kBq it is still visible on some spectra and has to be taken into account.

Appendix B

Used devices datasheets

Photomultiplier XP2020Q

12-stage
51mm (2"), Round tube

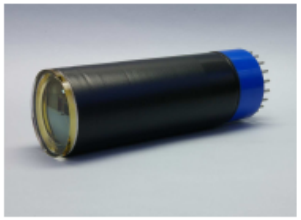

Applications
- ✓ Energy physics

Features
- ✓ Very Fast
- ✓ UV-sensitive
- ✓ Very low noise
- ✓ Good linearity

Description

Window material	Fused silica
Photocathode	Bi-alkali
Refr. Index at 420nm	1.48
Multiplier structure	Linear focused

Photocathode characteristics	Min	Typ	Max	Unit
Spectral range :		150-650		nm
Maximum sensitivity at :		420		nm
Sensitivity :				
Luminous :		70		µA/lm
Blue * :	7.5	10		µA/lmf
Radiant, at 420nm		80		mA/W
Characteristics with voltage divider A	**Min**	**Typ**	**Max**	**Unit**
Gain slope (vs supp. Volt., log/log)		9		
For a gain of		$3x10^7$		V
Supply voltage *	1750	2000	2600	V
Anode dark current *		10	100	nA
Background noise *		900	2500	cps
Single electron spectrum resolution		70		%
Peak to valley ratio		2.5		
Pulse amplitude resolution for ^{137}Cs		7.2		%
Gain halved for a magnetic field of :				
Perpendicular to axis "n" :		0.15		mT
Parallel to axis "n" :		0.12		mT
For a supply voltage of : 2000V	**Min**	**Typ**	**Max**	**Unit**
Linearity (2%) of anode current up to :		25		mA
Anode pulse :				
Rise time :		1.6		ns
Duration at half height :		3.7		ns
Transit Time :		28		ns

Typical spectral

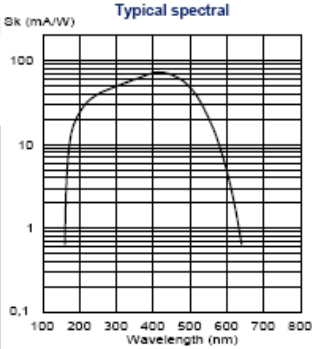

Typical gain curve

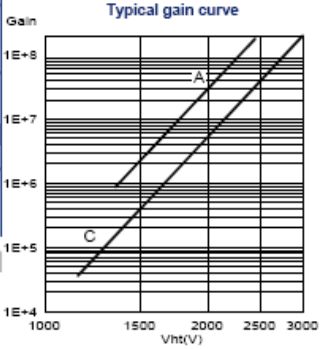

Recommended Voltage Divider

Type A for maximum gain

K	G	D1	D2	D3	D4	D5	D6	D7	D8	D9	D10	D11	D12	A	
1.2	2.8	1.2	1.8	1	1	1	1	1	1	1	1	1	1		(total : 17)

Type C for linearity

K	G	D1	D2	D3	D4	D5	D6	D7	D8	D9	D10	D11	D12	A	
1.2	2.8	1.2	1.8	1	1	1	1	1	1	1.5	1.5	3	2.5		(total : 21.5)

** characterisic measured and mentioned on the test ticket of each tube*

PHOTONIS

24/07/2007

Photomultiplier XP2020Q

Outline (dimensions in mm)

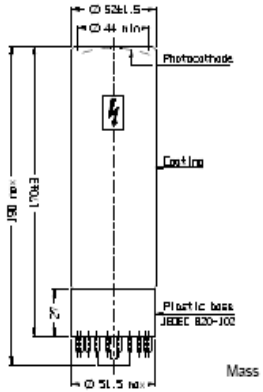

Mass : 240g

Accessories :
Socket : FE1120
Mu-metal shield : MS172
Voltage divider : VD124K/T

K: cathode
sp: short pin
G: focusing electrode

Dn: dynode
ic: internal connection
n: plane of symetry of the multiplier

A: anode
nc: not connected

nc: not connected
Ct: coating

Limiting values	Min	Max	Unit
Anode Luminous sensitivity		$2x10^5$	
Supply voltage		3000	V
Continuous anode current		0.2	mA
Voltage between :			
G and photocathode :		300	V
First dynode and PK :	210	800	V
Consecutive dynode (except 11 & 12) :		400	V
Dynodes D11 and D12 :		600	V
Anode and D12:	80	700	V
Ambient temperature :			
Short operation (<30 mn) :	-30	+80	°C
Continuous operation & storage :	-30	+50	°C

Variants

XP2020Q

Finishing
F with flying leads ⌀ 0.5
FB with flying leads and plastic base

Also, other variants can be made. Please, contact us to discuss any specific product requirements.

PHOTONIS

24/07/2007

HAMAMATSU

PHOTOMULTIPLIER TUBE ASSEMBLIES H6533/H6610

High Speed Response (Rise Time = 0.7ns, TTS = 0.16ns FWHM)
25mm (1 Inch) Diameter, 10 - stage, Bialkali Photocathode, Head - On Type

GENERAL

Parameter		H6533	H6610	Unit
Assembled Photomultiplier Tube		R4998	R5320	—
Spectral Response		300 to 650	160 to 650	nm
Wavelength of Maximum Response		420		nm
Photocathode	Material	Bialkali		—
	Minimum Effective Area	20		mm dia.
Window Material		Borosilicate glass	Synthetic silica	—
Dynode	Structure	Linear focused		—
	Number of Stages	10		—
Case		Magnetic shield case		—

MAXIMUM RATINGS (Absolute Maximum Values)

Parameter		Description/Value	Unit
Supply Voltage	Between Anode and Cathode	-2500	Vdc
Voltage Divider Current		0.36	mA
Average Anode Current		0.016	mA
Ambient Temperature		-30 to +50	°C

CHARACTERISTICS (at 25 °C)

Parameter		Min.	Typ.	Max.	Unit
Cathode Sensitivity	Luminous (2856 K)	60	70	—	μA/lm
	Blue (CS 5 - 58 filter)	6	9	—	μA/lm-b
Anode Sensitivity	Luminous (2856 K)	100	400	—	A/lm
Gain		—	5.7×10^6	—	—
Anode Dark Current (after 30 min. storage in darkness)		—	100	800	nA
Time Response	Anode Pulse Rise Time	—	0.7	—	ns
	Electron Transit Time	—	10	—	ns
	Transit Time Spread (T.T.S.)	—	0.16	—	ns

NOTE: Anode characteristics are measured with the voltage distribution ratio shown below.

VOLTAGE DISTRIBUTION RATIO AND SUPPLY VOLTAGE

Electrodes	K	G	Dy1	Dy2	Dy3	Dy4	Dy5	Dy6	Dy7	Dy8	Dy9	Dy10	P
Ratio	1.3	4.8	1.2	1.8	1	1	1	1	1	1.5	3	2.5	

Supply Voltage: -2250 Vdc, K: Cathode, Dy: Dynode, P: Anode, G: Grid
Acc to be connected to Dy7

PHOTOMULTIPLIER TUBE ASSEMBLIES H6533/H6610

Figure 1: Typical Spectral Response

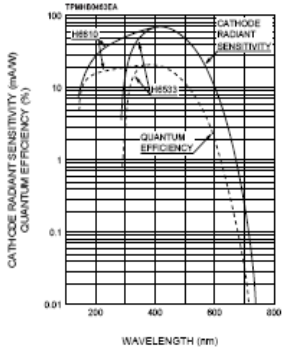

Figure 2: Typical Gain and Anode Dark Current

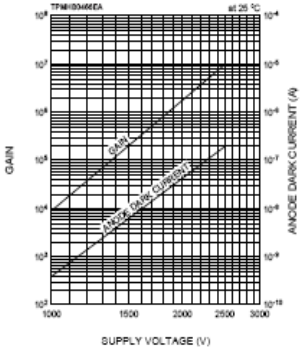

Figure 3: Dimensional Outline and Circuit Diagram (Unit: mm)

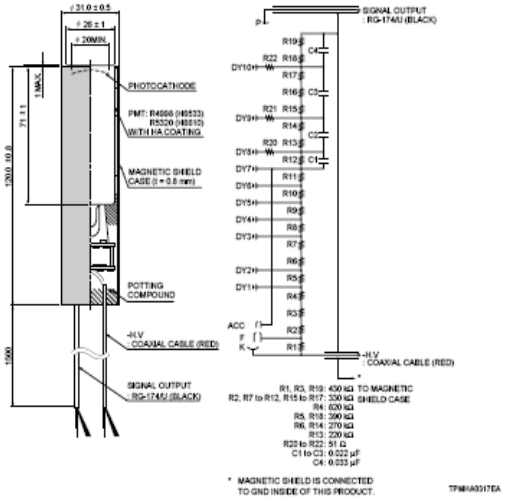

HAMAMATSU

HAMAMATSU PHOTONICS K.K., Electron Tube Center
314-5, Shimokanzo, Toyooka-village, Iwata-gun, Shizuoka-ken, 438-0193 Japan, Telephone:(81)539/62-5248, Fax:(81)539/62-2205
U.S.A.: Hamamatsu Corporation: 360 Foothill Road, P.O.Box 6910, Bridgewater, N.J. 08807-0910, U.S.A., Telephone:(1)908-231-0960, Fax:(1)908-231-1218
Germany: Hamamatsu Photonics Deutschland GmbH: Arzbergerstr. 10, D-82211 Herrsching am Ammersee, Germany, Telephone:(49)8152-375-0, Fax:(49)8152-2658
France: Hamamatsu Photonics France: S.A.R.L.: 8, Rue du Saule Trapu, Parc du Moulin de Massy, 91882 Massy Cedex, France, Telephone:(33)1 69 53 71 00, Fax:(33)1 69 53 71 10
United Kingdom: Hamamatsu Photonics UK Limited: Lough Point, 2 Gladbeck Way, Windmill Hill, Enfield, Middlesex EN3 7JA, United Kingdom, Telephone:(44)181-367-3560, Fax:(44)181-367-6384
North Europe: Hamamatsu Photonics Norden AB: Färögatan 7, S-164 40 Kista, Sweden, Telephone:(46)8-703-29-50, Fax:(46)8-750-58-95
Italy: Hamamatsu Photonics Italia S.R.L.: Via della Moia, I/E 20020 Arese, (Milano), Italy, Telephone: (39)2 935 81 733 Fax: (39)2 935 81 741

TPMH1199E01
FEB. 1998 SI
Printed in Japan (500)

NEW

APD

Si APD array
S8550

4 x 8 element APD array with low noise and enhanced short-wavelength sensitivity

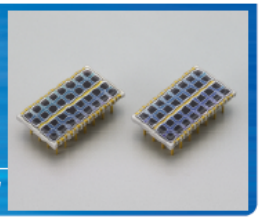

S8550 is an APD (avalanche photodiode) array designed for short wavelength detection, featuring low noise and low terminal capacitance. S8550 also offers uniform gain and small cross-talk between each element.

Features

- High sensitivity and low noise in short wavelength region
- Low terminal capacitance
- Optimized for blue light detection
- Uniform gain and low cross-talk variation between each element

Applications

- Low-light-level photometry in the visible range
- Detector systems combined with scintillator

■ General ratings

Parameter	Rating	Unit
Element size	1.6 × 1.6 (× 32 elements)	mm
Element pitch	2.3	mm
Package	Ceramic	-
Window material	Epoxy resin	-

■ Absolute maximum ratings

Parameter	Symbol	Value	Unit
Operating temperature	Topr	-20 to +60	°C
Storage temperature	Tstg	-20 to +80	°C

■ Electrical and optical characteristics (Ta=25 °C)

Parameter	Symbol	Condition	Min.	Typ.	Max.	Unit
Spectral response range	λ		-	320 to 1000	-	nm
Peak sensitivity wavelength	λp	M=50	-	600	-	nm
Quantum efficiency	QE	λ=420 nm	60	70	-	%
Breakdown voltage	VBR		-	400	500	V
Dark current	ID	per 1 element, M=50	-	10	50	nA
Terminal capacitance	Ct	per 1 element, M=50, f=10 kHz	-	10	-	pF
Gain	M		-	50	-	-

PRELIMINARY DATA
Sep. 2001

SOLID STATE DIVISION

HAMAMATSU

■ Quantum efficiency vs. wavelength

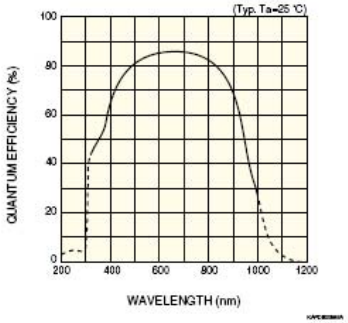

■ Gain vs. reverse voltage

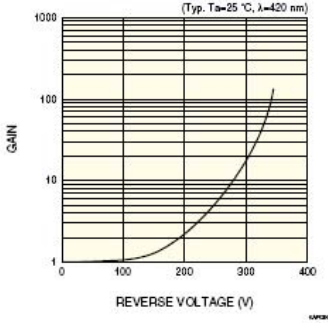

■ Dimensional outline (unit: mm)

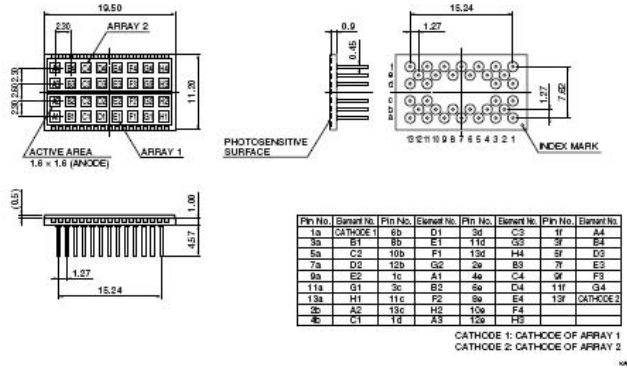

Pin No.	Element No.	Pin No.	Element No.	Pin No.	Element No.	Pin No.	Element No.
1a	CATHODE 1	6b	D1	3d	C3	1f	A4
3a	B1	8b	E1	11d	G3	3f	B4
5a	C2	10b	F1	13d	H4	5f	D3
7a	D2	12b	G2	2e	B3	7f	E3
9a	E2	1c	A1	4e	C4	9f	F3
11a	G1	3c	B2	6e	D4	11f	G4
13a	H1	11c	F2	8e	E4	13f	CATHODE 2
2b	A2	13c	H2	10e	F4		
4b	C1	1d	A3	12e	H3		

CATHODE 1: CATHODE OF ARRAY 1
CATHODE 2: CATHODE OF ARRAY 2

HAMAMATSU PHOTONICS K.K., Solid State Division
1126-1 Ichino-cho, Hamamatsu City, 435-8558 Japan, Telephone: (81) 053-434-3311, Fax: (81) 053-434-5184, http://www.hamamatsu.com
U.S.A.: Hamamatsu Corporation: 360 Foothill Road, P.O.Box 6910, Bridgewater, N.J. 08807-0910, U.S.A., Telephone: (1) 908-231-0960, Fax: (1) 908-231-1218
Germany: Hamamatsu Photonics Deutschland GmbH: Arzbergerstr. 10, D-82211 Herrsching am Ammersee, Germany, Telephone: (49) 08152-3750, Fax: (49) 08152-2658
France: Hamamatsu Photonics France S.A.R.L.: 8, Rue du Saule Trapu, Parc du Moulin de Massy, 91882 Massy Cedex, France, Telephone: 33-(1) 69 53 71 00, Fax: 33-(1) 69 53 71 10
United Kingdom: Hamamatsu Photonics UK Limited: 2 Howard Court, 10 Tewin Road, Welwyn Garden City, Hertfordshire AL7 1BW, United Kingdom, Telephone: (44) 1707-294888, Fax: (44) 1707-325777
North Europe: Hamamatsu Photonics Norden AB: Smidesvägen 12, SE-171 41 Solna, Sweden, Telephone: (46) 8-509-031-00, Fax: (46) 8-509-031-01
Italy: Hamamatsu Photonics Italia S.R.L.: Strada della Moia, 1/E, 20020 Arese, (Milano), Italy, Telephone: (39) 02-935-81-733, Fax: (39) 02-935-81-741

Cat. No. KAPD1009E01
Sep. 2001 DN

Appendix C

Spectra

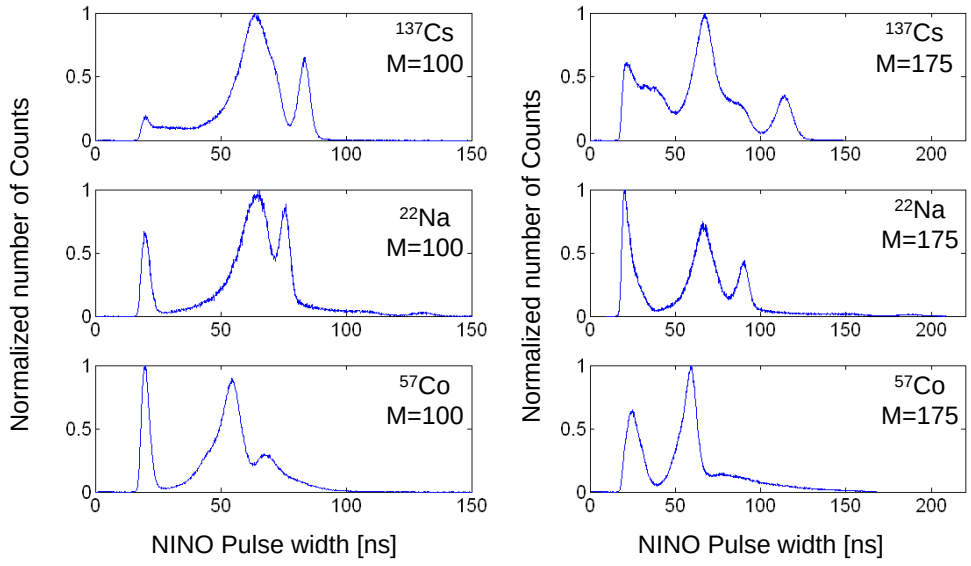

Figure C.1: Histograms of NINO output pulse width for ^{22}Na, ^{57}Co and ^{137}Cs radioactive sources at gain M=100 and M=175, with the crystal 1050.

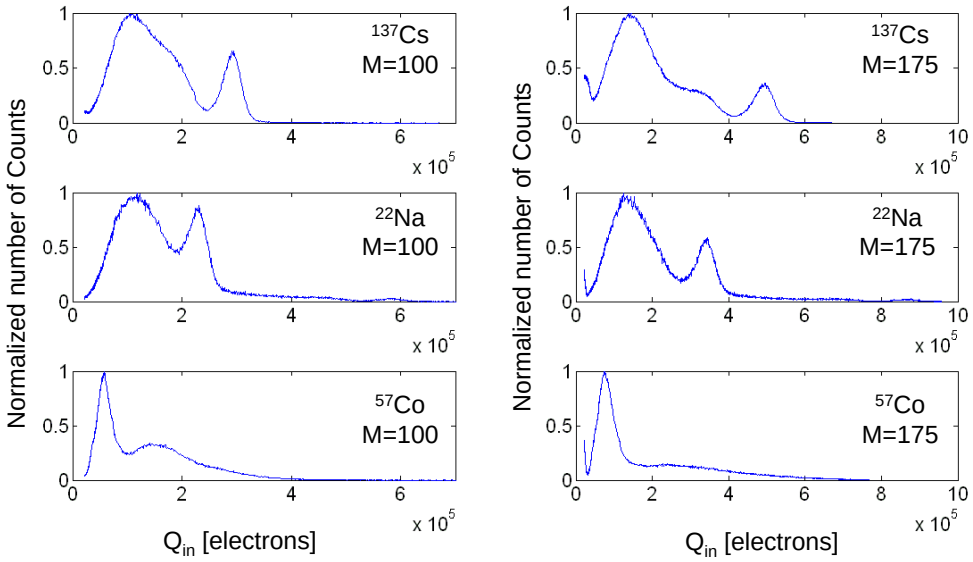

Figure C.2: Histograms of NINO output rescaled in equivalent input charge (number of electrons) for ^{22}Na, ^{57}Co and ^{137}Cs radioactive sources at gain M=100 and M=175, with the crystal 1050.

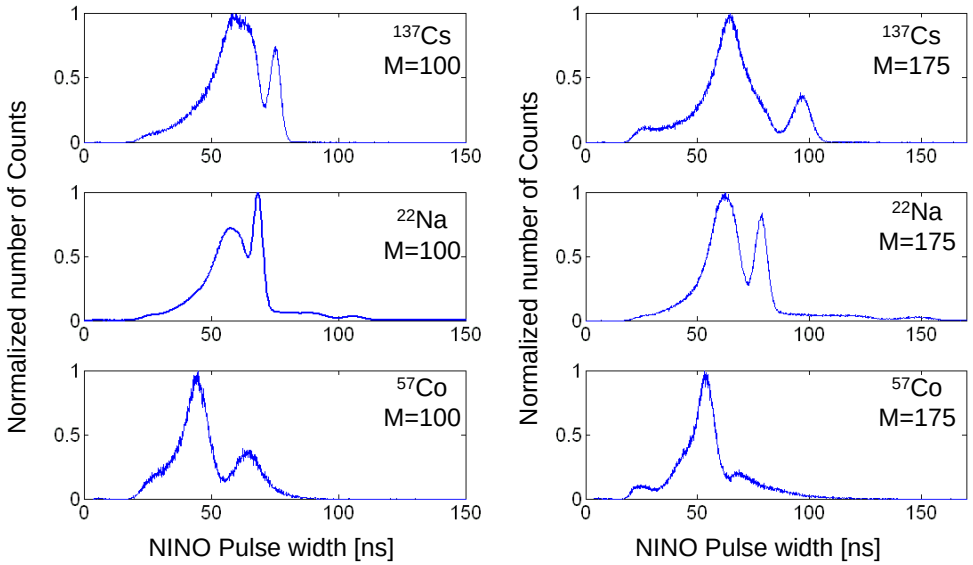

Figure C.3: Histograms of NINO output pulse width for ^{22}Na, ^{57}Co and ^{137}Cs radioactive sources at gain M=100 and M=175, with the crystal 1807.

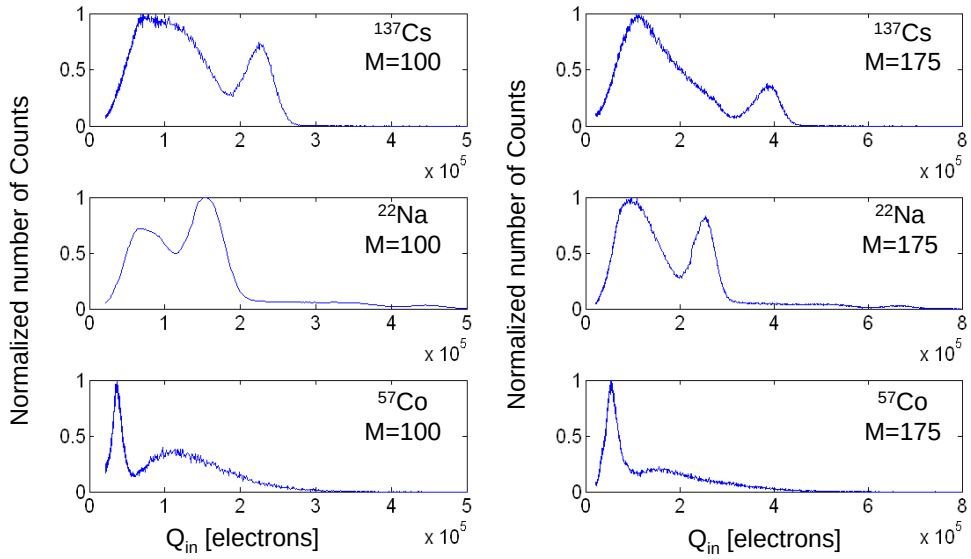

Figure C.4: Histograms of NINO output rescaled in equivalent input charge (number of electrons) for ^{22}Na, ^{57}Co and ^{137}Cs radioactive sources at gain M=100 and M=175, with the crystal 1807.

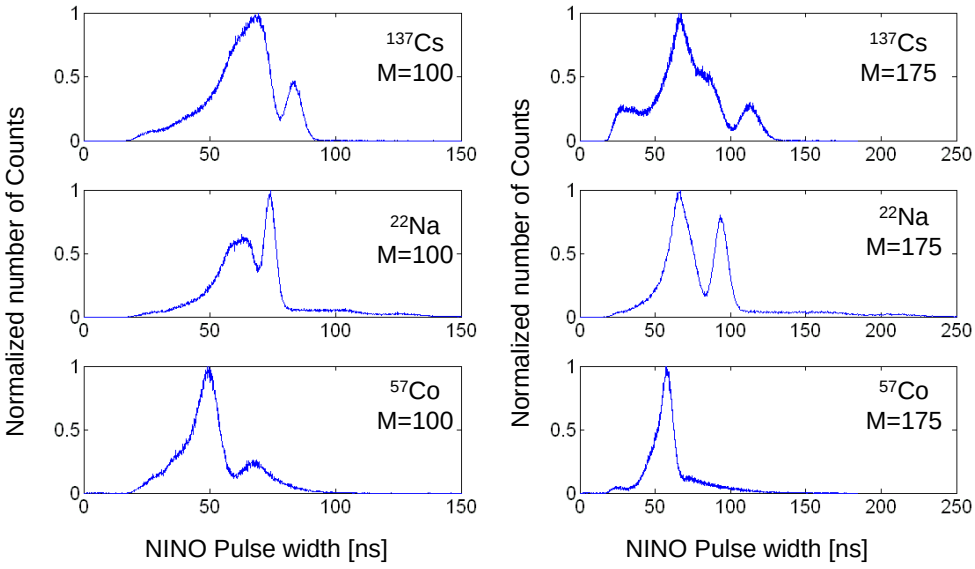

Figure C.5: Histograms of NINO output pulse width for ^{22}Na, ^{57}Co and ^{137}Cs radioactive sources at gain M=100 and M=175, with the crystal LYSO.

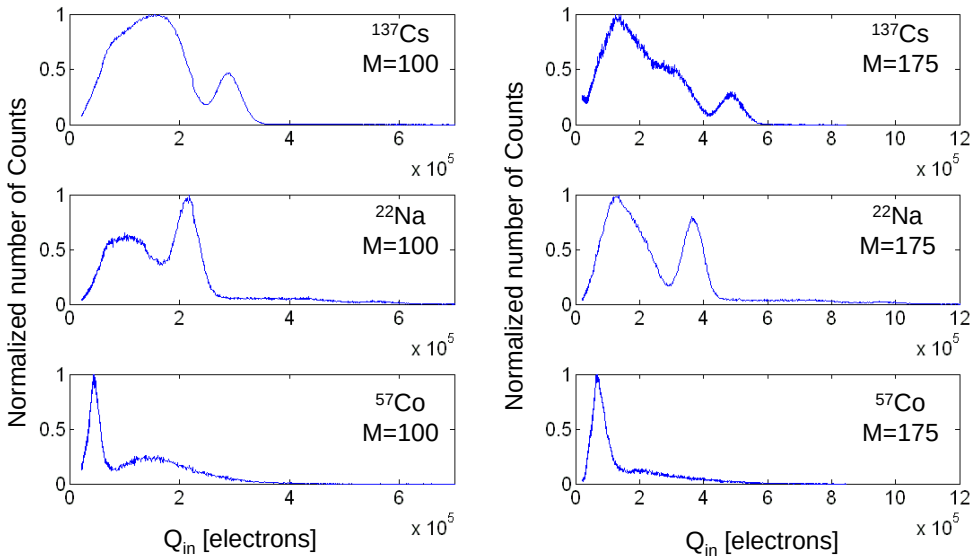

Figure C.6: Histograms of NINO output rescaled in equivalent input charge (number of electrons) for ^{22}Na, ^{57}Co and ^{137}Cs radioactive sources at gain M=100 and M=175, with the crystal LYSO.

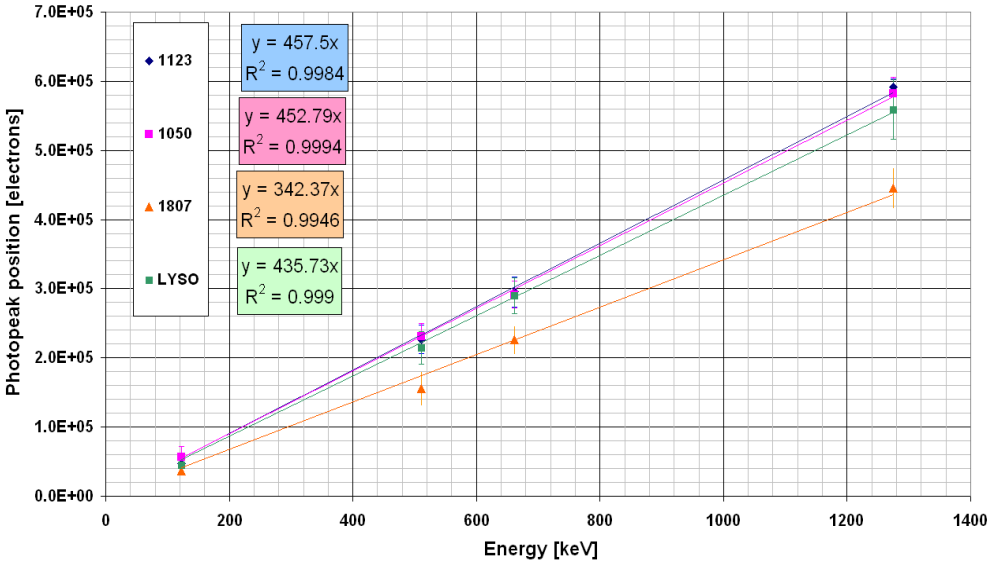

Figure C.7: Photopeak positions as a function of the energy for the 4 crystals studied, at gain M=100.

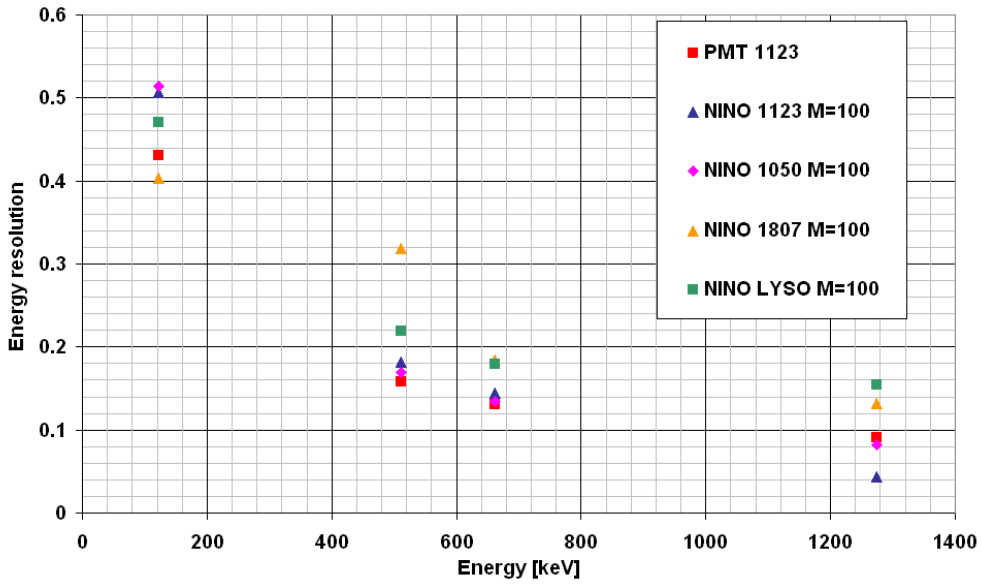

Figure C.8: Energy resolution as a function of the energy for the 4 crystals studied, at gain M=100.

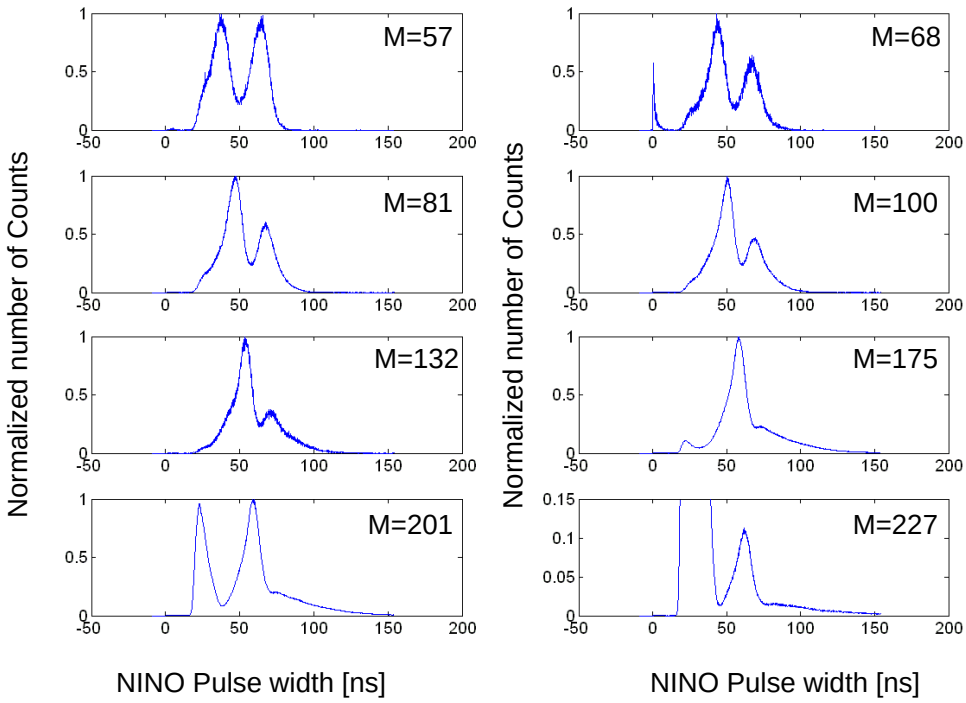

Figure C.9: Histograms of NINO output pulse width for ^{57}Coradioactive source at gains from M=57 to M=227, with the crystal 1123.

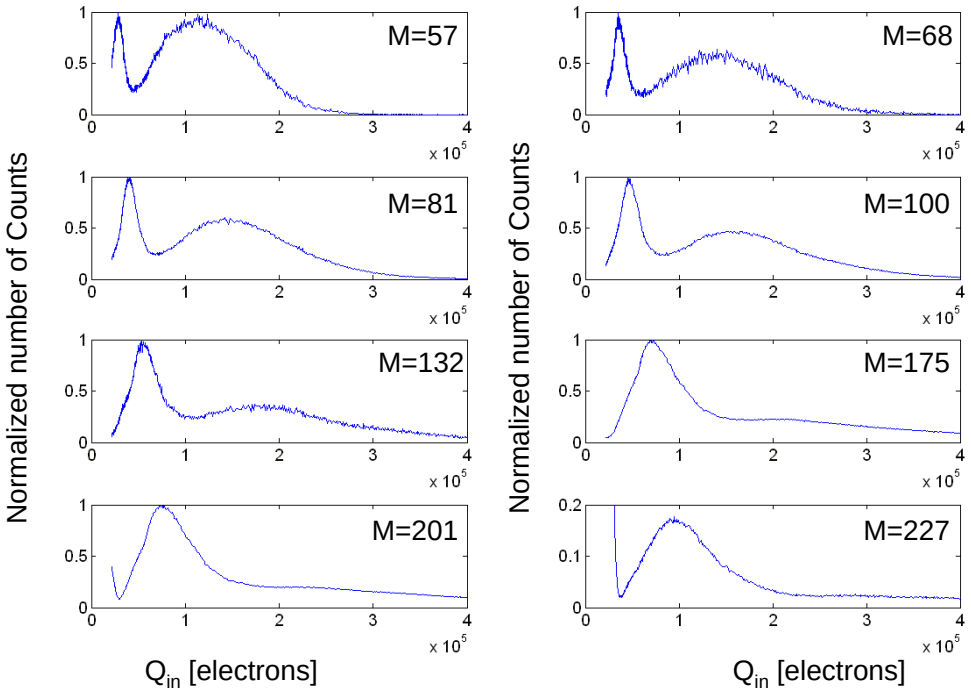

Figure C.10: Histograms of NINO output rescaled in equivalent input charge for ^{57}Coradioactive source at gains from M=57 to M=227, with the crystal 1123.

Appendix D

Second APD based detector system calibration

The second APD plate used in the coincidence setup for timing measurements is calibrated the same way than in chapter 3.1.3. The Figure D.1 and D.2 show similar electronic response to test and LSO-like charges.

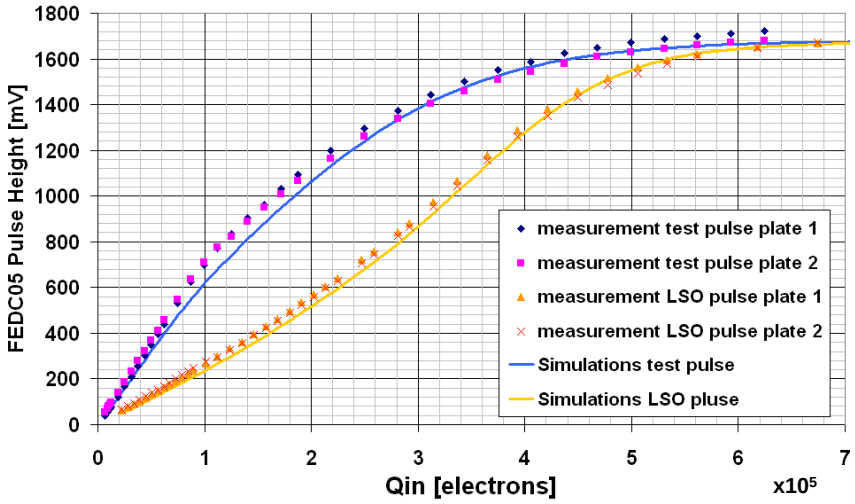

Figure D.1: Simulation and measurements of the FEDC05 pulse height as a function of the input charge for LSO pulses and test pulses, for the two plates used in the coincidence setup.

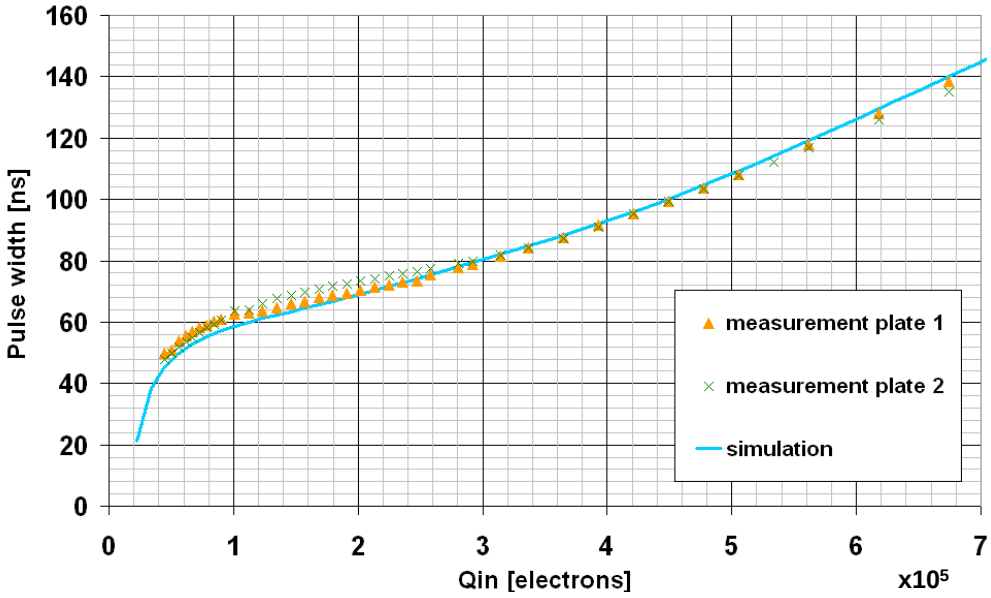

Figure D.2: Simulation and measurements of the NINO pulse width as a function of the input charge for LSO pulses, for the two plates used in the coincidence setup.

Bibliography

[Achenbach 07] P. Achenbach*et al.* *Measurement of propagation time dispersion in a scintillator.* Nuclear instrument and methods, vol. A 578, page 253, 2007.

[Alessio 06] A. Alessio & P. Kinahan. Nuclear medicine (2nd ed.), chapter PET Image Reconstruction. Henkin et al.,, Philadelphia, 2006.

[ALICE] ALICE. *http://aliceinfo.cern.ch.*

[Anghinolfi 04] F. Anghinolfi, P. Jarron, F. Krumenacher, E. Usenko & M. C. S. Williams. *NINO: An Ultrafast Low-Power Front-End Amplifier Discriminator for the Time-ofFlight Detector in the ALICE Experiment.* IEEE Transaction on Nuclear Science, vol. 51, page 1974, 2004.

[ATLAS] ATLAS. *http://atlas.web.cern.ch/Atlas/index.html.*

[BioCare] BioCare. *http://www.biocare-eu.com.*

[Bolle 09] E. Bolle*et al.* *A Novel PET Detector Concept with Full 3D Reconstruction.* to be published in Nuclear Instruments and Methods in Physics Research, 2009.

[Bonanno 09] G. Bonanno*et al.* *Precision measurements of Photon Detection Efficiency (PDE) for SiPM detectors.* to be published in Nuclear Instruments and Methods in Physics Research, 2009.

[Casey 03] M. E. Casey*et al.* *Analysis of timing performance for an APD-LSO scintillation.* Nuclear Instruments and Methods in Physics Research, vol. A 504, page 143, 2003.

[Cavalleri 71] G. Cavalleri*et al.* *Extention of Ramo's theorem as applied to induced charges in semiconductor detectors.* Nuclear Instruments and Methods in Physics Research, vol. 92, page 137, 1971.

[CERN] CERN. *http://www.cern.ch.*

[Christiansen 04] J Christiansen. *HPTDC High Performance Time to Digital Converter.* Technical report, CERN, Geneva, 2004. Version 2.2 for HPTDC version 1.3.

[Corsi 06] F. Corsi*et al.* *Electrical characterization of Silicon Photo-Multiplier Detectors for Optimal Front-End Design.* IEEE Nuclear Science Symposium Conference Record, vol. N30-222, page 1276, 2006.

[Corsi 07] F. Corsi*et al.* *Modelling a silicon photomultiplier (SiPM) as a signal source for optimum front-end design.* Nuclear Instruments and Methods in Physics Research, vol. A 572, page 416, 2007.

[Cova 07] S. Cova*et al.* *Avalanche photodiodes and quenching circuits for single photon detection.* Applied Optics, vol. 35, page 1956, 2007.

[CrystalClear] CrystalClear. *http://crystalclear.web.cern.ch/crystalclear.*

[Dapor 92] M. Dapor. *Monte Carlo simulation of backscattered electrons and energy from thick targets and surface films.* Physical Review B, vol. 46-2, page 618, 1992.

[Despeisse 06] M. Despeisse. *Characterization of a hydrogenated amorphous silicon sensor deposited on integrated circuits for particle detection.* PhD thesis, Institut Nationnal des Sciences Appliquees de Lyon, France, march 2006.

[Dinu 08] N. Dinu*et al.* *Electro-Optical Characterisation of SiPM: A Comparative Study.* Nuclear Instruments and Methods in Physics Research, vol. A, page 1, 2008.

[Dolgoshein 06] B. Dolgoshein*et al.* *Status report on silicon photomultiplier development and its applications.* Nuclear Instruments and Methods in Physics Research, vol. A 563, page 368, 2006.

[ESRF] ESRF. *http://www.esrf.eu.*

[FBK] FBK. *http://soi.fbk.eu/en/research/ios.*

[Hamamatsu] Hamamatsu. *http://sales.hamamatsu.com/ assets/ applications/ ETD/ pmt_handbook/ pmt_handbook_complete.pdf.*

[IMT] IMT. *http://www2.unine.ch/imt.*

[Jarron 96] P. Jarron*et al. A transimpedance amplifier using a novel current mode feedback loop.* Nuclear instrument and methods, vol. A 377, page 435, 1996.

[Kaplon 05] J. Kaplon & W. Dabrowski. *Fast CMOS Front END for Silicon Strip Detectors at LHC Experiment.* IEEE Transaction on Nuclear Science, vol. 52, page 2713, 2005.

[Kapusta 03] M. Kapusta*et al. Hamamatsu S8550 APD array for high resolution scintillator matrices readout.* Nuclear Instruments and Methods in Physics Research, vol. A 504, page 139, 2003.

[Karakash 06] A. Karakash*et al. Timing by silicon photomultiplier: A possible application for TOF measurements.* Nuclear Instruments and Methods in Physics Research, vol. A 567, page 353, 2006.

[Kayama 72] K. Kayama & S. Okayama. *Penetration and energy-loss theory of electrons in solid targets.* Journal of physics, vol. D5, page 43, 1972.

[Kim 09] C.L. Kim*et al. Optimizing timing resolution of SiPM sensors for use in TOF-PET detectors.* to be published in Nuclear Instruments and Methods in Physics Research, 2009.

[Knoll 00] G. F. Knoll. Radiation detection and measurements. John Wiley and sons, Inc, 2000. ISBN:978-0-471-07338-3.

[Kronberger 08] M. Kronberger. *Optimizationof the light extraction from heavy inorganic scintillators.* PhD thesis, Techniche universität, Wien, june 2008.

[Lapington 08] J. S. Lapington*et al. A Multi-channel High Time Resolution Detector for High Content Imaging.* Nuclear instrument and methods, 2008.

[Lecomte 98] R. Lecomte*et al. Investigation of GSO, LSO and YSO Scintillators using Reverse Avalanche Photodiodes.* IEEE Transaction on Nuclear Science, vol. 45, page 478, 1998.

[Lecoq 05] P. Lecoq*et al.* Inorganic scintillators for detector systems. Springer, New York, 2005. ISBN:0-306-40615-2.

[Lynch 66] F. J. Lynch. *Improved Timing With NaI(Tl).* IEEE Transaction on Nuclear Science, vol. 13, page 140, 1966.

[Marlow 04] F. Marlow & S.Eiden. *Refractive index determination on microscopic objects.* European journal of physics, vol. 25, page 439, 2004.

[McCallum 05] S. McCallum. *A four layer attenuation compensated PET detector based on APD arrays without discrete crystal elements.* Physics in medecine and biology, vol. 50, page 4187, 2005.

[McIntyre 66] R. J. McIntyre. *Multiplication noise in uniform avalanche diodes.* IEEE Transaction on Electronic Devics, vol. 13, page 164, 1966.

[Medipix] Medipix. *http://medipix.web.cern.ch/MEDIPIX/.*

[Melcher 91] C. L. Melcher & J. S. Schweitzer. *A promissing new scintillator: cerium doped lutetium oxyorthosilicate.* Nuclear instrument and methods, vol. A314, page 212, 1991.

[Montecchi 01] M. Montecchi*et al. Study of some optical glues for the Compact Muon Solenoid at the large hadron collider of CERN.* Nuclear Instruments and Methods in Physics Research, vol. A 465, page 329, 2001.

[Moses 79] W. W. Moses & M. Ullisch. *Factors influencing timing resolution in a commercial LSO PET camera.* IEEE Transaction on Nuclear Science, vol. 53, page 78, 1979.

[Moses 99] W.W. Moses. *Prospect for Time-of-Flight PET using LSO Scintillators.* IEEE Transaction on Nuclear Science, vol. 46, page 474, 1999.

[Moszynski 03] M. Moszynski*et al. Comparative study of PP0275C hybrid photodetector an XP2020Q photomultiplier in scintillation*

detection. NSS conference records, 19-25 oct. 2003, vol. 2, page 1363, 2003.

[Munyeme 05] G. Munyeme. *Experimental and Computer Modelling Studies of Metastability of Amorphous Silicon Based Solar Cells*. PhD thesis, Utrecht University, Germany, june 2005.

[Musienko] Y. Musienko. *Tutorial given at the NDIP08 conference*.

[Pédrini 05] C. Pédrini. *Scintillation mechanisms and limiting factors on each step of relaxation of electronic excitation*. Phys. Solid State, vol. 47, page 1359, 2005.

[pani 08] R. pani*et al. Ultra High Quantum Efficiency PMT for energy resolution measurements of $LaBr_3(Ce)$ scintillation crystals*. Nuclear instrument and methods, vol. 55, page 1000, 2008.

[Pavlov 05] N. Pavlov*et al. Gamma spectroscopy using a silicon photomultiplier and a scintillator*. IEEE Nuclear Science Symposium Conference Record, vol. N9-3, page 173, 2005.

[Pepin 04] C. Pepin*et al. Properties of LYSO and recent LSO scintillators for Phoswich PET detector*. IEEE Transaction on Nuclear Science, vol. 51, page 789, 2004.

[Photonique] Photonique. *http://www.photonique.ch/Prod_0701BG.html*.

[Pichler 04] B. J. Pichler*et al. Lutetium oxyorthosilicate block detector readout by Avalanche Photodiodes arrays for high resolution animal PET*. Physics in medecine and biology, vol. 49, page 4305, 2004.

[PicoQuant] PicoQuant. *http://www.picoquant.com*.

[Post 50] R. F. Post & L. I. Schiff. *Statistical Limitation on the Resolving Time of a Scintillation Counter*. Phys. Rev., vol. 80, page 1113, 1950.

[Powolny 08] F. Powolny*et al. A Novel Time-Based Readout Scheme For a Combined PET-CT Detector Using APDs*. IEEE Transaction on Nuclear Science, vol. 55, page 2465, 2008.

[PV-lab] PV-lab. *http://pvlab.epfl.ch/*.

[Ramo 39] S. Ramo. *Current induced by electron motion.* Proc. I.R.E., vol. 27, page 584, 1939.

[Sadygov 96] Z. Sadygov. *Russian patent N2086027.* 1996.

[Saleh 07] B. E. A. Saleh & M. C. Teich. Fundamentals of photonics. Wiley, 2007. ISBN:978-0-471-35832-9.

[SAMLAB] SAMLAB. *http://www-samlab.unine.ch/samlabepfl/home.htm.*

[Sark 02] W. Van Sark. *Methods of deposition of hydrogenated amorphous silicon for Device applications.* PhD thesis, Utrecht University, Germany, 2002.

[Schleien 98] Schleien, Slaback & Birky. Handbook of Health Physics and Radiological Health, chapter 8-20. Lippincott Williams & Wilkins, Baltimore, 1998.

[Siegmund 04] W.H. Siegmund. *High performance micro-channel plates detector.* Nuclear Instruments and Methods in Physics Research, vol. A 525, page 12, 2004.

[Spanoudaki 07] V.C. Spanoudaki*et al. Use of single photon counting detector arrays in combined PET/MR: characterization of LYSO-SiPM detector modules and comparison with LSO-APD detector.* JINST 2 P1202, 2007.

[Spieler 05] H. Spieler. Semiconductor detector systems. Oxford science publication, 2005. ISBN:978-0-19-852784-8.

[Staebler 77] D. L. Staebler & C. R. Wronsky. *Reversible conductivity changes in discharge-produced amorphous Si.* Applied Physics Letters, vol. 31, page 292, 1977.

[Street 91] R.A. Street. Hydrogenated amorphous silicon. Cambridge university press, 1991.

[Surti 07] S. Surti*et al. Performance of Philips Gemini TF PET/CT Scanner with Special Consideration for Its Time-of-Flight Imaging Capabilities.* Journal of Nuclear Medicine, vol. 48-3, page 471, 2007.

[Suyama 04] M. Suyama*et al. Development of a Multipixel Hybrid Photodetector With High Quantum Efficiency and Gain.* IEEE Transaction on Nuclear Science, vol. 51, page 1056, 2004.

[Suzuki 93] H. Suzuki & T. A. Tombrello. *Light Emission Mechanism of* $Lu_2SiO_3 : Ce$. IEEE Transaction on Nuclear Science, vol. 40, page 380, 1993.

[TOF] TOF. *http://www.youtube.com/watch?v=kLa36SmiC4Q*.

[Varella 07] J. Varella*et al. Clear-PEM: A PET imaging system dedicated to breast cancer diagnostics*. Nuclear Instruments and Methods in Physics Research, vol. A 571, page 81, 2007.

[Vinke 09] R. Vinke*et al. A Study of Multi-Pixel Photon Counter for TOF PET and its Challenges*. to be published in Nuclear Instruments and Methods in Physics Research, 2009.

[VirginiaSC] VirginiaSC. *http* : *//www.virginiasemi.com/pdf/Optical*%20*Properties*%20*of*%20*Silicon*71502.*pdf*.

[Weber 04] M. J. Weber. *Scintillation: mechanisms and new crystals*. Nuclear instrument and methods, vol. A 527, page 9, 2004.

[Westcott 48] C. H. Westcott. *A study of expected loss rates in the counting of particles from pulsed sources*. Proc. Roy. Soc., vol. A 194, page 508, 1948.

[Wittke] J.H. Wittke. *http://www4.nau.edu/microanalysis/Microprobe/Interact-Effects.html), year = 2006*.

[Wiza 79] J. Wiza. *Microchannel Plate Detectors*. Nuclear Instruments and Methods, vol. 162, page 587, 1979.

[Wright 06] A.G. Wright*et al. Exact expression for the variance of the photon emission process in scintillation counter*. Nuclear Instruments and Methods in Physics Research, vol. A 564, page 185, 2006.

[Wyrsch 08] N. Wyrsch*et al. Performance and Transient Behavior of Vertically Integrated Thin-film Silicon Sensors*. State-of-the-Art Sensors Technology in Switzerland, vol. 8, page 4656, 2008.

[XCOM] XCOM. *http://physics.nist.gov/PhysRefData/Xcom/Text/XCOM.html*. vol. Photon Cross Sections Database.

[Zaidi 07] H. Zaidi*et al. Simultaneous PET/NMR will replace PET/CT as the molecular multimodality imaging platform of choice.* Medical Physics, vol. 34-5, page 1525, 2007.

[Zecotek] Zecotek. *http://www.zecotek.com.*